THE NUMERICAL PREDICTION OF FLOW AND HEAT TRANSFER IN ROD-BUNDLE GEOMETRIES

BY

V. RAMACHANDRA, B.Sc (Eng)

THESIS SUBMITTED FOR THE DEGREE OF
DOCTOR OF PHILOSOPHY
IN THE FACULTY OF ENGINEERING
UNIVERSITY OF LONDON
AND
FOR THE DIPLOMA OF MEMBERSHIP
OF IMPERIAL COLLEGE

Heat Transfer Section,
Mechanical Engineering Dept.,
Imperial College of Science & Technology,
London S.W.7.

May, 1979

TO MY PARENTS

ABSTRACT

A three-dimensional, finite-difference procedure has been utilized in the solution of the parabolic partial-differential equations which govern the steady flow of fluid through an interior subchannel of a bare rod bundle. The rods are assumed to be smooth, and the incompressible coolant flow is parallel to the axes of the rods. A special non-orthogonal coordinate system has been developed to represent the irregular geometry of the flow regions considered. The versatility of the method has been demonstrated by its application to other non-circular passages such as triangular and elliptic ducts.

Flow and heat-transfer phenomena under both laminar and turbulent conditions have been studied. In the latter case, the turbulence has been represented by way of transport equations for the mean turbulent kinetic energy and its rate of dissipation. These have been employed in conjunction with an algebraic formulation for the Reynolds-stresses in the cross-stream plane of the channel, in order to predict the nature and influence of the secondary flow field. This approach has also been adopted in the successful computation of the flow behaviour in equilateral-triangular ducts.

Rod-bundle geometries involving both triangular and square lattices have been investigated, and calculations have been made for both the developing and fully-developed regimes. Local distributions of velocities, kinetic energy, Reynolds-stresses, wall shear-stress, heat-transfer coefficients etc, together with overall parameters of the flow such as friction factors and Stanton numbers have been predicted over a wide range of rod spacings. Wherever possible, detailed comparison of the results obtained with experimental data has been performed: in general, the agreement observed is good.

PREFACE

I have been a postgraduate research student in the Mechanical Engineering Department of Imperial College, London, since October 1975. This thesis presents the results of work performed within the Department, under the supervision of Professor Brian Spalding, during the period November, 1976 to January, 1979.

The first year of my stay was spent in acquiring knowledge of numerical methods and computer programming, both of which were fields in which I had only a faint acquaintance prior to my arrival at Imperial College. This knowledge was gained by following postgraduate courses and by employing the STABLE code, owned by CHAM Ltd., to solve various problems involving fully three-dimensional 'parabolic' flow situations. Some of the interesting results of this early work has been presented in a Departmental report (Ramachandra and Spalding, 1976). A revised version of STABLE (called STABLER), developed at CHAM Ltd., formed the basis from which the computational work reported here was constructed. The early stages of the research on rod-bundle flows was spent in the exploration of ways of dealing with the irregular geometries involved; methods that involved the use of orthogonal meshes and special boundary treatments were tried, but inaccuracies and even numerical instabilities dogged the calculations. The use of a non-orthogonal mesh had been proposed by Professor Spalding, but it only became apparent sometime later that

this involved the detailed finite-difference formulation of all the additional terms that accrue from the use of such a grid. Private conversations with A. Abdelmeguid, a research colleague, on this matter, helped in setting me on the right track.

I wish to acknowledge my deep gratitude to a number of individuals who have helped make my stay at Imperial College more than worthwhile. First and foremost, I must thank Professor Spalding for his kind and patient supervision; he has encouraged me when my spirits were flagging and he has made occasional, constructive criticisms of my technical writing. Thanks are due to Miss Sue Farmiloe and Mrs. Maggie Dean, who have always been eager to help in personal and administrative matters. Dr. Tony Ma has also been of assistance in such matters. The social intercourse I have enjoyed with research colleagues such as A.G. Awn, George Carroll, Deji Demuren, Amin Baghdadi, M. El. Hadidy and Charles Rapley has been lively and stimulating. I am also grateful to Miss Sally Chambers for her patient and excellent typing of this thesis.

Finally, I must record my sincere gratitude to the Senate of the University of London, for having provided me with a three-year Postgraduate Studentship which enabled me to undertake this work.

V. Ramachandra

May, 1979
Imperial College.

TABLE OF CONTENTS

Page No.

Page No.

Page No.

6. PREDICTION OF TURBULENT FLOW IN EQUILATERAL-TRIANGULAR DUCTS 144

CHAPTER 1

INTRODUCTION

1.1 THE PROBLEM CONSIDERED

Nuclear reactor fuel elements generally consist of a cluster of parallel rods arranged in a symmetrical pattern, each rod being composed of fissile material encased in a suitable cladding. The heat generated in the rods by the nuclear-fission process is extracted by the circulation of a coolant through the open spaces between the rods; the coolant flows longitudinally over the surface of each rod. A schematic representation of a typical rod-bundle cross-section is shown in figure (1.1.1). Fluid flow in such a rod bundle is a complex three-dimensional phenomenon, and a basic understanding of the flow and heat-transfer behaviour is essential to the achievement of optimum design performance during normal operating conditions.

The traditional method of procuring such knowledge has been to build a scale model of the fuel element assembly and to perform forced-convection experiments under the anticipated range of operating conditions. Measurements of velocities and temperatures are then used to develop correlations for pressure drop and heat-transfer coefficients as functions of Reynolds number and geometry. This approach, however, has severe limitations: a new test model must be built for each new geometry investigated, and scaling from model to design size is

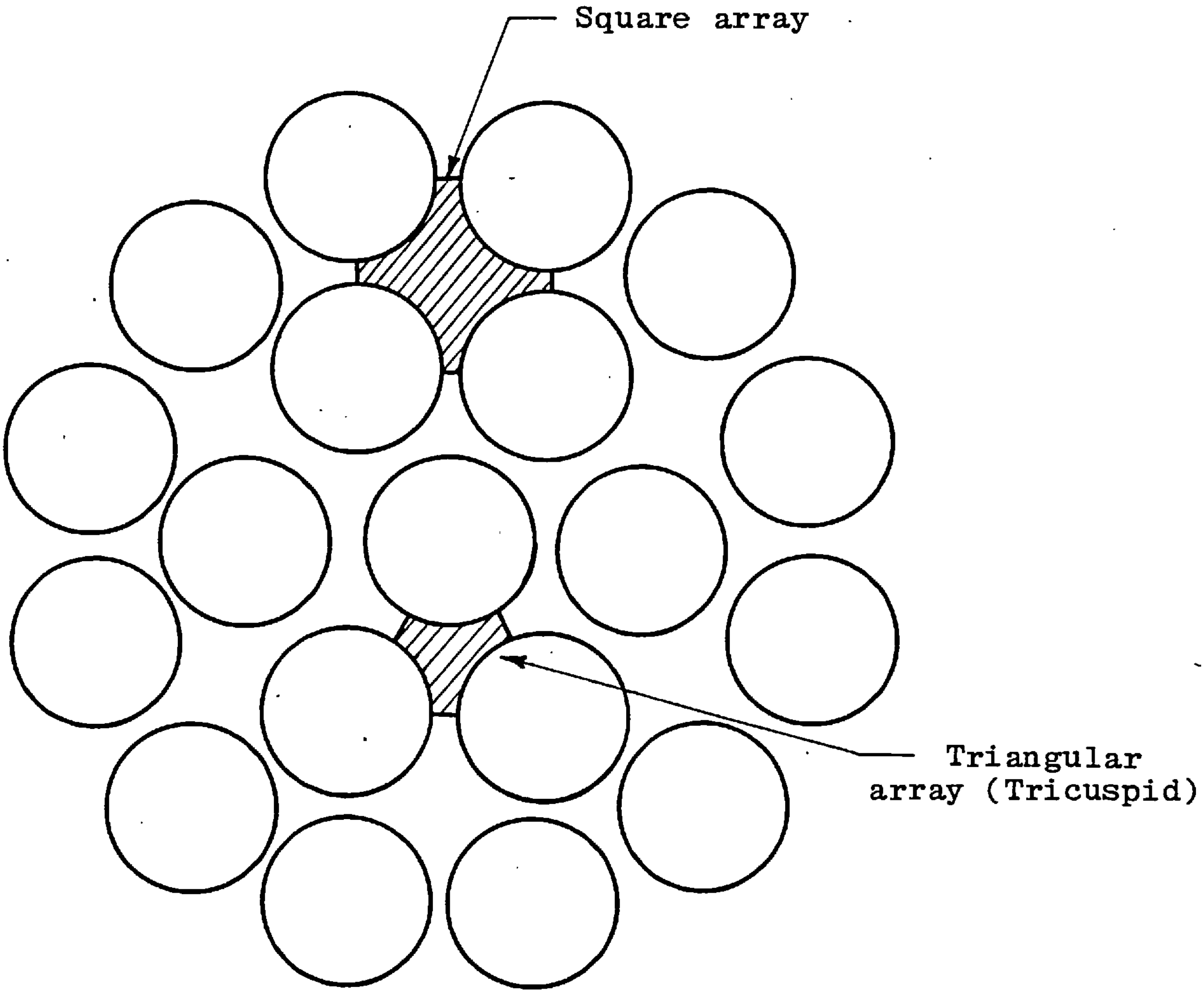

FIGURE 1.1.1: CROSS-SECTION OF A TYPICAL FUEL-ELEMENT BUNDLE

often difficult. Secondly, limitations on the measuring techniques and considerations of expense usually restrict data to just global flow and heat-transfer rates, although detailed velocity and temperature distributions are often required. Finally, the correlations developed from these measurements are frequently valid only over the limited range of parameters considered.

A more flexible and attractive alternative has been afforded in recent years by the rapid growth in computer technology and the development of numerical prediction schemes with regard to fluid flow phenomena. These computer-based methods may be resolved into two basically different types of approach: so-called 'lumped-parameter' and 'distributed-parameter' methods.

In the lumped-parameter approach, the rod bundle is divided into a number of sub-channels by arbitrarily defined boundaries, and mean values of velocities and enthalpy are evaluated for each sub-channel via the solution of volume-averaged conservation equations for momentum and energy. Some typical sub-channel shapes have been depicted in figure(1.1.1). The equations for each sub-channel are coupled with those of its neighbours via global transport coefficients, which are fed in as empirical input. The lumped-parameter technique is presently the most practical means of rod-bundle analysis. However, it is critically dependent on the provision of accurate information regarding the local convective and diffusive processes within sub-channels, if it is to yield reliable predictions for the design engineer.

The distributed parameter approach attempts to provide such information by solving the time-averaged equations for momentum and energy transport for individual sub-channels. Basic calculations are made for a bare rod-bundle, i.e. without spacers and heat-transfer-augmenting devices; and the problem is often simplified by the assumption of an 'infinite' lattice of rods, so that attention may be directed to small regions of the flow. For example, due to symmetry considerations, the characteristic flow area to be analysed in a regular triangular array of rods is that shown cross-hatched in figure (1.1.2). This assumption is an excellent approximation for the interior sub-channels of the large rod clusters designed for most power reactors.

This type of analysis is indispensable to fundamental reactor technology, since further progress on local descriptions of practical rod bundles can only be expected when the behaviour of the bare rod bundle has been well understood and predicted with sufficient accuracy. This latter aim has however been hampered by uncertainties regarding the treatment of turbulence in the equations, and by the difficulty of incorporating the irregular geometries considered into a satisfactory numerical solution procedure. A detailed review of past work in this field is given in chapter 2 of this thesis.

1.2 THE PRESENT CONTRIBUTION

The present study concerns the application of a finite-

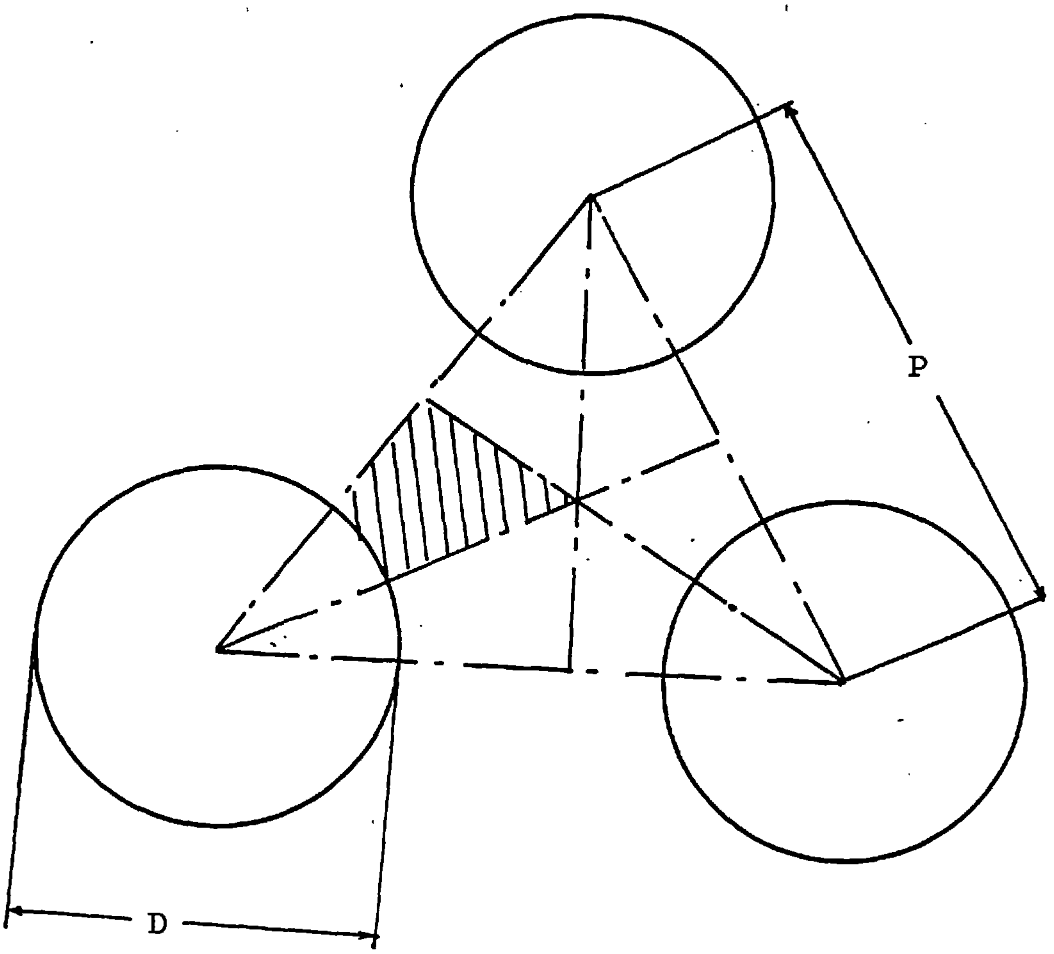

P/D = Aspect ratio

FIG. 1.1.2: CHARACTERISTIC ROD-BUNDLE FLOW REGION

difference calculation procedure to the solution of the partial-differential equations governing the three-dimensional flow and heat transfer in the interior sub-channels of bare rod-bundle assemblies. The rods are assumed to be smooth, and the fluid properties independent of temperature. The flow is steady and incompressible and is characterized by a predominant flow direction which is parallel to the rod axes. The existence of a predominant flow direction ensures that:

(a) Flow properties are convected only from upstream regions to downstream, and not vice versa;

(b) Diffusive transport along that direction is small and may be neglected.

The equations were formulated with reference to a non-orthogonal coordinate system which was constructed such that the coordinate lines were constant with the boundaries of the physical flow domain illustrated in figure (1.1.2). Since, in the Navier-Stokes equations, the boundary conditions are the dominant influence on the character of the solution, the generation of such a coordinate system is an important aspect of the general numerical solution.

The finite-difference equations were solved by means of a numerical algorithm called SIMPLE (an acronym for Semi-Implicit Method for Pressure-Linked Equations) developed by Patankar and Spalding (1972). This procedure involves a marching-integration technique along the predominant flow direction with only two-dimensional computer storage being required for the dependent variables. In the present study, calculations have been performed for both laminar and turbulent flows in rod bundles, and the results obtained compared with all available experimental data. Furthermore, the procedure has been successfully applied to the prediction of laminar and turbulent flow in other non-circular geometries, e.g. the equilateral-triangular duct.

The treatment of turbulence has been effected by way of a two-equation turbulence 'model'; this employs additional partial differential equations for the transport of two local properties of the turbulence, namely the time-averaged kinetic energy of turbulence and the volumetric rate of its dissipation. An important feature of the flow in non-circular geometries is the existence of secondary currents in the cross-sectional plane of the duct. This necessitates a novel treatment for the turbulent-stresses acting in this plane; the practice adopted here was based on the work of Launder and Ying (1973), who, in their computations of square-duct flow, calculated the stresses in question from a simplified algebraic form of the general transport equation for the turbulent-stresses.

1.3 OUTLINE OF THE THESIS

The remaining sections of the thesis which describe the present study in greater detail are arranged thus: in the following chapter a brief review is made of previous experimental and analytical investigations of flow and heat transfer in rod-bundle geometries. In chapter 3, the partial-differential equations which govern the flow situations considered in this thesis are derived in the non-orthogonal coordinate system. The turbulence 'model' approach is discussed, and the mathematical details of the present treatment of turbulence are also given. In chapter 4, the above equations are transformed into their finite-difference equivalents, and the method used for their solution is presented. Validation of the procedure for laminar flow and heat transfer in non-circular ducts and rod bundles is discussed in chapter 5.

The present method has also been employed to compute the fully-developed turbulent flow in an equilateral-triangular duct: this is described in chapter 6. In chapter 7, the results for turbulent flow and heat transfer in rod bundles are presented, while chapter 8 summarizes the main achievements of the present study and makes recommendations for future research. The final sections of the thesis contain a description of the nomenclature used, a list of the references cited in the text and three short appendices which provide supplementary details regarding the mathematical formulation of the problem.

CHAPTER 2

PAST WORK

2.1 INTRODUCTION

This chapter contains a brief review of various theoretical and experimental studies of flow and heat transfer in regular arrays of bare rods that have been reported in the relevant literature over the last two decades. The chapter divides naturally into two main sections: the first, very much the smaller in length, concerns the few theoretical studies of laminar flow that have been performed, while, in the second, the major turbulence investigations are discussed.

2.2 LAMINAR FLOW

An early analytical treatment of laminar flow in an infinite rod bundle was made by Sparrow and Loeffler (1959). Starting with the axial-momentum equation they solved for the fully-developed velocity profile, expressing the result in the form of a truncated trigonometric series and obtaining numerical solutions by a six-point matching method. They also calculated the fully-developed value of the pressure-drop as a function of rod spacing (i.e., pitch to diameter ratio, P/D); the results were published for arrays arranged in both square and triangular patterns. Axford (1967) has also solved the velocity problem for longitudinal laminar flow over an infinite triangular lattice of rods; he employed a finite Fourier cosine transform and a point-matching method. Axford's equations for the velocity profile agree with the results of Sparrow and Loeffler.

Utilizing this solution as their initial datum, Sparrow, Loeffler and Hubbard (1961) solved the temperature equation in a similar manner for fully-developed flow and heat transfer in an equilateral-triangular array, assuming as their boundary condition a uniform wall temperature in the peripheral direction and a uniform wall heat-flux along the length of the rods. Later, Dwyer and Berry (1970) repeated these calculations and obtained identical results; they also extended the cases investigated to include the thermal boundary condition of a constant wall heat-flux in both the axial and circumferential directions. They published tables of Nusselt numbers and calculated the variation of local heat-transfer coefficients around the rod perimeter, over a wide range of pitch-diameter ratios.

Experimental work on either the fully-developed heat transfer or the entrance flow region in bare rod bundles have not been reported to date.

2.3 TURBULENT FLOW: THEORETICAL INVESTIGATIONS

2.3.1 Graphical and empirical methods:

Historically, the first reported attempt to provide information on velocity and temperature variations in a triangular lattice of rods was that of Deissler and Taylor (1956). Their technique was to divide the characteristic flow region into a number of radial segments bounded by "velocity-gradient" lines across which no momentum transport was assumed to occur. From force balances on each of these segments and the assumption of a universal velocity profile in the radial direction, constant-velocity lines were determined. The calculation was repeated, iteratively, until the requirement that "velocity-gradient" lines be perpendicular to constant-velocity lines was satisfied. The temperature field in the coolant was obtained from a heat-balance between successive radial segments, with the circumferential heat transport neglected.

Dwyer (1966) improved on the above scheme by introducing "temperature-gradient" lines, defined so as to intersect constant-temperature lines at right angles. However, the tediousness of the iterative-graphical procedure, the assumption of a circular tube velocity distribution and the impossibility of accounting for the effect of cross-stream velocities, have resulted in this method being of little more than historical interest.

In their first assault on the problem, Eifler and Nijsing (1966) set up momentum and heat balances for radial flow segments, and described the circumferential momentum and energy transport in terms of radially-averaged properties of the flow. In this manner, the two-dimensional fully-developed flow situation was reduced to a one-dimensional problem. A similar approach was adopted more recently by Kokorev et al. (1971).

Two immediate objections to this approach are: (a) the effects of cross-stream motions caanot be estimated, and (b) the mathematical simplifications introduced are in conflict with the symmetry conditions prevailing at the boundaries of the domain.

The converse of the above method is to perform the averaging process in the angular direction only. This, indeed, is the basis of an early treatment by Dwyer and Tu (1960), in which the characteristic flow region was replaced by an annular segment of equivalent flow area. The problem was then solved by means of the known fundamental solutions for annular geometries. This "equivalent-annulus" approach has been adopted by a number of investigators, among others Maresca and Dwyer (1964), Friedland and Bonilla (1961) and Graber (1970), in the calculation of fully-developed Nusselt numbers for liquid-metal flows in rod-bundles with wide spacings and uniform heat generation. The technique is clearly inapplicable to rod-bundles with $P/D < 1.5$, where circumferential effects become significant.

The total transfer of momentum in a channel occurs by way of a diffusive component caused by molecular friction and small-scale turbulent eddies, and a convective transfer arising from the large-scale motion of eddies. Ibragimov and co-workers (1966) suggested that convective transport of momentum became important for channels with sharply varying cross-sectional shapes. They argued that, in such cases, the influence of the large eddy motion would be greatest in the direction parallel to and adjacent to the wall, where the velocity varies slowly. Normal to the channel walls, the effect is negligible because of the diffusion that predominates. These considerations prompted them to propose a semi-empirical relation for the wall shear-stress distribution, determined purely from geometrical parameters, which, for a rod array subchannel may be written as:

$$\frac{\tau_w(\theta)}{\overline{\tau_w}} = C \left[1 - \exp\left\{ - \frac{7.7}{\Phi^{0.8}} \cdot \frac{\tilde{y}(\theta)}{\tilde{y}_{av}} \right\} \right] , \qquad (2.3.1)$$

where,

$$\Phi = \frac{A_c}{\tilde{y}^2_{av}} , \qquad (2.3.2)$$

A_c = subchannel flow area

$\tilde{y}(\theta)$ = distance from wall to maximum-velocity line

$\tilde{y}_{av}$ = average value of $\tilde{y}(\theta)$;

C is a normalization constant calculated from the condition,

$$\frac{1}{\Delta\theta} \int_0^{\Delta\theta} \frac{\tau_w(\theta)}{\overline{\tau_w}} \, d\theta = 1 . \qquad (2.3.3)$$

Along with equation (2.3.1) and the Blasius friction-factor relationship for circular pipes, the further assumption was made that the universal logarithmic velocity profile prevailed normal to the channel wall. In a later paper (Ibragimov et al. 1967), they offered an expression for the ratio between the friction-factor for any specified geometry and that for a circular tube.

This method was incorporated by Bender and Magee (1969) into the VELVET-II code, developed for the computation of temperature fields in rod-bundles cooled by liquid metals.

The generality of Ibragimov's method constitutes its chief attraction, but, unfortunately, the method is incapable of yielding any information on secondary motions that affect the heat transfer. Moreover, the assumption of a wall shear-stress distribution that is solely a function of geometry and independent of Reynolds number is dubious on theoretical grounds, since turbulence parameters are often dependent on the Reynolds number. Further, the assumption of a universal velocity profile along radial lines is not generally valid.

2.3.2 Numerical methods:

Numerical solution techniques have been applied in recent years by several investigators in the calculation of fully-developed flow and heat transfer in smooth rod assemblies. The starting-point for these analyses is the axial momentum equation, which, in cylindrical coordinates may be written as:

$$\rho u \frac{\partial w}{r\partial\theta} + \rho v \frac{\partial w}{\partial r} = - \frac{\partial p}{\partial z} + \frac{1}{r}\frac{\partial}{\partial\theta}\left(\mu\frac{\partial w}{r\partial\theta}\right) + \frac{1}{r}\frac{\partial}{\partial r}\left(\mu r \frac{\partial w}{\partial r}\right)$$

$$- \frac{1}{r}\frac{\partial\overline{u'w'}}{\partial\theta} - \frac{1}{r}\frac{\partial}{\partial r}(\overline{rv'w'}) \quad . \qquad (2.3.4)$$

In the majority of investigations, no account was taken of the existence of secondary flow, and the turbulent shear stresses were related to the axial-velocity gradients by a coefficient defined as the "eddy diffusivity" of momentum, eg.,

$$\overline{v'w'} = - \varepsilon_{m.r} \frac{\partial w}{\partial r} \quad . \qquad (2.3.5)$$

Similarly, a "thermal eddy diffusivity" is defined so that the turbulent heat-fluxes in the energy equation are given by expressions such as,

$$\overline{v'T'} = - \varepsilon_{H.r} \frac{\partial T}{\partial r} \quad . \qquad (2.3.6)$$

Many expressions have been proposed for the variation of $\varepsilon_{M.r}$ and $\varepsilon_{H.r}$ over the cross-section of the subchannel. Such expressions are either deduced theoretically or inferred from measurements of the velocity distribution and the relevant cross-correlations.

Bender, Switick and Field (1967) applied the mixing-length theory of Prandtl (1925) to rod-bundle flows. The turbulent stresses were written in the form

$$\overline{v'w'} = - c\, \ell_c^2 \left| \frac{\partial w}{\partial r} \right| \frac{\partial w}{\partial r} \quad , \qquad (2.3.7)$$

$$\overline{u'w'} = - c\, \ell_c^2 \left| \frac{\partial w}{r\partial \theta} \right| \frac{\partial w}{r\partial \theta} \quad ; \qquad (2.3.8)$$

In these equations ℓ_c is the turbulent "mixing-length", obtained from a formula suggested by Buleev (1964), and c is an empirical constant. One major criticism is that, in this model, the eddy diffusivities are forced to zero wherever the respective velocity gradients vanish. Wall shear variations calculated with these formulae were found to be unrealistically high.

Eifler and Nijsing (1967) were the first investigators to make allowance for secondary flow in their calculations. They proposed a phenomenological explanation of secondary flow, based on the experimental observation of fluid ejection away from a wall (Kline et al. 1967), the rate of which is directly related to the local wall shear stress. They concluded that in the presence of a lateral wall shear-stress gradient a circular motion arises which tends to transport high-momentum fluid through the mainflow in the direction of decreasing wall shear. For the characteristic flow domain of the infinite rod array, this motion has been schematically represented in figure (2.3.1). This reasoning led them to deduce the following expression for the circumferential component of the secondary flow:

$$u = F\left\{\sqrt{\frac{\tau_w}{\rho}}\,,\ \Delta\theta\right\} . F\left\{\frac{y}{\bar{y}}\right\} \qquad (2.3.9)$$

where $\Delta\theta$ is the angular extent of the flow domain. The following shapes were proposed for the functions in equation (2.3.9):

$$F\left\{\sqrt{\frac{\tau_w}{\rho}},\ \Delta\theta\right\} \equiv 2\ C_{sec} \sqrt{\frac{\bar{\tau}_w}{\rho}} \cdot \frac{d}{d\theta} \left\{ \left(\frac{\tau_w}{\bar{\tau}_w}\right)^{\frac{1}{2}} \right\} \cdot \Delta\theta\ , \qquad (2.3.10)$$

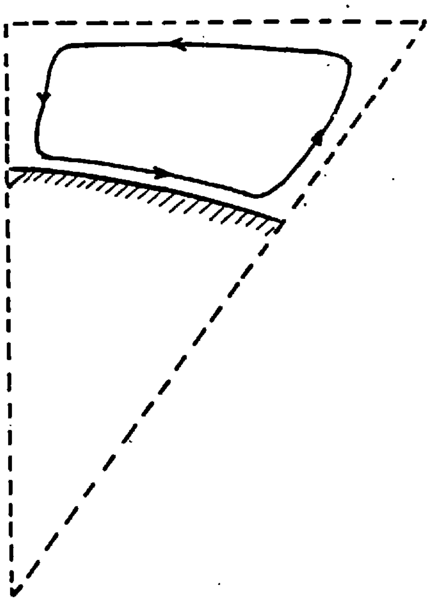

FIG. 2.3.1: SECONDARY FLOW PATTERN POSTULATED BY NIJSING (1967)

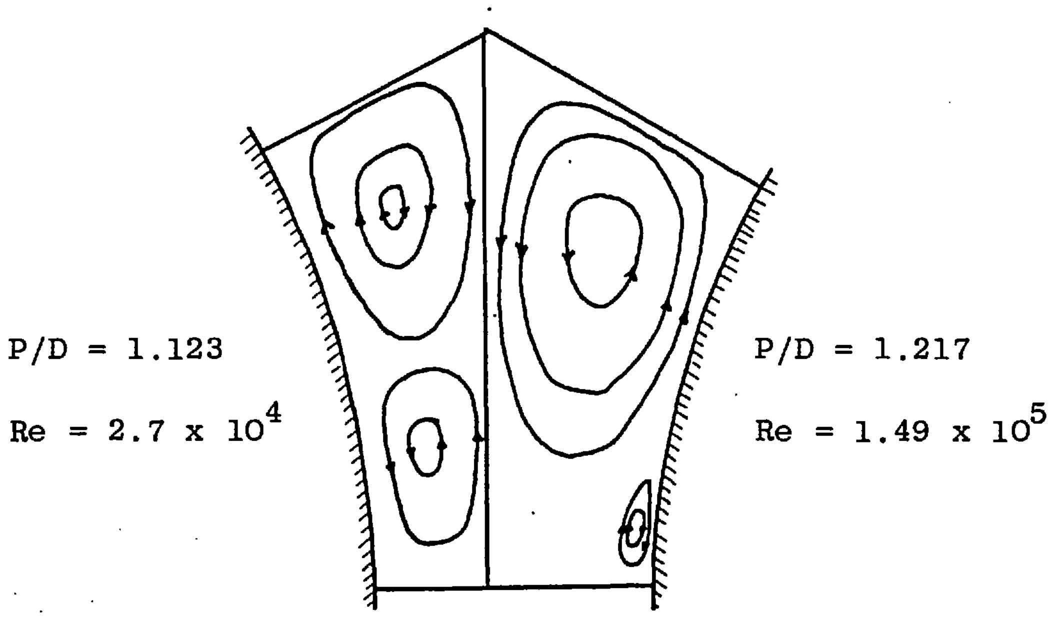

FIG. 2.3.2: SECONDARY FLOW STREAMLINES AS PREDICTED BY CARAJILESCOV AND TODREAS (1976)

$$F\left(\frac{y}{y}\right) \equiv \cos\left(\frac{\pi y}{y}\right) \quad . \qquad (2.3.11)$$

The constant C_{sec} was set equal to 0.6, and the following formulae were employed for the eddy diffusivities:

$$\varepsilon_{M.r} = C_r\ \tilde{y}\ \sqrt{\frac{\tau_w}{\rho}} \quad , \qquad (2.3.12)$$

$$\varepsilon_{M.\theta} = 0.154\ \tilde{y}\ \sqrt{\frac{\tau_w}{\rho}} \quad . \qquad (2.3.13)$$

Here C_r assumed to be a function of the aspect ratio P/D and the Reynolds number. Eifler and Nijsing were compelled to prescribe arbitrarily the peripheral velocity profile, given above, because of the lack of secondary flow measurements. However, measurements of the wall shear-stress distribution obtained by, among others, Kjellstrom (1971) show that for $P/D > 1.2$, the local wall shear does not rise monotonically from $\theta = 0^o$ to $\theta = 30^o$, but instead shows a peak at an intermediate angular position. Such a distribution would induce a more complex secondary flow pattern than that suggested by Eifler and Nijsing.

Buleev (1964) has postulated a model of turbulent eddy interaction in which two mechanisms of momentum exchange with the surrounding medium are envisaged. In the first mechanism, the eddy exchanges momentum with the medium via molecular interaction. In the second, the eddy disintegrates into smaller eddies under the impact of friction forces, and is transported through the fluid. From these hypotheses Buleev was able to calculate the probability that a given eddy would reach the point in the flow where the turbulent stress tensor was to be determined. Ramm and Johannsen (1975) applied these ideas of Buleev, along with some minor changes, to the solution of the momentum and energy equations for rod-bundle flow. Secondary motions were neglected, and artificial boundaries were introduced to limit the flow region which influenced the turbulence properties prevailing at a given point. Anisotropy of the turbulence was described by postulating different macrolengths of turbulence for different directions in the flow. Although this approach has the attractiveness of starting with physical mechanisms, many arbitrary assumptions are required before they take mathematical shape. Moreover, since hardly any comparison with experimental data was made by the authors, the utility of this model has yet to be demonstrated.

Meyder (1975) has reported a finite-difference method for the solution of the axial-momentum and temperature equations describing the flow in a central subchannel of a rod bundle. Meyder assumed the absence of cross-stream motions, and prescribed the eddy diffusivity from the Van Driest (1956) formula for the 'mixing-length' near a wall. The predicted velocity profiles showed only qualitative agreement with experimental data. Meyder consequently enhanced the momentum transfer in the circumferential direction by introducing an anisotropic eddy diffusivity model: starting with the general linear equation of state for a turbulent flow expressed in terms of eddy diffusivities, and involving Prandtl's mixing-length hypothesis, he derived simple algebraic relations for different mixing-lengths in the radial and circumferential directions. The values of the unknown constants appearing in the formulae were adjusted so that the computed wall shear stress distribution was in acceptable agreement with the data of Kjellstrom (1971). There was a considerable improvement in the predicted velocity profile in the radial direction. Nevertheless, the deficiency of this approach is plain: adjustment to experimental results is obtained by 'fixing' anisotropy factors, so that the essential validity of the model is still left in question.

Carajilescov and Todreas (1976) have recently studied the hydrodynamic behaviour in a triangular array of rods by means of a one-equation statistical model of turbulence. They reduced the conservation equations for fully-developed turbulent flow to equations for the axial momentum, vorticity and stream-function; these were then cast into finite-difference form and solved by the method of successive displacements. The secondary flow was computed by adopting the formulation of Launder and Ying (1973) for the Reynolds-stresses in the cross-stream plane. Details of this formulation, together with a brief review of higher-order statistical models of turbulence, will be given in the following chapter.

Lack of information regarding the distribution of the turbulence length-scale prompted Carajilescov and Todreas to undertake an experiment of their own in a triangular array of aspect ratio 1.123. The experimental results for the length-scale were then fed into their computational code, and the constants in the model optimized to ensure satisfactory accord between theory and experiment. Comparison between their calculations for different aspect ratios and the experimental data of other authors was quite favourable. The predicted secondary flow patterns for two different rod spacings are shown schematically in figure (2.3.2). A major drawback of Carajilescov's method is the dependence on experimental input in order to solve the equations.

2.4 TURBULENT FLOW: EXPERIMENTAL INVESTIGATIONS

2.4.1 Hydrodynamics

The major part of the experimental work devoted to the study of turbulent flow in rod clusters has been aimed at the determination of the hydraulic resistance and hence the power required to pump the coolant. It is only relatively recently that detailed measurements of the local flow characteristics have been performed.

A systematic investigation of the fully-developed axial-velocity distributions in triangular arrays was undertaken by Eifler and Nijsing (1967); they employed a Pitot tube to measure the local mean velocities in arrays of aspect ratios 1.05, 1.10 and 1.15, for three different values of the Reynolds number. Palmer and Swanson (1961) measured circumferential axial-velocity variations for air flow through a closed-periphery duct composed of two adjacent cells of an infinite triangular rod bundle with a relative pitch of 1.015. They used a fine

Pitot tube near the wall and in the extremely narrow gap region, and a Kiel-probe elsewhere. More recently, Subbotin and co-workers (1971) in Russia investigated axial velocities (Pitot tube) and wall shear-stress distributions (Preston tube) for P/D ratios of 1.05, 1.10 and 1.20, in the Reynolds-number range 18000-81000. The cross-sectional shape of the test sections employed in all these studies is depicted in figure (2.4.1(a)). Although this duct shape is not an accurate simulation of the infinite rod bundle owing to the presence of spacer elements, a correction can be made for this effect in the evaluation of the data, as indicated by Eiffler and Nijsing (1967). The latter recommend the use of a test section with a cross-section as shown in figure (2.4.1(b)); this, indeed, is in current use in their ISPRA laboratory.

The first comprehensive measurements in rod bundles originated from AB Atomenergi, Sweden, where a project on fundamental studies of turbulent transport has been underway for several years. Kjellstrom (1971) measured mean axial velocities, wall shear-stress variations and the distributions of five components of the Reynolds-stress tensor (constant temperature hot-wire anemometry, single wire and 45° slanting wire) for air flow through an array with P/D equal to 1.217, at Reynolds numbers in the range 149000-355000. He also attempted to measure secondary flows but his data showed some considerable scatter. Hall and Svenningsson (1971), working with the same experimental facility as Kjellstrom, determined wall shear-stress distributions and peripheral secondary velocities at a Reynolds number of 270 000 . The measurements, in two

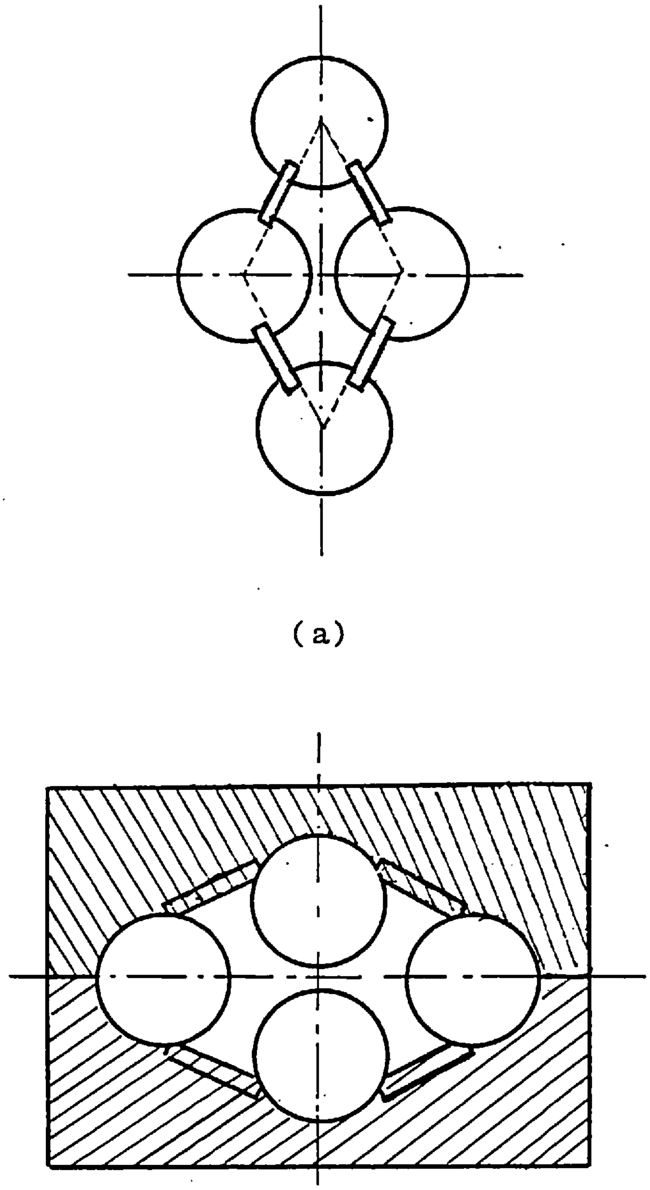

(a)

(b)

FIG. 2.4.1: TYPICAL CROSS-SECTIONS OF TEST SECTIONS FOR HYDRODYNAMIC AND HEAT TRANSFER STUDIES (AFTER Nijsing (1972))

neighbouring flow cells, indicated these velocities to be about one per cent of the bulk average axial velocity, but since some of the flow was found to cross the cell boundaries the possibility of a measuring error was recognised by the authors.

The most complete single set of experimental measurements to date are those of Trupp and Azard (1975), who utilized a hot-wire anemometer to investigate mean axial velocities, turbulence intensities, shear stresses and the power spectra of the axial turbulence for P/D ratios 1.20, 1.35 and 1.50, over a Reynolds-number range 12000-84000. Wall shear distributions were measured with a Preston tube. Data on the tangential shear-stress $\overline{u'w'}$ showed appreciable scatter, so that no information could be obtained regarding the relative magnitudes of the radial and peripheral eddy diffusivities. Trupp and Azard believed that they had indirectly established the presence of secondary flows after a careful examination of their experimental data. They postulated a basic secondary flow pattern for the flow region under study as consisting of a single cell of counter-clockwise circulation similar to that shown in figure (2.3.1); they inferred that the strength and influence of the motion increased with decreasing aspect ratio.

Carajilescov and Todreas (1976) adopted a laser Doppler anemometer (LDA) to make measurements of the mean axial velocity, turbulence intensities and pressure-drop in a flow of water within a test section designed to simulate a typical interior subchannel of a rod bundle with aspect ratio (P/D) equal to 1.123. The LDA was operated in a "fringe" mode with forward scattering, and refraction of the laser beams on the curved surfaces in the rig were reduced to negligible levels by the use of thin transparent films, with water present on either side of the film. Measurements were performed for a Reynolds number of 27000. A search for secondary motions proved inconclusive: the experimental error involved precluded identification of secondary velocities with magnitude less than 0.67 per cent of the bulk axial velocity.

2.4.2 Heat transfer:

Although several experimental investigations of heat transfer in rod bundles have been performed, the overwhelming majority of them either involve the use of devices such as spacers, roughened rods, turbulence promoters etc. or refer to liquid-metal flows, the treatments of which lie beyond the scope of this thesis. Also, much of the experimental information concerning gas and water flows apply only to the particular configuration and (often) ill-defined thermal boundary conditions tested. Consequently in this brief survey of the relevant literature, only the more ambitious type of investigations will be reviewed.

One of the earliest studies reported was that of Dingee and Chastain (1956), who tested both square and triangular lattices at pitch-diameter ratios of 1.12, 1.20 and 1.27 with water in a nine-rod cluster; the range of Prandtl number tested was 1.18 to 1.75 and the Reynolds number range was 10^4 to 10^6. The error quoted was about eight per cent. The authors concluded that (1) the heat-transfer coefficients for the smaller aspect ratio was represented adequately by the usual correlation for circular tubes, but the date for the larger spacings lay about fifteen per cent higher, and (2) there was no variation of wall temperature around the periphery of the heated rods. However, the experiment was unsatisfactory in that the rods were heated by connecting them in parallel and passing a current through the walls; no attempt was made to relate the results to either the constant-temperature or constant-heat-flux boundary condition. The inability to detect circumferential temperature variations was very probably due to the large scatter in the data.

Palmer and Swanson (1961) investigated a very close spacing (P/D = 1.015) using a large-scale seven-rod bundle with dummy rods at the wall to simulate an infinite array. The employed low-temperature air and covered the Reynolds-number range 10 000 to 60 000. They concluded that (1) the circular-tube correlation represented the mean heat-transfer coefficient for this pitch-diameter ratio, (2) the peripheral variation of local heat-transfer coefficient was a factor of 3 for a Reynolds number of 20 000, decreasing with increasing Reynolds number. The apparatus used (thick-walled, electrically heated rod) provided neither constant heat flux nor constant wall temperatures, but the authors conjectured on physical grounds that there was no appreciable difference between the two heating conditions.

Hoffman et al. (1961) performed heat-transfer experiments on a seven-rod prototype of a reactor fuel element with a P/D ratio of 1.71. Mass-transfer tests, which involved coating the rod surfaces with naphthalene, were also conducted for two additional pitch-diameter ratios, namely 1.2 and 1.4. However, agreement between comparable heat- and mass-transfer tests was poor. The results lacked generality because the bounding channel wall had a strong influence on the local heat-transfer rates. The authors also deduced, from their data, the presence of significant cross-flows in the rod cluster.

Subbotin et al. (1964) have summarized the work of several Russian investigators. Much of the work is with reference to liquid metals, but some work with water as coolant is also reported. For the latter data at P/D = 1.0, the heat transfer and friction factor were substantially below the circular-tube correlations, and both increased with increasing rod spacing. The peripheral wall temperature around the rods was appreciable for P/D = 1.0, but became negligible for $P/D > 1.10$.

Sutherland and Kays (1966) have investigated the fully-developed heat transfer in triangular rod arrays for pitch-diameter ratios of 1.15 and 1.25 over a wide range of Reynolds number. The coolant used was air, and each rod in the array was uniformly and consecutively heated, and "fundamental solutions", which describe the influence of one rod on the others were measured. These experimentally determined fundamental solutions were incorporated into a method of analysis which involved the technique of superposition to predict the heat transfer in arrays of various spacings and with arbitrary power distribution from rod to rod and around the periphery of the rods. In the determination of fundamental solutions, the circumferential wall temperature variation around the heated rod was of the order of the experimental uncertainty.

A similar technique was utilized by Redman, McKee and Rule (1966) who examined flow passages designed to represent cells in infinite triangular lattices of tubes with P/D ratios of 1.0, 1.10, 1.25 and 1.5. Thin metallic strips deposited on the poorly conducting surfaces of the tubes served as the heating elements; in this way the heat flux could be built-up around the circumference of each rod, and from the measured temperature distributions step-wise "influence functions" were determined. The latter were used to predict the response to a uniform wall heat flux; the mean Stanton numbers calculated from the Colburn equation were found to be somewhat lower than the experimental values. Peripheral variations in the local Stanton number were also calculated from the measured influence functions.

Marek, Maubach and Rehme (1973) have reported measurements of pressure drop and heat-transfer in square lattices of 9 and 16 rods, respectively, installed in a square channel. The investigations were performed in a helium test rig for Reynolds numbers between 10^4 and $3x10^5$. The rods were electrically heated, and wall temperatures of the central and corner rods were measured by soldering Ni - NiCr thermocouples into the tube walls. The measured bulk Nusselt numbers for the 9-tube bundle showed a considerable amount of scatter; on average, they were about 7 per cent below the Dittus-Boelter relation for circular tubes. The results for the larger bundle were even lower. The authors concluded that a safe statement on the heat-transfer behaviour of rod bundles in square arrays would not be possible until more systematic experiments became available.

CHAPTER 3

MATHEMATICAL FORMULATION

3.1 INTRODUCTION

The present chapter and the next provide the detailed groundwork of the theoretical calculations reported in this thesis. The mathematical problem is defined here, chiefly by way of the differential equations which have to be solved, while the following chapter describes their method of solution. The problem itself may be discussed mathematically under two main sections: the first concerns the employment of a special non-orthogonal coordinate system to deal with the irregular geometry investigated, and the derivation of the relevant conservation equations for fluid motion; the second involves the method adopted to effect closure of the equations in the case of turbulent flow.

In the rod bundles, and many other duct configurations, the flow cross-section conforms neither to Cartesian nor to polar forms. If, for instance, a cylindrical polar-coordinate grid, with its origin coincident with a point on the axis of a rod, were to be used to describe the flow domain shown in figure (1.1.2), it would be evident that the outer boundaries of the domain would not lie on lines of constant radius or constant angle. This introduces great difficulties in the specification of the boundary conditions, which exercise a dominant influence on the solution of the Navier-Stokes equations. Consequently, it is important to devise a new coordinate system in which the flow boundaries are coincident with the coordinate surfaces. The details of such a procedure are described herein.

Some comments on the mathematical treatment of turbulence are required here. The difficulties involved in the calculation of turbulent flows via solution of the full, transient form of the Navier-Stokes equations are well known. Any numerical calculation scheme would require an enormously fine mesh and minute time-steps in order to sufficiently resolve the details of the turbulence. The alternative procedure, now commonly adopted, is to solve the time-averaged equations, so that the dependent variables become the time-averaged velocities, pressure etc; the influence of turbulence is seen in the equations in the form of 'Reynolds stresses' and 'turbulent flux' terms, which involve time-averaged products of fluctuating quantities. These terms are evaluated via a set of hypothesis embodied in a 'turbulence model.' Details of the model adopted in the present calculations are to be found later on in this thesis.

3.2 THE NON-ORTHOGONAL COORDINATE SYSTEM

3.2.1 The general concept

The system of curvilinear coordinates chosen is depicted by way of section-projections in figure (3.2.1). The z-coordinate is aligned with the axial flow direction (normal to the plane of the paper), while the η and ξ coordinates serve to define the geometry in the cross-stream plane. Since, in all the problems investigated in this thesis, the duct geometry is invariant in the axial direction, the η-ξ surfaces always intersect orthogonally with the z-coordinate lines.

The point O in figure (3.2.1) represents the origin of the (η,ξ,z) coordinate system. It is to be noted that the η = constant surfaces and the ξ = constant surfaces are not mutually orthogonal. These surfaces have been defined in the following way. The projections of the set of ξ = constant surfaces on the cross-stream plane are a family of straight lines which emanate radially from O. The projections of the η = constant surfaces form a family of curves which intersect the radial lines so as to divide the latter into segments of uniform relative size. In the characteristic rod-bundle geometry (figure 1.1.2), O is taken to be a point on the axis of a rod, the inner boundary of the domain consists of a cylindrical arc representing the rod surface, and the outer boundary is a plane which bisects the space between adjacent rods. Between these boundaries, the η = constant surfaces vary in shape, merging from cylindrical arcs on the inside to planes on the outside.

3.2.2 The mathematical definition

The relationship between the (η,ξ,z) and the (r,θ,z) coordinate systems is expressed by the following definitions:

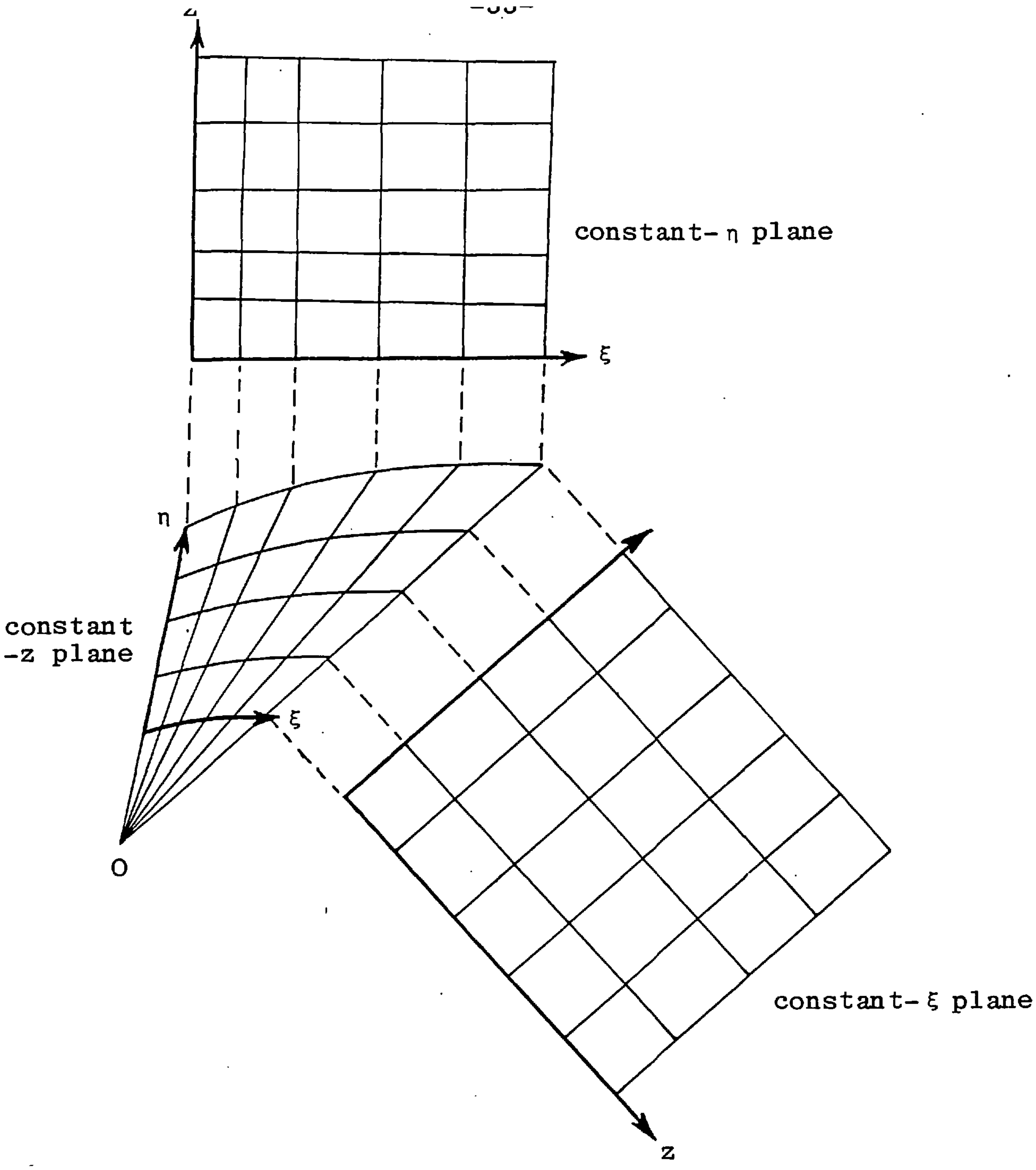

FIGURE 3.2.1: THE (η ,ξ ,z) COORDINATE SYSTEM

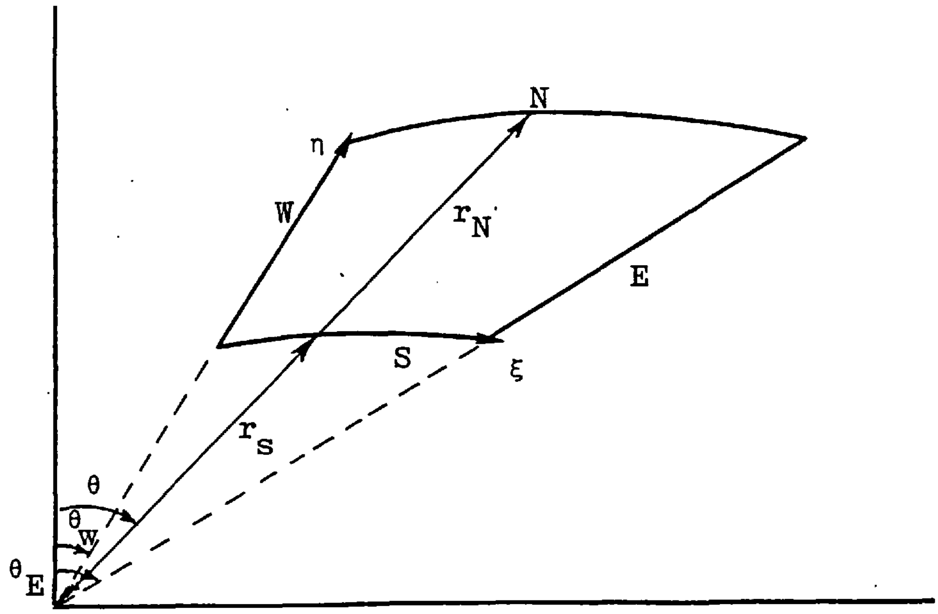

FIGURE 3.2.2: RELATIONSHIP OF (η, ξ) COORDINATES TO POLAR (r,θ) COORDINATE SYSTEM

$$\eta \equiv \frac{r - r_S}{r_N - r_S} \quad , \qquad (3.2.1)$$

$$\xi \equiv \frac{\theta - \theta_W}{\theta_E - \theta_W} \quad . \qquad (3.2.2)$$

Here, the subscripts, N, S, W and E refer respectively to the North, South, West and East boundaries in the $\eta \sim \xi$ plane of the calculation domain, as illustrated in figure (3.2.2). Thus the flow region of interest is contained wholly within the surfaces $\eta = 0$, $\eta = 1$, $\xi = 0$ and $\xi = 1$. θ_E and θ_W are constants, and define the angular width of the flow domain. r_N and r_S are, in general, functions of the angular position.

3.2.3 The velocity components

Although a set of non-orthogonal coordinates has been employed to define the calculation domain, it is not necessary that the velocity components chosen for solution be aligned with the directions of the coordinate axes. In the present work, the orthogonal set of radial (v), circumferential (u) and axial (w) components of velocity, as used in the cylindrical-polar system, have been retained as the dependent variables in the new coordinate system.

3.3 CLASSIFICATION OF THE FLOW

It has become customary in numerical fluid dynamics to classify (ref. Gosman et al, (1969)) steady-flow phenomena into two main categories: 'elliptic' and 'parabolic'. In 'elliptic' flows - which, strictly speaking, embrace all flows excepting wholly supersonic ones - the perturbations of conditions at any point in the flow can affect conditions at a given point. In 'parabolic' flows, on the other hand, it is assumed that conditions at a particular location within the flow are influenced only by upstream events. This is valid when the following conditions are met:

(i) There is no 'recirculation' i.e. velocities in one direction (termed the main flow direction) are everywhere positive.

(ii) Diffusive transport in the main flow direction is negligible.

(iii) Velocities at a given location are not affected by the downstream pressure field.

In the rod-bundle flows studied in this thesis recirculation does not exist. Further, the Reynolds numbers considered are high enough for no significant transfers of momentum or energy to occur by diffusion in the axial direction. Also, since the rods are taken to be straight, no sharp curvatures of the streamlines do arise: so (iii) is a valid assumption to make. The flow is also fully three-dimensional, owing to the lack of symmetry of the flow geometry. Consequently, the flows investigated here may be classified as three-dimensional and parabolic. The significance of this 'parabolicity' is that the equations governing the flow may be solved by means of a single marching integration from one end of the duct to the other. The details of this will be clarified in the following chapter.

3.4 THE GOVERNING EQUATIONS

3.4.1 The (r, θ, z) coordinate system:

As a consequence of the above classification, the conservation equations describing the steady flow of an incompressible, constant-property fluid may be written in their parabolic form in (r, θ, z) coordinates as follows:

Mass Continuity

$$\frac{1}{r}\frac{\partial}{\partial r}(rv) + \frac{1}{r}\frac{\partial u}{\partial \theta} + \frac{\partial w}{\partial z} = 0 \quad , \tag{3.4.1}$$

Angular Momentum

$$\frac{1}{r}\frac{\partial}{\partial r}(\rho r v u) + \frac{1}{r}\frac{\partial}{\partial \theta}(\rho u^2) + \frac{\partial}{\partial z}(\rho w u) + \rho\,\frac{uv}{r} = -\frac{1}{r}\frac{\partial p}{\partial \theta}$$
$$+ \frac{1}{r}\,\frac{\partial \tau_{\theta\theta}}{\partial \theta} + \frac{1}{r^2}\frac{\partial}{\partial r}(r^2 \tau_{r\theta}) \quad , \tag{3.4.2}$$

Radial Momentum

$$\frac{1}{r}\frac{\partial}{\partial r}(\rho r v^2) + \frac{1}{r}\frac{\partial}{\partial \theta}(\rho v u) + \frac{\partial}{\partial z}(\rho w v) - \rho\,\frac{u^2}{r} = -\frac{\partial p}{\partial r}$$
$$+ \frac{1}{r}\,\frac{\partial \tau_{\theta r}}{\partial \theta} + \frac{1}{r}\frac{\partial}{\partial r}(r \tau_{rr}) - \frac{\tau_{\theta\theta}}{r} \quad , \tag{3.4.3}$$

Axial Momentum

$$\frac{1}{r}\frac{\partial}{\partial r}(\rho r v w) + \frac{1}{r}\frac{\partial}{\partial \theta}(\rho u w) + \frac{\partial}{\partial z}(\rho w^2) = -\frac{\partial \bar{p}}{\partial z}$$
$$+ \frac{1}{r}\,\frac{\partial \tau_{\theta z}}{\partial \theta} + \frac{1}{r}\frac{\partial}{\partial r}(r \tau_{rz}) \quad . \tag{3.4.4}$$

In the above equations, the symbols u, v and w stand respectively for the velocity components in the angular, radial and axial directions; p represents the fluid pressure, and ρ the density of the fluid, assumed constant. The foregoing dependent variables are, of course, time-averaged values. Note that body forces, such as buoyancy, have been neglected. The 'τ's represent the shear stresses acting in the fluid.

The left-hand side of the axial momentum equation represents the convective transport of axial momentum in the three coordinate directions, while the 'τ' terms on the right-hand side of the equation represent the transfer of axial momentum in the θ and r directions by way of viscous and turbulent-mixing effects. It will be noted that there is no term involving τ_{zz}. This is in accordance with the assumption made for a parabolic flow that there is no diffusive transfer of momentum in the axial direction.

Furthermore, since it is presumed that there is no pressure transmission from downstream in the fluid, the variation of $\frac{\partial p}{\partial z}$ over the cross-stream plane of the duct is quite small. Hence it is possible to calculate $\frac{\partial p}{\partial z}$ quite independently of the momentum balances in the θ- and r- directions. The practice adopted is to employ a pressure $\bar{p}$, which may be interpreted as the average pressure over the cross-section, in the axial momentum equation. $\bar{p}$ is then a function only of z. The appreciable simplification achieved by this "pressure-uncoupling" (Patankar and Spalding (1972)) will be made plain in the following chapter.

The shear stresses appearing in the momentum equations above comprise molecular and turbulent components.

$$\tau_{rr} = 2\mu \frac{\partial v}{\partial r} - \rho \overline{v'^2} \tag{3.4.5}$$

$$\tau_{\theta\theta} = 2\mu \left(\frac{1}{r}\frac{\partial u}{\partial \theta} + \frac{v}{r}\right) - \rho \overline{u'^2} \tag{3.4.6}$$

$$\tau_{r\theta} = \mu \left(\frac{\partial u}{\partial r} + \frac{1}{r}\frac{\partial v}{\partial \theta} - \frac{u}{r}\right) - \rho \overline{u'v'} = \tau_{\theta r} \tag{3.4.7}$$

$$\tau_{\theta z} = \mu \frac{\partial w}{r\partial \theta} - \rho \overline{u'w'} = \tau_{z\theta} \tag{3.4.8}$$

$$\tau_{rz} = \mu \frac{\partial w}{\partial r} - \rho \overline{v'w'} = \tau_{zr} \tag{3.4.9}$$

The terms $\rho \overline{u'^2}$, $\rho \overline{u'v'}$ etc. are time-averaged products of velocity fluctuations and are known as 'Reynolds stresses'. They represent momentum transfer by the turbulent motions.

3.4.2 The (η,ξ,z) coordinate system

From the defining relations (3.2.1) and (3.2.2), the continuity and momentum equations in the non-orthogonal (η,ξ,z) coordinate system may be obtained by transformation of the equations given above. The following further definitions are required:

$$\Delta r \equiv r_N - r_S \quad , \tag{3.4.10}$$

$$\Delta \theta \equiv \theta_E - \theta_W \quad , \tag{3.4.11}$$

$$G \equiv \frac{1}{r} \left\{ \frac{dr_S}{d\theta} + \eta \, \frac{d(r_N - r_S)}{d\theta} \right\} \quad . \tag{3.4.12}$$

Substitution of the shear-stress relations (3.4.5) to (3.4.9) into the momentum equations (3.4.2) to (3.4.4), and transformation to the new coordinate system, leads to the equations given below. The details of the derivation appear in Appendix A.

Continuity

$$\frac{1}{r\Delta r} \frac{\partial}{\partial \eta} \{r(v-uG)\} + \frac{1}{r\Delta\theta} \frac{\partial u}{\partial \xi} + \frac{u}{r\Delta r} \frac{\partial (Gr)}{\partial \eta} + \frac{\partial w}{\partial z} = 0 \quad , \tag{3.4.13}$$

Angular Momentum

$$\begin{aligned} &\frac{\rho}{r\Delta r} \frac{\partial}{\partial \eta} \{r\,(v-uG)u\} + \frac{\rho}{r\Delta\theta} \frac{\partial (u^2)}{\partial \xi} + \rho \, \frac{\partial (uw)}{\partial z} + \rho \frac{uv}{r} \\ &\quad = -\frac{1}{r\Delta\theta} \frac{\partial p}{\partial \xi} + \frac{G}{\Delta r} \frac{\partial p}{\partial \eta} + \frac{\mu}{r\Delta\theta} \frac{\partial}{\partial \xi} \left[\frac{1}{r\Delta\theta} \frac{\partial u}{\partial \xi} - \frac{G}{\Delta r} \frac{\partial u}{\partial \eta} \right] \\ &\quad + \frac{\mu}{r\Delta r} \frac{\partial}{\partial \eta} \left[\frac{(1+G^2)r}{\Delta r} \frac{\partial u}{\partial \eta} - \frac{G}{\Delta\theta} \frac{\partial u}{\partial \eta} \right] + \frac{2\mu}{r\Delta\theta} \frac{\partial v}{\partial \xi} - \frac{2\mu G}{\Delta r} \frac{\partial v}{\partial \eta} \\ &\quad - \mu \frac{u}{r^2} + \left[\frac{\mu}{r\Delta\theta} \frac{\partial u}{\partial \xi} - \frac{\mu G}{\Delta r} \frac{\partial u}{\partial \eta} - \rho u^2 \right] \frac{1}{r\Delta r} \frac{\partial (Gr)}{\partial \eta} \\ &\quad - \frac{\rho}{r\Delta\theta} \frac{\partial (\overline{u'^2})}{\partial \xi} + \frac{\rho G}{\Delta r} \frac{\partial (\overline{u'^2})}{\partial \eta} - \frac{\rho}{\Delta r} \frac{\partial (\overline{u'v'})}{\partial \eta} - 2 \, \frac{\rho \overline{u'v'}}{r} \quad . \end{aligned} \tag{3.4.14}$$

Radial Momentum

$$\begin{aligned} &\frac{\rho}{r\Delta r} \frac{\partial}{\partial \eta} \{ r\,(v-uG)v \} + \frac{\rho}{r\Delta\theta} \frac{\partial (uv)}{\partial \xi} + \rho \, \frac{\partial (vw)}{\partial z} - \rho \, \frac{u^2}{r} \\ &\quad = -\frac{1}{\Delta r} \frac{\partial p}{\partial \eta} + \frac{\mu}{r\Delta\theta} \frac{\partial}{\partial \xi} \left[\frac{1}{r\Delta\theta} \frac{\partial v}{\partial \xi} - \frac{G}{\Delta r} \frac{\partial v}{\partial \eta} \right] \end{aligned}$$

$$+ \frac{\mu}{r\Delta r}\frac{\partial}{\partial\eta}\left[\frac{(1+G^2)r}{\Delta r}\frac{\partial v}{\partial\eta} - \frac{G}{\Delta\theta}\frac{\partial v}{\partial\xi}\right] - \frac{2\mu}{r^2\Delta\theta}\frac{\partial u}{\partial\xi} + \frac{2\mu G}{\Delta r}\frac{\partial u}{\partial\eta}$$

$$- \frac{\mu v}{r^2} + \left[\frac{\mu}{r\Delta\theta}\frac{\partial v}{\partial\xi} - \frac{\mu G}{\Delta r}\frac{\partial v}{\partial\eta} - \rho uv\right]\frac{1}{r\Delta r}\frac{\partial(Gr)}{\partial\eta}$$

$$- \frac{\rho}{\Delta r}\frac{\partial(\overline{v'^2})}{\partial\eta} - \frac{\rho}{r\Delta\theta}\frac{\partial(\overline{u'v'})}{\partial\xi} + \frac{\rho G}{\Delta r}\frac{\partial(\overline{u'v'})}{\partial\eta} + \rho\frac{(\overline{u'^2} - \overline{v'^2})}{r} ,$$

$$(3.4.15)$$

Axial Momentum

$$\frac{\rho}{r\Delta r}\frac{\partial}{\partial\eta}\{r(v-uG)w\} + \frac{\rho}{r\Delta\theta}\frac{\partial(uw)}{\partial\xi} + \rho\frac{\partial(w^2)}{\partial z} = -\frac{d\bar{p}}{dz}$$

$$+ \frac{\mu}{r\Delta\theta}\frac{\partial}{\partial\xi}\left[\frac{1}{r\Delta\theta}\frac{\partial w}{\partial\xi} - \frac{G}{\Delta r}\frac{\partial w}{\partial\eta}\right]$$

$$+ \frac{\mu}{r\Delta r}\frac{\partial}{\partial\eta}\left[\frac{(1+G^2)r}{\Delta r}\frac{\partial w}{\partial\eta} - \frac{G}{\Delta\theta}\frac{\partial w}{\partial\xi}\right] + \left[\frac{\mu}{r\Delta\theta}\frac{\partial w}{\partial\xi}\right.$$

$$\left. - \frac{\mu G}{\Delta r}\frac{\partial w}{\partial\eta} - \rho uw\right]\frac{1}{r\Delta r}\frac{\partial(Gr)}{\partial\eta} - \frac{\rho}{r\Delta r}\frac{\partial(r\overline{v'w'})}{\partial\eta}$$

$$- \frac{\rho}{r\Delta\theta}\frac{\partial(\overline{u'w'})}{\partial\xi} + \frac{\rho G}{\Delta r}\frac{\partial(\overline{u'w'})}{\partial\eta} . \qquad (3.4.16)$$

These are the desired equations of motion in their general form. Here G, defined according to equation (3.4.12) is a measure of the degree of non-orthogonality of the particular geometry investigated. If G = 0, then the above equations reduce to the polar-cylindrical form.

Laminar flow form of the equations

If the flow is laminar, then the terms involving the components of the Reynolds stress in the above equations are all set to zero.

The turbulent-viscosity form of the equations

The equations as they stand are incomplete; some means of either calculating or specifying the Reynolds stress terms is required for solution. It has become common practice (reference Launder and Spalding, 1972) to express the Reynolds stresses in terms of a fictitious 'turbulent viscosity' (symbol μ_t) in such a way that they become analogous to the viscous stresses. So,

$$\rho\overline{v'w'} = -\mu_t\left(\frac{1}{\Delta r}\frac{\partial w}{\partial \eta}\right) \quad , \tag{3.4.17}$$

$$\rho\overline{u'w'} = -\mu_t\left[\frac{1}{r\Delta\theta}\frac{\partial w}{\partial \xi} - \frac{G}{\Delta r}\frac{\partial w}{\partial \eta}\right] \quad , \tag{3.4.18}$$

$$\rho\overline{u'v'} = -\mu_t\left[\frac{1}{\Delta r}\frac{\partial u}{\partial \eta} + \frac{1}{r\Delta\theta}\frac{\partial v}{\partial \xi} - \frac{G}{\Delta r}\frac{\partial v}{\partial \eta} - \frac{u}{r}\right] \quad , \tag{3.4.19}$$

$$\rho\overline{u'^2} = -\mu_t\left[\frac{2}{r\Delta\theta}\frac{\partial u}{\partial \xi} - \frac{2G}{\Delta r}\frac{\partial u}{\partial \eta} + \frac{2v}{r}\right] + \frac{2}{3}\rho k \quad , \tag{3.4.20}$$

$$\rho\overline{v'^2} = -\mu_t\left(\frac{2}{\Delta r}\frac{\partial v}{\partial \eta}\right) + \frac{2}{3}\rho k \quad . \tag{3.4.21}$$

where k, the time-averaged kinetic energy of the turbulent motion is defined by

$$k = \frac{1}{2}\left(\overline{u'^2} + \overline{v'^2} + \overline{w'^2}\right) \quad . \qquad (3.4.22)$$

Because of the similarity of form of the laminar and turbulent-stress relations, it is convenient to combine them and work with an 'effective viscosity' (symbol μ_{eff}) defined according to:

$$\mu_{eff} = \mu + \mu_t \qquad (3.4.23)$$

The momentum equations above may now be re-written in terms of the effective viscosity. The complete forms of all three equations are given in full in Appendix B. Only the final result for the axial velocity is quoted below.

$$\begin{aligned} \frac{\rho}{r\Delta r}\frac{\partial}{\partial\eta}\{\, r(v-uG)w \,\} + \frac{\rho}{r\Delta\theta}\frac{\partial(uw)}{\partial\xi} + \rho\frac{\partial(w^2)}{\partial z} &= -\frac{d\bar{P}}{dz} \\ &+ \frac{1}{r\Delta\theta}\frac{\partial}{\partial\xi}\left[\frac{\mu_{eff}}{r\Delta\theta}\frac{\partial w}{\partial\xi} - \mu_{eff}\frac{G}{\Delta r}\frac{\partial w}{\partial\eta}\right] \\ &+ \frac{1}{r\Delta r}\frac{\partial}{\partial\eta}\left[\mu_{eff}\frac{(1+G^2)r}{\Delta r}\frac{\partial w}{\partial\eta} - \mu_{eff}\frac{G}{\Delta\theta}\frac{\partial w}{\partial\xi}\right] \qquad (3.4.24) \\ &+ \left[\frac{\mu_{eff}}{r\Delta\theta}\frac{\partial w}{\partial\xi} - \mu_{eff}\frac{G}{\Delta r}\frac{\partial w}{\partial\eta} - \rho uw\right]\frac{1}{r\Delta r}\frac{\partial(Gr)}{\partial\eta} \quad . \end{aligned}$$

This operation has served merely to transfer attention from the Reynolds stresses to the turbulent viscosity. Some of the ways of determining μ_t that have been popular in recent years will be briefly reviewed in section 3.6.

The use of an 'algebraic stress model'

In the present work - for reasons which will become clearer later on - the turbulent viscosity hypothesis has not been used to evaluate the Reynolds stresses appearing in the u and v equations. Instead an alternative 'algebraic stress model' is employed. In this, equations (3.4.14) and (3.4.15) are used as they stand, algebraic expressions are obtained for the stresses themselves, and the latter are introduced as additional sources of momentum. However, equation (3.4.24) is employed without change.

3.5 THE CONSERVATION EQUATION FOR A GENERAL SCALAR PROPERTY

The conservation equations for scalar properties such as enthalpy, chemical species concentration etc. display a similarity of form; consequently they may be represented by a single equation property ϕ. The boundary-layer form of the transport equation for ϕ - derived from the general equation by neglecting the axial diffusive flux term - is given below in cylindrical-polar coordinates.

ϕ -conservation

$$\frac{\rho}{r}\frac{\partial}{\partial r}(rv\phi) + \frac{\rho}{r}\frac{\partial}{\partial \theta}(u\phi) + \rho\frac{\partial}{\partial z}(w\phi) = \frac{1}{r}\frac{\partial}{\partial \theta}\left(\frac{\Gamma_\phi}{r}\frac{\partial \phi}{\partial \theta}\right) + \frac{1}{r}\frac{\partial}{\partial r}\left(r\,\Gamma_\phi\frac{\partial \phi}{\partial r}\right) - \rho\left[\frac{1}{r}\frac{\partial(\overline{u'\phi'})}{\partial \theta} + \frac{1}{r}\frac{\partial(\overline{rv'\phi'})}{\partial r}\right] + S_\phi \quad . \qquad (3.5.1)$$

Here S_ϕ represents any source (or sink) of ϕ; $\rho\,\overline{u'\phi'}$ and $\rho\,\overline{v'\phi'}$ are known as the 'turbulent fluxes' of ϕ and represent the transport of ϕ by the turbulent motion. The quantity Γ_ϕ is the laminar exchange coefficient, and is often written as:

$$\Gamma_\phi = \frac{\mu}{\sigma_\ell} \quad . \tag{3.5.2}$$

Hence, σ_ℓ is the ratio of the laminar diffusion coefficients for momentum and for ϕ. When the quantity in question is enthalpy (or temperature), σ_ℓ is the familiar 'Prandtl number' of the fluid.

ϕ - conservation equation in (η,ξ,z) coordinates

Equation (3.5.1) may be transformed into the (η,ξ,z) coordinate system by means of the definitions (3.2.1) and (3.2.2); details of the transformation are given in Appendix A. The final result is:

$$\begin{aligned}
&\frac{\rho}{r\Delta r}\frac{\partial}{\partial\eta}\{r(v-uG)\phi\} + \frac{\rho}{r\Delta\theta}\frac{\partial(u\phi)}{\partial\xi} + \rho\frac{\partial(w\phi)}{\partial z} \\
&\quad = \frac{1}{r\Delta\theta}\frac{\partial}{\partial\xi}\left[\frac{\Gamma_\phi}{r\Delta\theta}\frac{\partial\phi}{\partial\xi} - \Gamma_\phi\frac{G}{\Delta r}\frac{\partial\phi}{\partial\eta}\right] \\
&\quad + \frac{1}{r\Delta r}\frac{\partial}{\partial\eta}\left[\Gamma_\phi\frac{(1+G^2)r}{\Delta r}\frac{\partial\phi}{\partial\eta} - \Gamma_\phi\frac{G}{\Delta\theta}\frac{\partial\phi}{\partial\xi}\right] \\
&\quad + \left[\frac{\Gamma_\phi}{r\Delta\theta}\frac{\partial\phi}{\partial\xi} - \Gamma_\phi\frac{G}{\Delta r}\frac{\partial\phi}{\partial\eta} - \rho u\phi\right]\frac{1}{r\Delta r}\frac{\partial(Gr)}{\partial\eta} \\
&\quad - \rho\left[\frac{1}{r\Delta\theta}\frac{\partial\overline{u'\phi'}}{\partial\xi} - \frac{G}{\Delta r}\frac{\partial\overline{u'\phi'}}{\partial\eta} + \frac{1}{r\Delta r}\frac{\partial(\overline{rv'\phi'})}{\partial\eta}\right] \\
&\quad + S_\phi \quad .
\end{aligned} \tag{3.5.3}$$

It is customary to write the turbulent-fluxes in terms of a 'turbulent transport coefficient' $\mu_{t,\phi}$, defined in a manner analogous to that for μ_t:

$$\rho\overline{v'\phi'} = -\Gamma_{t,\phi}\frac{1}{\Delta r}\frac{\partial\phi}{\partial\eta} \quad , \qquad (3.5.4)$$

$$\rho\overline{u'\phi'} = -\Gamma_{t,\phi}\left[\frac{1}{r\Delta\theta}\frac{\partial\phi}{\partial\xi} - \frac{G}{\Delta r}\frac{\partial\phi}{\partial\eta}\right] \quad . \qquad (3.5.5)$$

The variation of $\mu_{t,\phi}$ within the flow is usually in close accord with the variation of the turbulent viscosity. Thus it is useful to connect it with the latter by way of a turbulent Prandtl-Schmidt number, $\sigma_{t,\phi}$, according to the following equation:

$$\sigma_{t,\phi} = \frac{\mu_t}{\Gamma_{t,\phi}} \quad , \qquad (3.5.6)$$

One may then work with the 'effective transport coefficient' defined from,

$$\Gamma_{eff,\phi} \equiv \Gamma_\phi + \Gamma_{t,\phi} \quad . \qquad (3.5.7)$$

The final version of the ϕ-equation may now be written in terms of $\Gamma_{eff,\phi}$. In the special case of the energy equation, with constant fluid properties and no heat generation in the fluid, we have:

$$\frac{\rho c_p}{r\Delta r}\frac{\partial}{\partial\eta}\{\, r(v-uG)T \,\} + \frac{\rho c_p}{r\Delta\theta}\frac{\partial(uT)}{\partial\xi} + \rho c_p\frac{\partial(wT)}{\partial z}$$

$$= \frac{1}{r\Delta\theta}\frac{\partial}{\partial\xi}\left[\frac{\Gamma_{eff,T}}{r\Delta\theta}\frac{\partial T}{\partial\xi} - \frac{\Gamma_{eff,T}}{\Delta r} G\frac{\partial T}{\partial\eta}\right]$$

$$+ \frac{1}{r\Delta r}\frac{\partial}{\partial\eta}\left[\Gamma_{eff,T}\frac{(1+G^2)r}{\Delta r}\frac{\partial T}{\partial\eta} - \frac{\Gamma_{eff,T}}{\Delta\theta} G\frac{\partial T}{\partial\xi}\right]$$

$$+ \left[\frac{\Gamma_{eff,T}}{r\Delta\theta}\frac{\partial T}{\partial\xi} - \Gamma_{eff,T}\frac{G}{\Delta r}\frac{\partial T}{\partial\eta} - \rho uT\right]\frac{1}{r\Delta r}\frac{\partial(Gr)}{\partial\eta} \quad , \qquad (3.5.8)$$

with,

$$\Gamma_{eff,T} = \frac{\mu}{\sigma_\ell} + \frac{\mu_t}{\sigma_{t,T}} \quad . \qquad (3.5.9)$$

3.6 THE TURBULENCE MODEL APPROACH

In the equations for conservation of momentum given in section 3.4, there appeared terms involving the time-averaged products of velocity fluctuations, which were interpreted as turbulent (or Reynolds) stresses. Similarly in the transport equation for the general scalar property ϕ in a turbulent flow, given in section 3.5, there arose 'turbulent fluxes' which were time-averaged products of velocity and ϕ fluctuations. Any set of additional differential or algebraic equations, which would enable these quantities to be evaluated, is referred to as a "turbulence model".

3.6.1 Turbulent viscosity models

The concept of a 'turbulent viscosity', which relates the Reynolds stresses to velocity gradients in the flow, has already been introduced. The relevant equations are (3.4.17) to (3.4.21).

Several authors have proposed various ways of calculating μ_t. In a two-dimensional boundary-layer flow, for instance, μ_t may be calculated from a prescribed algebraic expression for the variation of the mixing-length ℓ_m (e.g. Patankar and Spalding, 1970). A more complicated way of calculating μ_t is to relate it to the turbulence kinetic energy k (equation 3.4.22) and a length-scale of turbulence ℓ. k is then determined via a transport equation, and ℓ is prescribed algebraically (e.g. Runchal (1969), Launder and Ying (1973)). These two approaches are, for obvious reasons, referred to as 'mixing-length' and 'one-equation' models respectively. A critical assessment of the merits and demerits of many such models is to be found in the book by Launder and Spalding (1972). Both types of model suffer from the major drawback than ℓ_m and ℓ are known with certainty for only the simplest types of flow. In a full three-dimensional flow, as in the rod-bundle and other duct geometries investigated here, it is almost impossible to prescribe a satisfactory distribution of length-scale.

Consequently, two-equation models, in which a second property of the turbulence[*] is solved for along with k, have come into vogue in recent years. Of these the most popular has been the $k \sim \varepsilon$ model developed initially by Harlow and Nakayama

---

[*] Footnote: the second variable has the general form $k^m \ell^n$ (see Launder and Spalding, 1972). For the $k \sim \varepsilon$ model, $m = 3/2$, $\ell = -1$.

(1968). The assumption is made that the turbulence is adequately characterized by two quantities: k, and ε, the rate of dissipation of k per unit mass of material. Both k and ε are regarded as obeying "transport equations", not unlike those described earlier for the transport of momentum and energy. Although this is an extreme simplification of the complexities of turbulent flow, the model contains a sufficient element of both to be the basis of useful predictions. The turbulent viscosity is calculated from the following relation:

$$\mu_t = C_\mu \rho \frac{k^2}{\varepsilon} \quad . \qquad (3.6.1)$$

where C_μ is an empirical constant.

The k$\sim\varepsilon$ model, and other two-equation models, have enjoyed a fair degree of success in the prediction of turbulent flows. Among the diverse flow situations investigated in recent years with the aid of the k$\sim\varepsilon$ model are the following: free turbulent flows (Launder et al, 1972), flow in a curved duct (Pratap and Spalding, 1975), two-dimensional flows in furnaces (Khalil et al, 1975), turbulent buoyant jets (McGuirk, 1975) and two-dimensional wall boundary-layers (Singhal and Spalding, 1975). In general, the performance of the model is satisfactory. Jones and Launder (1972) have modified the model for application to low-Reynolds-number flows; the modifications include the replacement of constants such as C_μ (equation 3.6.1) by functions of the local turbulent-Reynolds-number.

Nevertheless, despite the success of turbulent viscosity models in many applications, several important shortcomings in the basic approach may be identified. Some of these, of not immediate concern here, are discussed by Launder and Spalding (1972). One important defect (discussed below), however, is directly relevant to the asymmetric three-dimensional duct flows considered in this thesis.

It has long been established (Nikuradse, 1926) that for turbulent flow in square and rectangular channels, secondary motions arise in the cross-stream plane. These motions, although having a magnitude of only a few per cent of the main velocity, exercise an appreciable influence on the friction and heat-transfer performance of the duct. Brundrett and Baines (1964) have postulated that the flow is caused by imbalances among the Reynolds stresses in the cross-stream plane due to the sharply changing geometry. Consequently any calculation procedure that does not allow for these motions is seriously deficient; for example, friction factors for flow in a square duct are underestimated by more than ten per cent by neglecting secondary flow (Launder and Ying, 1973). A turbulence model of the turbulent-viscosity type is unable to predict this flow (see Ramachandra and Spalding, 1976) and thus requires some modifications.

3.6.2 Reynolds stress models

The most general and direct approach is to construct and solve differential transport equations for the Reynolds stresses themselves and for higher-order correlations. Such equations have been formulated for two-dimensional boundary-layer flows by Daly and Harlow (1968), Hanjelic and Launder (1972) and Launder et al. (1973), while Naot et al. (1972) have developed a differential stress model for square channels. The cost of generality, however, has been greater complexity. In most flow situations of interest, the appropriate form of modelling to be employed for the various terms in the equations is highly uncertain. Moreover, the computational cost of solving seven or more strongly-coupled non-linear partial differential equations for the turbulence field alone, is a powerful deterrent to the use of such a method in engineering calculations. So, the art of Reynolds stress modelling is still in its infancy and requires further nurturing before it can hold its own as a viable computational tool.

Fortunately, though, under certain circumstances it is possible to reduce the stress equations to algebraic relations by making certain simplifications regarding the convection and diffusion terms. For example, Rodi (1972) related the net transport of stress by continued convection and diffusion to that for the turbulence energy; while Launder and Ying (1973), in their successful square-duct predictions, chose to neglect these terms altogether.

In the present work, the method of Launder and Ying (1973) has been adopted to model the stresses in the momentum equations for the cross-stream velocities. The method yields simple algebraic expressions linking the stresses $\overline{u'^2}$, $\overline{v'^2}$ and $\overline{u'v'}$ to gradients in the axial velocity, and to k and ε.

It has been demonstrated (Gessner and Emery, 1976) that, in this case, the stresses in the axial-momentum equation may still be correctly evaluated via the turbulent viscosity. Unlike Launder and Ying who calculated ε through a prescribed global length-scale distribution, the present work employs the two-equation k∿ε model, thus providing (and solving) a transport equation for ε. The mathematical relations are given in the following two sections.

3.7 THE LAUNDER-YING ALGEBRAIC STRESS MODEL

In general, the exact form of the Reynolds stress transport equations for steady, incompressible flow may be written, in cartesian tensor notation, as follows:

$$\underbrace{u_k \frac{\partial \overline{u_i' u_j'}}{\partial x_k}}_{\text{I (convection)}} = \underbrace{- \left(\overline{u_j' u_k'} \frac{\partial u_i}{\partial x_k} + \overline{u_i' u_k'} \frac{\partial u_j}{\partial x_k} \right)}_{\text{II (generation)}} \underbrace{- 2\nu \left(\overline{\frac{\partial u_i'}{\partial x_k} \cdot \frac{\partial u_j'}{\partial x_k}} \right)}_{\text{III (dissipation)}}$$

$$\underbrace{+ \overline{\frac{p'}{\rho} \left(\frac{\partial u_i'}{\partial x_j} + \frac{\partial u_j'}{\partial x_i} \right)}}_{\text{IV (redistribution)}} \underbrace{- \frac{\partial}{\partial x_k} \left[\overline{u_i' u_j' u_k'} - \nu \frac{\partial \overline{u_i' u_j'}}{\partial x_k} + \overline{\frac{p'}{\rho} (\delta_{jk} u_i' + \delta_{ik} u_j')} \right]}_{\text{V (diffusion)}} \qquad (3.7.1)$$

where $\overline{\rho u_i' u_j'}$ is the Reynolds stress tensor and $\overline{u_i' u_j' u_k'}$ is the triple velocity-correlation tensor.

Equation (3.7.1) represents a balance of:

I - the rate of convection of $\overline{u_i' u_j'}$.

II - the rate of generation of the stress by the mean velocity field.

III - the rate of dissipation of the stress into thermal energy.

IV - the rate at which energy is distributed amongst the components of the fluctuating velocities by the action of the pressure fluctuations.

V - the rate of diffusion of the stress.

In simplifying the above equation, Launder and Ying made the following assumptions:

(i) The viscous diffusion term in V may be ignored for flows at high Reynolds numbers.

(ii) On the basis of arguments presented by Hanjalic and Launder (1972), diffusion resulting from fluctuating pressure-velocity interactions may also be neglected as a first approximation.

(iii) The generation terms for $\overline{u'^2}$, $\overline{v'^2}$ and $\overline{u'v'}$ are negligible, because the lateral motions are small in magnitude compared with the main velocity.

(iv) The effect of convection is small, especially near walls where the secondary flow influence is greatest, and so may be ignored.

(v) For high-Reynolds-number flows, dissipation occurs in the small-scale motion where the turbulence is locally isotropic. Under these conditions the term III in equation

(3.7.1) may be represented as,

$$2\nu\,\left(\overline{\frac{\partial u_i'}{\partial x_k}\cdot\frac{\partial u_j'}{\partial x_k}}\right) = \frac{2}{3}\,\delta_{ij}\,\varepsilon \quad . \qquad (3.7.2)$$

where ε is the (isotropic) dissipation rate. Following Hanjalic and Launder (1972), the triple velocity-correlation tensor associated with diffusion was written in terms of second-order correlations as follows:

$$\overline{u_i'u_j'u_k'} = -\,C_s\,\frac{k}{\varepsilon}\left(\,\overline{u_i'u_\ell'}\,\frac{\partial\overline{u_j'u_k'}}{\partial x_\ell} + \overline{u_j'u_\ell'}\,\frac{\partial\overline{u_k'u_i'}}{\partial x_\ell} + \overline{u_k'u_\ell'}\,\frac{\partial\overline{u_i'u_j'}}{\partial x_\ell}\,\right) \qquad (3.7.3)$$

where C_s is an empirical constant.

The final task of simulating the pressure-redistribution term IV in equation (3.7.1) was performed by employing the form proposed by Rotta (1951) and extended by Hanjalic and Launder (1972). The details of this may be found in the paper by Launder and Ying (1973) and (in its three-dimensional form) in Tatchell (1975).

The final results for the (kinematic) stresses in the cross-stream plane are quoted below. They are, for reasons of simplicity, given in cartesian coordinates, where u_1 and u_2 are the velocities in the cross-stream directional x_1 and x_2 respectively, and u_3 the velocity in the axial (x_3-direction.

$$\overline{u_1'^2} = \alpha_1\,k - \alpha_2\,C\mu\,\frac{k^3}{\varepsilon^2}\,\left(\frac{\partial u_3}{\partial x_1}\right)^2 \quad , \qquad (3.7.4)$$

$$\overline{u_2'^2} = \alpha_1 k - \alpha_2 C\mu \frac{k^3}{\varepsilon^2} \left(\frac{\partial u_3}{\partial x_2}\right)^2 , \qquad (3.7.5)$$

$$\overline{u_1'u_2'} = - \alpha_2 C\mu \frac{k^3}{\varepsilon^2} \frac{\partial u_3}{\partial x_1} \frac{\partial u_3}{\partial x_2} , \qquad (3.7.6)$$

$$\overline{u_1'u_3'} = - C\mu \frac{k^2}{\varepsilon} \frac{\partial u_3}{\partial x_1} , \qquad (3.7.7)$$

$$\overline{u_2'u_3'} = - C\mu \frac{k^2}{\varepsilon} \frac{\partial u_3}{\partial x_2} . \qquad (3.7.8)$$

Here, α_1 and α_2 are constants defined according to:

$$\alpha_1 \equiv \frac{(22C_{\phi 1} - 26 C_{\phi 2} - 10)}{33 (C_{\phi 1} - 2 C_{\phi 2})} , \qquad (3.7.9)$$

$$\alpha_2 \equiv \frac{4 (3C_{\phi 2} - 1)}{11 (C_{\phi 1} - 2C_{\phi 2})} . \qquad (3.7.10)$$

Where $C_{\phi 1}$ and $C_{\phi 2}$ are, in turn, empirical constants whose values were determined by Launder and Ying from an analysis of experimental data. The values are given in Table (3.9.1) in Section 3.9.

Equations (3.7.7) and (3.7.8) indicate that the turbulent viscosity hypothesis is valid for the stresses which lie in planes parallel to the primary velocity. However, the implication of equations (3.7.4) to (3.7.6) is that the stress-field in the cross-stream plane of the duct is due to the mean strain-rates in planes normal to it; this is contrary to the concept of a scalar turbulent viscosity. It is the stress-field caused in this way which gives rise to the turbulence-induced secondary motions discussed earlier.

The final form of the stress equations pertaining to the non-orthogonal coordinate system used in the present work are derived from equations (3.7.4) to (3.7.8) by elementary coordinate transformations.

They are:

$$\overline{u'^2} = \alpha_1 k - \alpha_2 C\mu \frac{k^3}{\varepsilon^2} \left\{\frac{1}{r\Delta\theta} \frac{\partial w}{\partial \xi} - \frac{G}{\Delta r} \frac{\partial w}{\partial \eta}\right\}^2 , \qquad (3.7.11)$$

$$\overline{v'^2} = \alpha_1 k - \alpha_2 C\mu \frac{k^3}{\varepsilon^2} \left\{\frac{1}{\Delta r} \frac{\partial w}{\partial \eta}\right\}^2 , \qquad (3.7.12)$$

$$\overline{u'v'} = - \alpha_2 C\mu \frac{k^3}{\varepsilon^2} \left(\frac{1}{\Delta r} \frac{\partial w}{\partial \eta}\right) \left(\frac{1}{r\Delta\theta} \frac{\partial w}{\partial \xi} - \frac{G}{\Delta r} \frac{\partial w}{\partial \eta}\right) , \qquad (3.7.13)$$

$$\overline{u'w'} = - \frac{\mu_t}{\rho} \left\{\frac{1}{r\Delta\theta} \frac{\partial w}{\partial \xi} - \frac{G}{\Delta r} \frac{\partial w}{\partial \eta}\right\} , \qquad (3.7.14)$$

$$\overline{v'w'} = - \frac{\mu_t}{\rho} \left(\frac{1}{\Delta r} \frac{\partial w}{\partial \eta}\right) . \qquad (3.7.15)$$

Equations (3.7.11) to (3.7.15), combined with equation (3.6.1) for μ_t, and the differential equations for k and ε to be given in the next section, constitute a satisfactory closure to the momentum equations (3.4.14) to (3.4.16).

3.8 STATEMENT OF THE EQUATIONS FOR k AND ε

Stated below are the modelled transport equations for k and ε, which were discussed in the earlier sections. The idea that turbulence energy is an entity, like the concentration of a chemical species, which can be created, transported and destroyed, was first proposed by Kolmogorov (1942). A similar equation was first formulated for ε by Daly and Harlow (1970).

(r, θ, z) coordinates:

The differential equations for steady, high-Reynolds number flows are (in their boundary-layer form):

$$\frac{\rho}{r}\frac{\partial}{\partial\theta}(uk) + \frac{\rho}{r}\frac{\partial}{\partial r}(rvk) + \rho\frac{\partial}{\partial z}(wk) = \frac{1}{r^2}\frac{\partial}{\partial\theta}\left(\Gamma_{eff,k}\frac{\partial k}{\partial\theta}\right) + \frac{1}{r}\frac{\partial}{\partial r}\left(r\,\Gamma_{eff,k}\frac{\partial k}{\partial r}\right) + G_k - \rho\varepsilon \quad , \qquad (3.8.1)$$

$$\frac{\rho}{r}\frac{\partial}{\partial\theta}(u\varepsilon) + \frac{\rho}{r}\frac{\partial}{\partial r}(rv\varepsilon) + \rho\frac{\partial}{\partial z}(w\varepsilon) = \frac{1}{r^2}\frac{\partial}{\partial\theta}\left(\Gamma_{eff,\varepsilon}\frac{\partial \varepsilon}{\partial\theta}\right) + \frac{1}{r}\frac{\partial}{\partial r}\left(r\,\Gamma_{eff,\varepsilon}\frac{\partial \varepsilon}{\partial r}\right) + \frac{\varepsilon}{k}(C_1 G_k - C_2\rho\varepsilon) \; . \qquad (3.8.2)$$

Here, G_k is the rate of generation of the turbulence energy, and is calculated from :

$$G_k \equiv \mu_t \left[2 \left\{ \left(\frac{1}{r} \frac{\partial u}{\partial \theta} + \frac{v}{r} \right)^2 + \left(\frac{\partial v}{\partial r} \right)^2 \right\} + \left\{ r \frac{\partial}{\partial r} \left(\frac{u}{r} \right) + \frac{1}{r} \frac{\partial v}{\partial \theta} \right\}^2 + \left(\frac{\partial w}{\partial r} \right)^2 + \left(\frac{1}{r} \frac{\partial w}{\partial \theta} \right)^2 \right] \qquad (3.8.3)$$

When, as in the present problem, the cross-stream velocities are small, G_k may be written simply as:

$$G_k = \mu_t \left[\left(\frac{\partial w}{\partial r} \right)^2 + \left(\frac{1}{r} \frac{\partial w}{\partial \theta} \right)^2 \right] \qquad (3.8.4)$$

<u>(η, ξ, z) coordinates</u>:

The transformation of the above equations into the non-orthogonal (η, ξ, z) coordinate system is deduced from the transformation for the general variable ϕ, given in section A.2 of Appendix A. The final results are:

<u>k-equation</u>

$$\frac{\rho}{r\Delta r} \frac{\partial}{\partial \eta} \{ r\,(v-uG)k \} + \frac{\rho}{r\Delta\theta} \frac{\partial}{\partial \xi} (uk) + \rho \frac{\partial}{\partial z} (wk)$$

$$= \frac{1}{r\Delta\theta} \frac{\partial}{\partial \xi} \left[\frac{\Gamma_{eff,k}}{r\,\Delta\theta} \frac{\partial k}{\partial \xi} - \frac{\Gamma_{eff,k}}{\Delta r} . G \frac{\partial k}{\partial \eta} \right] + \frac{1}{r\Delta r} \frac{\partial}{\partial \eta} \left[\Gamma_{eff,k} \frac{(1+G^2)r}{\Delta r} \frac{\partial k}{\partial \eta} \right.$$

$$\left. - \Gamma_{eff,k} \frac{G}{\Delta\theta} \frac{\partial k}{\partial \xi} \right] + \left[\frac{\Gamma_{eff,k}}{r\Delta\theta} \frac{\partial k}{\partial \xi} - \Gamma_{eff,k} \frac{G}{\Delta r} \frac{\partial k}{\partial \eta} - \rho u k \right] \frac{1}{r\Delta r} \frac{\partial (Gr)}{\partial \eta}$$

$$+ G_k - \rho\varepsilon \qquad ; \qquad (3.8.6)$$

ε-equation

$$\frac{\rho}{r\Delta r}\frac{\partial}{\partial\eta}\{\, r(v-uG)\varepsilon\} + \frac{\rho}{r\Delta\theta}\frac{\partial}{\partial\xi}(u\varepsilon) + \rho\frac{\partial}{\partial z}(w\varepsilon)$$

$$= \frac{1}{r\Delta\theta}\frac{\partial}{\partial\xi}\left[\frac{\Gamma_{eff,\varepsilon}}{r\Delta\theta}\frac{\partial\varepsilon}{\partial\xi} - \Gamma_{eff,\varepsilon}\frac{G}{\Delta r}\frac{\partial\varepsilon}{\partial\eta}\right] + \frac{1}{r\Delta r}\frac{\partial}{\partial\eta}\left[\Gamma_{eff,\varepsilon}\frac{(1+G^2)r}{\Delta r}\right.$$

$$\left.\cdot\frac{\partial\varepsilon}{\partial\eta} - \Gamma_{eff,\varepsilon}\frac{G}{\Delta\theta}\frac{\partial\varepsilon}{\partial\xi}\right] + \left[\frac{\Gamma_{eff,\varepsilon}}{r\Delta\theta}\frac{\partial\varepsilon}{\partial\xi} - \Gamma_{eff,\varepsilon}\frac{G}{\Delta r}\frac{\partial\varepsilon}{\partial\eta} - \rho u\varepsilon\right].$$

$$\cdot\frac{1}{r\Delta r}\frac{\partial}{\partial\eta}(Gr) + \frac{\varepsilon}{k}(C_1 G_k - C_2\rho\varepsilon) \quad ; \qquad (3.8.7)$$

With G_k given by,

$$G_k = \mu_t\left[\left(\frac{1}{r\Delta\theta}\frac{\partial w}{\partial\xi} - \frac{G}{\Delta r}\frac{\partial w}{\partial\eta}\right)^2 + \left(\frac{1}{\Delta r}\frac{\partial w}{\partial\eta}\right)^2\right] . \qquad (3.8.8)$$

μ_t is of course defined by equation (3.6.1). The similarity of the above equations to that for temperature (equation (3.5.9)) is immediately apparent. However it will be noticed that the equations for k and ε contain source and sink terms. In accordance with the discussion in section (3.5), $\Gamma_{eff,k}$ and $\Gamma_{eff,\varepsilon}$ are related to μ_t according to the following definitions:

$$\Gamma_{eff,k} \equiv \mu + \frac{\mu_t}{\sigma_{t,k}} \quad , \qquad (3.8.9)$$

$$\Gamma_{eff,\varepsilon} \equiv \mu + \frac{\mu_t}{\sigma_{t,\varepsilon}} \quad . \qquad (3.8.10)$$

The values of the (assumed) constants $\sigma_{t,k}$ and $\sigma_{t,\varepsilon}$, together with those for C_1 and C_2 which appear in the equation for ε, will be given in the following section.

3.9 AUXILIARY INFORMATION

Equations (3.4.13) to (3.4.16), (3.5.8). (3.8.6) and (3.8.7) comprise a system of seven coupled partial-differential equations that describe the flow and heat-transfer behaviour under consideration. Additionally, auxiliary relationships such as equations (3.7.11) to (3.7.15), (3.6.1) and (3.8.9) to (3.8.10), serve to relate the unknown terms in each of the equations to the dependent variables of these equations. The complete mathematical specification of the flow problem, however, requires the following further information.

(a) Initial conditions, i.e. initial values of dependent variables corresponding to the position along the predominant flow direction (the z-direction) at which solution of the equation set begins. Note that, because of the parabolic character of the equations, conditions at the exit need not be specified; they are an outcome of the calculation.

(b) Boundary conditions, i.e. the constraints on all the dependent variables at the four boundaries of the cross-sectional plane for all values of z. Only the following types of physical boundary will be encountered in the present study: stationary channel walls and planes of symmetry. At the former, all components of velocity are zero. For the turbulence quantities wall conditions are deduced from experimental knowledge of near-wall turbulent flows in a manner described in chapter 4. At a plane of symmetry, the normal velocity is zero, and the normal gradient of all other quantities is also zero.

Note: the full set of boundary conditions peculiar to each flow pattern studied in this thesis will be given in detail in the chapter appropriate to that problem.

(c) The values of the 'universal' constants. Listed in Table (3.9.1) are the values assigned in the present study to the various constants which appear in the turbulence model described earlier*. The values are those recommended by earlier users of the model, and have been determined through a combination of data analysis and detailed computer optimization. No adjustments have been made during the course of the present study.

In general, the potency of a turbulence model is measured by the universality of its constants. In other words, a good model is one that is capable of accurately predicing a number of flow situations with a fixed set of constants.

3.10 CLOSURE

In summary, the mathematical framework of the present work has been presented in this chapter. The partial-differential

---

* Footnote: the values given are, strictly, for high-Re flows. For low-Re flows, the 'constants' should all be made functions of the turbulent Reynolds number $(\frac{\rho k^{\frac{1}{2}} \ell}{\mu})$.

TABLE 3.9.1: TURBULENCE-MODEL CONSTANTS

Constant	Appearance	Value Used	Basic of choice
C_μ	Equation (3.6.1)	0.09	Measurements of τ and k near to a wall - Launder and Spalding (1972)
C_1	Equation (3.8.2)	1.44	Measurement of turbulence near to a wall- Launder & Spalding (1972). Value adjusted after fine turning over a wide range of flow situations
C_2	Equation (3.8.2)	1.92	Decay of turbulence behind a grid - Launder & Spalding (1972)
$C_{\phi 1}$	Equation (3.7.9)	2.6	Decay of non-isotropic turbulence - Launder & Ying (1973)
$C_{\phi 2}$	Equation (3.7.9)	0.37	Plane homogenous shear flow - Launder & Ying (1973)
κ	Equation (4.5.1)	0.42	Measurements of velocities in Couette flow near a wall
E	Equation (4.5.1)	9.0	
$\sigma_{t,k}$	Equation (3.8.9)	1.0	Physical arguments suggest that $\sigma_{t,k}$ & $\sigma_{t,\varepsilon}$ should be near unity. Values shown are the result of computer optimization over a wide range of flows - Launder & Spalding (1972)
$\sigma_{t,\varepsilon}$	Equation (3.8.10)	1.23	
$\sigma_{t,T}$	Equation (3.5.9)	0.85	Analysis of heat transfer data in circular pipe - Kestin & Richardson (1963)

equations that govern the three-dimensional parabolic flow have been derived in the non-orthogonal coordinate system developed for rod-bundle analysis. In the case of turbulent motion, closure of the equations is achieved via the provision of transport equations for the kinetic energy and the dissipation rate of turbulence. The special treatment furnished by Launder and Ying (1973) for the Reynolds-stress terms in the cross-stream momentum equations has been reviewed; this algebraic stress formulation, when coupled with the transport equations for k and ε, forms the basis of the turbulent-flow computations reported in this thesis.

CHAPTER 4

THE SOLUTION PROCEDURE

4.1 INTRODUCTION

4.1.1 Preliminary Remarks

In the previous chapter, the partial-differential equations which govern the three-dimensional flows considered in this thesis were set out, along with accompanying auxiliary relations. The task of the present chapter is to describe the numerical procedure which has been employed in the solution of these equations.

As was mentioned in chapter 1, the so-called "finite-difference" approach has been used, in which attention is focussed on a finite number of points within the domain of interest, regularly located on a "finite-difference grid". Each grid point is surrounded by a fictitious "control volume"; and the finite-difference equations connecting the values of variables at the different grid points are obtained by approximate integration of the differential equations over these control volumes. Owing to the irregular geometry of the flow domain, a non-orthogonal grid, based on the non-orthogonal coordinate system developed in chapter 3, was rendered necessary.

The resulting finite-difference equations are non-linear and strongly coupled. Hence, special care has to be expended in the implementation of a convergent iterative solution scheme. One such scheme, the SIMPLE (Semi-Implicit Method for Pressure-Linked Equations) method of Patankar and Spalding (1972), has proved to be highly successful, and so was adopted in the present study. This method exploits to full advantage the parabolic nature of the flow: a marching-integration procedure is employed, and at any given position along the duct, the dependent variables are solved successively over the whole cross-stream plane. A "guess-and-correct" procedure is used to solve the momentum equations: the velocity field is calculated from a guessed pressure distribution which is then adjusted via the continuity equation; the "pressure-corrections" so deduced are then used to correct the velocity field so that continuity is satisfied everywhere.

The calculation procedure, therefore, comprises the following main stages:-

(a) Subdivision of the flow domain into finite regions by a suitable finite-difference grid.
(b) Derivation of the relevant finite-difference equations by integration of the differential equations over these finite regions (called "cells" or "control volumes").
(c) Solution of the resulting set of algebraic equations.

A detailed description of each of these stages is presented below.

4.1.2 Outline of the chapter

This chapter comprises four main sections: Section 4.2 describes in detail the special finite-difference grid that has been employed in the present calculations. In section 4.3 the differential equations are integrated and the desired finite-difference expressions obtained. The method of solution of these finite-difference equations is described in section 4.4; while the manner in which boundary conditions are incorporated into the solution procedure, and the special treatment afforded to the near-wall region in turbulent flow are discussed in section 4.5.

4.2 GENERAL CONCEPT

4.2.1 The finite-difference grid

The finite-difference grid consists of a number of intersecting grid lines disposed over the three-dimensional flow domain. The family of grid lines in the cross-stream plane are mutually non-orthogonal, as described in chapter 3. The mathematical description of the grid is to be found in section (3.2) of that chapter. The intersections of these lines, known as "grid nodes", serve as reference locations for the identification of the discrete values of the flow variables. The spacing between such grid nodes need not be uniform but may be varied so as to locate more of them in regions of steep property variations. The choice of an appropriate grid size is often a compromise between accuracy and economy: the computed results must be independent of grid-fineness to within the stipulated degree of accuracy, which in turn is usually determined by cost considerations.

4.2.2 The location of variables

Figure 4.2.1 shows the manner in which the flow variables are located in the finite-difference grid. The pressure, axial velocity w, and all scalar properties such as turbulence kinetic energy, temperature etc. are stored at the grid nodes, while the velocity components in the cross-stream plane are placed midway between adjacent grid nodes. The dashed envelopes shown in the figure are for purposes of identification: the variables enclosed by a given dashed loop are denoted by the same subscript. This "staggered-grid" arrangement has a two-fold advantage:

(i) The velocities are stored midway between the pressures that drive them; hence, the pressure-gradients may be conveniently calculated.

(ii) the cross-stream velocities are directly available for the calculation of the convective fluxes of flow properties stored at the grid nodes.

4.2.3 Control volumes

The 'control volumes' represent small arbitrary regions surrounding each node, over which the differential equations are integrated in order to obtain their equivalent finite-difference forms. Realistic assumptions are made regarding the variation of variables between grid nodes. This micro-

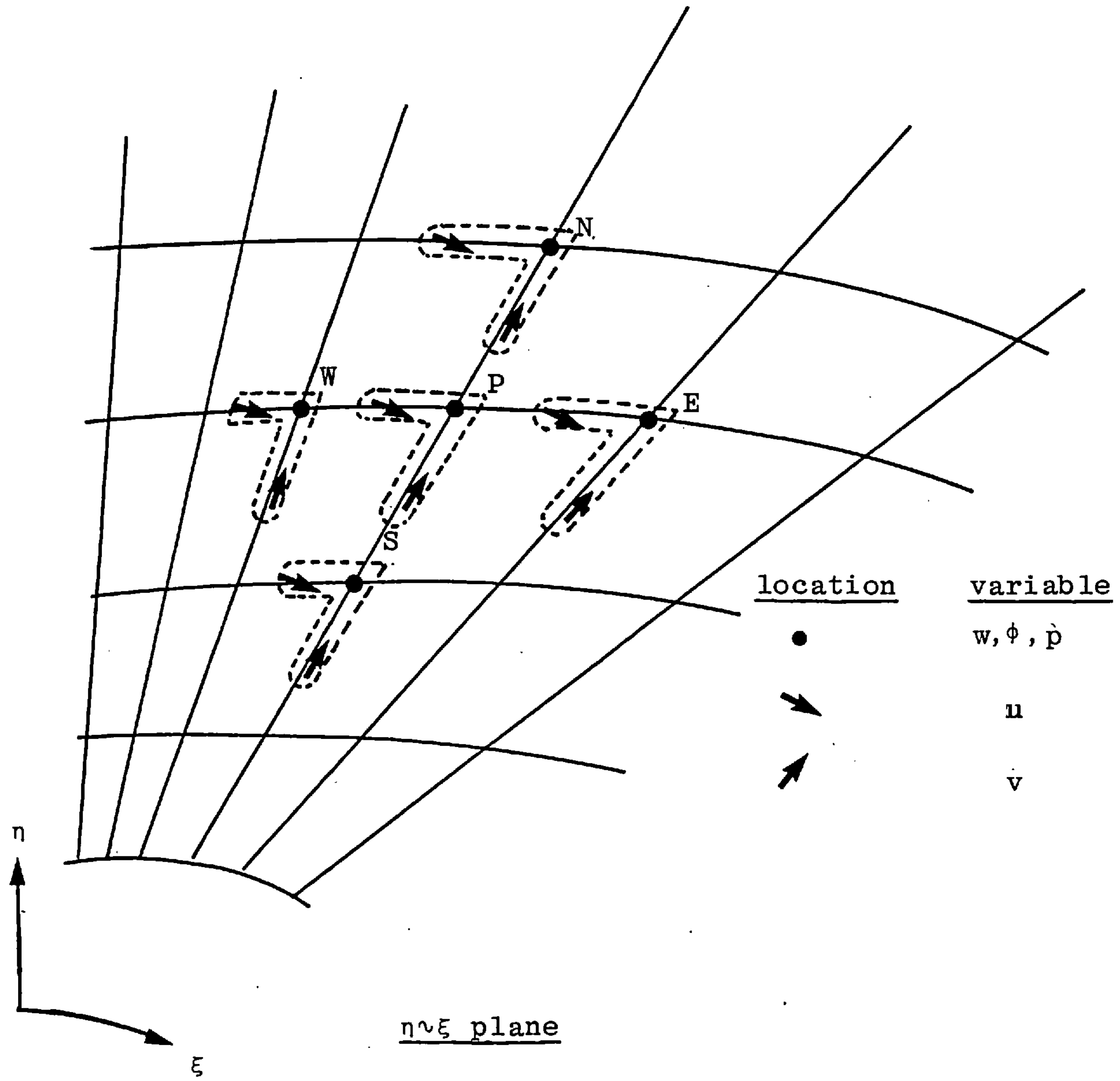

$\eta \sim \xi$ plane

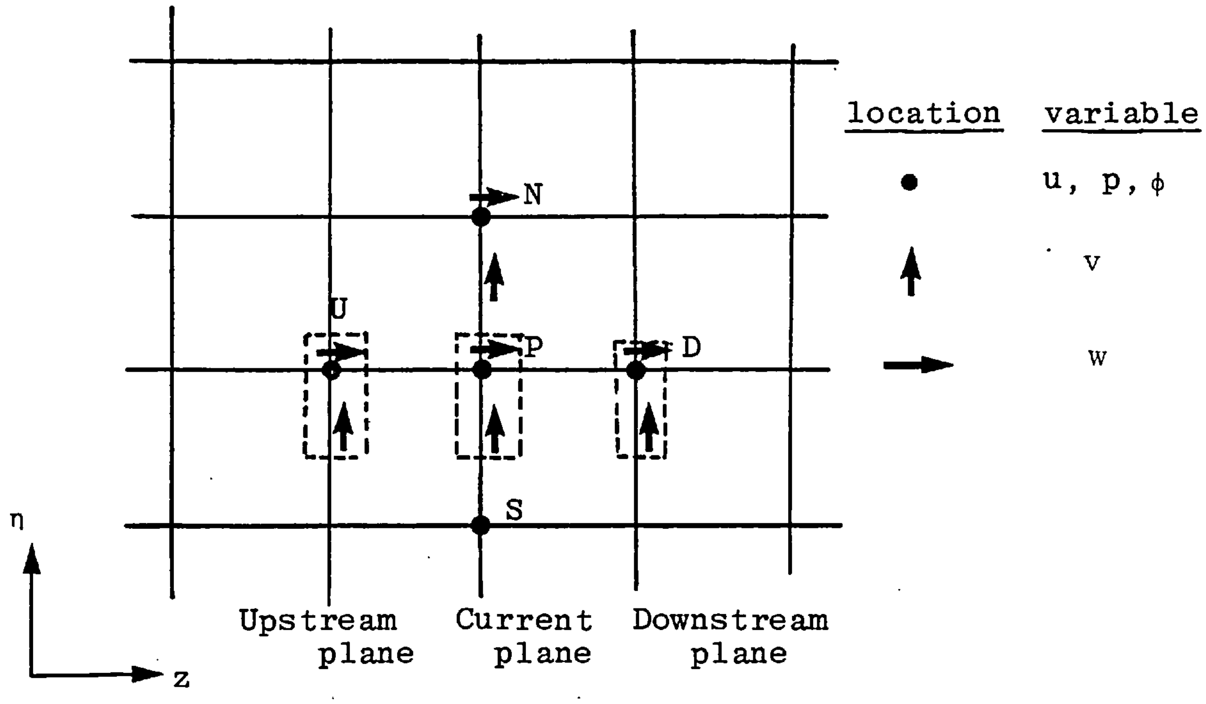

$\eta \sim z$ plane

FIG. 4.2.1: LOCATION OF VARIABLES ON FINITE-DIFFERENCE GRID

integral technique ensures that the finite-difference equations satisfy the relevant conservation principle.

Figure 4.2.2 depicts the control volumes for the velocity components and for the general variable ϕ. P is a typical grid node, and its five nearest neighbours are denoted by N, S, E, W & U. ϕ_N is the value of ϕ prevailing at the node N, ϕ_S is the value of ϕ at node S, and so on. The lateral boundaries of the control volume for ϕ and w lie midway between adjacent nodal points, and the upstream and downstream faces contain the upstream and downstream nodes respectively.

4.2.4 Modifications near boundaries

The staggered-grid system described above presents a few difficulties in calculating the flow variables situated adjacent to the boundaries of the flow domain. In order to overcome these difficulties slightly different practices are employed for locating the near-boundary velocities. Figure 4.2.3 shows the location of velocities near the boundaries. The new locations of the near-boundary velocities also modify the associated control volumes; these changes are also illustrated in the figure.

4.3 THE FINITE-DIFFERENCE EQUATIONS

4.3.1 Integration of the differential equations

It was observed in chapter 3 that the partial-differential equations which govern the transport of momentum, enthalpy, turbulence kinetic energy and dissipation rate have the same

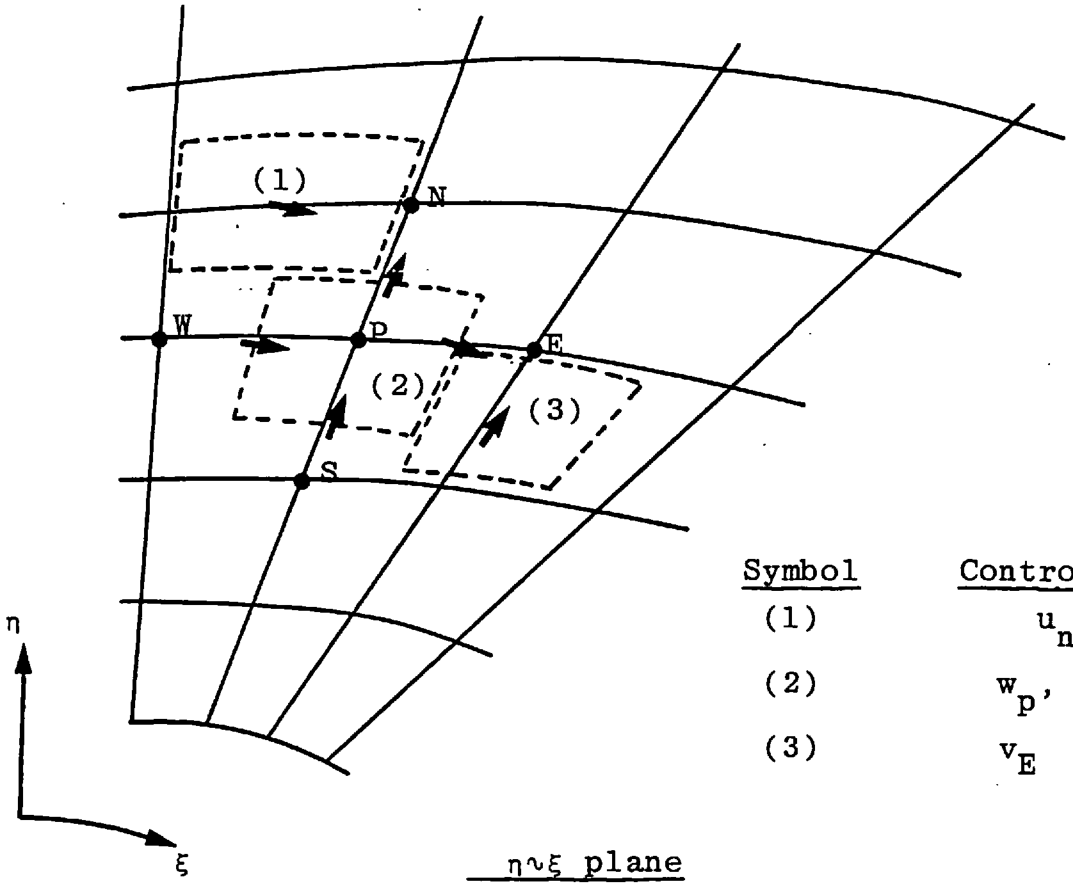

Symbol	Control Volume for:
(1)	u_n
(2)	w_p, ϕ_p, Continuity
(3)	v_E

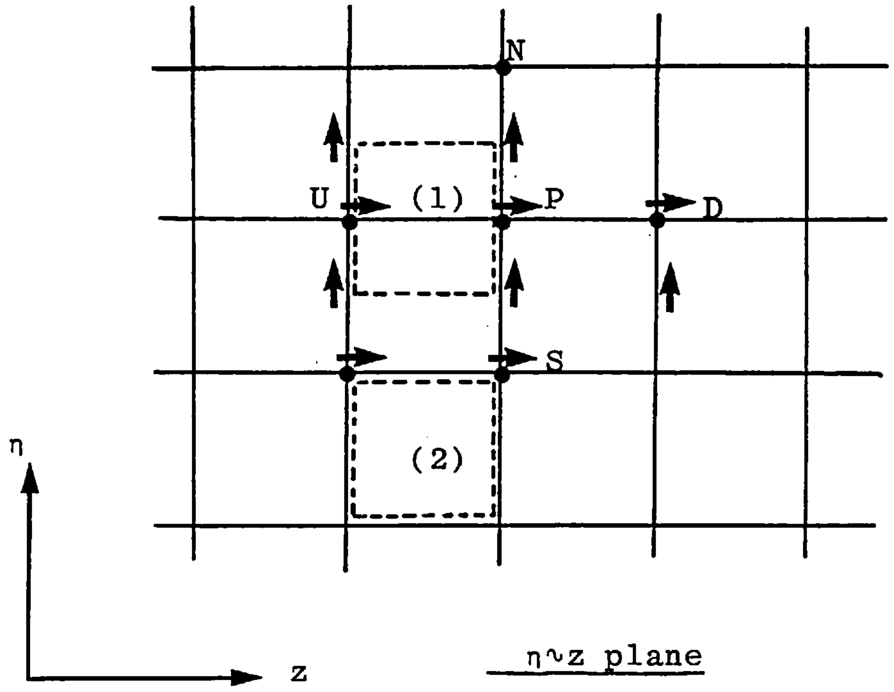

Symbol	Control Volume for:
(1)	u_p, w_p, ϕ_p
(2),	v_S

FIG. 4.2.2: DEFINITION OF CONTROL VOLUMES

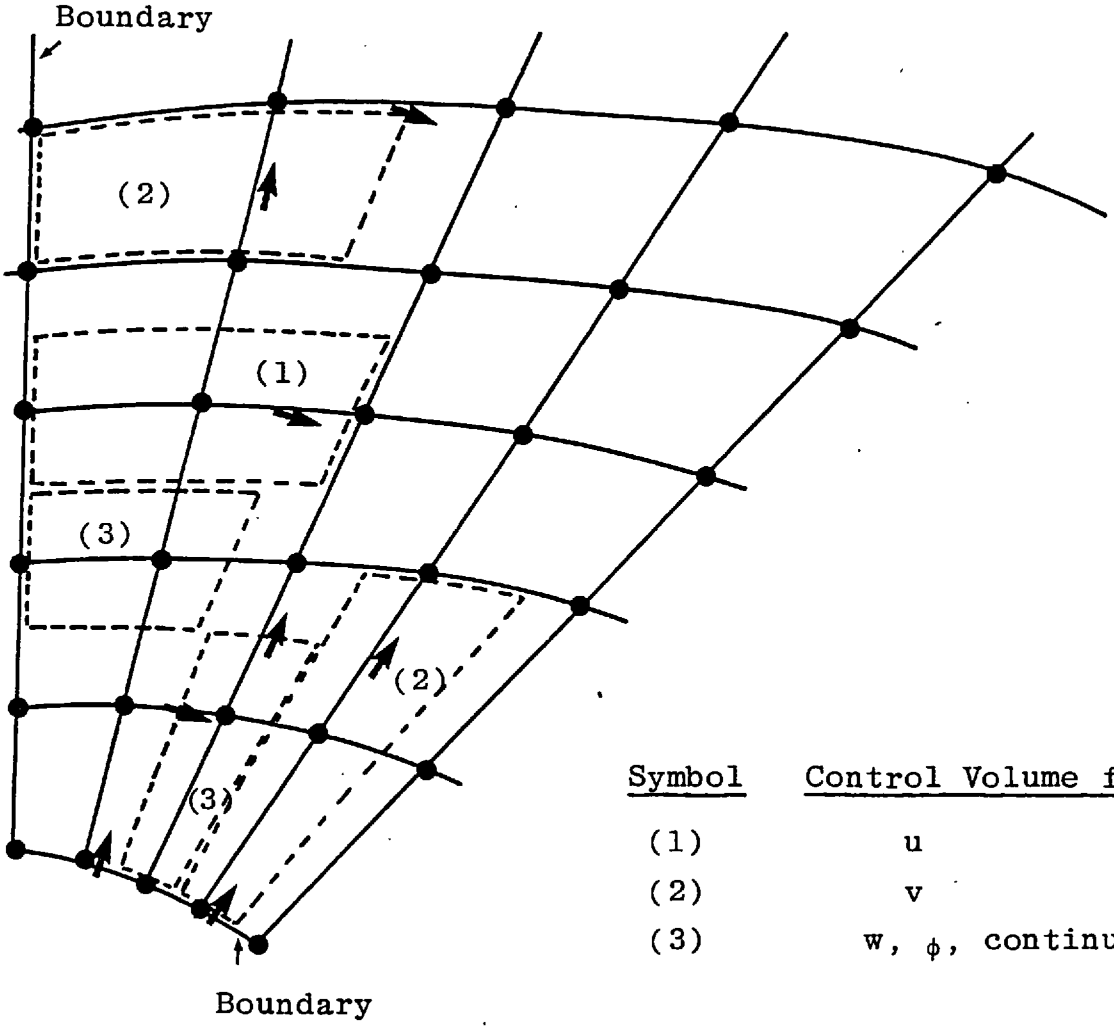

Symbol	Control Volume for:
(1)	u
(2)	v
(3)	w, ϕ, continuity

cross-stream plane

FIG. 4.2.3: NEAR-BOUNDARY CONTROL VOLUMES

general form, namely as follows:

$$\begin{aligned}
&\frac{\rho}{r\Delta r}\frac{\partial}{\partial\eta}\{r(v-uG)\phi\} + \frac{\rho}{r\Delta\theta}\frac{\partial(u\phi)}{\partial\xi} + \rho\,\frac{\partial(w\phi)}{\partial z} = \frac{1}{r\Delta\theta}\frac{\partial}{\partial\xi}\left[\frac{\Gamma_{\phi,\mathrm{eff}}}{r\Delta\theta}\frac{\partial\phi}{\partial\xi}\right.\\
&\qquad \left. - \frac{\Gamma_{\phi,\mathrm{eff}}G}{\Delta r}\frac{\partial\phi}{\partial\eta}\right] + \frac{1}{r\Delta r}\frac{\partial}{\partial\eta}\left[\Gamma_{\phi,\mathrm{eff}}\frac{(1+G^2)r}{\Delta r}\frac{\partial\phi}{\partial\eta} - \Gamma_{\phi,\mathrm{eff}}\frac{G}{\Delta\theta}\frac{\partial\phi}{\partial\xi}\right]\\
&\qquad + \left[\frac{\Gamma_{\phi,\mathrm{eff}}}{r\Delta\theta}\frac{\partial\phi}{\partial\xi} - \Gamma_{\phi,\mathrm{eff}}\frac{G}{\Delta r}\frac{\partial\phi}{\partial\eta} - \rho u\phi\right]\frac{1}{r\Delta r}\frac{\partial(Gr)}{\partial\eta} + S_\phi \;.
\end{aligned}\tag{4.3.1}$$

The nomenclature employed here is the same as that in the previous chapter. The equations for the different variables are distinguished from one another through the values of $\Gamma_{\phi,\mathrm{eff}}$ and the 'source' term S_ϕ. This is clarified in Table 4.3.1, from which the individual equations may be directly obtained. This similarity of form may be exploited in deriving the appropriate finite-difference equations.

Equation (4.3.1) is now integrated over the control volume for the ϕ variable appropriate to the arbitrary grid node P. The control volume face in the cross stream plane is depicted in figure 4.3.1. The notation in the figure is self-explanatory. Note that while the captions N, E etc. refer to the nodal points, the small letters, n, e, etc. denote cell interfaces. Also, U refers to the node immediately upstream of P. The volume of the cell is given by

$$\Delta V = \Delta S \; \Delta z \qquad . \tag{4.3.2}$$

TABLE 4.3.1: THE COEFFICIENTS IN THE ϕ-EQUATIONS

ϕ	Γ_ϕ	S_ϕ
1	0	0
v	μ	$-\frac{1}{\Delta r}\frac{\partial p}{\partial \eta} - \frac{2\mu}{r^2\Delta\theta}\frac{\partial u}{\partial \xi} + \frac{2\mu G}{r\Delta r}\frac{\partial u}{\partial \eta}$ $-\frac{\mu v}{r^2} - \frac{1}{\Delta r}\frac{\partial \overline{v'^2}}{\partial \eta} - \frac{1}{r\Delta\theta}\frac{\partial \overline{u'v'}}{\partial \xi}$ $+\frac{G}{\Delta r}\frac{\partial \overline{u'v'}}{\partial \eta} + \frac{(\overline{u'^2} - \overline{v'^2})}{r}$.
u	μ	$-\frac{1}{r\Delta\theta}\frac{\partial p}{\partial \xi} + \frac{G}{\Delta r}\frac{\partial p}{\partial \eta} + \frac{2\mu}{r^2\Delta\theta}\frac{\partial v}{\partial \xi}$ $-\frac{2\mu G}{r\Delta r}\frac{\partial v}{\partial \eta} - \mu\frac{u}{r^2} - \frac{1}{r\Delta\theta}\frac{\partial \overline{u'^2}}{\partial \xi}$ $+\frac{G}{\Delta r}\frac{\partial \overline{u'^2}}{\partial \eta} - \frac{1}{\Delta r}\frac{\partial \overline{u'v'}}{\partial \eta} - \frac{2\overline{u'v'}}{r}$.
w	$\mu + \mu_t$	0
k	$\mu + \frac{\mu_t}{\sigma_{t,k}}$	$G_k - \rho\varepsilon$
ε	$\mu + \frac{\mu_t}{\sigma_{t,\varepsilon}}$	$\frac{\varepsilon}{k}(C_1G_k - C_2\rho\varepsilon)$
T	$\frac{\mu}{\sigma_\ell} + \frac{\mu_t}{\sigma_{t,T}}$	0

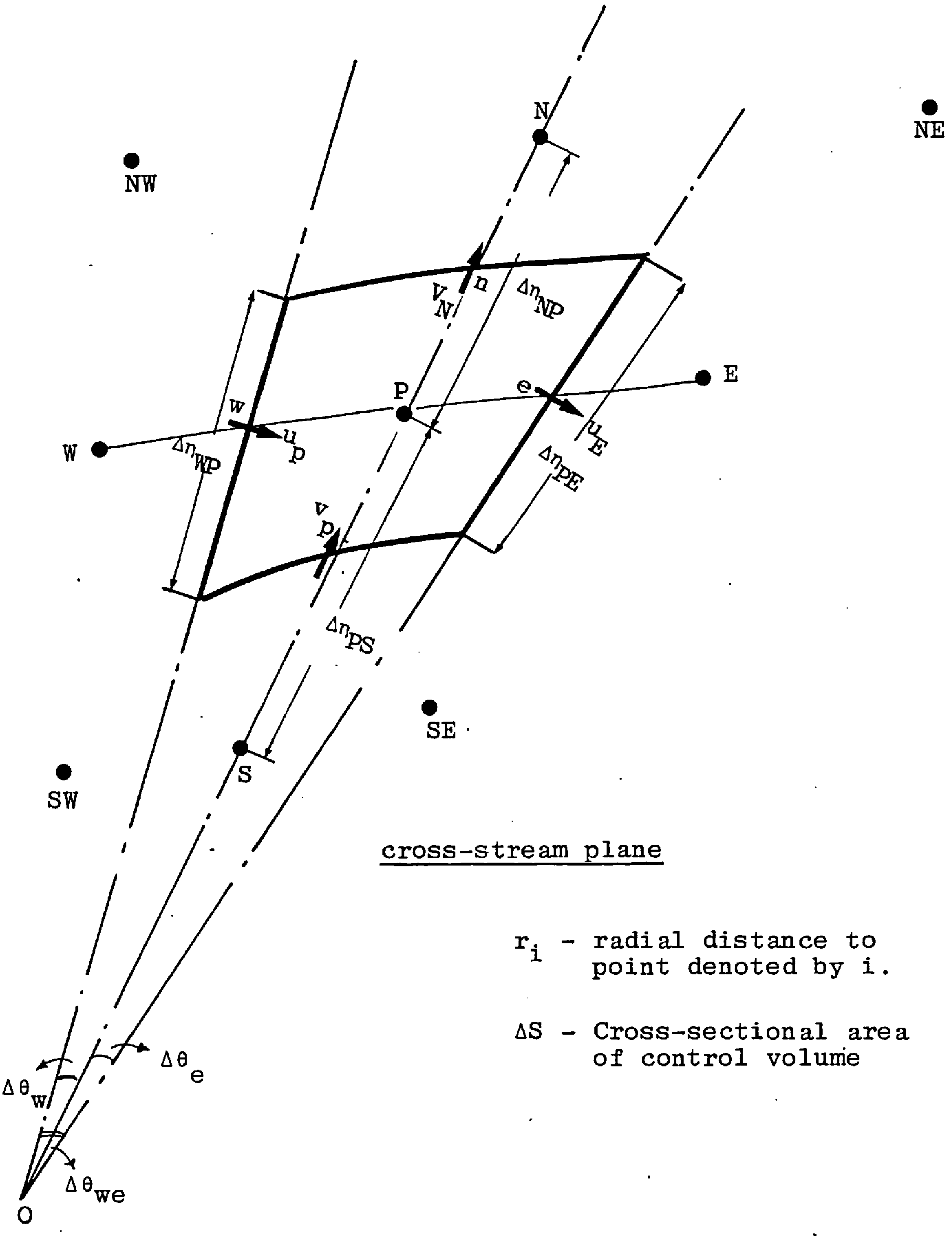

r_i - radial distance to point denoted by i.

ΔS - Cross-sectional area of control volume

FIGURE 4.3.1: MAIN CONTROL SURFACE FOR NODE P

where ΔS is the area of the $\eta \sim \xi$ surface shown in the figure, and Δz the inter-modal width in the z-direction.

It is demonstrated in Appendix C that the third term on the right-hand side of equation (4.3.1) vanishes when the latter is integrated over the control cell. The integration is performed in Appendix C; the final integral equivalent of equation (4.3.1) is given below.

$$\underbrace{\int_{z_u}^{z_p}\int_{\eta_s}^{\eta_n}\left[\rho u\phi - \frac{\Gamma^{*}}{r\Delta\theta}\frac{\partial\phi}{\partial\xi} + \Gamma\frac{G}{\Delta r}\frac{\partial\phi}{\partial\eta}\right]_{w}^{e}\Delta r \, d\eta dz}_{\text{I}}$$

$$+ \underbrace{\int_{z_u}^{z_p}\int_{\xi_w}^{\xi_e}\left[\rho(v-uG)\phi - \frac{\Gamma(1+G^2)}{\Delta r}\frac{\partial\phi}{\partial\eta} + \frac{\Gamma G}{r\Delta\theta}\frac{\partial\phi}{\partial\xi}\right]_{s}^{n} r\Delta\theta \, d\xi dz}_{\text{II}}$$

$$+ \underbrace{\int_{\xi_w}^{\xi_e}\int_{\eta_s}^{\eta_n}\left[\rho W\phi\right]_{u}^{p} r\Delta r\Delta\theta d\eta d\xi}_{\text{III}} = \underbrace{\int_{z_u}^{z_p}\int_{\xi_w}^{\xi_e}\int_{\eta_s}^{\eta_n} S_{\phi} \, r\Delta r\Delta\theta d\xi d\eta dz}_{\text{IV}} . \qquad (4.3.3)$$

4.3.2 Physical meaning of the terms in the equations

Before proceeding to the final formulation of the desired finite-difference equivalent of equation (4.3.1), it is

---

[*] Footnote: Here and throughout the remainder of this section, the subscripts 'ϕ,eff' are, for the sake of convenience, omitted from the diffusion coefficient Γ.

worthwhile to consider the physical meaning of the various integrals in the above equation.

The first integral, labelled I, represents the net transport of ϕ by convection (the ρ term) and diffusion (the Γ terms) across the east and west faces of the control volume. The velocity u is normal to these faces, but the gradient of normal to the east face, say, which is required for the diffusion calculation, is the vector sum of the gradient in the direction of the line from P to E and of the component tangential to that face. In the case of an orthogonal grid, the latter component would not appear, since the line from P to E would be normal to the east face of the cell.

Similarly, the integral term II on the left-hand side of equation (4.3.3) represents the net convective and diffusive flux of ϕ through the north and south faces of the control volume. Here the first term in the integral expresses the resultant convective component of the flux in the direction normal to the north and south faces, while the second and third terms represent the net normal diffusion - comprising the vector sum of the radial and circumferential gradients - across the same faces. Hence, all the terms involving 'G' in the integrals in equation (4.3.3) above are due directly to the "sheared" shape of the control volumes in the non-orthogonal grid. In the normal course of events with an orthogonal grid, the finite-difference equation connecting the value of ϕ at P with its neighbours would only make reference to the nearest neighbours N, S, E and W; however, it is now to be expected that, owing to the additional G-terms, the equation in the non-orthogonal grid will also include values of ϕ at the more remote neighbours NW, NE, SW and SE.

Finally, note that the term III in equation (4.3.3) represents the net axial convective flux of ϕ through the downstream and upstream faces, while term IV is simply the net 'source' of ϕ in the cell. Equation (4.3.3), therefore, expresses the overall conservation of ϕ for the control volume surrounding P.

4.3.3 Final finite-difference form

In order to discretize the various integral terms in equation (4.3.3), certain assumptions must first be made regarding the variation of ϕ between grid nodes. The assumptions made here are:

(a) For diffusion in the $\eta \sim \xi$ plane, the variation of ϕ between adjacent nodes is assumed to be linear.

(b) For the convective flux in the $\eta \sim \xi$ plane, account is taken of the local flow direction: the value of ϕ transported across a cell face is taken to be the value prevailing at the grid node on the upwind side of the face. The "upwind-differencing" scheme is not only physically realistic, but also ensures the stability of the iterative procedure.

(c) For convection in the z-direction, the value of ϕ which is convected to the upstream value ϕ_u, whose variation in the cross-stream plane is assumed to be step wise, i.e. ϕ_u is constant over the dotted region shown in figure 4.2.2 but changes abruptly at its edges, to the values at the neighbouring nodes.

Equation (4.3.3) may now be written as the following finite-difference form:

$$L_e^{\xi}\,\phi_E - L_w^{\xi}\,\phi_W + L_n^{\eta}\,\phi_N - L_s^{\eta}\,\phi_S + F_P\,\phi_P - F_u\,\phi_U$$

$$= T_e^{\xi}\,(\phi_E - \phi_P) - T_w^{\xi}\,(\phi_P - \phi_W) + T_n^{\eta}\,(\phi_N - \phi_P)$$

$$- T_s^{\eta}(\phi_P - \phi_S) + S_{\phi,u} + S_{\phi,P}\,\phi_P + S'_{\phi,u}\;. \qquad (4.3.4)$$

In the above equation, the symbols L, T and F stand for the following expressions:

$$L_e^{\xi} = \text{AMAX}\left[\,0,\; -\rho u_E\;\Delta\eta_{PE}\;\Delta z\,\right]$$

$$L_w^{\xi} = \text{AMAX}\left[\,0,\; \rho u_P\;\;\Delta\eta_{WP}\;\Delta z\,\right]$$

$$L_n^{\eta} = \text{AMAX}\left[\,0,\; -\rho\{v_N - \frac{G_n}{4}\,(u_P + u_E + u_N + u_{NE})\}\;r_n\;\;\Delta\theta_{we}\;\Delta z\right]\;,$$

$$L_s^{\eta} = \text{AMAX}\left[\,0,\; \rho\,\{\,v_P - \;\frac{G_s}{4}\,(u_P + u_E + u_S + u_{SE})\}\;r_s\;\;\Delta\theta_{we}\;\Delta z\right]\;,$$

$$T_e^{\xi} = \frac{\Gamma_e\;\;\Delta\eta_{PE}\;\Delta z}{r_e\;\;\delta\theta_e}\;,$$

$$T_w^{\xi} = \frac{\Gamma_w\;\Delta\eta_{WP}\;\;\Delta z}{r_w\;\delta\theta_w}\;,$$

$$T_n^{\eta} = \Gamma_n \frac{(1+G_n^2)\; r_n\; \Delta\theta_{we}\; \Delta z}{\delta\eta_{NP}} \quad ,$$

$$T_s^{\eta} = \Gamma_s \frac{(1+G_s^2)\; r_s\; \Delta\theta_{we}\; \Delta z}{\delta\eta_{PS}} \quad ,$$

$$F_u = (\rho w)_u\; \Delta S \quad ,$$

$$F_p = (\rho w)_p\; \Delta S \quad ,$$

with,

$$\Delta S = r_p\; \Delta\theta_{we}\; 0.5\; (\delta\eta_{NP} + \delta\eta_{PS}) \quad . \qquad (4.3.5)$$

The notation used is that of figure 4.3.1. The terms $S_{\phi,u}$ and $S_{\phi,p}\phi_p$ in equation (4.3.4) represent the contribution due to the source terms; they have been obtained by linearizing S_ϕ so that the integral labelled IV in equation (4.3.3) may be written as:

$$\int\int\int_{\Delta v} S_\phi\; r\Delta r\Delta\theta d\xi d\eta dz = S_{\phi,U} + S_{\phi,P}\; \phi_P \quad . \qquad (4.3.6)$$

where U and P refer to the upstream and 'current' values respectively.

Finally, the last term in equation (4.3.4) has been written as a pseudo-source $S'_{\phi,u}$; it comprises the components of the diffusional flux terms which involve the remote grid nodes NW, SW etc. In the evaluation of the gradients of ϕ, central-difference formulae have been employed. The full expression for $S'_{\phi,u}$ is given below:

$$S'_{\phi,u} = -\frac{1}{4}\left\{\frac{G_e \Gamma_e}{\Delta\eta_{PE}} (\phi_N + \phi_{NE} - \phi_S - \phi_{SE}) \ \Delta\eta_{PE} \ \Delta z\right.$$

$$\left. - \frac{G_w \Gamma_w}{\Delta\eta_{WP}} (\phi_N + \phi_{NW} - \phi_S - \phi_{SN}) \ \Delta\eta_{WP} \ \Delta z \right\}$$

$$- \frac{1}{4}\left\{\frac{G_n \Gamma_n}{r_n \Delta\theta_{we}} (\phi_E + \phi_{NE} - \phi_W - \phi_{NW}) \ r_n \ \Delta\theta_{we} \ \Delta z\right.$$

$$\left. - \frac{G_s \Gamma_s}{r_s \Delta\theta_{we}} (\phi_E + \phi_{SE} - \phi_W - \phi_{SW}) \ r_s \ \Delta\theta_{we} \ \Delta z\right\} \qquad (4.3.7)$$

The expressions (4.3.5) (4.3.7) may be substituted into equation (4.3.4) to yield the following equation for ϕ_P:

$$\phi_P = A_E^{\phi} \phi_E + A_W^{\phi} \phi_W + A_N^{\phi} \phi_N + A_S^{\phi} \phi_S + B^{\phi} \qquad (4.3.8)$$

where,

$$A_E^{\phi} = A'_E / A'_P \quad ,$$

$$A_W^{\phi} = A'_W / A'_P \quad ,$$

$$A_N^{\phi} = A'_N / A'_P \quad ,$$

$$A_S^{\phi} = A_S'/A_P' ,$$

$$B^{\phi} = B'/A_P' ,$$

and

$$A_E' = T_e^{\xi} - L_e^{\xi} ,$$

$$A_W' = T_w^{\xi} - L_w^{\xi} ,$$

$$A_N' = T_n^{\eta} - L_n^{\eta} ,$$

$$A_S' = T_s^{\eta} - L_s^{\eta} ,$$

$$B' = S_{\phi,u} + S_{\phi,u}' + F_u\phi_u ,$$

$$A_P' = A_E' + A_W' + A_N' + A_S' - S_{\phi,P} + F_P . \qquad (4.3.9)$$

Equation (4.3.8) represents the final form of the required finite-difference equivalent of the differential equation (4.3.1). It relates ϕ_P to the ϕ values at neighbouring nodes on the numerical grid. Note that no downstream nodes appear in the equation; it is this feature which allows the use of a marching solution procedure.

Momentum Equations

The finite-difference counterparts of the three momentum equations are, by analogy with the general equation (4.3.8), deduced to be as follows:

$$w_P = A_E^W w_E + A_W^W w_W + A_N^W w_N + A_S^W w_S + B^W + D_P^W (\bar{P}_U - \bar{P}_P); \qquad (4.3.10)$$

$$u_P = A_E^U u_E + A_W^U u_W + A_N^U u_N + A_S^U u_S + B^u + D_P^U (P_W - P_P); \qquad (4.3.11)$$

$$v_P = A_E^V v_e + A_W^V v_W + A_N^V v_N + A_S^V v_S + B^v + D_P^V (P_S - P_P); \qquad (4.3.12)$$

The A and B coefficient in the above equations have similar meanings to those in equation (4.3.9). The new symbols D_P^W, D_P^U, D_P^V are defined according to:

$$D_P^W = \Delta S/A_P^{'W} \quad ,$$

$$D_P^U = \Delta\eta_{WP} \; \Delta z/A_P^{'U} \quad ,$$

$$D_P^V = r_s \; \Delta\theta_{we} \; \Delta z/A_P^{'V} \quad . \qquad (4.3.13)$$

The A's have the same meanings as in equation (4.3.9). Note the following modifications for the u and v equations.

(i) The computational cells for u and v are different from those for other ϕ's, as illustrated in figure 4.2.2. Hence, the appropriate inter-nodal distances and cell dimensions must be used in evaluating the A's and B's.

(ii) The transport coefficients and mass fluxes for the u and v control volumes must be calculated in an appropriate manner.

(iii) In the u-equation, the radial component of pressure that appears has been absorbed into the B term by calculating it explicitly from the upstream pressure field.

The Continuity Equation

The discretized form of the continuity equation may be obtained by directly substituting a value of unity for ϕ in the integral equation (4.3.3) and setting S_ϕ to zero. The resulting expression is:

$$(\rho C_e^u u_E - \rho c_w^u u_P) + (\rho C_n^v V_N - \rho C_s^v V_P) + (\rho C_p^w W_P - \rho C_p^w W_u) = 0 \tag{4.3.14}$$

where the quantities C^u, C^v and C^w represent the cell areas normal to the corresponding velocity components. V_P and V_N are defined as follows:

$$V_P \equiv v_p - \frac{1}{4} G_s (u_P + u_E + u_S + u_{SE}) \quad ,$$

$$V_N \equiv v_N - \frac{G_n}{4} (u_P + u_E + u_N + u_{NE}) \quad . \tag{4.3.15}$$

4.4 THE "SIMPLE" SOLUTION METHOD

4.4.1 Main features

The SIMPLE (Semi-Implicit Method for Pressure-Linked Equations) procedure of Patankar and Spalding (1972) was implemented to solve simultaneously the finite-difference equations (4.3.8), (4.3.10) to (4.3.12) and (4.3.14). The unknowns in these equations are the three velocity components u, v and w, the pressure and the scalar flow variables. Since the longitudinal momentum equation is not coupled with the lateral momentum equations, it may be solved independently, provided the coefficients and the pressure-gradient terms are correctly prescribed. The main features of the solution procedure as used in the present study are described below:

(1) A 'guess-and-correct' procedure is used to calculate the pressure and velocity fields at a given longitudinal station. The momentum equations are first solved for an estimated pressure field. The mean pressure $\bar{p}$ and the axial velocities are thereupon corrected by reference to continuity and the axial momentum equation so as to ensure that the mass flow rate through the cross-sectional plane is the same as the flow rate at the inlet of the duct. The lateral velocities are corrected via a 'pressure-correction' equation so that local mass continuity is satisfied.

(2) The flow variables are computed by 'marching' through the flow domain in the predominant flow direction, i.e. the z-direction. All variables are calculated at a given cross-stream plane before proceeding downstream. Usually it is sufficiently accurate to employ only upstream values in computing the variable field over a cross-stream plane; however, because of the non-linearity of the finite-difference equations it is sometimes necessary to refine the calculation by iteration before a given step can be regarded as having been completed.

(3) The finite-difference equations are solved by a tri-diagonal matrix algorithm (TDMA) along lines in the η and ξ directions; when the equations are solved along lines of constant η, the variable values at adjacent ξ-locations are kept fixed, and vice versa.

(4) Only two-dimensional arrays, at most, are required to store the values of all variables and finite-difference coefficients. These arrays are updated as the solution moves from station to station.

4.4.2 Calculation of velocities and pressure

Preliminary values for the cross-stream velocities are calculated* from:

---

* Footnote: These equations are solved by a fast alternating-direction TDMA method, which is described in section 4.4.3.

$$u^*_P = A^U_E\, u^*_E + A^U_W\, u^*_W + A^U_N\, u^*_N + A^U_S\, u^*_S + B^U + D^U_P\,(p^*_W - p^*_P), \qquad (4.4.1)$$

$$v^*_P = A^V_E\, v^*_E + A^V_W\, v^*_W + A^V_N\, v^*_N + A^V_S\, v^*_S + B^V + D^V_P\,(p^*_S - p^*_P). \qquad (4.4.2)$$

where the superscript * on u and v denotes that they are obtained from an assumed pressure field P* (in most cases the P*'s will be set equal to the upstream pressures).

The velocities so obtained will not, in general, satisfy the continuity equation (equation (4.3.14)); there will therefore exist at each cell, a finite "mass error" m_p, defined as follows:

$$m_p = \rho C^w_p\,(W_p - W_U) + (\rho\, C^v_n\, V^*_N - C^v_s\, V^*_p) + (\rho\, C^u_e\, u^*_E - \rho\, c^u_w\, u^*_p), \qquad (4.4.3)$$

where V^*_p is defined, from equation (4.3.15), as:

$$V^*_p = v^*_p - \frac{1}{4}\, G_s\,(u^*_P + u^*_E + u^*_S + u^*_{SE}) \quad . \qquad (4.4.4)$$

A set of "pressure-corrections" (p') are now calculated in such a way that the resulting velocity corrections (u' and V') will reduce these mass errors to zero.

So,

$$(\rho\, C^u_e\, u'_E - \rho\, C^u_w\, u'_p) + (\rho\, C^v_n\, V'_N - \rho\, C^v_s\, V'_p) = -\, m_p \quad . \qquad (4.4.5)$$

This is accomplished by relating the velocity and pressure corrections in an approximate linear manner. Namely,

$$u'_P = E^U_P\,(p'_W - p'_P) \quad ,$$

$$V'_P = E^V_P\,(p'_S - p'_P) \quad . \qquad (4.4.6)$$

The question of how the coefficients E^U and E^V are evaluated will be deferred till later.

Substitution of equation (4.4.6) (and of equations of the same form for U'_E and V'_N) into equation (4.4.5) leads to the following "pressure-correction" equation:

$$p'_P = A^P_E\,p'_E + A^P_W\,p'_W + A^P_N\,p'_N + A^P_S\,p'_S + B^P \quad . \qquad (4.4.7)$$

where,

$$A^P_N = \rho\,C^V_n\,E^V_N\,/\,A^P_P \quad ,$$

etc.

$$B^P = -\,m_p\,/\,A^P_P \quad ,$$

$$A^P_P = \rho\,(C^U_e\,E^U_E + C^U_w\,E^U_P) + \rho\,(C^V_n\,E^V_N + C^V_S\,E^V_P) \;. \qquad (4.4.8)$$

This equation is solved to obtain values for the p's. The pressures and velocities are then corrected as follows:

$$p_P = p^*_P + p'_P \quad , \qquad (4.4.9)$$

$$u_P = u^*_P + u'_P \quad , \qquad (4.4.10)$$

$$v_P = v_P^* + V_P' + \frac{1}{4} G_S (u_P' + u_E' + u_S' + u_{SE}') \quad . \qquad (4.4.11)$$

Evaluation of E^U and E^V

The full expression for, for example, u_P', is obtained by subtracting equation (4.4.1) from equation (4.3.11);

$$u_P' = A_E^U u_E' + A_W^U u_W' + A_N^U u_N' + A_S^U u_S' + D_P^U (p_W' - p_P') \qquad (4.4.12)$$

In order to arrive at a relation of the required linear form (equation (4.4.6)), it is necessary to make some assumption regarding the velocity corrections at neighbouring nodes. In the original method of Patankar and Spalding (1972), all these terms were neglected, so that

$$E_P^U = D_P^U \quad . \qquad (4.4.13)$$

This assumption, however, was found to lead to numerical instabilities when the axial step length Δz was prescribed to be larger than the lateral grid dimensions.

The problem was overcome by Tatchell (1975) who proposed that, in a systematically developing flow, the velocity corrections at neighbouring nodes may, as a good approximation, be set equal to that at P. The expression for E_P^U, therefore, becomes:

$$E_P^U = D_P^U / \{ 1 - (A_E^U + A_W^U + A_N^U + A_S^U) \} \quad . \qquad (4.4.14)$$

This modified relation has been used throughout the present work.

Calculation of mean pressure

The axial-momentum equation is first solved for an estimated[*] mean pressure-gradient to yield a w^* field.

$$w_P^* = A_E^W w_E^* + A_W^W w_W^* + A_N^W w_N^* + A_S^W w_S^* + B^W + D_P^W (\bar{p}_U - \bar{p}_P^*). \qquad (4.4.15)$$

A correction to $\bar{p}_P^*$, $(\bar{p}_P')$, is then calculated so that the corrected velocities satisfy the overall continuity equation for the duct, which may be stated as:

$$\sum_{\text{all nodes}} (\rho w_P C_P^W) = \dot{m} \qquad (4.4.16)$$

where $\dot{m}$ is the total mass inflow at the channel inlet, since fluid loss through the walls does not occur in the present study.

A velocity-correction w_P' is defined so that,

$$w_P' = E_P^W \bar{p}_P' \quad ; \qquad (4.4.17)$$

In accordance with the practice discussed earlier, E_P^W is calculated from:

$$E_P^W = D_P^W / \{1 - (A_E^W + A_W^W + A_N^W + A_S^W)\} \quad . \qquad (4.4.18)$$

Combination of equation (4.4.15) with equations (4.4.16)

---

[*] Footnote: The usual practice is to estimate $\bar{p}_P^*$ from the upstream gradient: i.e., $\left(\frac{d\bar{p}^*}{dz}\right)_P = \left(\frac{d\bar{p}}{dz}\right)_U$

and (4.4.17) yields the following value for $\bar{p}'_P$:

$$\bar{p}'_P = \frac{\dot{m} - \Sigma(\rho w^* C^W)_P}{\Sigma(\rho E^W\ C^W)_P} \quad . \qquad (4.4.19)$$

4.4.3 Method of solution of the difference equations

Reference has been made above to 'solving' finite-difference equations of the form of equation (4.3.8). In SIMPLE this is accomplished by the use of an alternating-direction version of the well-known tridiagonal matrix algorithm (TDMA). The TDMA sweeps are performed in the η and ξ directions as follows. First, for the ξ-direction sweep, equation (4.3.8) is written as:

$$\phi_P^I = A_E^\phi\ \phi_E^I + A_W^\phi\ \phi_N^I + (A_N^\phi\ \phi_N + A_S^\phi\ \phi_S + B^\phi) \quad , \qquad (4.4.20)$$

where the superscript I denotes values obtained after the first sweep and the terms in brackets are taken as known.

Equation (4.4.20) is solved by elimination, and the second sweep is performed in a similar manner for the η-direction. The equation now solved is,

$$\phi_P^{II} = A_N^\phi\ \phi_N^{II} + A_S^\phi\ \phi_S^{II} + (A_E^\phi\ \phi_E^I + A^\phi \phi_W^I + B^\phi\ ) \quad . \qquad (4.4.21)$$

This completes the double sweep. Since the expressions in the brackets in equations (4.4.20) and (4.4.21) are based on old ϕ's, the double sweep must be repeated in order to obtain an accurate (i.e. converged) solution. For equations for variables other than p', convergence is rapid, and one double sweep usually suffices. However, for the p'-equation, convergence is slower; for the solutions reported in this thesis between five and thirty double sweeps were required.

4.4.4 Summary of the calculation procedure

The following main sequence of operations is performed at each longitudinal station:-

(1) First, the u* and v* fields are calculated from equations (4.4.1) and (4.4.2), using the upstream pressure distribution.

(2) The axial velocity field w* is calculated (equation (4.4.15)) from the upstream pressure-gradient.

(3) The mean pressure-correction is then evaluated from equation (4.4.19) and the w's and $\bar{p}$ are corrected.

(4) All scalar variables (k, ε, T in turbulent flow with heat transfer) are solved for (equation (4.3.8)). The convection terms used here are evaluated from the upstream values of the variables.

(5) The coefficients in the pressure-correction equation (equation (4.4.7)) are calculated and the p's deduced. Lateral velocities and pressures are thus corrected.

(6) The whole cycle is repeated until further changes are reduced to below an acceptable level.

(7) The solution proceeds to the next downstream station.

The above solution procedure, embodied in the computer code STABLER (Steady Three-dimensional Analyser of Boundary-Layer Equations, Revised), was employed in all the calculations presented in this thesis.

4.5 INCORPORATION OF AUXILIARY INFORMATION

4.5.1 Boundary conditions

Reference was made in section (3.9) to the two types of boundary condition encountered in this thesis: namely, whether the value of a variable or the value of its flux is specified. The incorporation of either kind of boundary condition into the calculation procedure is easy, and is achieved by either modifying the source term or the appropriate coefficient in the finite-difference equation for the near-boundary control volumes.

Conditions at the inlet to the channel are specified by simply assigning the relevant starting values for all grid nodes at the first $\eta \sim \xi$ plane.

4.5.2 Treatment of near-wall regions

The near-wall region poses some special problems in the numerical computation of turbulent flows. Close to a wall the variations of the flow properties is so steep that excessively fine grids are required there for accurate calculations. Furthermore, the equations developed for k, ε

and the Reynolds stresses are valid only for fully-turbulent flows; modifications to the model are required in regions where the local Reynolds number of turbulence $(=\rho k^{\frac{1}{2}}\ell/\mu)$ is low.

There are two possible approaches to the treatment of the near-wall region: either the use of an empirical "wall-function" method or the modelling of the low-Reynolds-number phenomena. In the present investigations, the former method has been adopted, chiefly because of its greater economy in both computer storage and computer time. The use of wall functions permits the near-wall grid node to be placed far from the wall in the fully-turbulent region.

Launder and Spalding (1973) have summarized the wall-functions that have been proposed and used by various authors. It is these wall functions, with their appropriate extension to three dimensions, which have been employed here.

The practice adopted is as follows:

If P is the grid node adjacent to the wall - but sufficiently far from the wall for the turbulent Reynolds number at P to be much greater than unity - then, the logarithmic velocity profile is presumed to prevail at P.

So,

$$\frac{\overrightarrow{W_P}}{(\tau_w/\rho)^{\frac{1}{2}}} = \frac{1}{\kappa}\,\ell n\left(\frac{Ey_P(\rho\tau_w)^{\frac{1}{2}}}{\mu}\right) , \qquad (4.5.1)$$

where the subscript P refers to the values at node P, while the subscript w denotes values at the wall. y_P is the normal distance of P from the wall and κ and E are the well-known constants whose values are listed in Table 3.9.1. $\overrightarrow{W_P}$ is the resultant velocity at P and is assumed to be parallel to the wall shear-stress.

The variation of k and ε in the uniform-shear layer near the wall may be deduced from solution of the kinetic energy equation (equation (3.8.6)) with convection and diffusion neglected, and from the knowledge that the length-scale varies linearly near the wall (see Launder and Spalding, 1972). The relevant expressions are:

$$\tau_W = \rho C_\mu^{\frac{1}{2}} k_P \quad , \qquad (4.5.2)$$

$$\varepsilon_P = C_\mu^{\frac{3}{4}} k_P{}^{3/2}/\kappa y_P \quad . \qquad (4.5.3)$$

Thus, the value of ε at the near-wall node is fixed according to equation (4.5.3) above; while for the k control-volume adjacent to the wall, diffusion of energy is set to zero, and the generation term modified by way of the wall shear-stress calculated from equation (4.5.4) below:

$$\tau_W = \frac{\rho\kappa \; C_\mu^{\frac{1}{4}} \; k_P^{\frac{1}{2}} \; \overrightarrow{W_P}}{\ln\left\{\dfrac{E y_P \; C_\mu^{\frac{1}{4}} \rho k_P^{\frac{1}{2}}}{\mu}\right\}} \quad . \qquad (4.5.4)$$

This expression is obtained by combining equations (4.5.1) and (4.5.2) above.

The wall functions for the transport of temperature (or enthalpy) are derived in a similar manner. A logarithmic temperature profile is assumed, the final expression being as follows:

$$\frac{\rho C_p (T_W - T_P)\,(\tau_W/\rho)^{\frac{1}{2}}}{\dot{Q}''_W\ \sigma_t} = \frac{1}{\kappa}\ \ell n \left\{ \frac{E y_P\ (\rho\tau_W)^{\frac{1}{2}}}{\mu} \right\} + P_T\ . \qquad (4.5.5)$$

where τ_W is given by equation (4.5.2) and $\dot{Q}''_W$ is the heat-flux from the wall. The additional term P_T represents the resistance offered by the laminar sublayer to the transport of heat. Jayatilleke (1965) has extensively catalogued the different functional expressions for P_T to be found in the literature. After comparison with experimental data, he himself proposed the following formula which he believed gave the best 'fit' to the data:

$$P_T = 9.24\ \{(\frac{\sigma_\ell}{\sigma_t})^{\frac{3}{4}} - 1\}\ \{1 + 0.29\ \exp\ (-0.007\ \sigma_\ell/\sigma_t)\}. \qquad (4.5.6)$$

where σ_ℓ and σ_t refer, respectively, to the laminar and turbulent Prandtl-numbers for temperature. This expression for P_T has been used in the present study.

4.6 CLOSURE

In this chapter, a novel non-orthogonal computational grid has been described in detail, and the partial-differential equations for parabolic flows integrated over the appropriate grid control volumes to yield equivalent finite-difference forms. The physical significance of the various terms in the latter equations were also discussed. Furthermore, a general solution scheme for these equations has been described, and special computational practices adopted for near-wall regions have been presented. This completes the mathematical formulation of the problems investigated in this thesis.

CHAPTER 5

LAMINAR FLOWS

5.1 INTRODUCTION

5.1.1 Objectives of the Study

The work reported in this chapter was performed with a two-fold purpose in view: firstly, to test the accuracy of the non-orthogonal finite-difference formulation developed in the previous two chapters of this thesis by its application to the calculation of velocity and temperature distributions in irregular geometries for which simple, exact solutions are available for comparison; and secondly, to predict the laminar flow and heat transfer behaviour of rod-bundles in equilateral-triangular and square configurations.

The equations solved, in each case, were the continuity relation, the three momentum equations and the temperature (energy) equation, in the forms appropriate to a constant-property laminar flow (see section 3.4).

The numerical model was first tested through employment in the solution of a simple pipe flow problem, and a comparison of the results obtained with the well-known polynomial profiles for axial velocity and temperature was made. Then two non-circular geometries, viz. the elliptic duct of arbitrary aspect ratio and the equilateral-triangular duct, were selected for investigation, since, in both cases, exact analytical solutions, with which the numerical results could be compared, exist. Moreover, since orthogonal finite-difference meshes are applicable to these geometries only with great difficulty, it was hoped that the relative ease and greater universality of the present procedure would be demonstrated.

Computations are presented here of the flow and heat-transfer performance of rod-bundles under laminar conditions; and comparisons are made, wherever possible, with the results of earlier authors whose work has been summarized briefly in section 2.2 of Chapter 2. Quantities calculated include local distributions of velocity, shear-stress, heat-transfer coefficient etc, as well as overall parameters of the flow such as rod-averaged Nusselt numbers and friction-factors, over a wide range of rod spacings. For the equilateral-triangular array of rods, three different wall heating conditions were investigated:-

(i) Uniform heat-flux in all directions, corresponding to the case studied by Dwyer and Berry (1970).

(ii) Uniform wall temperature in the circumferential direction, coupled with a uniform axial heat flux; this corresponds to the situation attended to by Sparrow, Loeffler and Hubbard (1961).

(iii) Uniform wall temperature in both the circumferential and axial directions.

The above sets of thermal boundary conditions will be referred to as A, B and C respectively.

Although in reality the flows in reactor cores are highly turbulent, the theoretical study of the laminar flow case is of some interest in connection with abnormal operation of a power reactor, such as may arise from a partial blockage of a fuel sub-assembly.

5.1.2 Outline of the chapter

The rest of this chapter consists of three main sections: section 5.2 contains a discussion of the test cases which were investigated with a view to checking the mathematical formulation. Computations performed with the present procedure for rod-bundle flow and heat-transfer are reported and discussed in section 5.3, while section 5.4 closes the chapter with a brief assessment of the results achieved.

5.2 TEST CASES

5.2.1 The circular duct

A preliminary test of the equations derived for the non-orthogonal grid was performed by obtaining solutions for the velocity and temperature fields under fully-developed conditions in a straight, circular pipe.

The calculation domain was similar in shape to that used later for rod-bundle flows, and was located in a quadrant of the pipe as illustrated in figure (5.2.1(a)). A point on the axis of the pipe was taken as the origin of the coordinate system, and the family of η-lines coincided with the radii of the circle about that point. The boundaries of the domain were arbitrary fluid surfaces. The well-known fully-developed

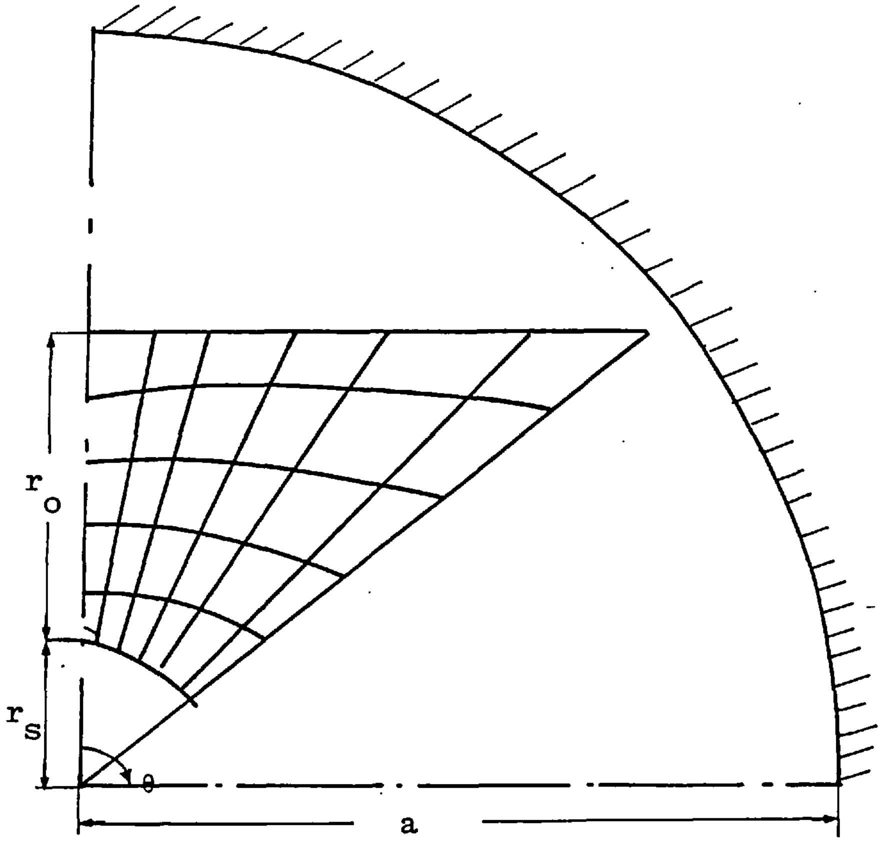

FIG. 5.2.1(a): CALCULATION DOMAIN FOR CIRCULAR DUCT

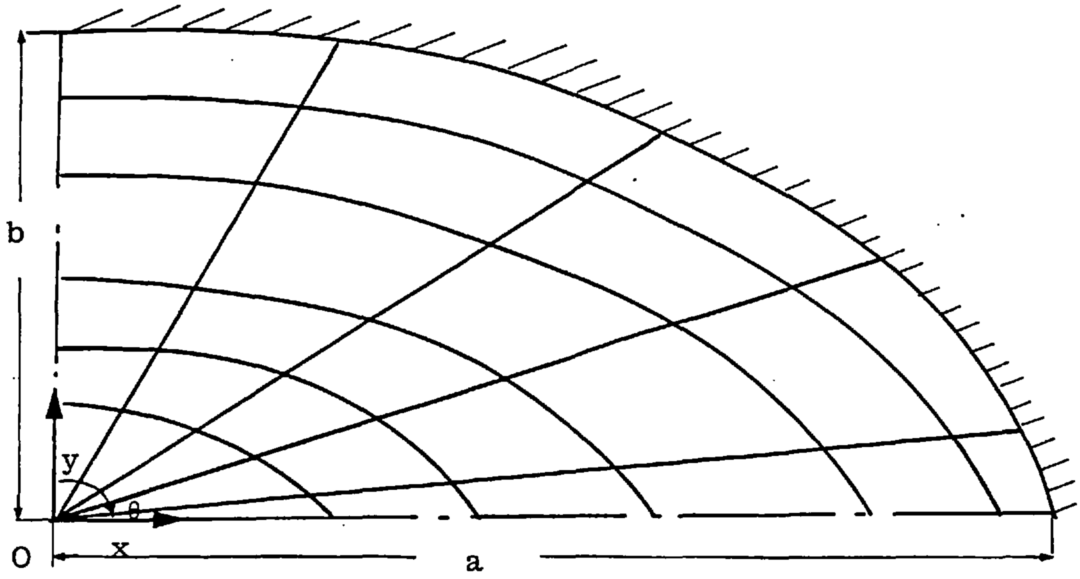

FIG. 5.2.1(b): CALCULATION DOMAIN FOR ELLIPTIC DUCT

solutions for the velocities and temperatures, corresponding to a given flow-rate and a constant heat flux on the pipe wall, were prescribed on the boundaries; the object of the exercise was to compute the values of velocity and temperatures at the internal grid nodes.

5.2.1.1 Computational details:

A uniform 12x12 grid was employed in the $\eta \sim \xi$ plane, and integration performed until the axial velocity w and the temperature $(T_W - T)$, where T_W was the wall temperature, at all internal nodes reached their constant final values. Some computations were made with a 17x17 grid, and results to the same degree of accuracy as before were obtained. The velocity solution was executed first, and this was then used as input in the integration of the temperature equation.

5.2.1.2 Inlet and boundary conditions:

Velocity solution:

At $z = 0$; $\quad u = v = 0 \quad ,$ (5.2.1)

$w = \text{constant} \quad ;$ (5.2.2)

$z > 0$; $\quad u = v = 0$, at $\xi = 0$; $\xi = 1$; $\eta = 0$; $\eta = 1$, (5.2.3)

$w = 2\bar{w}\left(1 - \left(\frac{r}{a}\right)^2\right)$, at $\xi = 0$; $\xi = 1$; $\eta = 0$, $\eta = 1$. (5.2.4)

Temperature solution:

At $z = 0$; $\quad u = v = 0 \quad ,$ (5.2.5)

$T = \text{constant} \quad ,$ (5.2.6)

$$w = 2\bar{w}\left(1 - \left(\frac{r}{a}\right)^2\right) \qquad ; \qquad (5.2.7)$$

$$z > 0; \quad T_W - T = \frac{4\dot{Q}''_w}{k_L a}\left(\frac{3}{16}a^2 + \frac{r^4}{16a^2} - \frac{r^2}{4}\right) \quad ,$$

$$\text{at } \xi = 0;\ \xi = 1;\ \eta = 0,\ \eta = 1\ . \qquad (5.2.8)$$

5.2.1.3 Results:

The predicted velocity distribution within the calculation domain is compared with the exact parabolic profile in figure (5.2.2). The angular width of the domain in this case was 60 degrees, and the values chosen for the parameters r_o and r_s (see fig. 5.2.1(a)) are given in the figure.

Similar comparisons are made in figure (5.2.3) between the predicted temperatures and the analytical temperature-profile corresponding to a constant wall heat flux thermal boundary condition. It is seen that the numerical results for both axial velocity and temperature are almost coincident with the analytical solutions.

5.2.2 The elliptic duct

A more rigorous test of the procedure is afforded by the case of a straight elliptic duct of arbitrary aspect ratio. A quadrant of the duct (see figure 5.2.1(b)) was spanned by the non-orthogonal grid described in chapter 4. In this case, the η = constant surfaces from a family of concentric ellipsoids about the axis of the duct. The aspect ratio, λ, is defined as b/a, where b is the half-length of

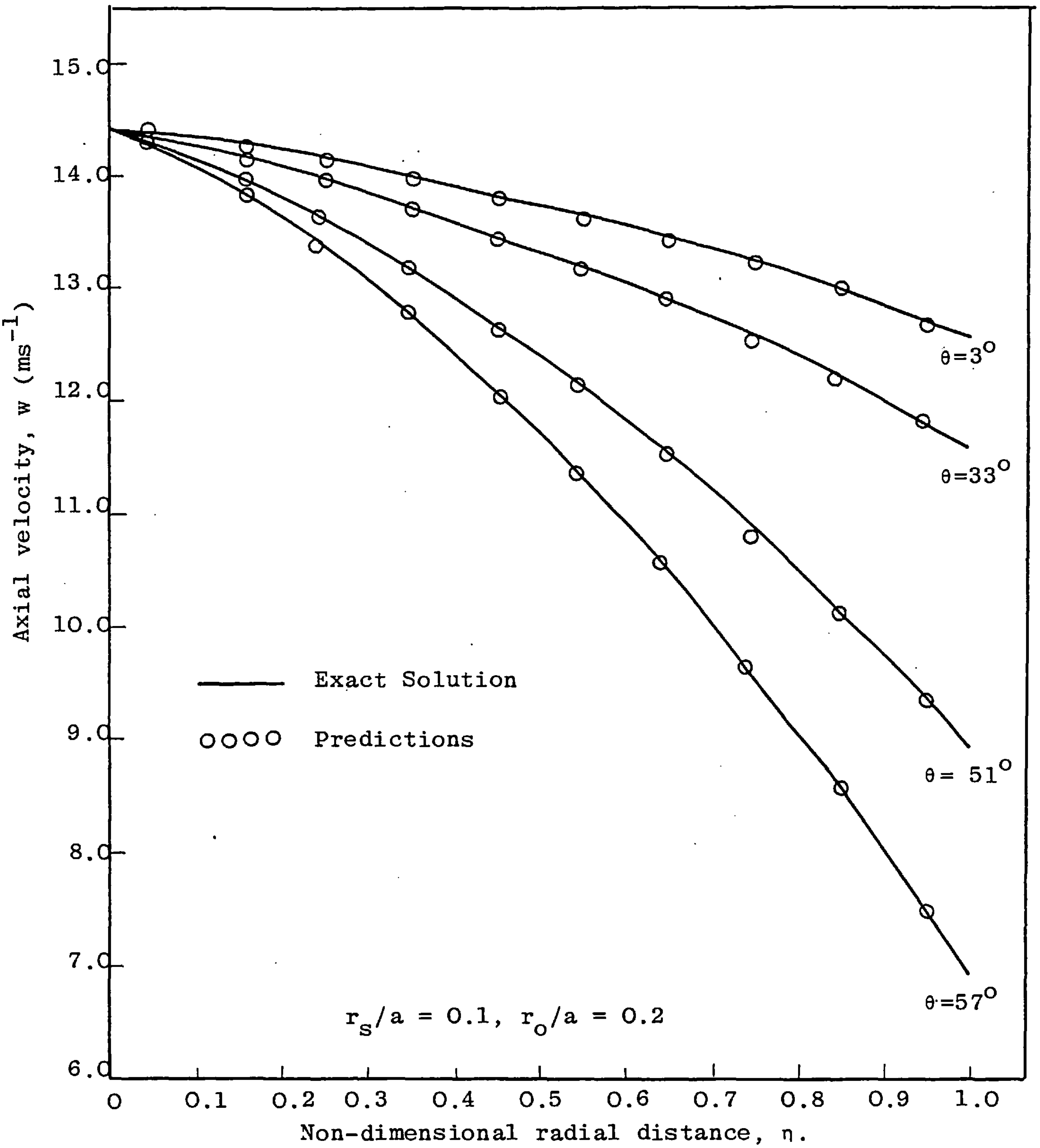

FIG. 5.2.2: LAMINAR VELOCITY-PROFILES IN CIRCULAR DUCT

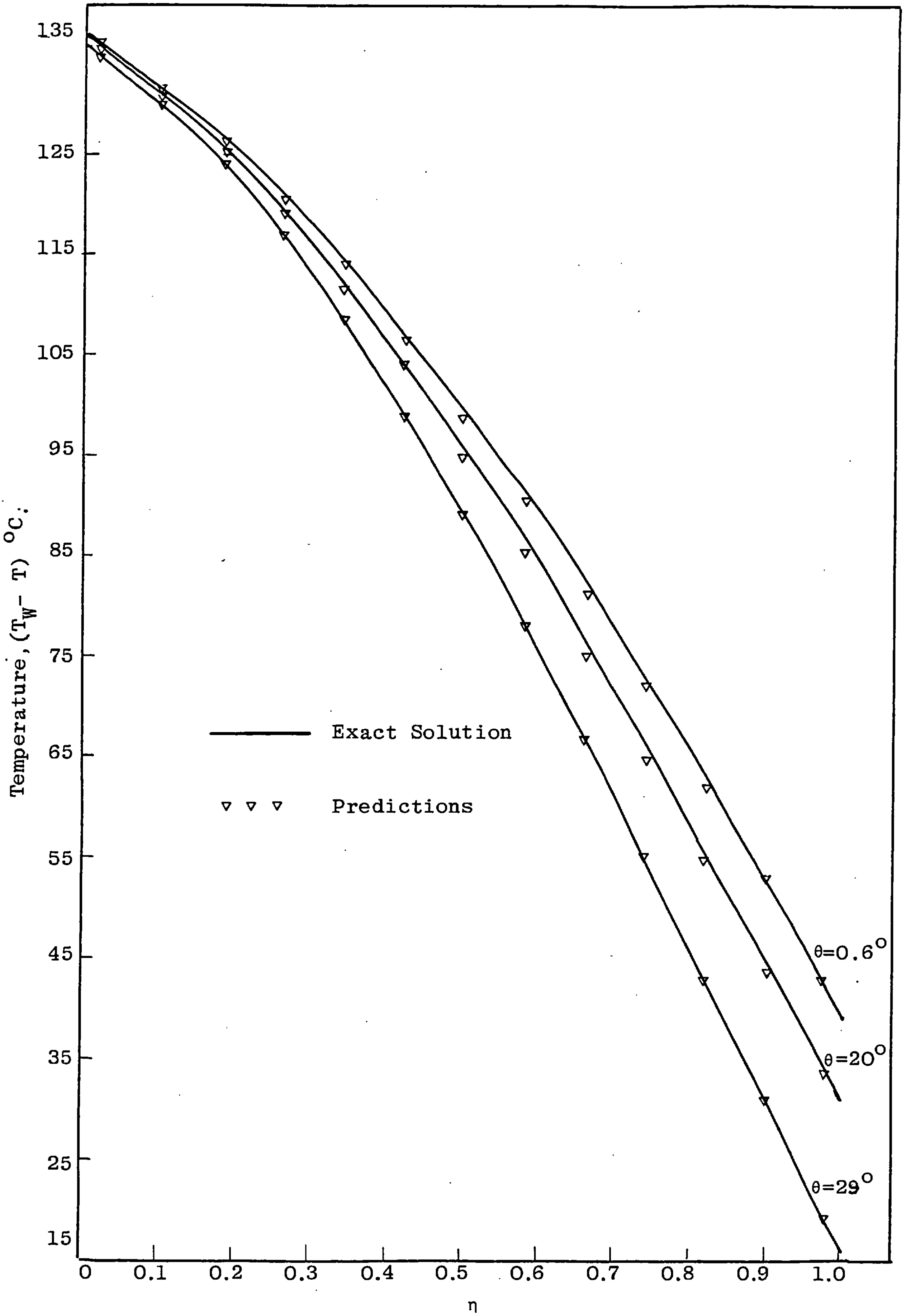

FIG. 5.2.3: TEMPERATURE- PROFILES IN CIRCULAR DUCTS

of the minor axis and a the half-length of the major axes of the ellipse.

The exact velocity-profile (fully-developed) in such a duct is given by (see, for example, Rohsenow and Hartnett, 1973):-

$$w = 2\bar{w} \left[1 - \left(\frac{x}{a}\right)^2 - \left(\frac{y}{b}\right)^2 \right] \quad . \qquad (5.2.9)$$

where $\bar{w}$ is the mean axial velocity over the cross-section of the duct. Hence, since all the grid nodes lie on ellipsoidal surfaces, a velocity solution independent of angular position and parabolic along any η-line is to be expected.

Heat transfer computations were made of the cooling of a fluid in an elliptic duct with a uniform wall temperature less than the fluid temperature at the inlet. This corresponds to the situation studied analytically by Dunwoody (1962), using a complex-variable technique. He obtained values of the heat transfer rate as a function of the longitudinal distance down the duct. The results were later checked and extended by Schenk and Han (1967).

A second thermal boundary condition investigated was that of a uniform heat input in both the axial and peripheral directions. This corresponds to the problem analysed by Iqbal et al. (1972), whose treatment of free and combined convection, by means of a variational procedure, included tables of Nusselt numbers for the case of pure forced convection.

5.2.2.1 Computational details:

For the calculations involving ducts of aspect ratio greater than 0.6, satisfactory results were obtained with a cross-stream grid comprising 12x12 uniformly distributed nodes. For smaller aspect ratios, however, a 19x19 grid, with a greater concentration of nodes near the major axis of the ellipse, was required before accurate, essentially grid-independent results were attained.

Fully-developed velocity conditions were assumed to have been reached when the w-profiles ten hydraulic diameters apart were consistent to within one per cent. An axial step length of one per cent of the equivalent hydraulic diameter (D_e) was chosen at the inlet, and this was increased exponentially until a value of 0.5 D_e was reached. For the velocity solution, one integration per step sufficed, but for the calculation of temperature, 3-5 iterations at each station were necessary for convergence.

The manner in which the thermal boundary conditions were introduced into the computational procedure will be described later, when rod-bundle flows are considered.

5.2.2.2 Inlet and boundary conditions

Velocity solution

At $z = 0$; $\quad u = v = 0 \quad ,$ (5.2.10)

$w = \text{constant} \quad ;$ (5.2.11)

$z > 0$; $\quad u = v = w = 0, \text{ at } \eta = 1 \quad ;$ (5.2.12)

$$\frac{\partial u}{\partial \xi} = \frac{\partial v}{\partial \xi} = \frac{\partial w}{\partial \xi} = 0, \quad \text{at } \xi = 0;\ \xi = 1\ ; \qquad (5.2.13)$$

$$\frac{\partial u}{\partial \eta} = \frac{\partial w}{\partial \eta} = 0\ , \quad \text{at } \eta = 0 \qquad (5.2.14)$$

Temperature solution

At $z = 0$; W = fully-developed solution , (5.2.15)

T = constant ; (5.2.16)

$z > 0$; $T = T_W$, at $\eta = 1$ (Const. Temp. case) (5.2.17)

$$k \frac{\partial T}{\partial n} = \dot{Q}''_w\ , \quad \text{at } \eta = 1 \text{ (Const. Flux case)} \qquad (5.2.18)$$

$$\frac{\partial T}{\partial \xi} = 0\ , \quad \text{at } \xi = 0;\ \xi = 1\ ; \qquad (5.2.19)$$

$$\frac{\partial T}{\partial \eta} = 0\ , \quad \text{at } \eta = 0 \qquad (5.2.20)$$

5.2.2.3 Results:

Figures (5.2.4(a)) and (5.2.4(b)) show the results obtained for the fully-developed velocity profiles in an elliptic duct of aspect ratio 0.6 when, (a) the terms involving the function G (equation 3.4.12) - which arise through the non-orthogonality of the grid - are omitted from the axial-momentum equation, and (b) the complete equation is programmed and solved. It is evident that in case (a) the expected angular independence is not obtained. This discrepancy worsens with diminishing aspect ratio, i.e. with

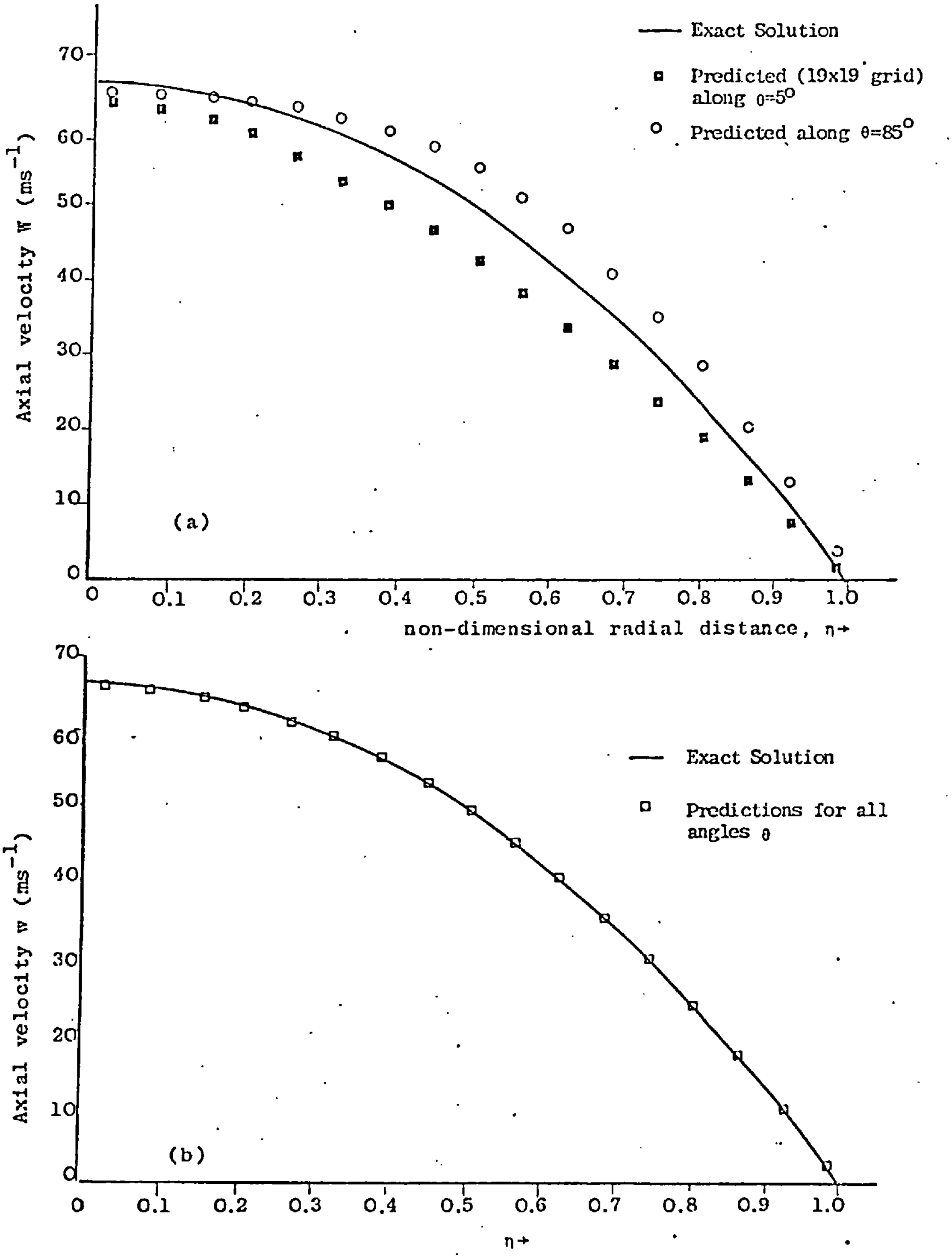

FIG. 5.2.4: VELOCITY PROFILES IN ELLIPTIC DUCT (ASPECT RATIO = 0.60)
(a) NO "G-TERMS". IN W-EQUATION
(b) "G-TERMS' INCLUDED IN W-EQUATION.

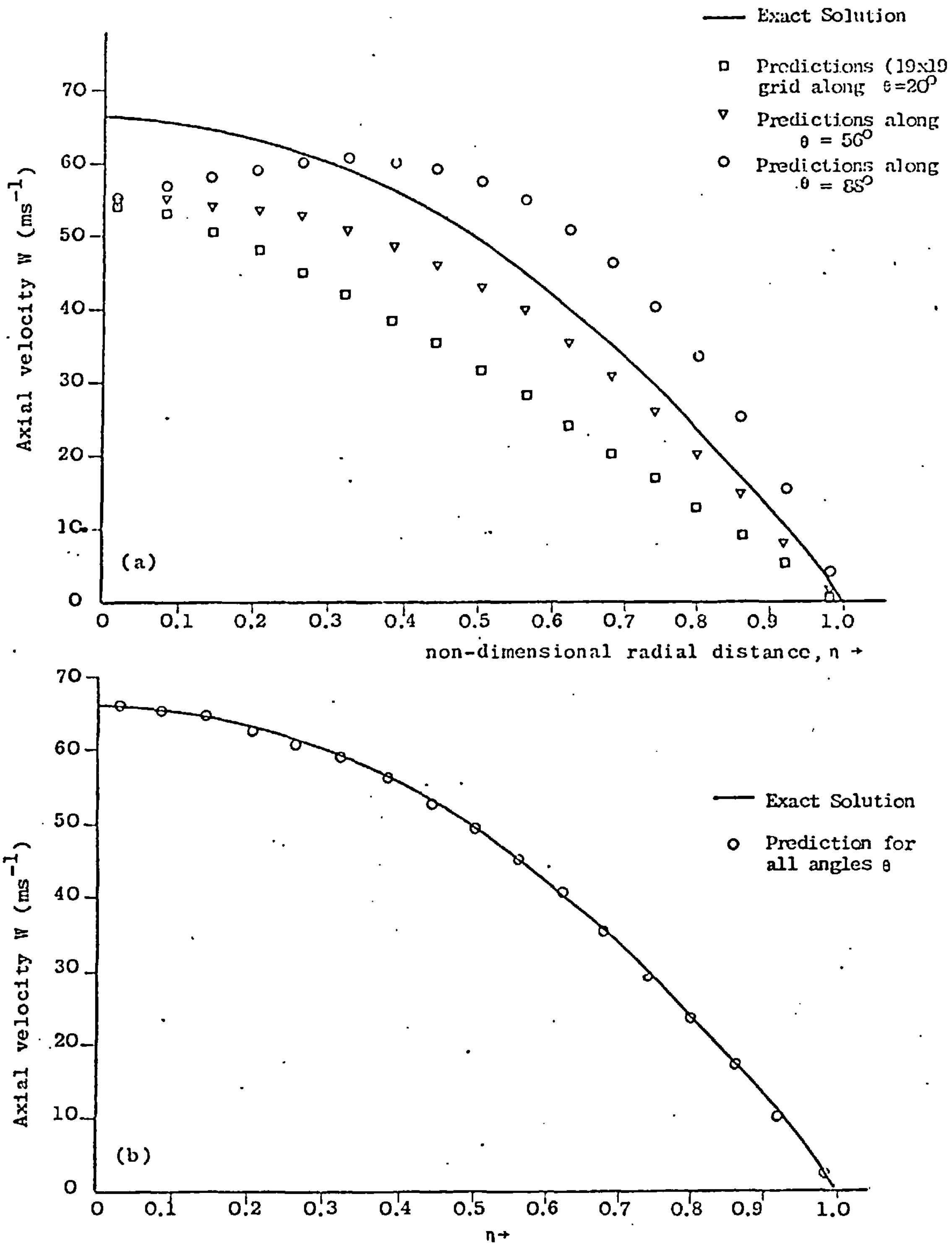

FIG. 5.2.5: VELOCITY PROFILES IN ELLIPTIC DUCT (ASPECT RATIO = 0.3)
(a) NO EXTRA "G-TERMS' IN W-EQUATION
(b) "G-TERMS" INCLUDED IN W-EQUATION

increasing grid non-orthogonality, and this is clearly demonstrated by figures (5.2.5(a)) and (5.2.5(b)) which show profiles corresponding to a value of λ of 0.3.

Figure (5.2.6) depicts the variation of the wall shear-stress around the periphery of the duct for two different aspect ratios. The ordinate in the figure is the shear-stress, non-dimensionalized through division by the averaged shear-stress, while the abscissa is the angular position θ. The analytical solution shown is from the summary by Shah and London (1971). This peripheral variation is one of the interesting features of flows in non-circular geometries. As is obvious from physical considerations, the maximum shear-stress occurs at the position aligned along the minor axis, where $\theta = 0^o$. Flattening of the duct leads to an enhanced non-uniformity of the stress distribution. It is clear that the solution of the complete "non-orthogonal" equations, developed earlier in this thesis, yields excellent agreement with the analytical results for velocity and wall shear-stress over a range of duct aspect ratios.

The temperature equation was solved in a similar manner. Figure (5.2.7) compares the predicted longitudinal variation of the 'cup-mixed' mean temperature difference $\bar{\theta}(z)$, averaged across the cross-section of the duct, with the curve obtained via the complex-variable method of Dunwoody (1962). $\theta(z)$ is defined according to:

$$\theta(z) = \frac{T - T_W}{T_i - T_W} \quad ; \qquad (5.2.21)$$

where T_W is the constant temperature at the duct wall, and

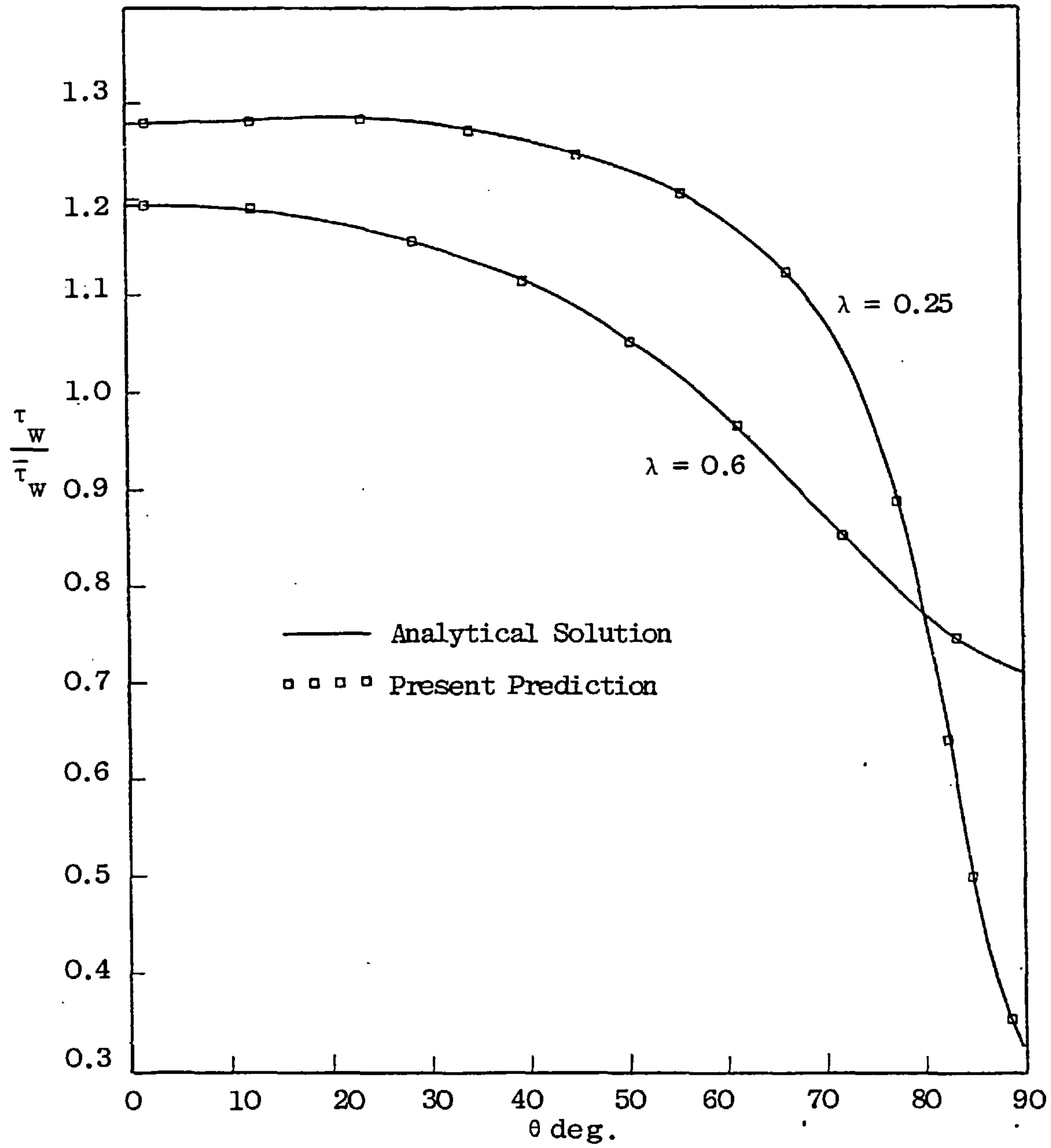

FIGURE 5.2.6: PERIPHERAL WALL SHEAR-STRESS DISTRIBUTIONS FOR ELLIPTIC DUCTS OF ASPECT RATIOS 0.25 AND 0.60.

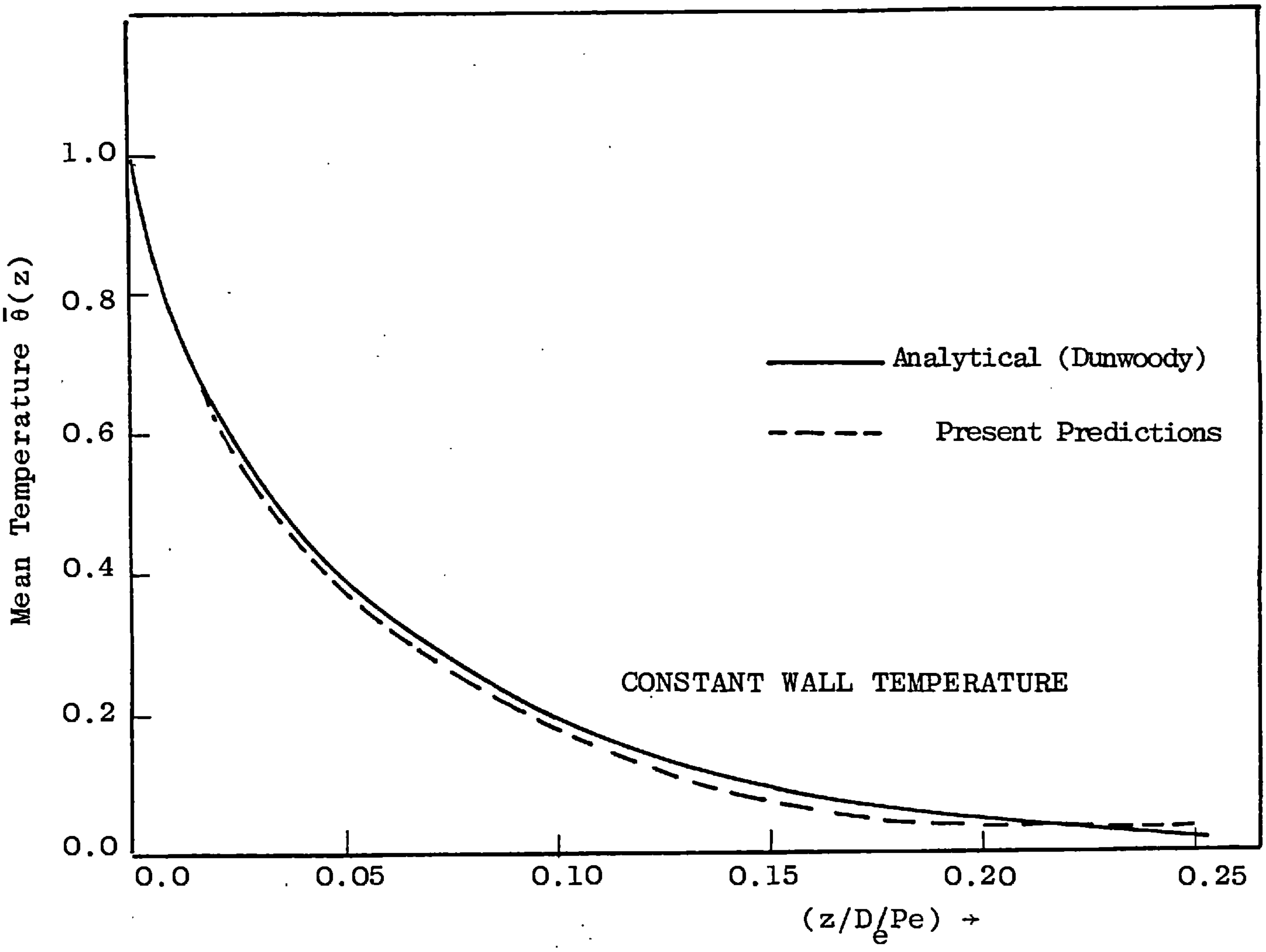

FIG. 5.2.7: VARIATION OF MEAN TEMPERATURE WITH AXIAL DISTANCE FOR ELLIPTIC DUCT (λ = 0.8)

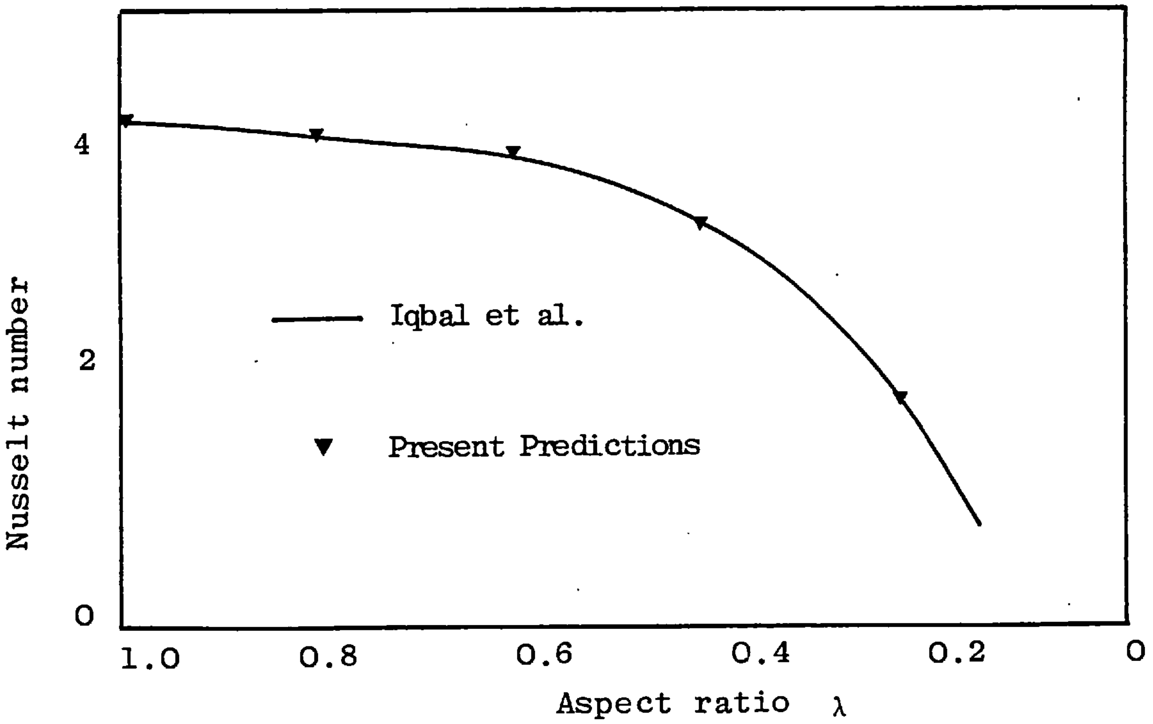

FIG. 5.2.8: NUSSELT NUMBERS FOR ELLIPTIC DUCTS (CONSTANT WALL HEAT FLUX)

assumed to be less than the inlet fluid temperature T_i. The abscissa in the figure is the parameter $(z/D_e/Pe)$, where z is the distance downstream from the inlet, Pe the Peclet number and D_e the equivalent hydraulic diameter of the flow region. Agreement between the present predictions and Dunwoody's results is very good.

The heat-transfer capability of the duct is normally expressed by way of the Nusselt number, defined according to,

$$Nu = \frac{\bar{h}\ D_e}{k_L} \quad , \qquad (5.2.22)$$

where $\bar{h}$ is the mean heat-transfer coefficient around the periphery of the duct, and k_L the molecular thermal conductivity of the fluid. Schenk and Han (1967) have extended Dunwoody's calculations for different aspect ratios, and published values of the Nusselt number Nu', defined according to:

$$Nu' = \frac{\bar{h}.2b}{k_L} \quad ; \qquad (5.2.23)$$

where 2b is the length of the minor axis of the duct. Nusselt numbers calculated in this way are given in Table (5.2.2) below, along with values obtained with the present procedure.

TABLE 5.2.2

λ	Nu' (Schenk)	Nu' (present)
0.80	3.31	3.29
0.50	2.88	2.90
0.25	2.59	2.62

The agreement between the two sets of results is very satisfactory.

Computed Nusselt numbers corresponding to the case of a constant wall heat flux in all directions are given in figure (5.2.8) as a function of aspect ratio. The analytical results are those obtained by Iqbal et al (1972) by way of a variational solution technique. Note that the Nu values are defined from equation (5.2.22) above. Once again, agreement between the present numerical predictions and the analytical results is gratifying.

5.2.3 The Equilateral-Triangular duct

The duct geometry is shown in figure (5.2.9). Half of the duct was spanned by a non-orthogonal grid, an apex of the duct serving as the origin of the coordinate system. This geometry was chosen for study because the large axial velocity gradients in both the radial and angular directions constitute useful tests of the accuracy of the discretized diffusion terms in the axial-momentum equation.

5.2.3.1 Computational details:

Computations were performed with a non-uniform 17x17 cross-stream grid, with a greater concentration of nodes in the vicinity of the walls than in the core. Grid independence of the results was confirmed by making comparative calculations with a 25x25 grid and observing essentially identical solutions. A maximum axial step length of 0.5 D_e was used and one integration performed per station, until the fully-developed velocity field was attained.

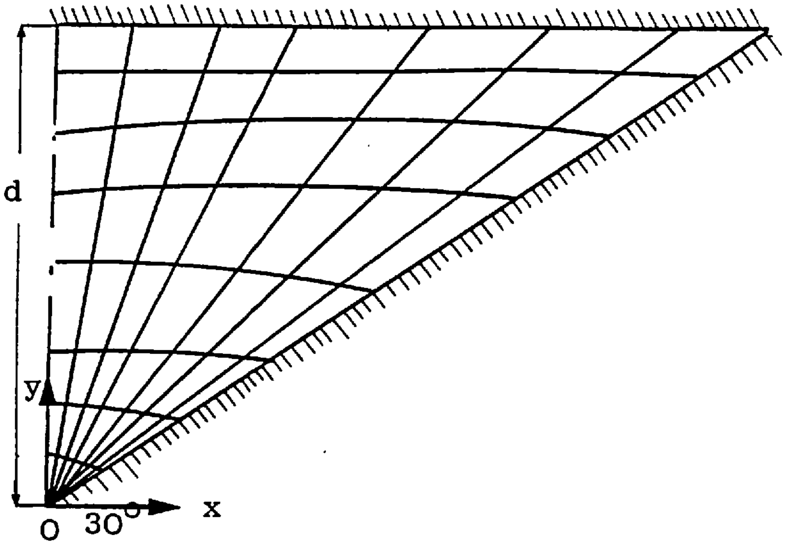

FIG. 5.2.9: CALCULATION DOMAIN FOR EQUILATERAL-TRIANGULAR DUCTS

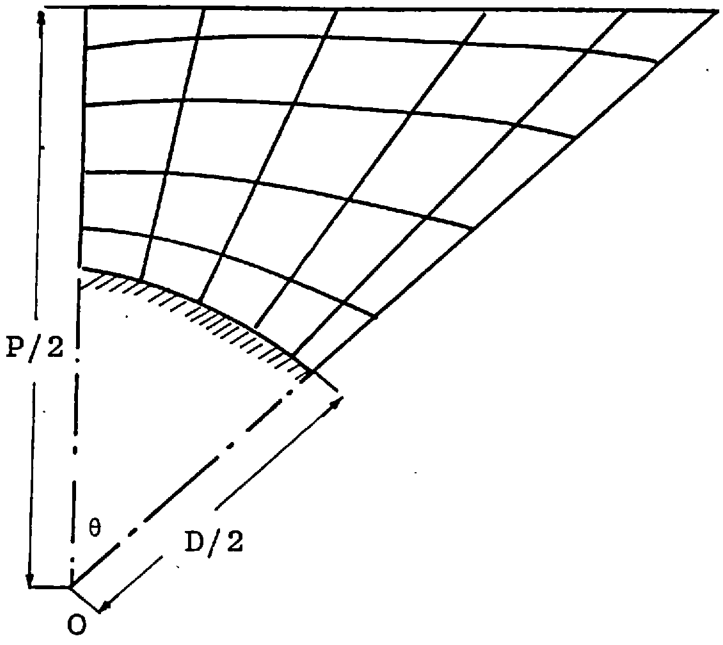

FIG. 5.2.10: CALCULATION DOMAIN FOR ROD BUNDLE

5.2.3.2 Inlet and boundary conditions:

At $z = 0$; $u = v = 0$, (5.2.24)

$w = \text{constant}$; (5.2.25)

$z > 0$; $u = v = w = 0$, at $\xi = 1$, $\eta = 1$, $\eta = 0$ (5.2.26)

$u = 0$, at $\xi = 0$; (5.2.27)

$\frac{\partial v}{\partial \xi} = \frac{\partial w}{\partial \xi} = 0$, at $\xi = 0$; (5.2.28)

5.2.3.3 Results

The exact solution for the point velocities in an equilateral triangular duct is (from Rohsenow and Hartnett, 1973):

$$w = -\frac{d\bar{p}}{dz} \cdot \frac{1}{4\mu}\left(1 - \frac{y}{d}\right)(3x^2 - y^2) \quad . \qquad (5.2.29)$$

$\frac{d\bar{p}}{dz}$ is the axial pressure-gradient (constant) and the symbols x, y and d are defined in figure (5.2.9).

In figure (5.2.11) the velocity field, obtained from the present numerical procedure, is plotted as a function of radial position η for any given angular location, the latter being measured from the duct bisector. The ordinate in the figure is the axial velocity, non-dimensionalized with respect to the mean velocity in the duct. The steep gradients of velocity are plainly evident. Also shown in the figure is the velocity-profile plotted from equation (5.2.29) and represented as a solid curve. The agreement between the latter and the numerical prediction is excellent.

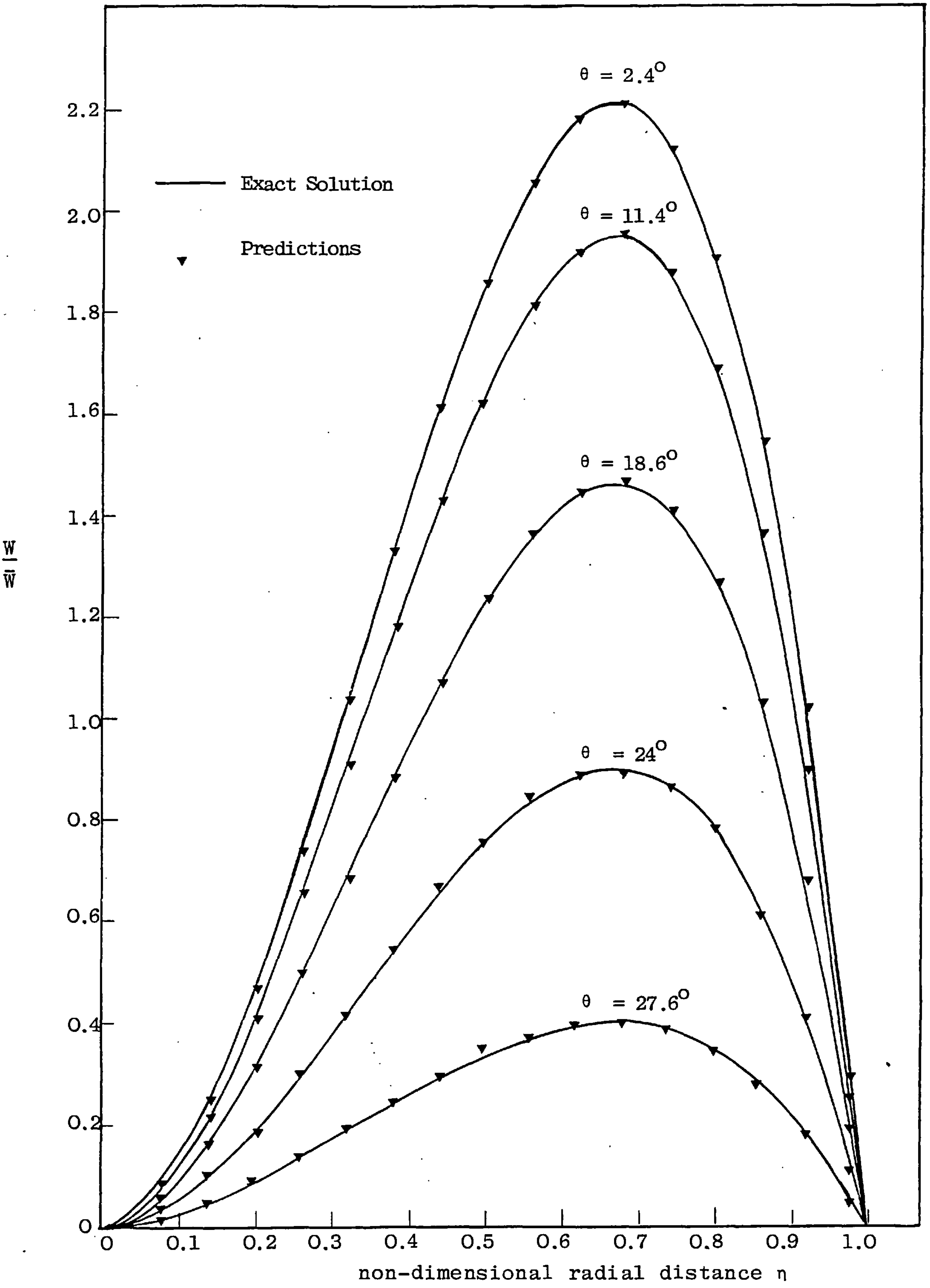

FIGURE 5.2.11: VELOCITY PROFILES IN EQUILATERAL-TRIANGULAR DUCT

5.3 ROD-BUNDLE FLOWS

The symmetry element in an infinite array of rods is the segment shown cross-hatched in figure (1.1.2). A non-orthogonal mesh was imposed on this segment in the manner indicated in figure (5.2.10), and computations made of both flow and heat-transfer parameters.

In the case of an equilateral-triangular array, for which most of the calculations presented in this thesis were performed, the angle θ_o in figure (5.2.10) has the value of 30 degrees; while for rods arranged in a square pattern, θ_o = 45 degrees. The general angular position θ is defined such that along the line of minimum separation between rods, θ = 0 degrees.

For the triangular array, the equivalent hydraulic diameter of the flow region is given by the following expression:

$$D_e = r_s \{ 2.20 (\frac{P}{D})^2 - 2.0 \} \quad , \qquad (5.3.1)$$

For the square array,

$$D_e = r_s \{ \frac{8}{\pi} (\frac{P}{D})^2 - 2.0 \} \quad , \qquad (5.3.2)$$

The parameter P/D, where $D = 2\, r_s$, is the "pitch-diameter ratio" of the configuration.

5.3.1 Inlet and boundary conditions:

The flow region shown in figure (5.2.10) is bounded by the following surfaces in the cross-stream plane:

(i) The rod wall (the south boundary, i.e. $\eta = 0$)

(ii) Two planes of symmetry which pass, on extrapolation, through the central axis of the rod. At these planes ($\xi = 0$ and $\xi = 1$) the normal flux of any quantity ϕ is zero. So,

$$\frac{\partial\phi}{r\partial\theta} = \frac{1}{r\Delta\theta}\frac{\partial\phi}{\partial\xi} - \frac{G}{\Delta r}\frac{\partial\phi}{\partial\eta} = 0 \quad ; \tag{5.3.3}$$

in the notation of the non-orthogonal coordinate system.

(iii) A north boundary ($\eta = 1$) comprising a plane of symmetry which bisects the region separating two adjacent rods. Here too, therefore, the normal flux is zero.

Hence,

$$\frac{\partial\phi}{\partial n} = 0 \quad , \tag{5.3.4}$$

where n is the normal to the boundary. In the (η,ξ) coordinate this may be expressed as:

$$\frac{(1+G^2)}{\Delta r}\frac{\partial\phi}{\partial\eta} - \frac{G}{r\Delta\theta}\frac{\partial\phi}{\partial\xi} = 0 \quad . \tag{5.3.5}$$

Thus, the complete set of inlet and boundary conditions are as follows:

Velocity solution

At $z = 0$; $\quad u = v = 0$; (5.3.6)

$w = \text{constant}$; (5.3.7)

$z > 0$; $\quad u = v = w = 0$ at $\eta = 0$; (5.3.8)

$$u = 0 \text{ at } \xi = 0;\ \xi = 1 \quad . \tag{5.3.9}$$

$$\frac{1}{r\Delta\theta}\frac{\partial\phi}{\partial\xi} - \frac{G}{\Delta r}\frac{\partial\phi}{\partial\eta} = 0, \quad \text{for } \phi = u,\ v,\ w \text{ at } \xi = 0;\ \xi = 1 \tag{5.3.10}$$

$$\frac{(1+G^2)}{\Delta r}\frac{\partial\phi}{\partial\eta} - \frac{G}{r\Delta\theta}\frac{\partial\phi}{\partial\xi} = 0, \text{ for } \phi = u,\ v,\ w \text{ at } \eta = 1\ . \tag{5.3.11}$$

Temperature solution

$$\text{At } z = 0; \quad \begin{aligned} &u = v = 0 \\ &w = \text{fully-developed solution} \\ &T = \text{constant} \end{aligned} \tag{5.3.12}$$

$$z > 0; \quad \frac{1}{r\Delta\theta}\frac{\partial T}{\partial\xi} - \frac{G}{\Delta r}\frac{\partial T}{\partial\eta} = 0, \quad \text{at } \xi = 0;\ \xi = 1\ . \tag{5.3.13}$$

$$\frac{(1+G^2)}{\Delta r}\frac{\partial T}{\partial\eta} - \frac{G}{r\Delta\theta}\frac{\partial T}{\partial\xi} = 0, \quad \text{at } \eta = 1. \tag{5.3.14}$$

Three different thermal boundary conditions at $\eta = 0$ were investigated (see section 5.1). The manner in which these were incorporated into the computational procedure is described in the following section.

5.3.2 Computational details

As in the calculations hitherto described, the finite-difference equations for u, v, w and T were solved by means of the solution method presented in chapter 4. The fully-developed velocity solution was first obtained, and this was then introduced as initial data for the temperature equation which was solved independently.

For both triangular and square arrays, calculations were performed with a uniform 15x15 grid in the cross-stream plane; grid independence was established by a comparison of the axial-velocity field with those obtained with non-uniform 19x19 and 23x23 grids. For calculations in the entrance region of the flow domain, an axial step length of 0.01 D_e, rising smoothly to a maximum 0.20 D_e, was employed. No additional iterations were required at any station. Fully-developed velocity solutions were obtained with a maximum step length of 0.50 D_e. The temperature solution was also obtained with a maximum step length of 0.50 D_e; however, 3-6 iterations per step were necessary for satisfactory convervence. A typical solution for the fully-developed hydrodynamic and temperature variables with a 15x15 grid required approximately 100 sec. of computer time on a CDC-6600 machine.

The three different heating constraints on the temperature equation were incorporated into the computational scheme as follows:

(i) Boundary condition A:- the wall heat flux was prescribed and introduced as a 'source' term (see section 4.3) for the control volumes adjacent to the rod wall, diffusion to the wall having been set to zero.

(ii) Boundary condition B:- this required a special treatment in the finite-difference scheme since the wall temperature at any axial station was not explicitly known. However, what was known, in any forward step, was the total heat input to the flow, viz.

$$\dot{Q}_W = \dot{Q}_W' \, \Delta z \quad , \tag{5.3.15}$$

where $\dot{Q}_W'$ is the (known) axial heat transfer per unit length of rod, and Δz the forward step length. For near-wall control volumes (for temperature) the finite-difference expression for the total heat flux over the next forward step is:

$$\Delta z \sum_{\text{rod wall}} - k_L \frac{(T_P - T_W)}{\delta y} \, r_s \, \delta\theta = \dot{Q}_W' \quad , \tag{5.3.16}$$

In the above expression, T_P is the temperature prevailing at the grid node P adjacent to the wall, T_W is the required wall temperature, δy is the normal distance of P from the wall, r_s the radius of the rod and k_L the thermal conductivity of the fluid. On re-arrangement, equation (5.3.16) yields:

$$T_W = \frac{\dot{Q}_W' + \sum\limits_{\text{rod wall}} \dfrac{k_L T_P}{\delta y} \, r_s \, \delta\theta}{\sum\limits_{\text{rod wall}} \dfrac{k_L \, r_s \, \delta\theta}{\delta y}} \quad . \tag{5.3.17}$$

This value of T_W was calculated from known and upstream values, and was stored on all wall boundary nodes prior to the calculation of the finite-difference coefficients in the temperature equation. It was found necessary to iterate on the latter three or four times before satisfactory convergence was obtained.

(iii) Boundary condition C:- A constant value of T_W was specified as initial datum, and stored at all wall nodes. The coefficients linking the latter to the near-wall nodes were set equal to zero and the heat flux at the wall introduced via the linearized source terms (see section 4.3) for the near-wall control cells.

5.3.3 Results and Discussion

5.3.3.1 Hydrodynamics:

(a) Developing flow:- Figure (5.3.1) shows the predicted development of pressure-drop with axial distance in triangular arrays for three different values of the pitch-diameter ratio. The ordinate in the figure represents the mean pressure difference between the inlet and an arbitrary station a distance z downstream, divided by the 'dynamic head'. It can be seen that the pressure falls very sharply near the entrance, due to the high shear-stresses in the thin wall boundary layers in this region. Far downstream, the pressure gradient assumes the constant fully-developed value. The smaller the value of P/D, the greater is the length of the entrance region. This is intuitively reasonable, since, at close spacings steep axial velocity gradients develop in the cross-stream plane, and so a longer length of duct is required for the initially uniform profile to settle down to its strongly non-uniform fully-developed state.

The actual development of the axial velocities down the

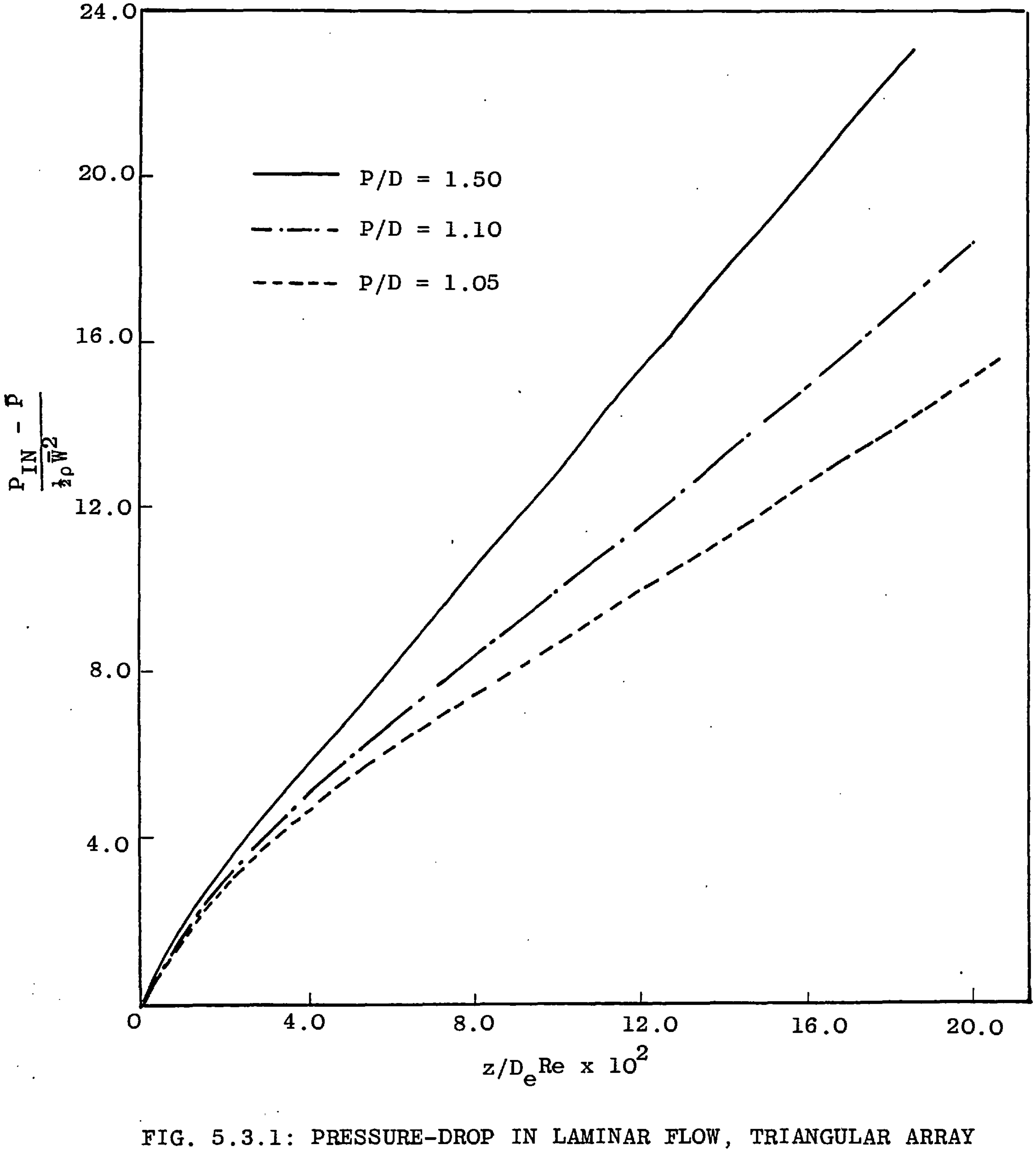

FIG. 5.3.1: PRESSURE-DROP IN LAMINAR FLOW, TRIANGULAR ARRAY

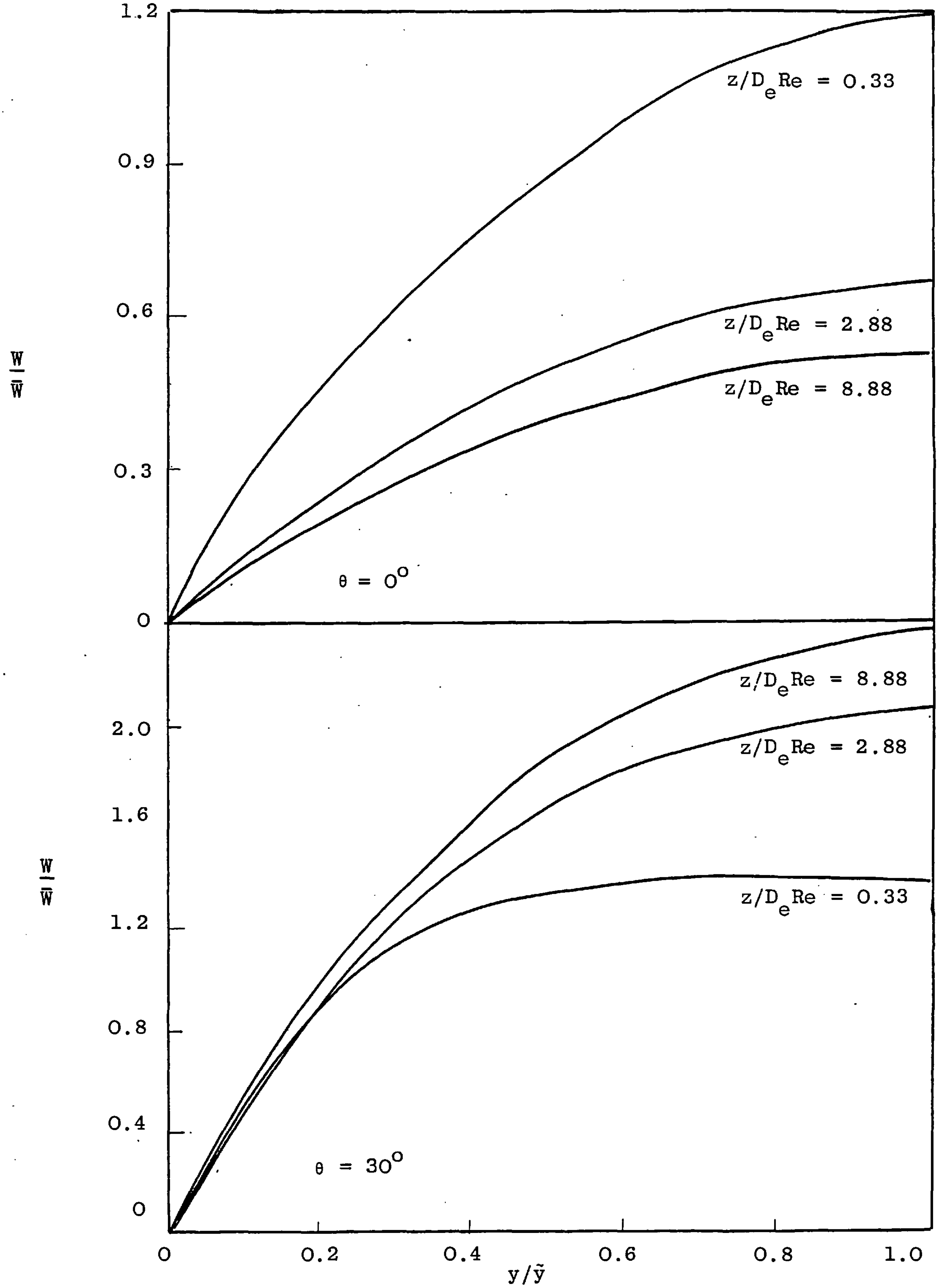

FIG. 5.3.2: DEVELOPING VELOCITY-PROFILES, TRIANGULAR ARRAY (P/D = 1.10)

length of the rods is illustrated in figure (5.3.2) for a typical value of P/D = 1.10. The velocities are plotted in the radial direction for two different angular positions, viz. $\theta = 0$ degrees, where the rods are at their minimum separation, and $\theta = 30$ degrees, where the rods are relatively farthest apart. The abscissa is the non-dimensional radial coordinate η, which may be written as:

$$\eta = y/\tilde{y} \qquad (5.3.18)$$

where y is the normal distance of any given point from the rod surface, and $\tilde{y}$ the distance between the rod surface and the maximum velocity plane (the north boundary of the calculation domain), corresponding to the angular location θ. It is seen from the figure that as the boundary layer develops along the rod length, momentum is transferred around the periphery of the rod from $\theta = 0$ degrees to $\theta = 30$ degrees. Moreover, fully-developed conditions are not attained simultaneously around the rod; the velocities along the 30^o line reach their fully-developed values approximately ten hydraulic diameters before the velocities along the 0^o position.

Unfortunately, no information of either an experimental or theoretical nature, with which the present predictions could be compared, is available to date.

(b) Fully-developed flow:-

Axial velocity distribution

As was indicated above, the velocity distribution in rod-

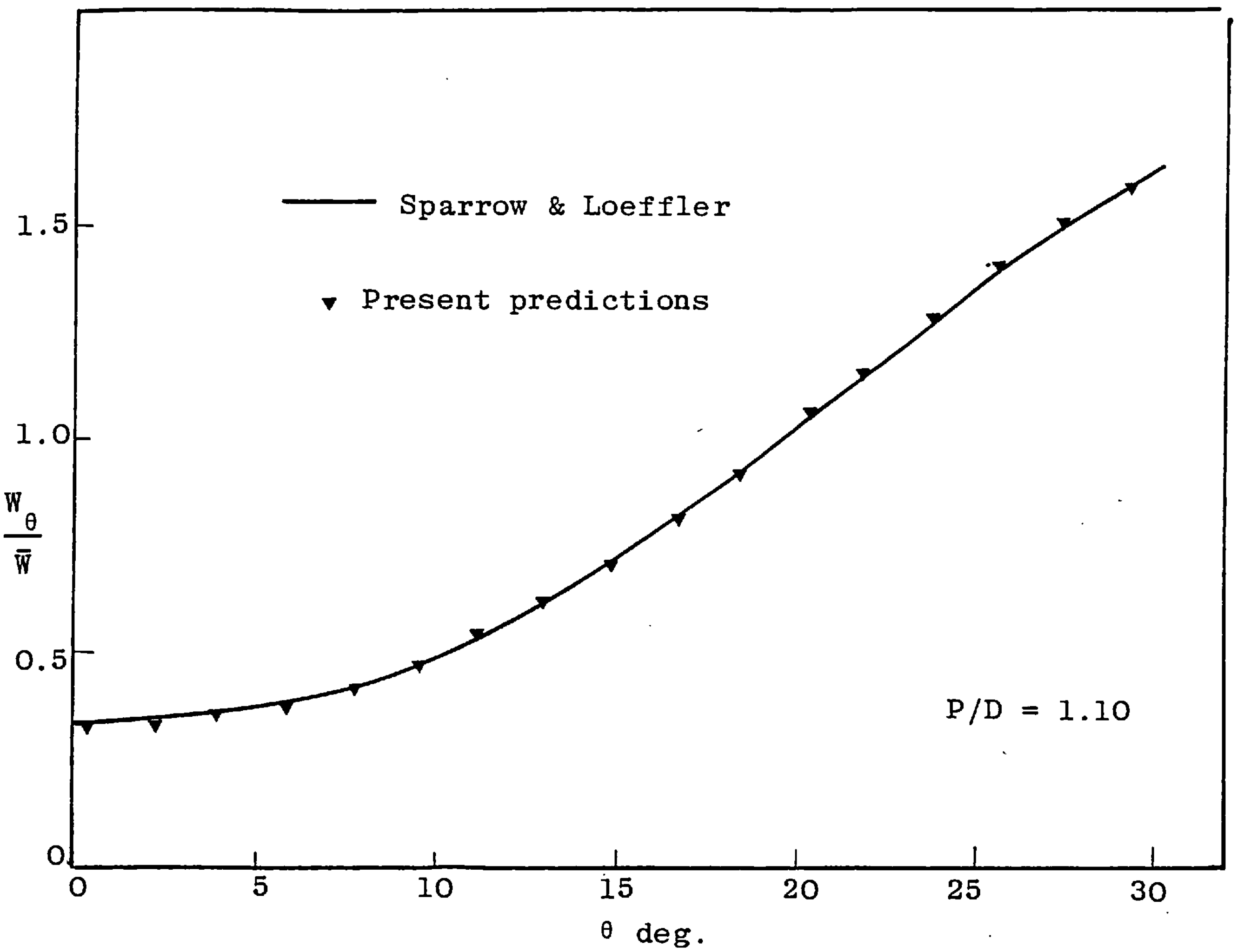

FIG. 5.3.3: PERIPHERAL VARIATION OF RADIALLY-AVERAGED VELOCITY

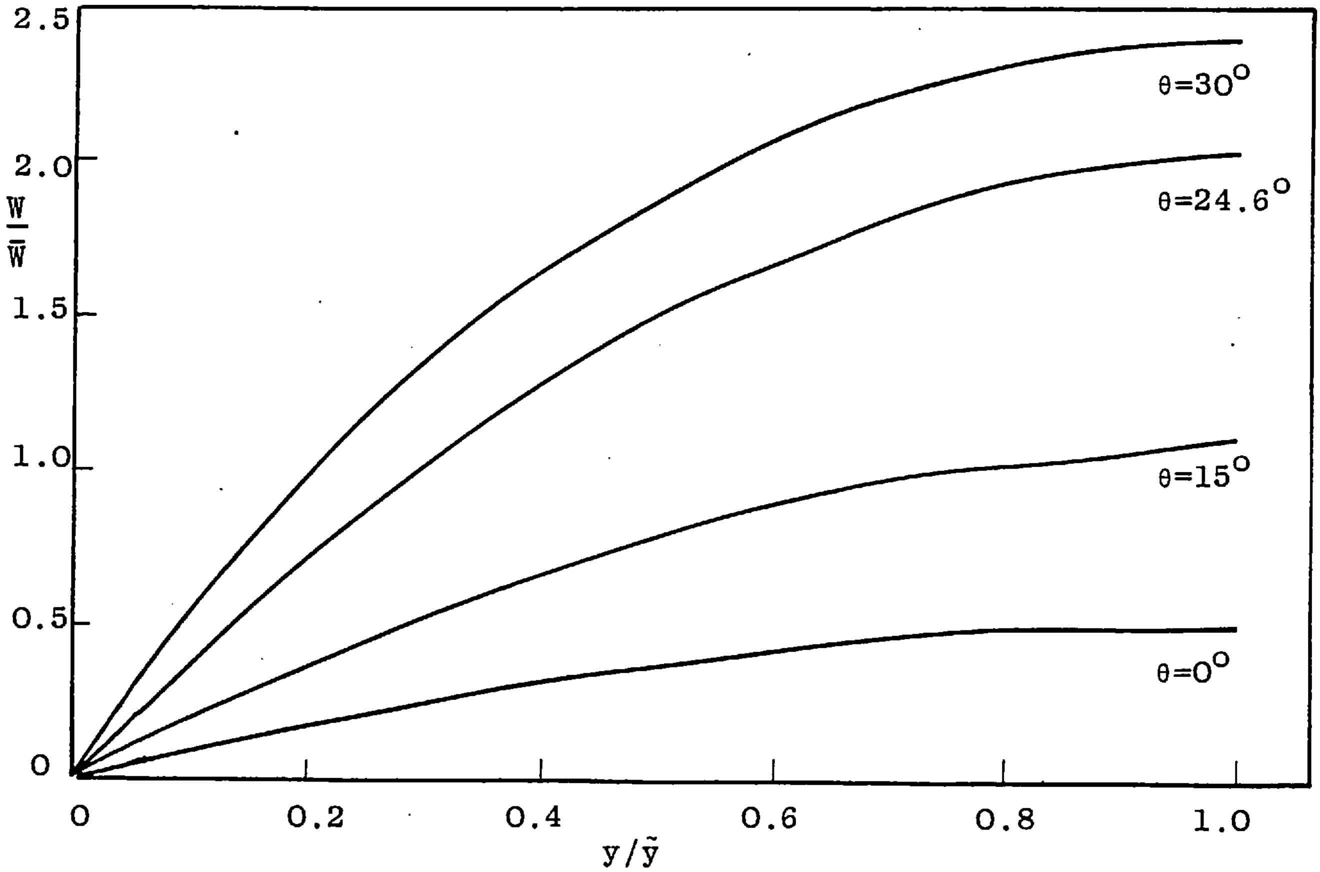

FIG. 5.3.4: VELOCITY-PROFILES (TRIANGULAR ARRAY, P/D = 1.10)

bundle flows is a strong function of the angular (or circumferential) position as well as the (radial) distance from the wall. This angular dependence of the axial velocity is of great interest, and a representative solution, corresponding to a triangular array with P/D = 1.10, is shown in figure (5.3.3). The ordinate in this figure represents the radially-averaged velocity w_θ at any circumferential location θ, non-dimensionalized with respect to the mean velocity $\bar{w}$ in the flow domain. Mathematically, w_θ is given by the following relation:

$$w_\theta \equiv \frac{\int_0^{\tilde{y}} w(y,\theta)dy}{\int_0^{\tilde{y}} dy} \qquad (5.3.19)$$

where y and $\tilde{y}$ are as in equation (5.3.18) above. The solid curve in the figure represents the analytical solution of Sparrow and Loeffler (1959), who obtained an expression for the velocity profile in the form of a trigonometric series. It is evident that the computed values are in excellent agreement with those calculated from the analytical solution.

The velocity profile in the radial direction is depicted in figure (5.3.4) as a function of angle θ, for the same geometry represented by the previous figure. The curves obtained from the analytical solution are indistinguishable from the present results shown in the figure.

Wall shear-stress distributions

Since the velocity distribution varies with angular position, so also will the local shear stress exerted by the wall on the fluid. The manner in which the shear stress varies is depicted in figures (5.3.5) and (5.3.6) for triangular and square arrays respectively. In each figure, the results for three different rod spacings are given. The ordinate in each figure is the local shear stress normalized with respect to the peripherally-averaged value.

The influence of neighbouring rods on the flow behaviour around a given rod is clearly evident from these figures. For open spacings, i.e. $P/D > 1.50$, the wall shear stress is uniform around the rod periphery; but as the rods are brought closer together, the asymmetry of the flow is enhanced by the interference of near neighbours, and so a greater dependence of the local shear stress on angular position is manifested. As would be expected on physical grounds, the highest shear-stress levels occur at the locations of maximum velocity ($\theta = 30$ degrees, and $\theta = 45$ degrees), and the lowest shear stresses at the location of lowest velocity ($\theta = 0$ degrees).

Excellent agreement between the computed solutions and the Sparrow-Loeffler results is obtained for both triangular and square configurations over the range of P/D ratios investigated.

Friction-factors

The friction-factor ∿ Reynolds-number dependence has been computed for each array as a function of rod spacing, and the results are plotted in figure (5.3.7). Note that the

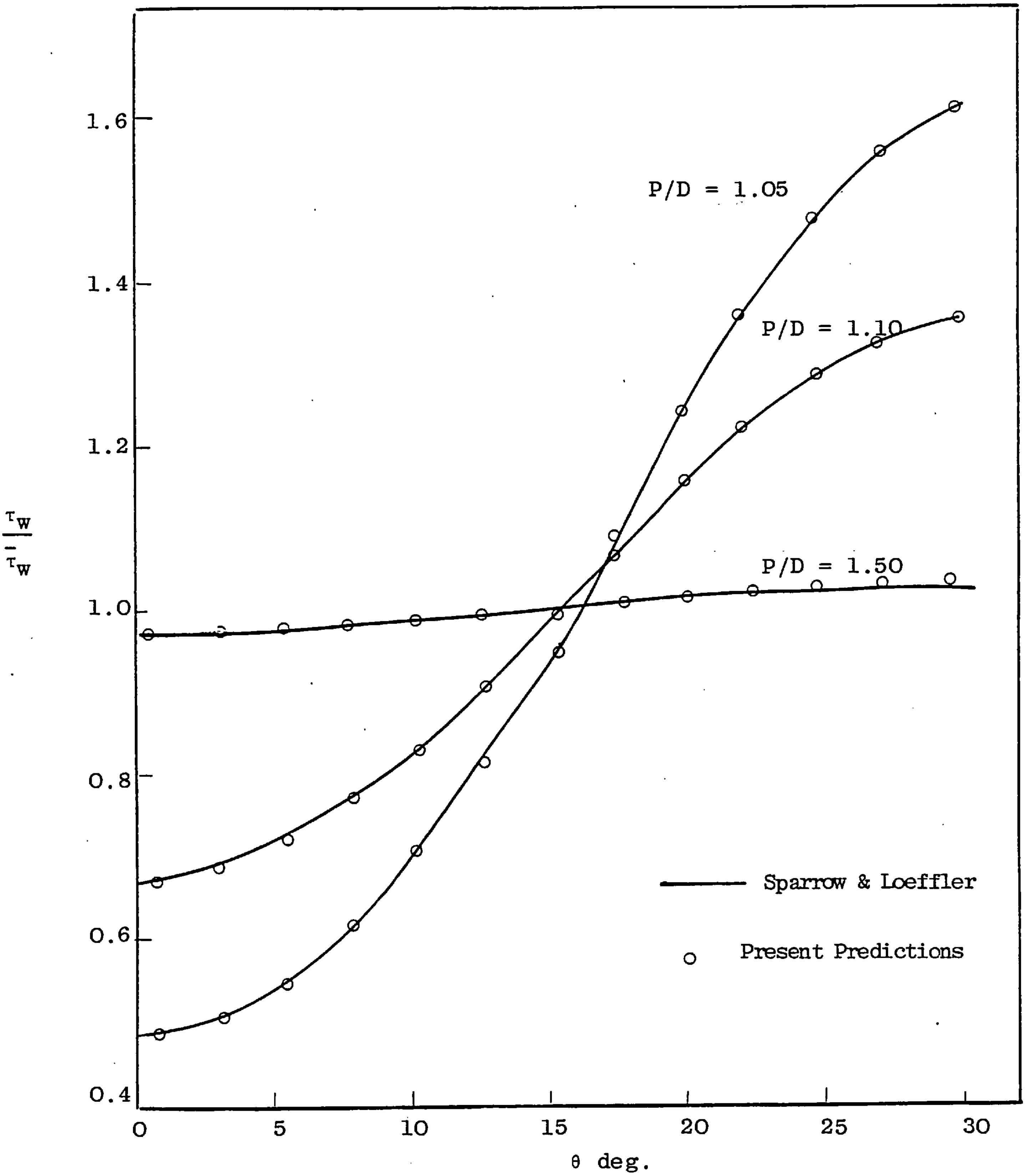

FIG. 5.3.5: PERIPHERAL DISTRIBUTION OF WALL SHEAR STRESS (EQUILATERAL TRIANGULAR ARRAY)

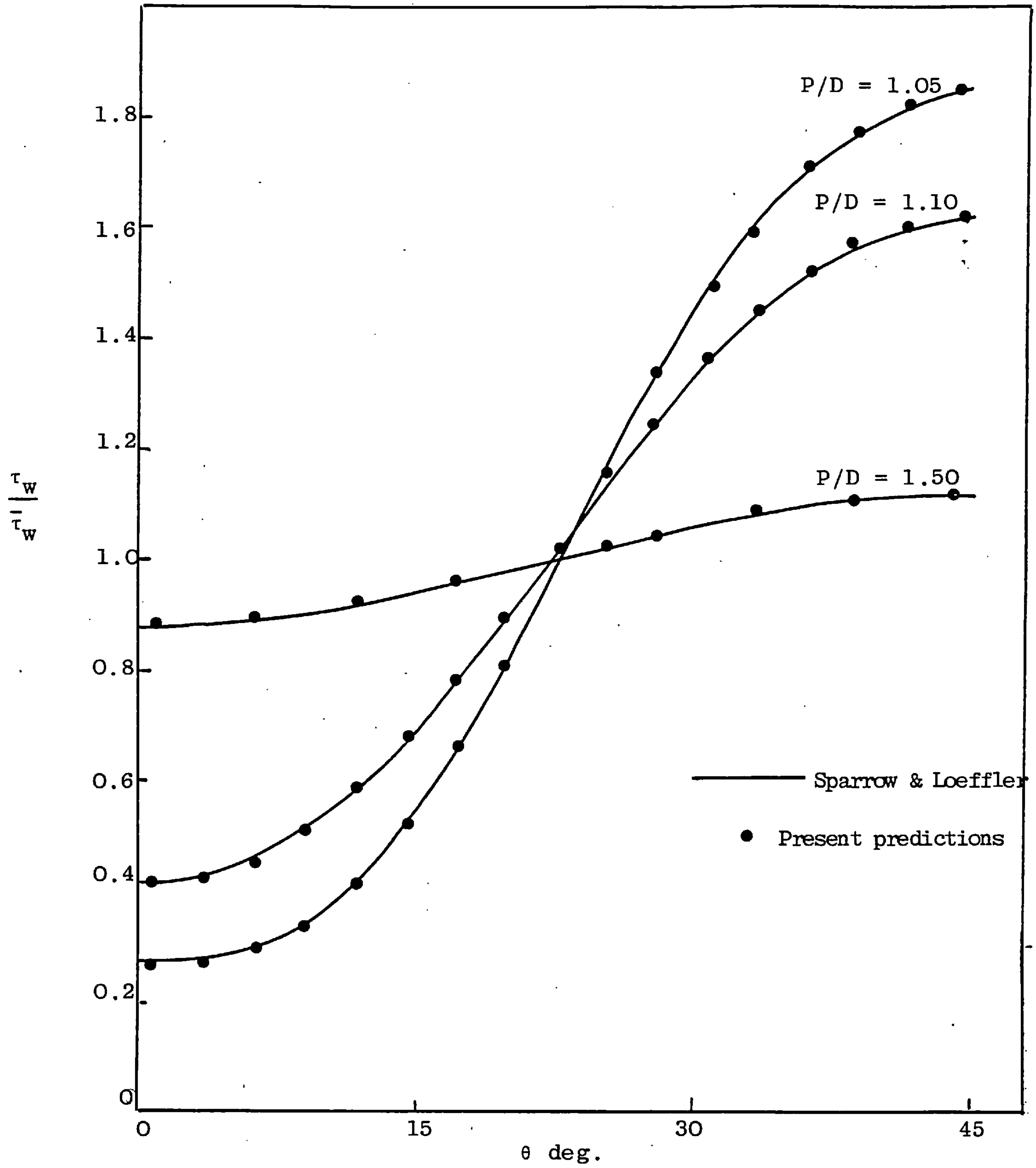

FIG. 5.3.6: PERIPHERAL DISTRIBUTION OF WALL SHEAR STRESS (SQUARE ARRAY)

Reynolds-number (Re_d) in this plot is based on the rod diameter, and that the abscissa is the "porosity", ε, which is a relative measure of the area available to the flow. For the triangular array, ε is given by:

$$\varepsilon = 1 - \frac{\sqrt{3}\,\pi}{6(P/D)^2} \quad , \qquad (5.3.20)$$

while, for the sqaure array:

$$\varepsilon = 1 - \frac{\pi}{4(P/D)^2} \quad . \qquad (5.3.21)$$

This choice of axes for the plots of figure (5.3.7) was made in order to directly compare the present predictions with those given in this form in the paper by Sparrow and Loeffler. Also, by relating the Reynolds-number to the rod diameter instead of the conventional 'hydraulic diameter', it is possible to given an intuitive explanation of the shape of the curves shown.

For a given flow and porosity, a rod in a triangular array is surrounded by more neighbours, and hence would be expected to feel a greater fluid resistance, than an identical rod in a square array. This, however, is only true for close spacings (small porosities), where the flow passages for the two geometries are appreciably different. At large spacings (large ε), when the effect of neighbouring rods is insignificant, and the flow passages are similar in shape, the curves for both arrays merge into one. It is

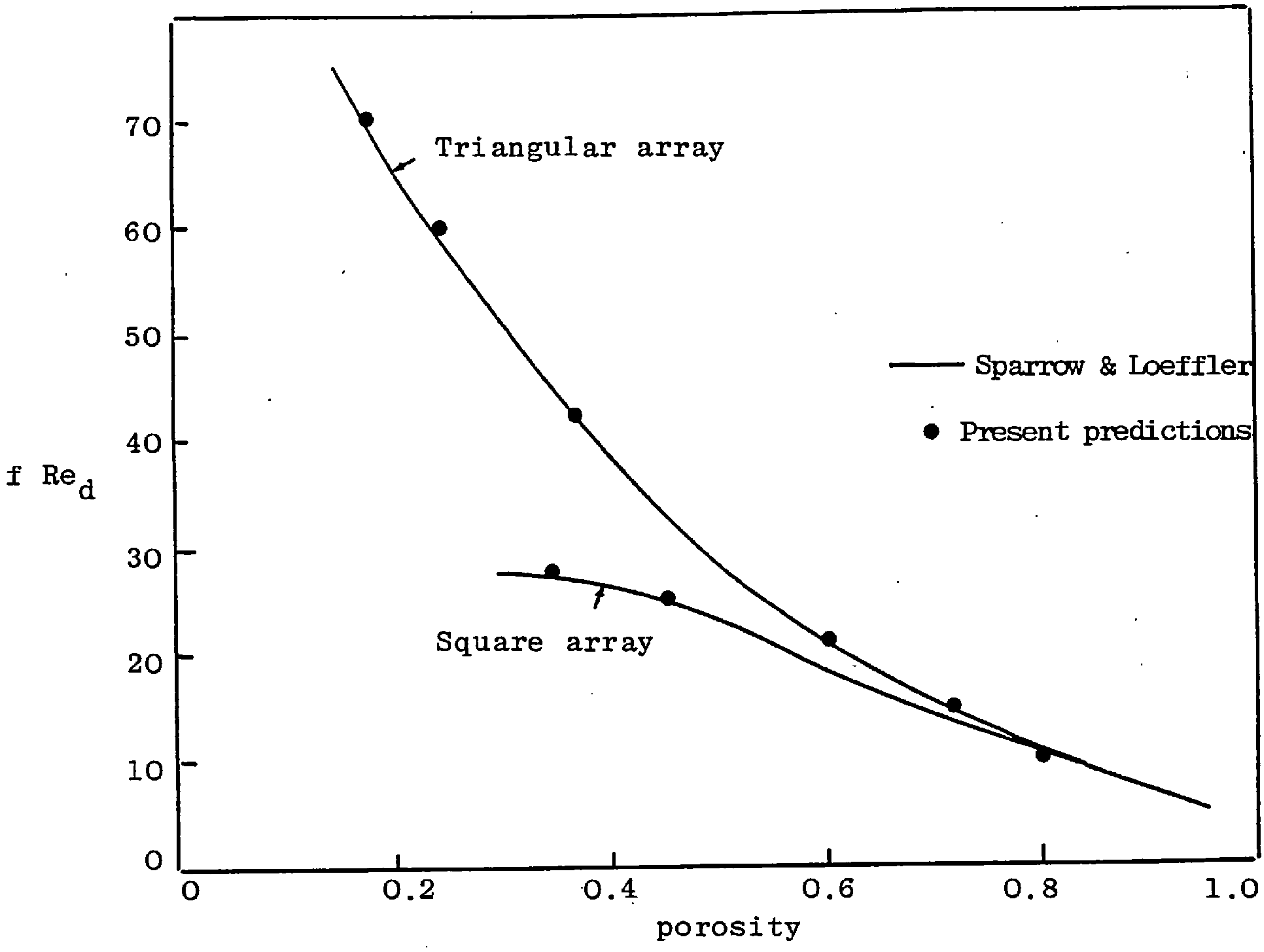

FIG. 5.3.7: FRICTION-FACTOR ~ REYNOLDS-NUMBER RELATION AS A FUNCTION OF POROSITY

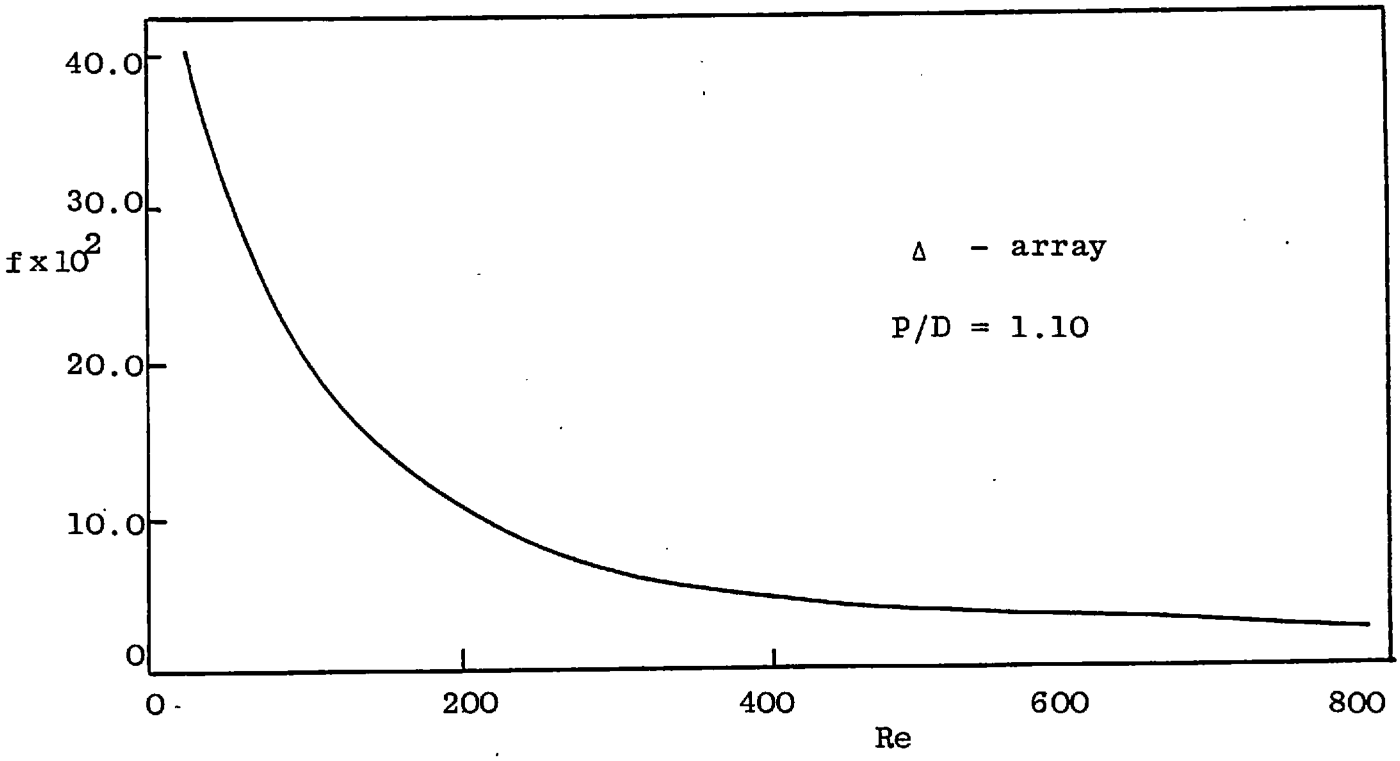

FIG. 5.3.8: FRICTION FACTOR ~ REYNOLDS-NUMBER CURVE

evident from figure (5.3.7) that the computed values are in excellent agreement with the results of Sparrow and Loefflers' analysis for the wide range of pitch-diameter ratios considered.

A representative friction-factor$\sim$ Reynolds-number relation for a triangular array with a P/D value of 1.10 is depicted in figure (5.3.8). Here, the conventional Reynolds-number, i.e. that based on D_e, is employed as the abscissa, and f is defined, as indeed for the previous figure, according to:

$$f = \frac{\bar{\tau}_w}{\frac{1}{2}\rho \bar{w}^2} \qquad (5.3.22)$$

5.3.3.2 Heat transfer

(i) Uniform wall heat flux in all directions (Boundary condition A) is:-

The heat-transfer characteristics of the flow have been calculated with the present numerical procedure for both developing and fully-developed heat-transfer conditions. Figure (5.3.9) illustrates the development of the heat transfer rate in the entrance region of a triangular array for three different rod spacings. Fully-developed hydrodynamic conditions and a uniform temperature profile at z = 0 have been assumed. The Nusselt numbers are defined according to:

$$Nu \equiv \frac{\bar{h} D_e}{k_L} \quad . \qquad (5.3.23)$$

where $\bar{h}$ is the peripherally-averaged heat-transfer coefficient between the heated rod surface and the moving fluid, and D_e is defined by equation (5.3.1). As was observed in the developing-flow calculations, the smaller the value of the pitch-diameter ratio the greater is the length of the thermal entrance region. For example, for the rod array with P/D = 1.20, the Nusselt number reaches its constant fully-developed value after an entrance length of about sixty equivalent hydraulic diameters; while for the rod array with P/D = 1.05, more than 100 equivalent diameters are required before the fully-developed value is attained.

Figure (5.3.10) shows the development of the average wall temperature $\bar{T}_W$ and the mean fluid temperature T_m along the length of the rod arranged in an array with P/D = 1.05. An arbitrary constant heat flux has been specified. T_m increases linearly from the entrance, as expected, while T_W rises rapidly at first and then gradually slows down to a rate of increase equal to that of T_m. It is when this identity of longitudinal gradient has been reached that 'fully-developed heat transfer' is said to have been attained.

The fully-developed values of Nusselt number have been catalogued in Table 5.3.1 for a wide range of pitch-diameter ratios. Also shown, for purposes of comparison, are the analytical solutions of Dwyer and Barry (1970). The agreement between the two sets of calculated Nusselt numbers is good. The Nusselt numbers corresponding to a square pattern of rods have also been computed, and are presented in figure (5.3.11). No other analysis of this geometry is currently available for comparison.

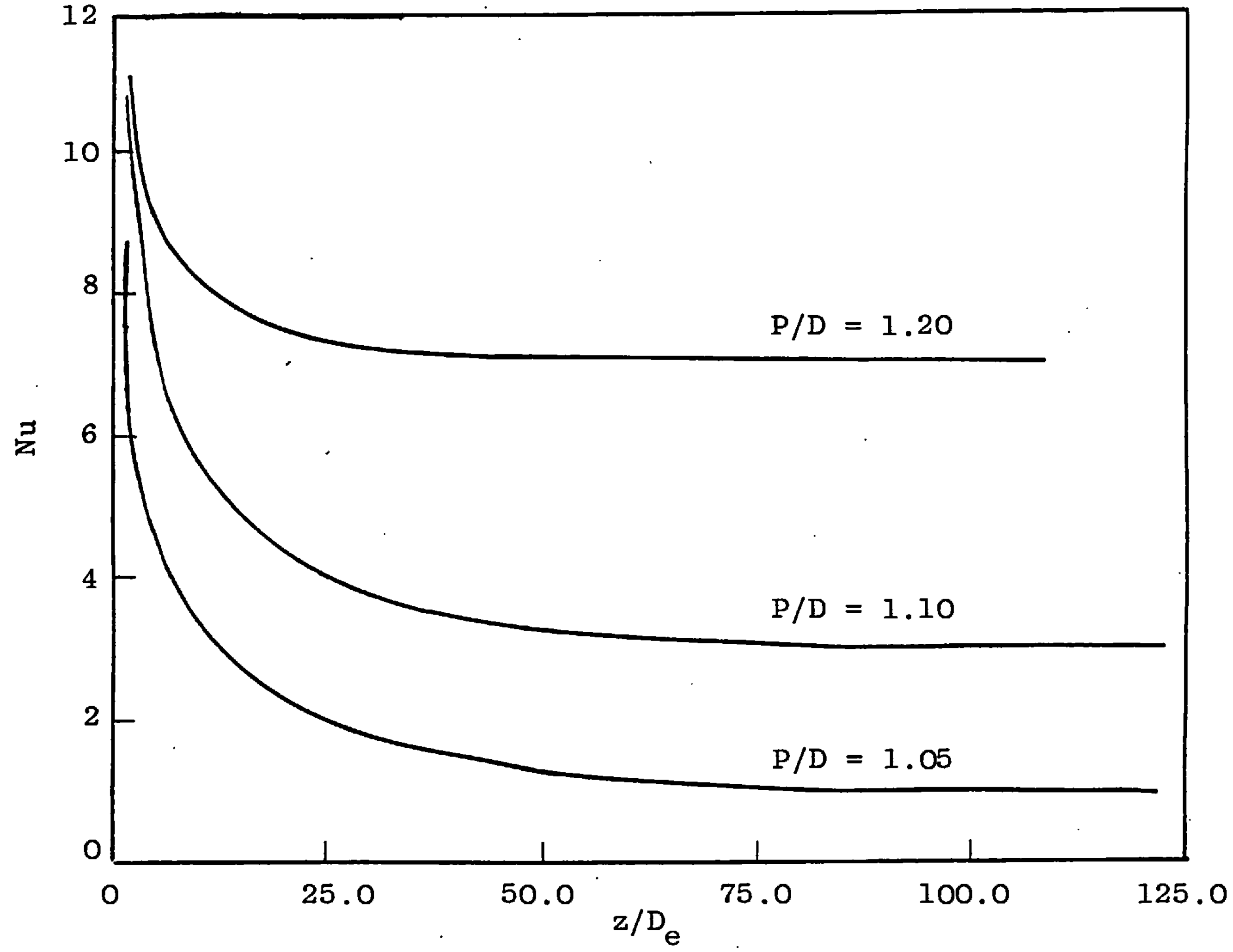

FIG. 5.3.9: NUSSELT NUMBER DEVELOPMENT; CONSTANT HEAT FLUX PROBLEM

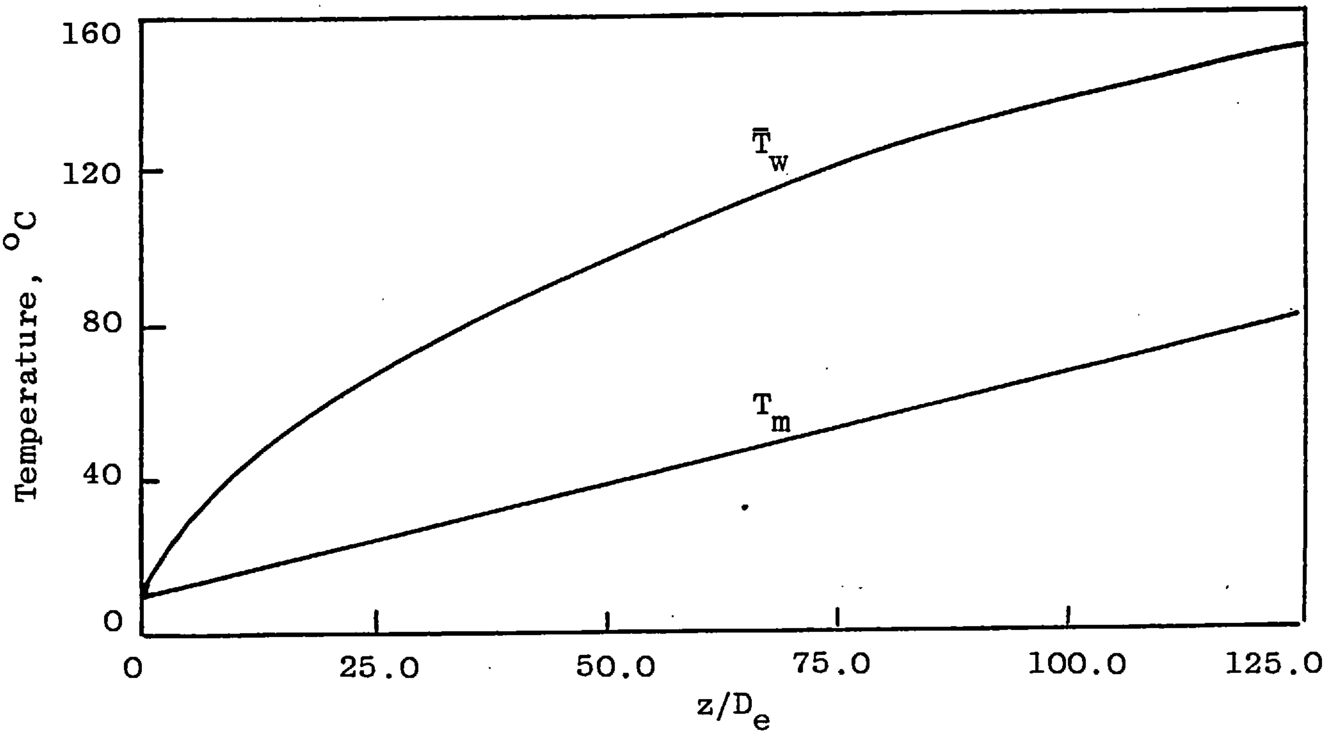

FIG. 5.3.10: TEMPERATURE DEVELOPMENT; CONSTANT HEAT FLUX

Table 5.3.1

P/D	Nu	Nu(Analytical)
1.03	0.58	0.58
1.05	1.06	1.06
1.07	1.72	1.70
1.10	2.96	2.94
1.20	6.95	6.90
1.30	9.12	9.03
1.50	11.28	11.22
1.80	13.75	13.66
2.00	15.38	15.26

A greater insight into the physical processes involved is offered by the investigation of the behaviour of the average heat-transfer coefficient $\bar{h}$. Figure (5.3.12) indicates the variation of the $\bar{h}/k_L$ over a wide range of pitch-diameter ratios. For large spacings, $\bar{h}$ decreases with increasing values of P/D, because the heat flow through the coolant is wholly in the radial direction. At very close spacings, however, circumferential heat transfer becomes dominant; hence, in this range of P/D ratio, $\bar{h}$ increase with an increase in the P/D ratio, all else being equal. The result is that the rod-average heat-transfer coefficient passes through a maximum as the value of P/D is varied over a wide range. From the figure, it is seen that the maximum value of $\bar{h}$ occurs at a P/D ratio of about 1.20; this is in accord with Dwyer and Berry's conclusions.

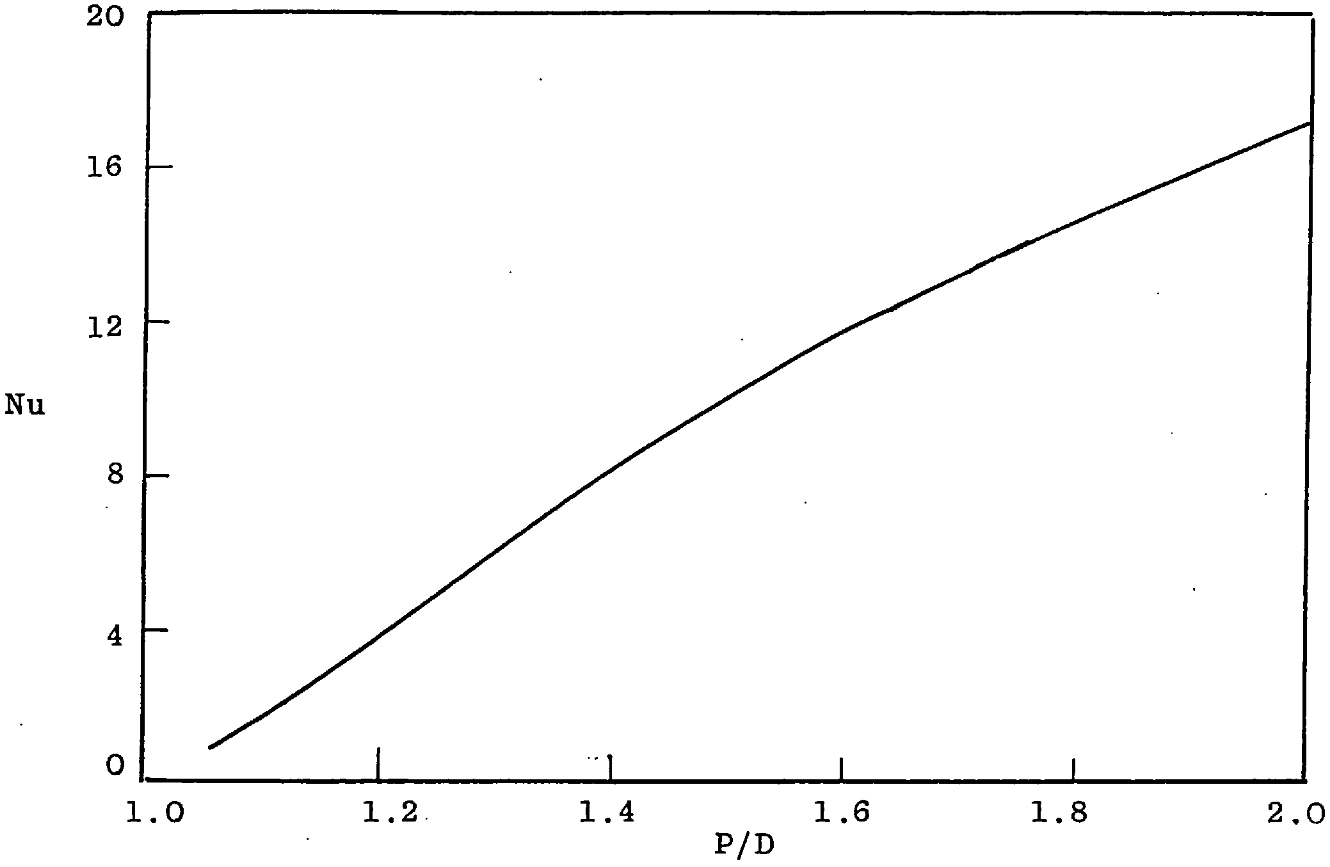

FIG. 5.3.11: NUSSELT NUMBERS FOR SQUARE ARRAY

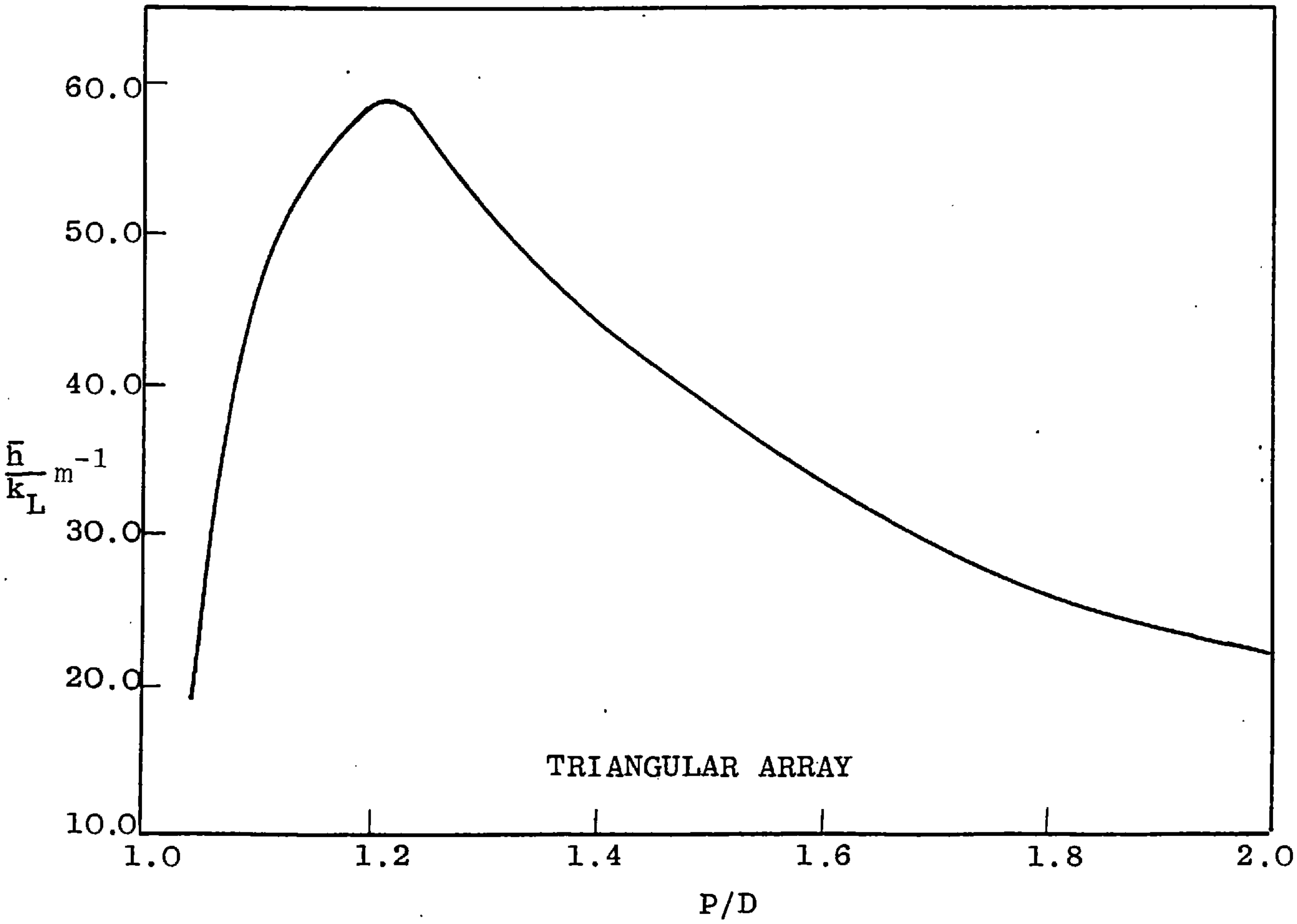

FIG. 5.3.12: VARIATION OF ROD-AVERAGE HEAT-TRANSFER COEFFICIENT WITH ROD SPACING

Another effect of practical importance is the variation of the local temperature around the surface of the rod. This variation is shown in figure (5.3.13); the ordinate represents a dimensionless temperature difference which is actually the reciprocal of the local Nusselt number. As anticipated on physical grounds, the peak temperature occurs at $\theta = 0$ deg., which is the location of the smallest open area for flow. For the situation corresponding to $P/D = 1.05$ there is a small region (between $\theta = 28$ degrees and $\theta = 30$ degrees) where the surface temperature is slightly less than the bulk temperature of the coolant. This small circumferential region of negative values of $(T_W - T_m)$ grows as the P/D ratio is further diminished.

Once again agreement between the present wall temperature predictions and those of Dwyer and Berry (1970) is seen to be excellent.

(ii) Uniform wall heat flux in axial direction and uniform wall temperature in the circumferential direction (Boundary condition B)

This boundary condition corresponds to the case of uniform internal heat generation in a fuel rod encased in a cladding of high thermal conductivity. Once again, the overall heat-transfer performance is described in terms of the rod-average Nusselt number, defined according to equation (5.3.23) and tabulated below. Shown alongside are the analytical solutions of Sparrow, Loeffler and Hubbard (1961), which were checked and extended over a wider P/D range by Dwyer and Berry (1970).

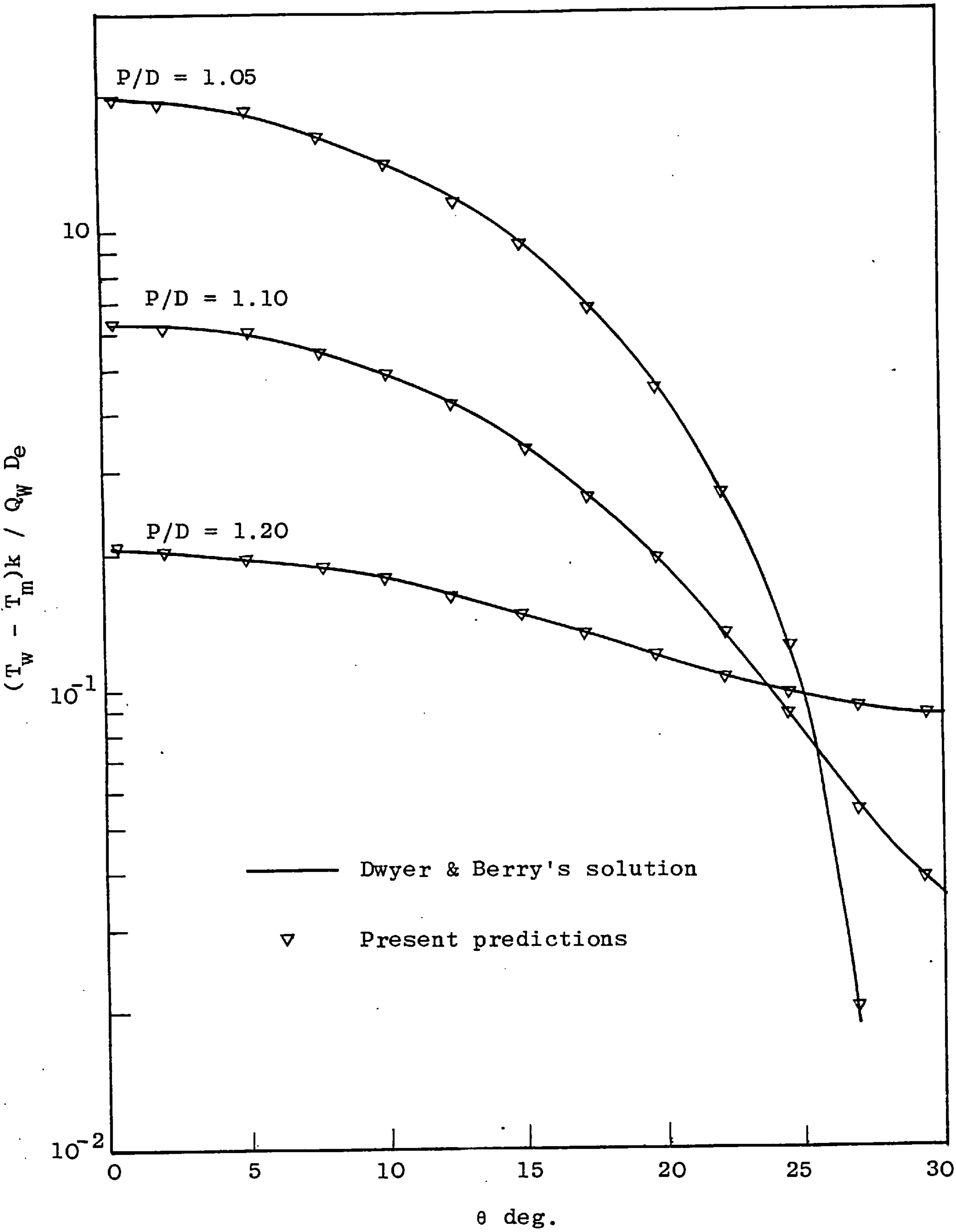

FIG. 5.3.13: PERIPHERAL VARIATION OF WALL TEMPERATURE
(BOUNDARY CONDITION A)

All values in the table are for fully-developed heat transfer in triangular arrays.

Table 5.3.2

P/D	Nu	Nu (Analytical)
1.03	2.11	2.14
1.05	2.79	2.82
1.10	4.58	4.62
1.20	7.44	7.48
1.30	9.10	9.19
1.50	11.20	11.26
1.80	13.48	13.68

The two sets of computations are in good agreement, which attests to the accuracy of both calculation methods. A comparison between Table (5.3.2) and table (5.3.1) reveals that for P/D ratios greater than about 1.30, the distinction between the cases of peripherally uniform temperature and peripherally uniform heat flux disappears.

Since the velocity distribution varies with angular position (figure 5.3.3) and the wall temperature is prescribed to be independent of angle, it is evident that there is a peripheral variation in the local heat transfer rate $\dot{Q}_W''$. In figure (5.3.4), $\dot{Q}_W''$, non-dimensionalized with respect to the average value, is shown as a function of peripheral location for three different rod spacings. For open spacings ($P/D > 1.50$) the heat transfer is essentially constant around the rod circumference. For closer spacings, however, the trend of the velocity profile towards greater asymmetry is

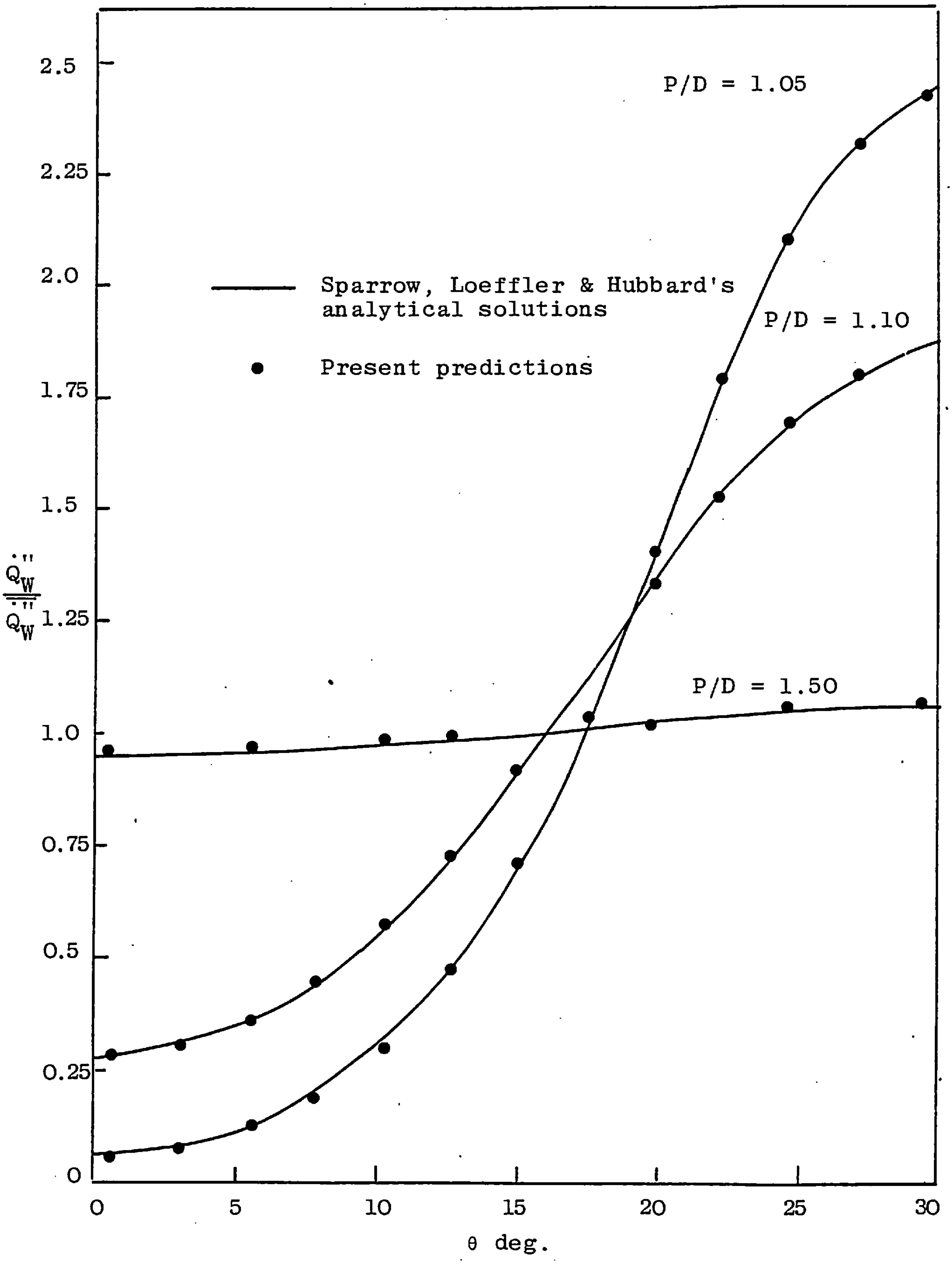

FIG. 5.3.14: PERIPHERAL WALL HEAT FLUX DISTRIBUTION (BOUNDARY CONDITION B)

accompanied by an increasing non-uniformity in the heat transfer rate.

(iii) Uniform wall temperature in all directions (Boundary Condition C)

Although this heating constraint is not of any interest to the heat-transfer specialist working with reactor fuel elements, it does arise in the operation of some steam condensor units. Calculated average Nusselt numbers for fully-developed heat transfer in triangular arrays are tabulated below in Table 5.3.3, for some representative P/D ratios. No other treatment of this boundary condition exists in the relevant heat-transfer literature.

Table 5.3.3

P/D	Nu
1.05	2.03
1.10	3.28
1.20	5.88
1.30	7.94
1.50	10.92
1.80	13.60

5.4 CLOSURE

In this chapter, the finite-difference equations formulated for the non-orthogonal coordinate mesh have been successfully tested in circular, elliptic and triangular duct flows with heat transfer under laminar conditions. The procedure has also been applied to the prediction of laminar flow and heat transfer in rod bundles for both triangular and square patterns. The universality of the method has been demonstrated by investigating three different thermal boundary conditions for the case of the equilateral-triangular array. In all cases, the computed local velocity field, wall shear-stress distributions, friction-factors, wall temperature variations et cetera have been compared with published results obtained via earlier analytical methods; and the agreement was found to be very good. Moreover, the superiority of the present method over such analytical techniques is clearly seen in the ability of the former to predict situations - such as the entrance flow region and the fully-developed heat transfer performance of square arrays - for which neither experimental data nor analytical results are currently available.

CHAPTER 6

PREDICTION OF TURBULENT FLOW IN EQUILATERAL-TRIANGULAR DUCTS

6.1 INTRODUCTION

6.1.1 Objectives of the study

The validation of the non-orthogonal finite-difference formulation developed in this thesis has been described in the preceding chapter for the case of laminar flow and heat transfer in a number of non-circular ducts. In the present chapter, attention is focussed on the fully-developed turbulent flow in a straight duct with a cross-sectional shape of an equilateral triangle. Predictions have been made of the flow behaviour in such a duct with the aid of the $k\sim\varepsilon$ turbulence model and the Launder-Ying algebraic stress formulation described in chapter 3.

Three motivations for the present study may be identified. Firstly, owing to its helical nature, the turbulent flow in an equilateral-triangular duct is of much interest to the turbulence investigator. This helical motion is caused by secondary currents which arise in the plane normal to the duct walls owing to the asymmetry of the cross-section. The capability of a two-equation model of turbulence, in conjunction with the Launder-Ying algebraic stress model, to correctly predict such motions needs to be demonstrated. Secondly, the asymmetric duct geometry constitutes a rigorous test of the accuracy and utility of the 'non-orthogonal' calculation procedure presented earlier. This geometry, moreover, may be seen as a rough approximation to an equilateral-triangular array of rods with a pitch-diameter ratio of unity. Thirdly, a detailed experimental investigation of the turbulent flow characteristics in such a duct has been performed recently by Aly, Tripp and Gerrard (1978); consequently, the predictions of the present model with respect to the mean velocity field, turbulent kinetic energy, wall shear-stress distribution etc. may be carefully assessed against the experimental results reported.

6.1.2 Review of previous work

Although square and rectangular ducts have been studied most extensively with both experimental and analytical techniques, similar studies for turbulent flow in triangular ducts are severely limited. Nikuradse (1930), following his pioneering investigations of square duct flow, observed that lines of constant mean velocity (isovels) in triangular ducts tended to bulge towards the corners, and concluded that secondary motions analogous to those existing in square ducts were present. His conclusions were confirmed by flow visualization. Cremers and Eckert (1962) measured mean axial velocities and five

Reynolds stresses in an isosceles triangular duct with an apex angle of 11.5° at a Reynolds number of 10900. They reported a lack of direct evidence for the existence of secondary flows, although contour plots of axial velocity fluctuations suggested the presence of secondary flows near the base. Carlson and Irvine (1961) investigated the pressure drop in acute-angled isosceles triangles and concluded that the friction-factors in these ducts were over-predicted by the Blasius equation by as much as twenty per cent. As in the case of a square duct, the 'equivalent hydraulic diameter' concept was clearly inadequate.

The first theoretical treatment of triangular ducts was that of Deissler and Taylor (1959) who applied a tedious semi-graphical procedure developed for non-circular duct shapes. No allowance was made for secondary flow. Kokorev et al. (1971) combined an experimental analysis of square duct flow with a theoretical estimate of the wall shear stress distribution is an isosceles triangular duct with a vortex angle of 20°. They assumed a universal velocity profile to prevail normal to the channel walls and a secondary flow was prescribed through the square duct results. Gerrard (1974) applied a finite-element technique to predict the axial velocity contours in an equilateral-triangular duct; the Reynolds stresses were represented by way of an eddy viscosity of the Van Driest type. Owing to the lack of experimental data as input, secondary flows were not taken into account.

Recently a joint experimental and analytical investigation of the turbulent flow in an equilateral triangular duct was undertaken by Aly, Trapp and Gerrard (1978). The experimental study was performed with air flowing through a duct of 12.7 cm sides, over a Reynolds number range of 53000 to 107300. Mean axial velocity and wall shear stress measurements at the highest Reynolds number were made with a large Pitot tube used in conjunction with a Betz projection manometer; while a Fuess manometer and a smaller Pitot probe was used at the lower Reynolds numbers. They found that friction factors, based on the equivalent hydraulic diameter, were about 6% lower than for pipe flow. Turbulence measurements were made with the use of constant-temperature linearized hot-wire anemometry. Secondary velocities were measured with both X-array probes and a rotatable miniature 45^{o} slanting probe. The observed secondary flow pattern consisted of six counter-rotating cells bounded by the corner bisectors of the duct. For each cell, the circulation was from the central core region to the corner via the corner-bisector, with fluid returning to the core along the wall.

Aly et al. (1978) also employed a computational technique, based on the general elliptic finite-difference procedure of Gosman et al. (1968) and the Reynolds stress representation of Launder and Ying, to predict the flow corresponding to the experimental conditions investigated. The continuity and momentum equations were reduced to an equation in terms of the vorticity and the stream-function. A fine numerical grid based on a cartesian coordinate system was used, and the turbulence length-scale distribution required to 'close' the governing equations was prescribed from the geometric formula suggested by Buleev (1963). The necessity of specifying a length-scale as input is an inherent drawback of this method. Moreover, the values of the constants appearing in the Launder-Ying formulation (see section 3.9) were inexplicably altered by the authors. The resulting predictions were in satisfactory agreement with their experimental data.

The calculations to be presented in the following pages were initiated independently of any knowledge regarding the work of Aly et al. The high-Reynolds-number $k\sim\varepsilon$ turbulence model described in section (3.8) was used in conjunction with the algebraic stress formulation of Launder and Ying (section 3.7); the values of the constants employed were those given earlier in section (3.9).

6.2 COMPUTATIONAL DETAILS

6.2.1 Calculation domain

Owing to the symmetry of the duct about its corner bisectors, it was only necessary to consider the flow domain shown cross-hatched in figure (6.2.1(a)). The entire triangular duct comprises six such domains of identical shape and size. The main flow direction is normal to the plane of the paper.

The non-orthogonal grid developed and described earlier in

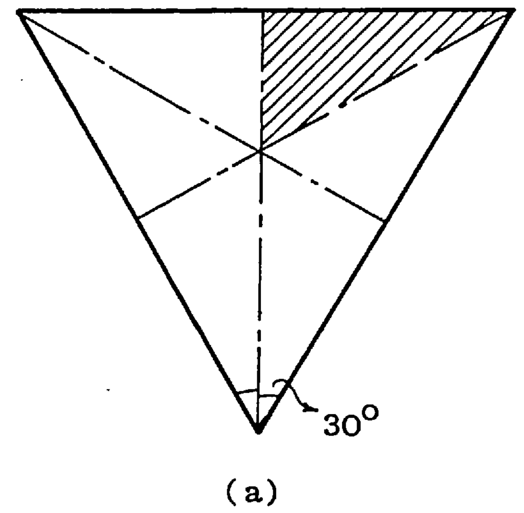

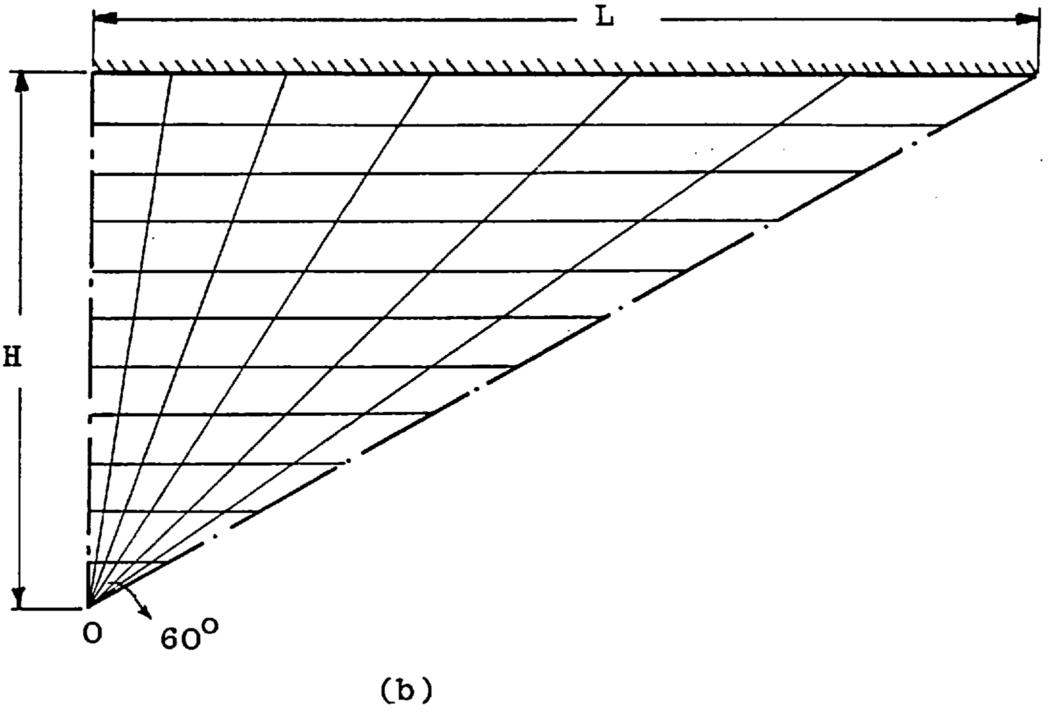

FIGURE 6.2.1: (a) EQUILATERAL-TRIANGULAR DUCT
(b) COMPUTATIONAL GRID

this thesis was employed to span the above flow domain in the manner indicated in figure (6.2.1(b)). In this case, the family of η = constant lines consists of straight lines running parallel to each other and to the wall of the duct. The ξ = constant grid lines emanate radially from the origin O, which is the centroid of the triangular cross-section. The intersection of the coordinate lines serve to define the grid nodes at which the main variables are stored in the finite- difference procedure.

The boundaries of the calculation domain are mathematically defined as follows: The South boundary consists of a circular arc of infinitesimal radius, the East and West boundaries are symmetry planes across which the flux of any variable is zero; while the North boundary is a stationary half-wall of the duct at which all momenta are destroyed.

6.2.2 Equations solved

The equations solved comprised the continuity and momentum equations (3.4.13) to (3.4.16), and the equations (3.8.6) and (3.8.7), together with the auxiliary relations (3.7.11) to (3.7.15) for the turbulence quantities. The values of the 'turbulence model' constants given in Table (3.9.1) of section (3.9) were used without modification. Some calculations were also performed in which the Reynolds-stress terms appearing in the u and v equations were represented via an isotropic turbulent viscosity; in these cases, the relevant momentum equations solved were (B.2) to (B.4). The solution scheme which was described in detail in chapter 4 was utilized in the solution of these equations.

6.2.3 Inlet conditions

The computations to be presented in the following pages were performed in two stages. In the first stage, the fully-developed flow field was obtained for the case when the u and v equations were solved via the conventional turbulent viscosity hypothesis, i.e. the secondary motion was neglected. This converged solution was subsequently employed as input for the calculations in which the formulation of Launder and Ying (1973) was used to represent the stress terms in the cross-stream momentum equations. Consequently, it is only necessary to specify here the inlet information provided for the first state of the calculation.

The initial cross-stream velocities were set to zero, and a uniform w-profile was assumed to prevail over the duct cross-section.

Initial distributions for the turbulent kinetic energy and the dissipation rate are generally specified from a knowledge of the turbulence at the inlet in the flow situation under study. However, since no such information exists in the present case, 'likely' conditions had to be estimated. Fortunately, the predictions are not very sensitive to these initial guesses. The following inlet profiles were prescribed for the turbulent kinetic energy and for the turbulence length-scale:

$$k = 0.02\, W_{IN}^2 \quad , \qquad (6.2.1)$$

$$\ell = 0.07\, D_H \quad . \qquad (6.2.2)$$

where W_{IN} is the uniform inlet velocity and D_H is the equivalent hydraulic diameter of the duct. The constant in equation (6.2.2) was varied in the range 0.07-0.40 and hardly any change in the predicted flow variables was detected at distances more than thirty equivalent-diameters downstream.

6.2.4 Boundary conditions

As mentioned in (6.2.1), the east and west boundaries of the flow domain are planes of symmetry, so that:

$$\frac{1}{\Delta\theta}\frac{\partial\phi}{\partial\xi} - \frac{Gr}{\Delta r}\frac{\partial\phi}{\partial\eta} = 0 \quad ; \qquad (6.2.3)$$

for any variable ϕ. Also, the angular velocity u (and, therefore, the convective flux of ϕ) is zero at both these boundaries. At the south boundary (an infinitesimal arc),

$$\frac{1}{\Delta r}\frac{\partial\phi}{\partial\eta} = 0 \quad . \qquad (6.2.4)$$

The manner in which these constraints were incorporated into the finite-difference solution scheme was described in section (4.5.1).

At the wall of the duct, the velocities and the kinetic energy of turbulence are zero. The "wall-function" approach outlined in section (4.5.2) was employed to deal with the steep property variations in the region. The assumptions of a linear length-scale variation and the proportionality of the wall shear to the turbulent energy were also introduced in the manner described in (4.5.2).

The assumptions made in the derivation of the Reynolds-stress expressions (equations (3.7.4) to (3.7.8)) are not valid in the region close to a wall. In the absence of any reliable method of calculating these terms in the vicinity of a wall, the practice was adopted here of simply neglecting these terms altogether for the near-wall control cells for the u-equation, and introducing the effect of the wall through the logarithmic wall function.

5.2.5 Grid and accuracy

Computations were performed with an initial axial forward step length of 0.01 D_H, which was subsequently expanded by a factor of 1.1 until a maximum value 0.25 D_H was reached. Fully-developed conditions were defined to have been attained when the velocities and turbulent quantities were consistant to within one per cent over an axial separation of ten equivalent diameters.

In the lateral directions, a non-uniform mesh comprising 20x20 nodes was employed. The numerical accuracy of the solutions obtained were checked by comparison with the results procured with a 30x30 grid. The effect of grid size on the axial-velocity profile is depicted in figure (6.2.2). The upper figure represents the velocity distribution (normalized by the bulk velocity) along the mid-wall bisector, while the lower figure indicates the velocity profile along the corner bisector of the duct. It is seen that the use of a 30x30 grid yields values that are within one per cent of those obtained with the 20x20 grid. Consequently, for reasons of economy, the latter grid distribution was adopted in the present computations. It is worth noting, however, that the magnitudes of the cross-stream velocities proved to be more sensitive to grid size than either the axial velocities or the turbulence quantities; maximum variations of about eight per cent were observed in the former when the finer grid was employed.

In the case of the 20x20 grid, 2-3 iterations per step were required in the developing region of the flow in order to secure convergence of the results. Solution of the pressure-correction equation was relatively slow: 15-25 double sweeps of the TDMA were found to be necessary for satisfactory convergence, whereas just one double sweep sufficed for the other equations.

6.3 RESULTS AND DISCUSSION

6.3.1 Secondary velocities

Figure (6.3.1) is a qualitative representative of the predicted secondary flow pattern in the duct cross-section.

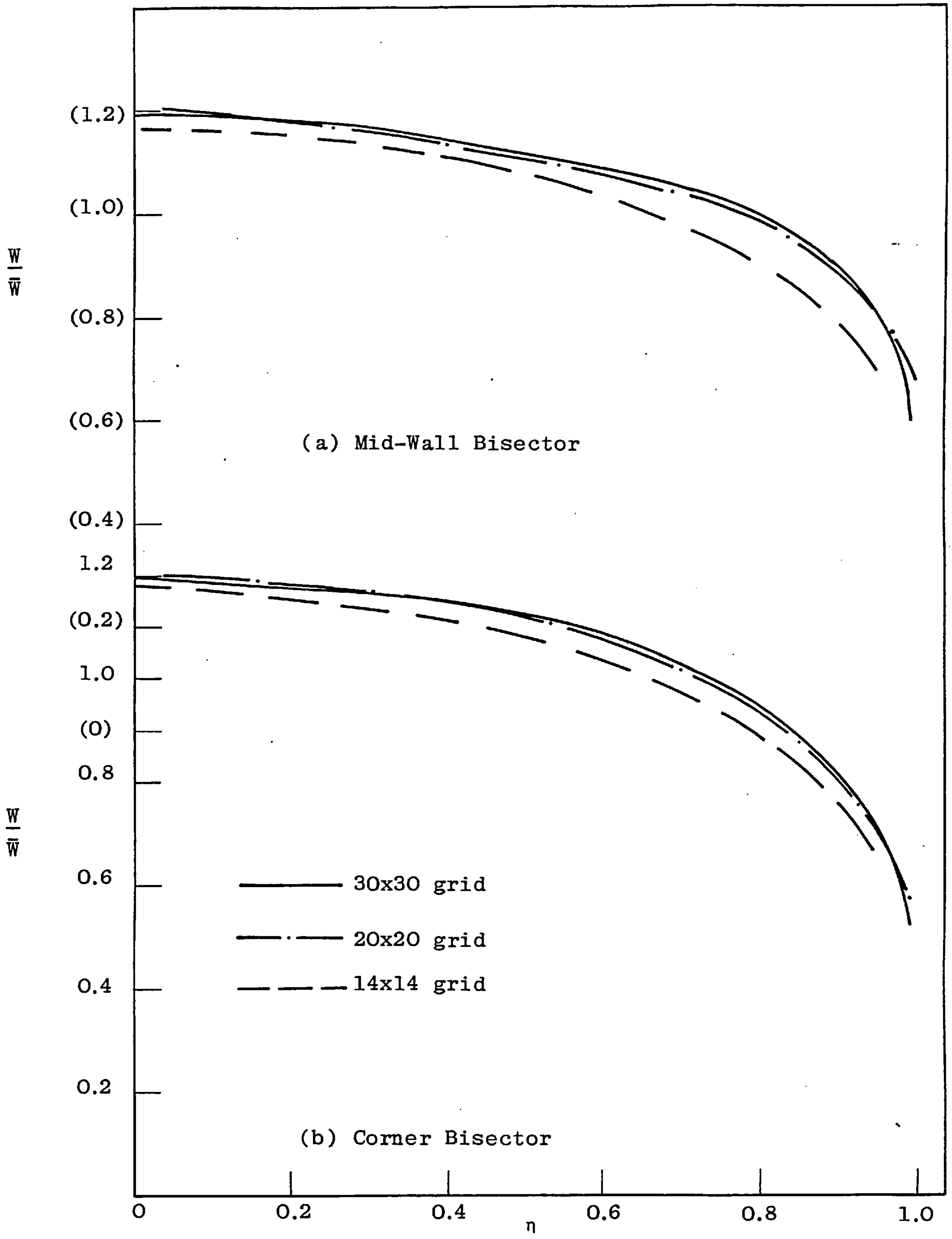

FIGURE 6.2.2: GRID-INDEPENDENCE TESTS FOR AXIAL VELOCITY IN EQUILATERAL-TRIANGULAR DUCT

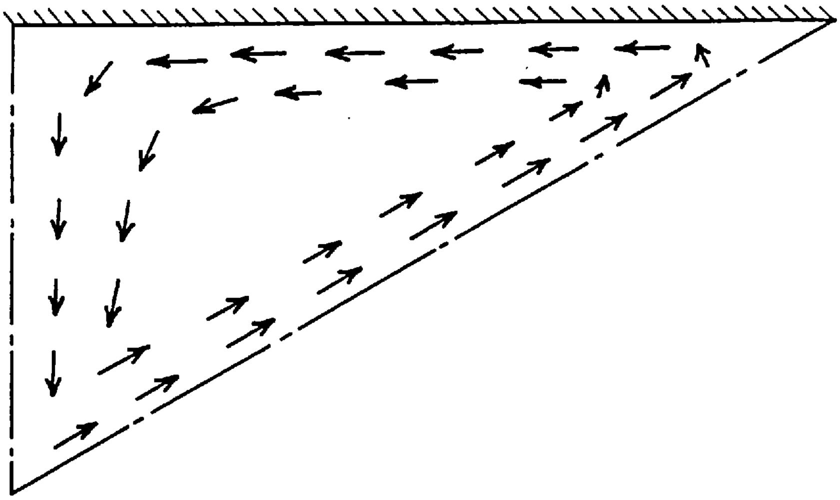

FIGURE 6.3.1: PREDICTED SECONDARY FLOW PATTERN

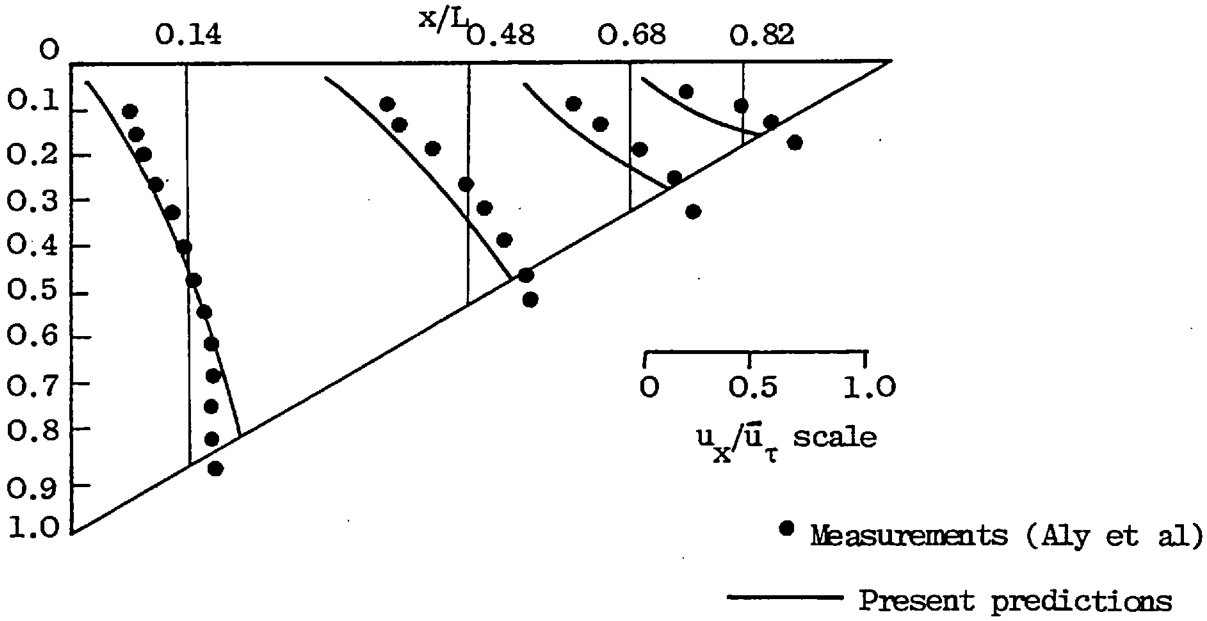

FIGURE 6.3.2: COMPARISON OF PREDICTED AND MEASURED X-DIRECTION VELOCITY, Re = 53000

In accordance with the observations of Nikaradse (1930) and Aly et al. (1978), it consists of a single cell of anti-clockwise rotation. High-momentum fluid from the centre of the duct is transported to the corner via a path adjacent to the corner bisector and returns along the wall.

The maximum secondary velocities occur in the return flow along the wall. This is indicated in figure (6.3.2), in which the resultant velocity u_x parallel to the duct wall (non-dimensionalized with respect to the average friction velocity $\overline{u}_\tau$) is plotted along different vertical planes. The circular points represent the measurements of Aly et al. which were made with both X-probes and a rotatable miniature 45^o slanting probe. The full curves are the present author's predictions, which were obtained by interpolation amongst the cross-stream velocities computed and stored at the finite-difference grid locations. x/L represents the non-dimensional distance along the wall, measured from the mid-wall bisector, and y/H is the relative distance normal to the wall.

It is seen that the predicted magnitudes of u_x/u_τ are in good agreement with the experimental data except in the region close to the corner. The maximum value of u_x was calculated to be about 2.2% of the bulk velocity in the duct; this was in contrast with the 1.5% determined by Aly et al. At least part of this discrepancy is attributable to the interpolation errors caused by the steep velocity variations in the corner region. However, the influence of the wall on the experimental probes would almost certainly have produced a deterioration in the measurement accuracy, and thus the actual magnitudes of the secondary velocities close to the wall - and especially in the corner of the duct - are subject to much uncertainty.

6.3.2 Local wall shear stress

The calculated distribution of the wall shear stress around the periphery of the duct is shown in figure (6.3.3), together with the measurements of Aly, Trapp and Gerrard (1978) corresponding to two different Reynolds numbers. The ordinate represents the local value of the shear stress at any position a distance x from the centre of the duct wall, normalized by the averaged value along the length of the wall.

Also shown in the figure is the curve obtained when no allowance is made for the influence of secondary flow, i.e. when an isotropic turbulent viscosity is employed to model the turbulent-stress terms in the cross-stream momentum equations. In this case u and v tend to zero in the fully-developed state, and the shear stress decreases smoothly from its peak value at the mid-wall towards the corner of the duct. In the latter region the shear stress is underestimated by as much as twenty per cent. There is very little dependence of the measured shear-stress distribution on the Reynolds number, in the range investigated by Aly et al. Clearly, the effect of secondary flow is to equalize

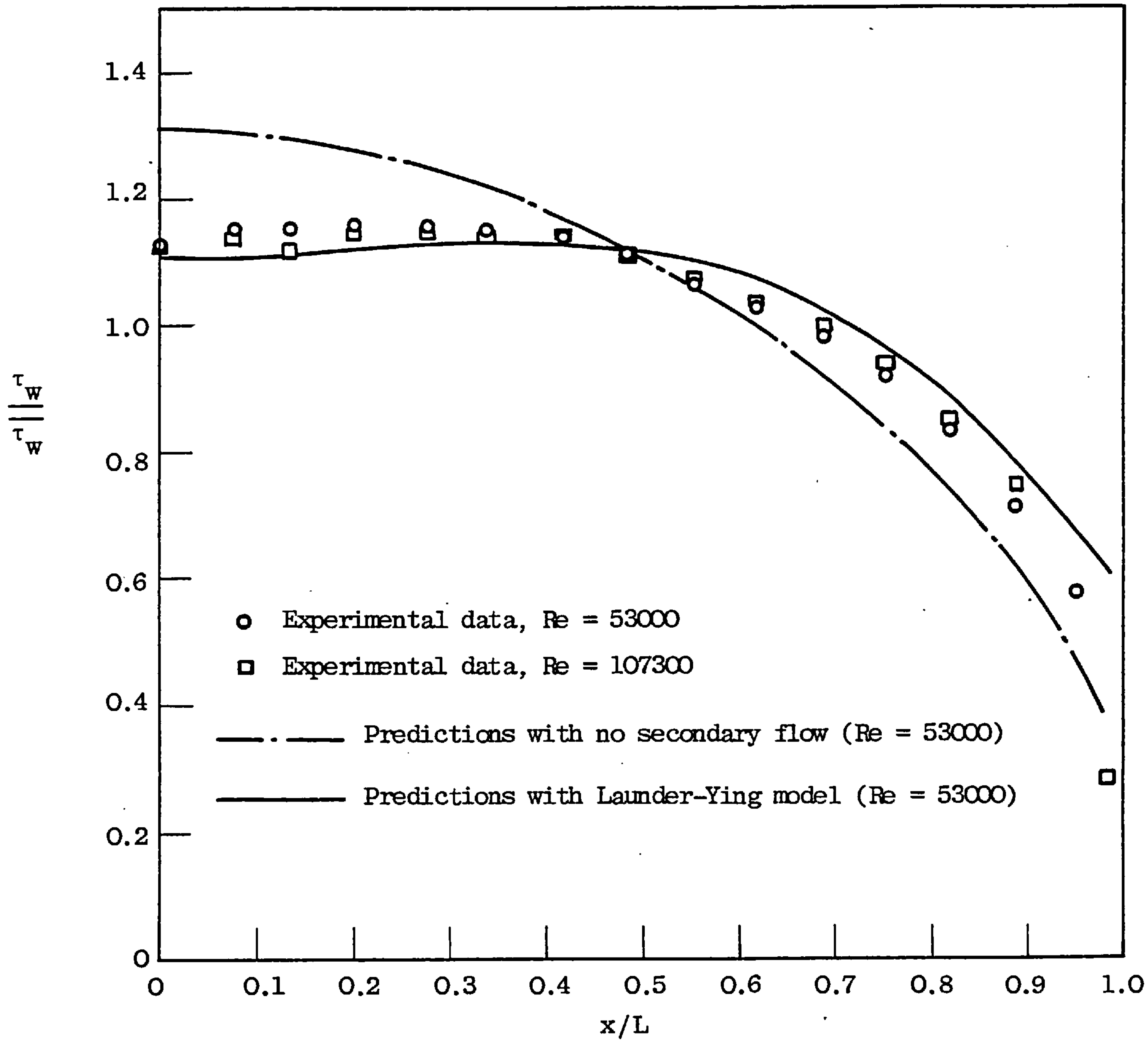

FIGURE 6.3.3: LOCAL WALL SHEAR-STRESS DISTRIBUTION, EQUILATERAL-TRIANGULAR DUCT

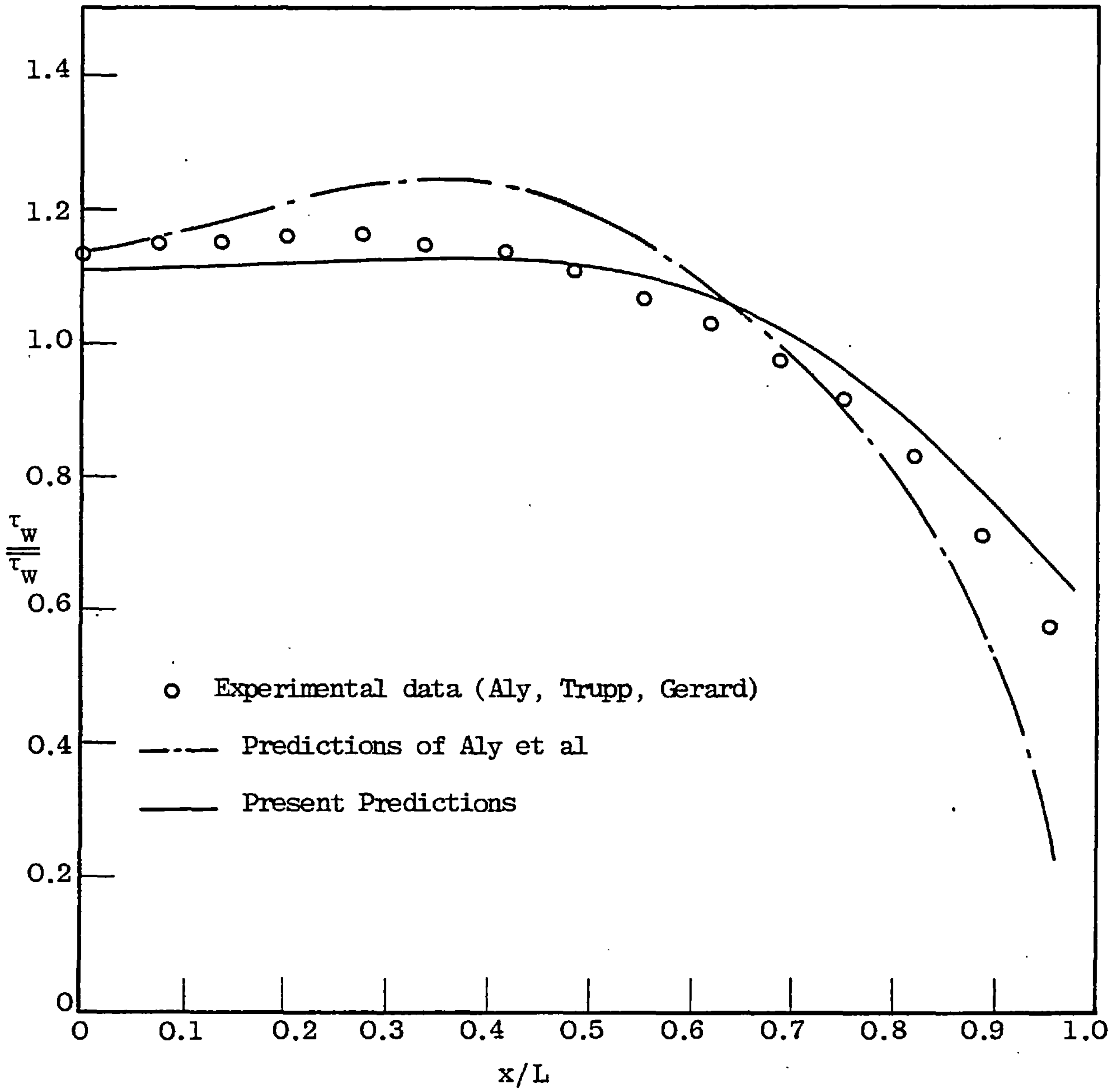

FIGURE 6.3.4: LOCAL WALL SHEAR-STRESS DISTRIBUTION: COMPARISON OF PREDICTIONS (Re = 53000)

to an appreciable degree the shear stress around the duct periphery.

Figure (6.3.4) compares the predicted shear-stress distribution with that computed by Aly et al. by way of an elliptic finite-difference scheme and a prescribed turbulence length-scale. The latter approach predicts a profile in which the peak value of the shear is displaced towards the corner, but not quite as far as for the square duct case, for which investigators have reported a maximum at $x/L \approx 0.5$ (see Launder and Ying (1973), Ramachandra and Spalding (1976)). However, the predictions obtained with the present method involving the $k\sim\varepsilon$ turbulence model indicate a more flattened distribution in which the peak is barely perceptible. This is more in accord with the measured distribution of Aly et al, as is evident from the figure. The shear stress is over-estimated near the corner of the duct; this may be due to increased anisotropy of the turbulence dissipation in this region, which invalidates some of the assumptions inherent in the model. However, agreement with the experimental data is very satisfactory over much of the duct periphery. Moreover, the use of the $k\sim\varepsilon$ model has obviated the need to guess a suitable length-scale, of the kind necessarily postulated by both Launder and Ying (1973) and Aly et al.

6.3.3 Mean axial velocities

Mean axial velocities in the equilateral-triangular duct were measured by Aly et al. with the aid of Pitot tubes,

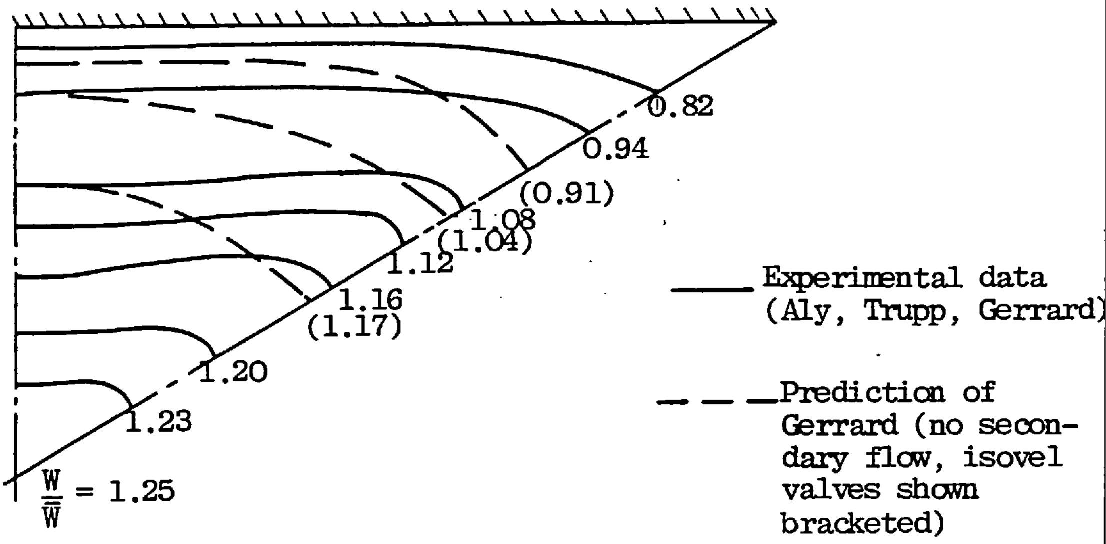

FIGURE 6.3.5: AXIAL-VELOCITY CONTOURS IN EQUILATERAL TRIANGULAR DUCT (Re = 53000)

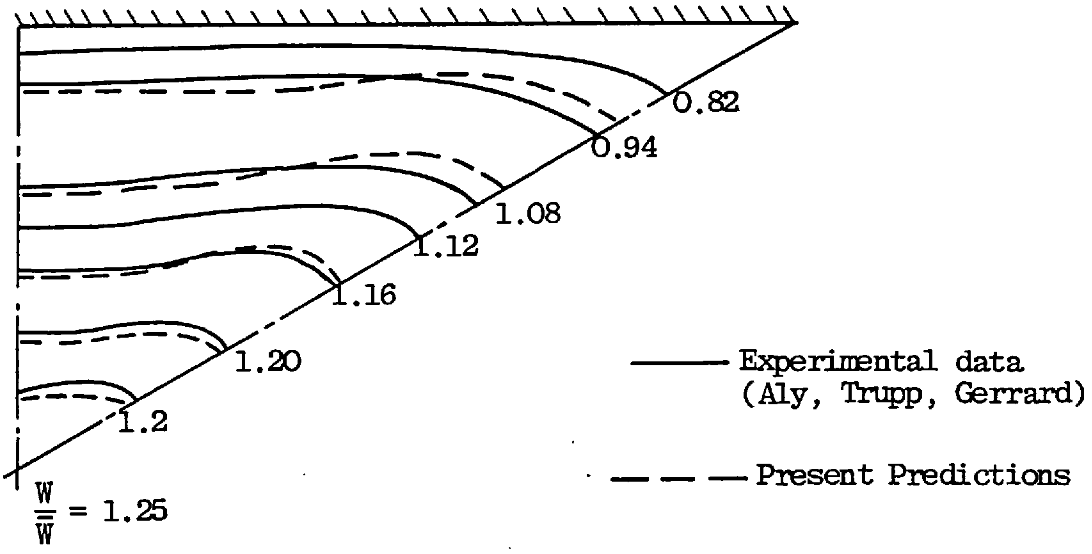

FIGURE 6.3.6: AXIAL-VELOCITY CONTOURS IN EQUILATERAL TRIANGULAR DUCT (Re = 53000)

and depicted in the form of plots of lines of constant velocity (isovels). One such plot has been reproduced in figure (6.3.5), in which the contour levels have been normalized by the bulk velocity. It was estimated that the measured velocities were accurate to within 1%, while the estimated accuracy of the bulk velocity (obtained by numerical integration of the point velocities over the duct cross-section) was ±2%. Also shown in figure (6.3.5) is the pattern predicted by Gerrard (1974) with a finite-element technique that neglected the presence of secondary flow. The distortion of the isovels produced by the secondary currents is appreciable. The latter tend to diminish the axial velocity in the central regions of the duct and to increase the velocity in the corner.

The isovel plots obtained with the present method have been superimposed on the experimental plot in figure (6.3.6). The influence of the secondary flow on the axial velocities is well predicted: the computed and measured distributions are nearly identical, except for small discrepancies near the corner-bisector and the duct centreline.

Figure (6.3.7) represents a similar plot for a higher Reynolds-number flow. There is a minor dependence of the distribution on the Reynolds number: the normalized centreline velocity is decreased as the value of Re increases. Once again, the agreement between the predicted contours and the measurements is good.

6.3.4 Turbulent kinetic energy

Aly et al. have presented measurements of the mean turbulent

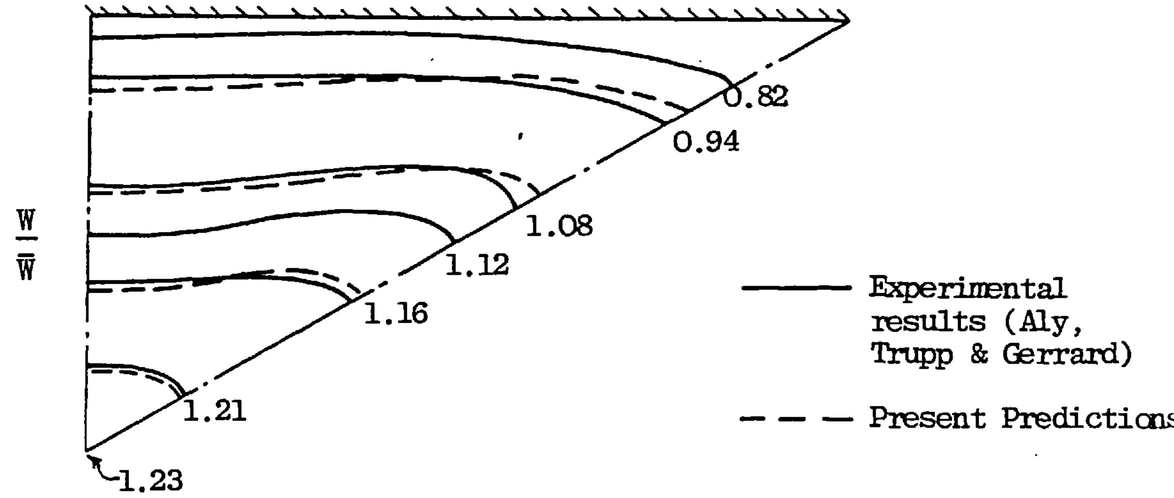

FIGURE 6.3.7: AXIAL-VELOCITY CONTOURS, Re = 1.07×10^5

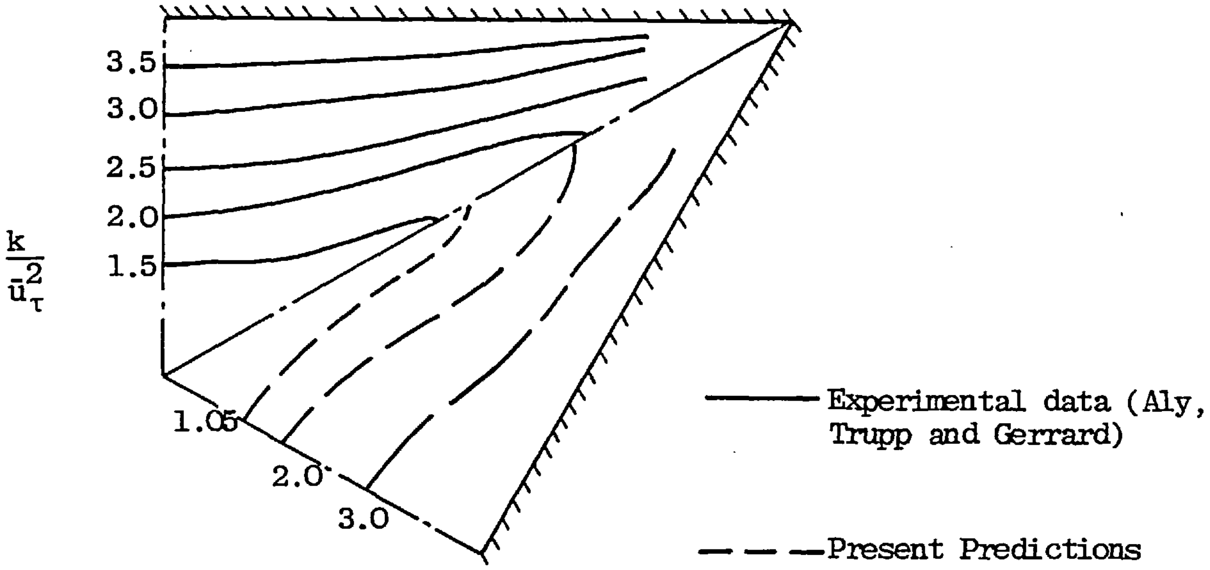

FIGURE 6.3.8: TURBULENCE KINETIC ENERGY CONTOURS, Re = 53000

kinetic energy in a triangular duct in the form of contour plots of $k/\bar{u}_\tau^2$, where $\bar{u}_\tau$ is the average friction velocity. Such a plot is shown in figure (6.3.8) for a Reynolds-number of 53000. Shown alongside is the k-distribution predicted via the present method. In accordance with observations in square ducts (Launder and Ying (1973)), the kinetic energy profile is more strongly affected by the secondary flow than either the axial velocity or the wall shear stress.

The calculated distribution of turbulent kinetic energy along the mid-wall bisector of the duct (the west boundary of the calculation domain, see figure 6.2.1(b)) is compared with the experimental points of Aly et al. in figure (6.3.9). As usual, the k values are greatest near the wall (y=0) where turbulence is generated, and lowest near the duct centreline. Agreement between prediction and experiment is good.

6.3.5 Normal stresses

The experimental values of turbulent kinetic energy described above were derived from measurements of the individual turbulence intensities $\overline{u'^2}$, $\overline{v'^2}$ and $\overline{w'^2}$ by means of hot-wire probes. Distributions of $\overline{u'^2}$ and $\overline{v'^2}$ along the mid-wall bisector of the duct are depicted in figures (6.3.11) and (6.3.12) respectively. The full curves shown in these figures represent the distributions calculated with the present method based on the Launder-Ying formulation. Aly et al. have not presented their own predictions of these

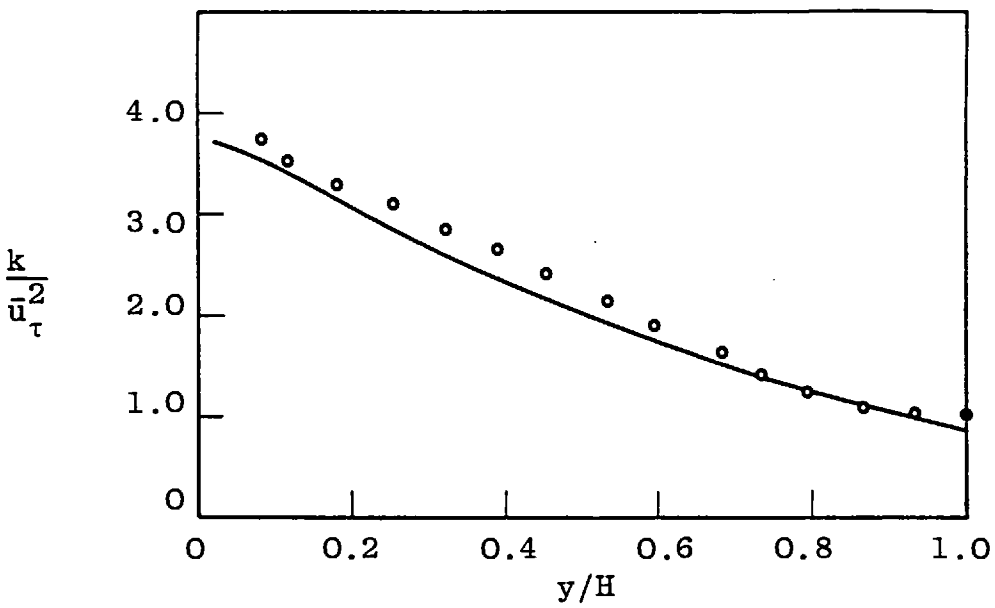

FIGURE 6.3.9: DISTRIBUTION OF TURBULENT ENERGY ALONG MID-WALL BISECTOR: COMPARISON WITH EXPERIMENTAL DATA.

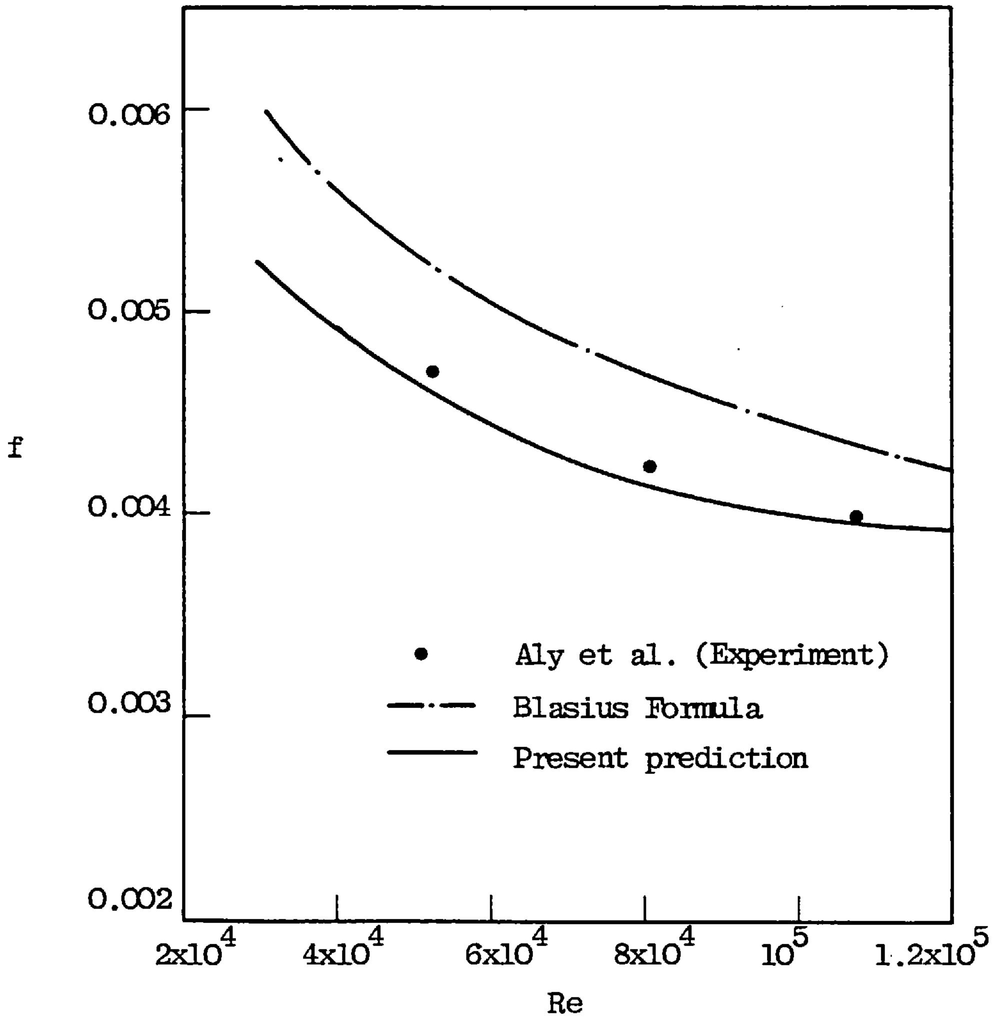

FIGURE 6.3.10: FRICTION FACTOR ∿ REYNOLDS NUMBER DEPENDENCE

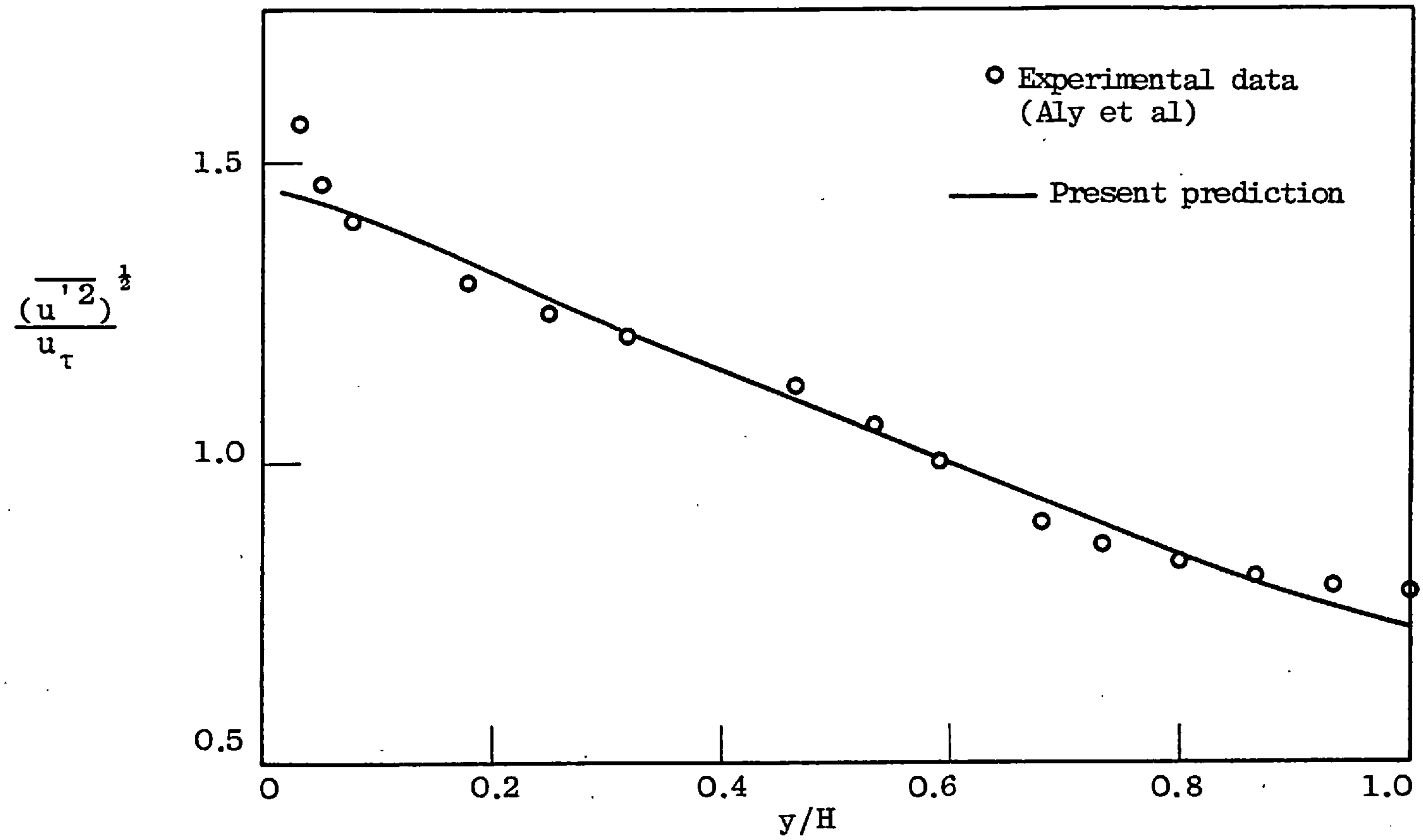

FIGURE 6.3.11: DISTRIBUTION OF $\overline{u'^2}$ ALONG MID-WALL BISECTOR

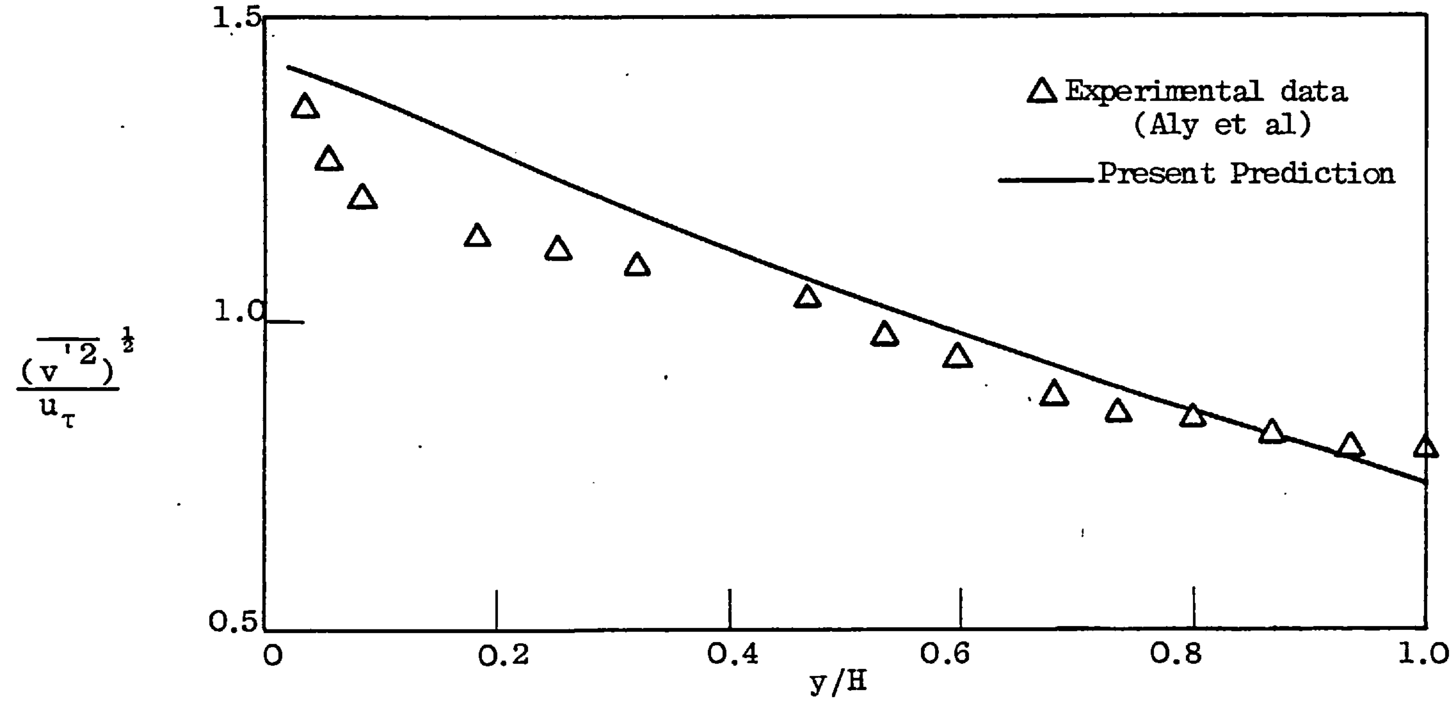

FIGURE 6.3.12: DISTRIBUTION OF $\overline{v'^2}$ ALONG MID-WALL BISECTOR

normal-stress profiles. There is reasonable agreement between the present calculations and the experimental data, especially for the velocity fluctuations parallel to the wall ($\overline{u'^2}$). The latter are seen to exceed those normal to the wall, although the differences in magnitude diminish and eventually disappear as the duct centre is reached.

6.3.6 Friction-factors

The dependence of the duct-friction-factor on the Reynolds-number was investigated, and the characteristic curve obtained is shown in figure (6.3.10), along with the values determined experimentally by Aly et al. for the three Reynolds numbers considered. The predicted friction-factors deviate by a maximum of about 3% from the experimental values; this, however, is comparable to the estimated accuracy of the measurements. In contrast, the values computed with the conventional Blasius correlation (based on the equivalent hydraulic diameter) lie about 8% above the experimental points.

6.4 CLOSURE

The present numerical procedure, incorporating the two-equation $k\sim\varepsilon$ model of turbulence and the Launder-Ying formulation for the Reynolds stresses, has been successfully applied to the prediction of fully-developed flow in an equilateral-triangular duct. The secondary flow pattern has been correctly predicted, although the magnitude of the secondary velocities close to the wall are slightly overestimated in comparison with the experimental data of Aly, Trapp and Gerrard (1978). The computed distributions of axial velocity, wall shear stress, turbulence energy etc. are in good agreement with the measurements of the above investigators.

The use of the $k\sim\varepsilon$ model has rendered unnecessary the prescription of a satisfactory turbulence length-scale, of the kind necessarily made by Aly et al. in the theoretical part of their investigation. Also, the generality of the model was preserved by making no modifications to the values of any of the empirical constants appearing in the turbulence equations. Moreover, the present calculations of axial velocity and wall shear variations represent a significant improvement on the latter's results.

CHAPTER 7

PREDICTION OF TURBULENT FLOW IN ROD BUNDLES

7.1 INTRODUCTION

Predictions have been made of the turbulent flow and heat-transfer phenomena in bare rod arrays of varying aspect ratio. The physical flow situation considered was that represented by the symmetry element (shown cross-hatched) in figure (1.1.2) of chapter 1: this region was mathematically defined by the (η, ξ, z) coordinate system and a computational grid imposed on it in the manner depicted in figure (5.2.10). The turbulence was treated by utilization of the $k \sim \varepsilon$ model in conjunction with the formulation of Launder and Ying (1973) for the cross-stream components of the Reynolds-stress tensor, as discussed in chapter 3.

Calculations have been performed for both developing and fully-developed flow; however, the emphasis throughout has been on the prediction of situations investigated in detail by experimental researchers and on the comparison of the present results with previous analyses. A review of these experimental and theoretical approaches to the problem has already been presented in chapter 2 of this thesis.

The rest of this chapter comprises three main sections: information on the computational aspects of the work are given in some detail in section 7.2; the major part of the work, consisting of the results obtained for the flow, turbulence structure and heat-transfer characteristics of rod bundles are presented and discussed in section 7.3. Finally, a brief summary of the achievements of this chapter is contained in section 7.4.

7.2 COMPUTATIONAL DETAILS

7.2.1 Calculation domain

As mentioned above, the domain of interest in the present calculations is that illustrated in figure (5.2.10): the figure represents the $\eta \sim \xi$ cross-sectional plane of the rod bundle, the main flow direction being normal to this plane. Details of the non-orthogonal coordinate system and finite-difference mesh have been given elsewhere (sections 3.2 and 4.2); it is sufficient merely to recall that the family of ξ = constant lines, on extrapolation, through the centre of the rod, while the η = constant curves vary smoothly from circular arcs near the rod surface to straight lines parallel to the outer boundary of the flow domain.

The boundaries of the flow region are mathematically represented as follows: the South boundary is the impermeable rod surface at which all velocities are zero, while the West, East and North boundaries are symmetry planes across which the fluxes of all variables are zero. For an equilateral-triangular array, the angular width of the domain is thirty degrees, and for a square array, forty-five degrees.

7.2.2 Equations solved

The equations solved were the continuity and momentum equations (3.4.13) to (3.4.16), and the equations (3.8.6) and (3.8.7) for the turbulence variables. The algebraic relations (3.7.11) to (3.7.15) were used to calculate the auxiliary variables in the above equations. For the heat transfer predictions, equation (3.5.8) was also solved. The values of the 'turbulence-model' constants given in table 3.9.1 of section 3.9 were employed without modification. Some results were obtained with the Reynolds-stress terms in the cross-stream momentum equations represented via an isotropic turbulent viscosity; in this case, the relevant momentum equations solved were (B.2) to (B.4). The marching-integration technique described in section (4.4) was utilized in the solution of these equations.

7.2.3 Inlet conditions

At the entrance to the duct (z=0), zero cross-stream velocities and a uniform axial-velocity profile were prescribed. In the absence of any information regarding the distribution of the turbulence quantities k and ε at the inlet, initial values were estimated. Fortunately, the fully-developed solutions and much of the developing flow field is not very sensitive to these initial guesses. The following uniform profiles were specified:

$$k = 0.02\, W_{IN}^2 \quad , \tag{7.2.1}$$

$$\ell = 0.07\, D_e \quad . \tag{7.2.2}$$

where W_{IN} is the (constant) axial velocity at the inlet, and D_e the equivalent hydraulic diameter of the flow domain, calculated from either equation (5.3.1) or (5.3.2).

In the heat transfer predictions, a constant temperature distribution was specified at the inlet and the fully-developed hydrodynamic field introduced as input to the temperature equation, which was solved separately.

7.2.4 Boundary conditions

At the radial (east and west) boundaries of the computational domain, the normal fluxes of all variables vanish.

Hence,

$$\frac{1}{r\Delta\theta}\frac{\partial\phi}{\partial\xi} - \frac{G}{\Delta r}\frac{\partial\phi}{\partial\eta} = 0 \quad , \qquad (7.2.3)$$

Moreover, the circumferential velocity u (and, therefore, the convection of ϕ) is zero at both these boundaries.

Similarly, the flux of ϕ normal to the north boundary (the maximum-velocity line) is also zero:

$$\frac{(1+G^2)}{\Delta r}\frac{\partial\phi}{\partial\eta} - \frac{G}{r\Delta\theta}\frac{\partial\phi}{\partial\xi} = 0 \quad . \qquad (7.2.4)$$

The manner in which these constraints were represented in the finite-difference solution scheme was described in section 4.5.1

At the wall, the velocities and turbulent kinetic energy are zero. The "wall-function" approach, presented in section

4.5.2, was adopted to deal with the steep property variations in this region. The assumptions of a linear length-scale distribution and the proportionality of the wall shear stress to the turbulent energy were used in the manner discussed in 4.5.2.

The assumptions involved in the derivation of the Reynolds-stress formulations (equations 3.7.11 - 3.7.15) are, strictly, invalid in the vicinity of a wall. In the absence of any reliable method of calculating these terms close to the wall, the practice was adopted (as in the triangular-duct predictions) of simply neglecting these terms altogether in the circumferential-velocity equation, and of introducing the influence of the wall via the logarithmic wall function .

7.2.5 Grid and accuracy

Computations were performed with an initial forward step length of 0.01 D_e, which was gradually expanded by a factor of ten per cent to a constant value of 0.50 D_e. Fully-developed hydrodynamic conditions were assumed to have been attained where the value of each independent flow variable was constant to within one per cent over an axial separation of ten hydraulic diameters. For the case of a uniform wall heat flux, fully-developed heat transfer was defined to occur with the invariance of (T_w - T_m) with longitudinal distance.

In the cross-stream plane of the duct, a non-uniform mesh comprising 21x21 nodes was employed. The grid-independence of the resulting solutions was confirmed by experimentation with finer meshes. Typical tests are illustrated in figures

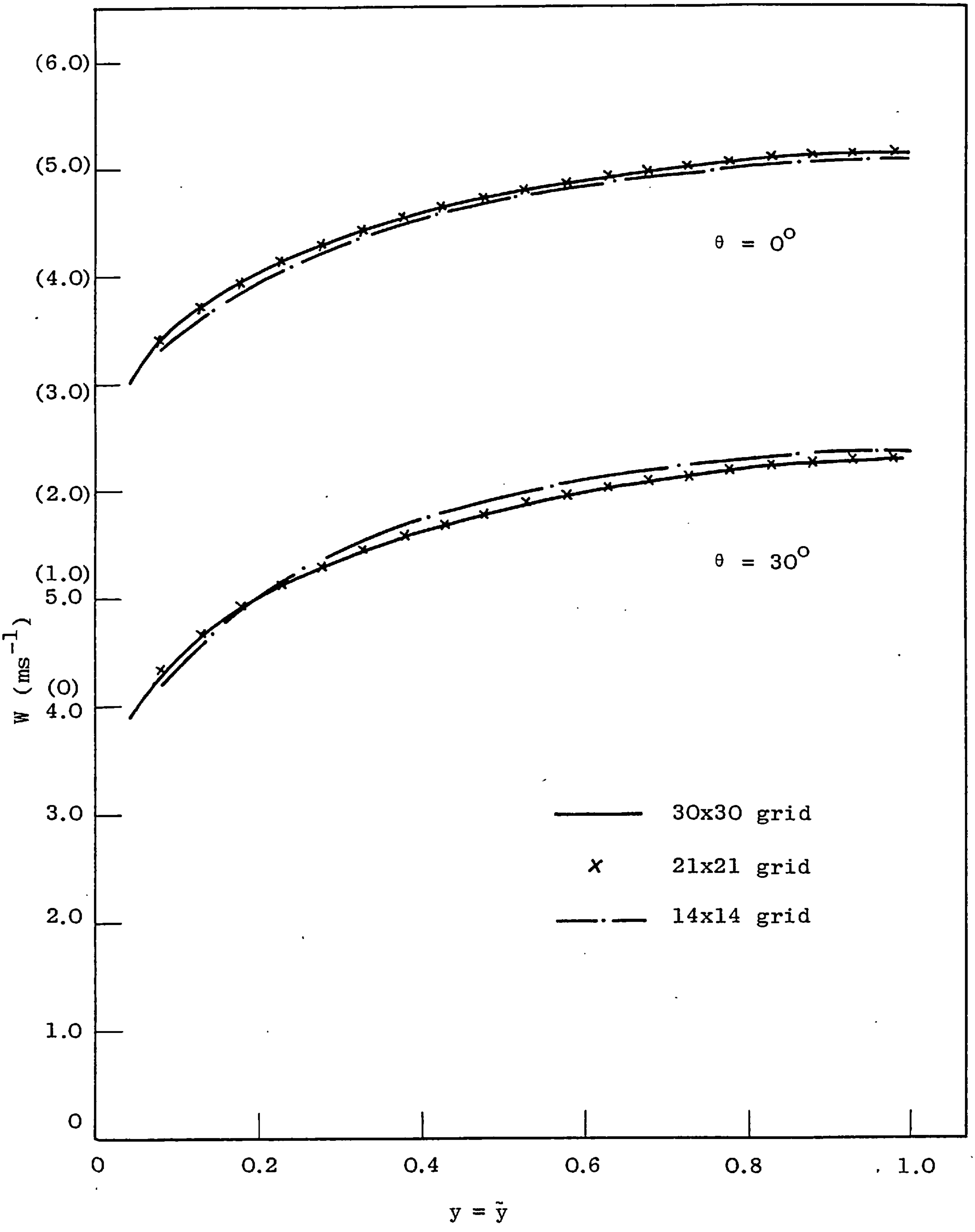

FIGURE 7.2.1: GRID-INDEPENDENCE TESTS FOR VELOCITY DISTRIBUTION (P/D = 1.123, Re = 27000).

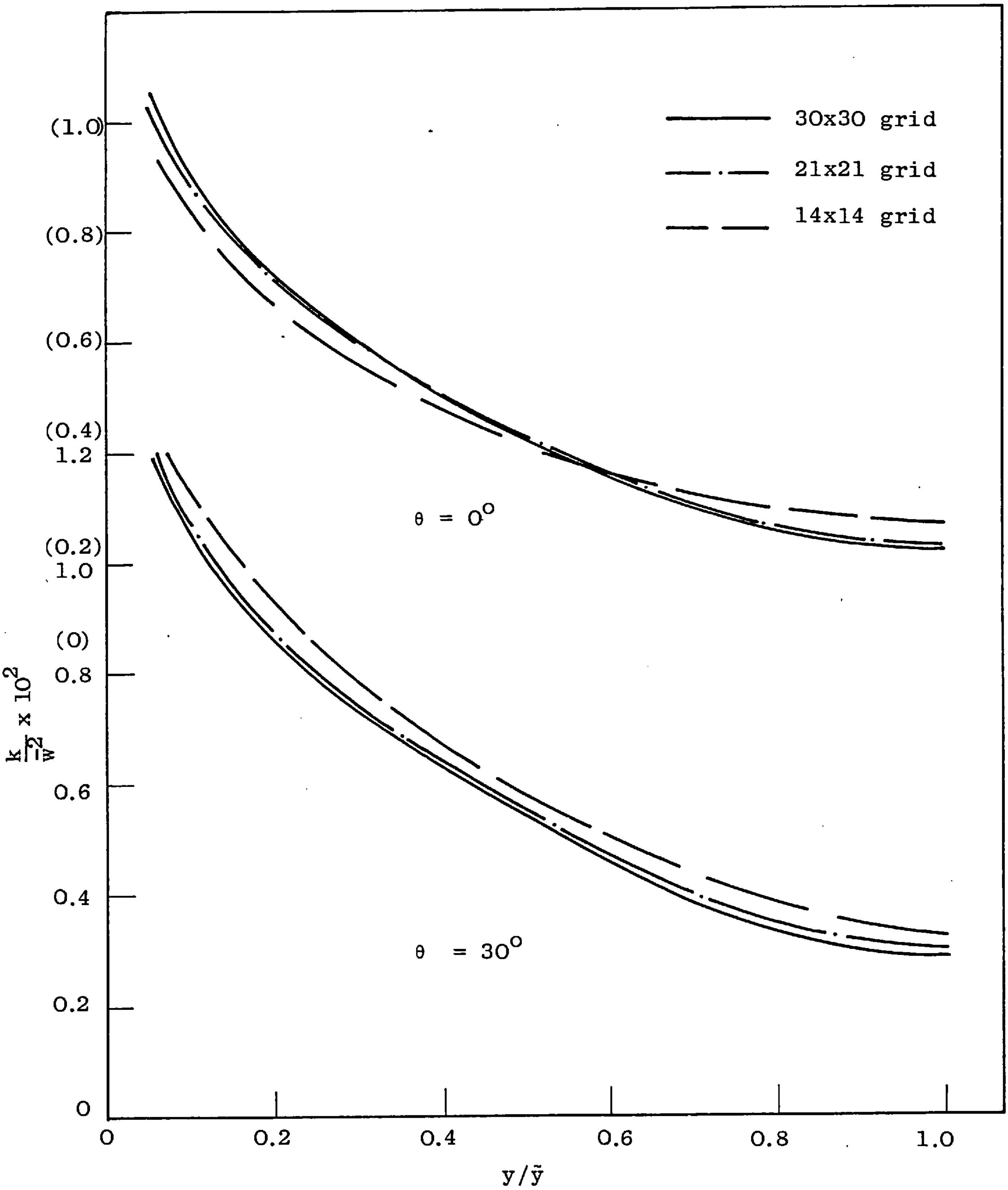

FIGURE 7.2.2: GRID-INDEPENDENCE TESTS FOR KINETIC ENERGY DISTRIBUTION (P/D = 1.123, Re = 27000).

(7.2.1) and (7.2.2). The former figure shows the distributions of the fully-developed axial velocity normal to the rod surface, for both the west (θ = 0 deg.) and east (θ = 30 deg.) boundaries of an equilateral-triangular array with aspect ratio (P/D) 1.123 and a Reynods number of 27 000 . These flow conditions correspond to the experimental flow situation of Carajilescov and Todreas (1976). The abscissa represents the non-dimensional distance from the wall, $y/\tilde{y}$, where $\tilde{y}$ is the radial distance between the wall and the maximum-velocity surface. It is seen that the values of w predicted with the aid of the 21x21 mesh are indistinguishable from the results obtained with the 30x30 mesh which contains more than twice as many nodes as the former; while, from figure (7.2.2), the predicted values of turbulent kinetic energy agree to within one per cent. It is worth noting that the magnitudes of the computed secondary velocities were more sensitive to grid dimensions: differences of up to five per cent between the velocities predicted by both grids were observed.

In the developing regime, 3-4 iterations per axial step were required to obtain well-converged results; however, the fully-developed solutions were independent of the number of iterations employed. 15-25 sweeps of the Tri-Diagonal Matrix algorithm (TDMA) were necessary for the solution of the pressure-correction equation before satisfactory convergence was achieved, whereas just one sweep sufficed for the other equations.

Computing costs were moderate: a typical calculation of the full hydrodynamic field with a 21x21 grid (no iterations) required 4 mins. of computer time and 30K storage on a CDC 6600 machine.

7.3 RESULTS AND DISCUSSION

7.3.1 Developing region

Although no experimental information on the developing flow regime in bare rod bundles has been reported to date, some representative results obtained with the aid of the present numerical technique have been included for interest. Figure (7.3.1) depicts the variation of mean pressure with longitudinal distance in three different rod arrays at identical Reynolds numbers. The ordinate represents the pressure at a given location (with reference to P_{IN}, the pressure at the entrance), divided by the 'dynamic pressure' ($\frac{1}{2}\rho\bar{w}^2$); while the abscissa gives the axial location downstream in terms of the equivalent hydraulic diameter. It is seen that, as in the laminar flow, the greater the relative "openness" of the geometry to the flow, the smaller is the pressure-drop required to overcome friction in the duct. However, the development length is not as strong a function of the P/D ratio as it is in the laminar case. In all three arrays represented in figure (7.3.1), the flow attained in fully-developed state after 90-120 equivalent diameters.

The manner in which the axial-velocity profile develops in the entrance region is illustrated by figure (7.3.2). The

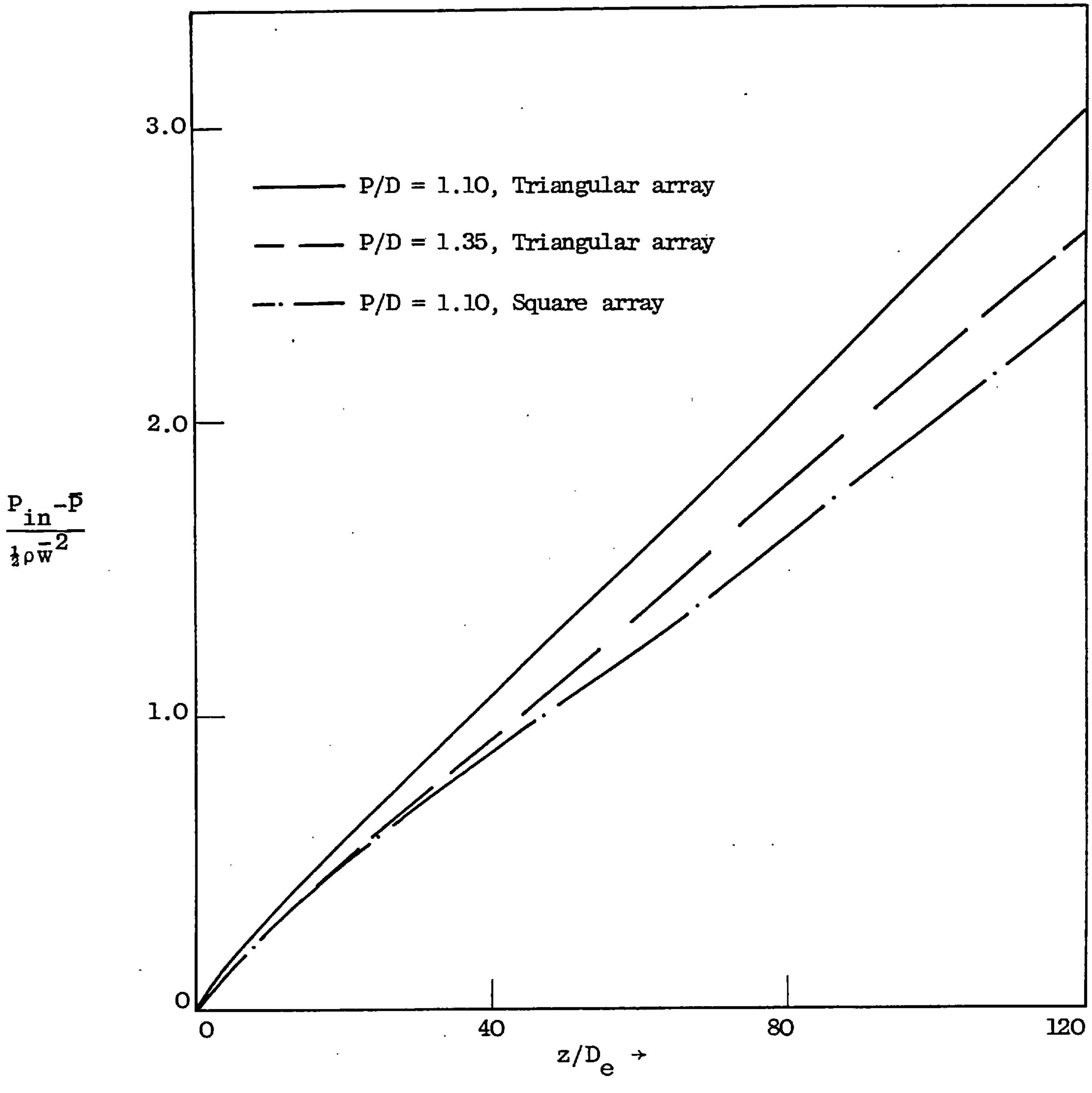

FIGURE 7.3.1: PRESSURE-DEVELOPMENT IN ROD-BUNDLE FLOW, Re = 60000

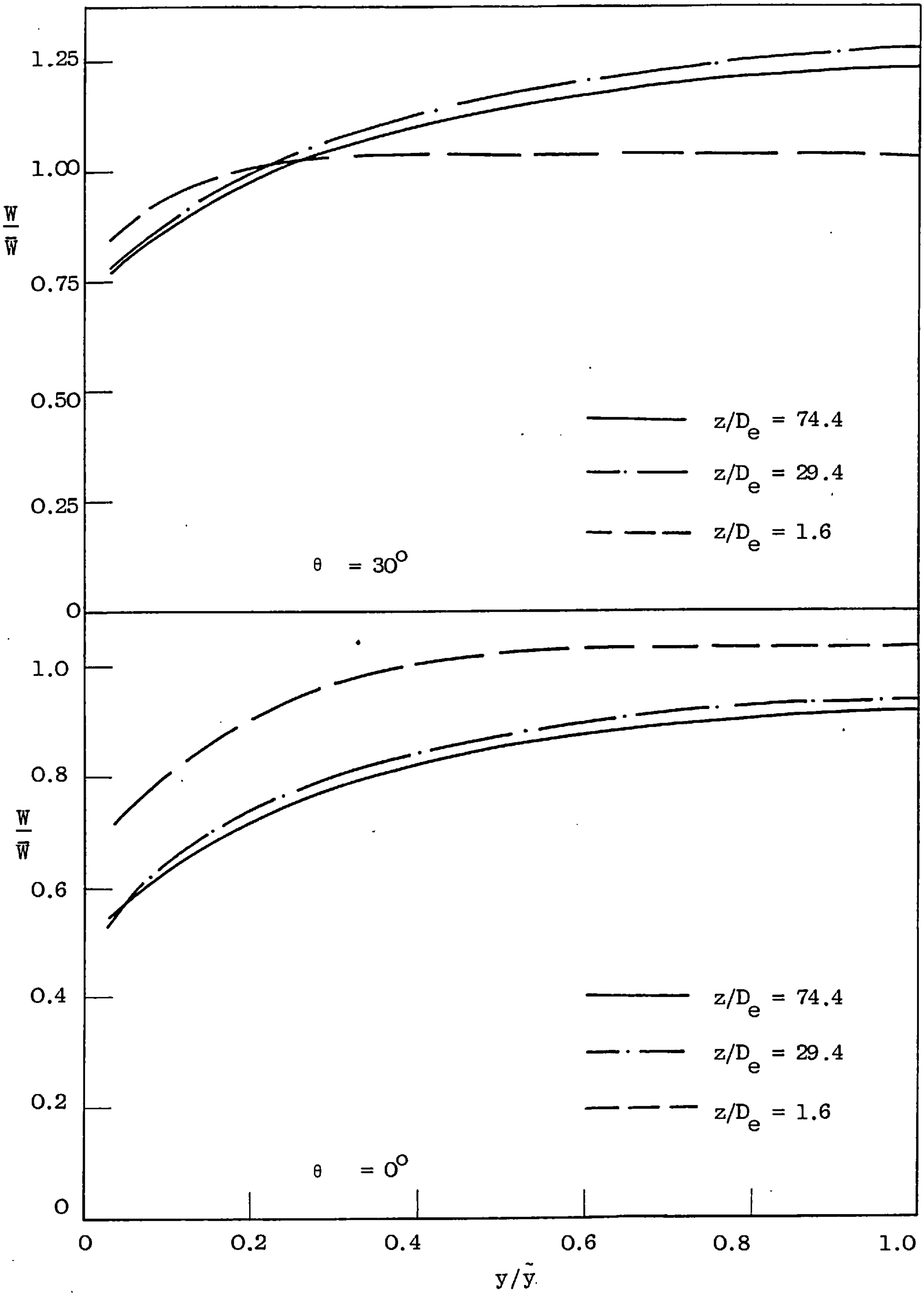

FIGURE 7.3.2: DEVELOPING AXIAL-VELOCITY PROFILES, P/D = 1.10, Re = 28000.

geometry and Reynolds number represented are those corresponding to the investigation of Carajilescov and Todreas (1976). Distributions along the radial boundaries of the domain at various axial stations are indicated in the figure. Momentum is transferred from the gap region ($\theta = 0^o$) around the periphery of the rod towards the east boundary ($\theta = 30^o$) as the flow develops. However, some momentum is also convected in the opposite direction by the build-up of secondary flow in the cross-stream plane of the channel. The fully-developed axial and secondary flow field, together with the turbulence and heat-transfer characteristic of the flow, are described in the following sections.

7.3.2 Mean axial-velocity distributions

Figures (7.3.3(a)), (7.3.3(b)), (7.3.4(a)) and (7.3.4(b)) show the axial-velocity profiles along lines normal to the rod walls for different angular locations, corresponding to the triangular-array geometries investigated experimentally by Eifler and Nijsing (1967). The ordinate in each frame represents the local axial velocity normalized with respect to the mean velocity in the duct, and the abscissa represents the non-dimensional radial position $y/\tilde{y}$, where $\tilde{y}$ is the radial distance from the wall to the maximum-velocity surface at the angular location θ. The experimental values were determined by means of a Pitot tube. Uncertainties in the position of the latter and its influence on the flow close to the wall constituted the chief sources of error in the measurements. Eifler and Nijsing estimated a maximum

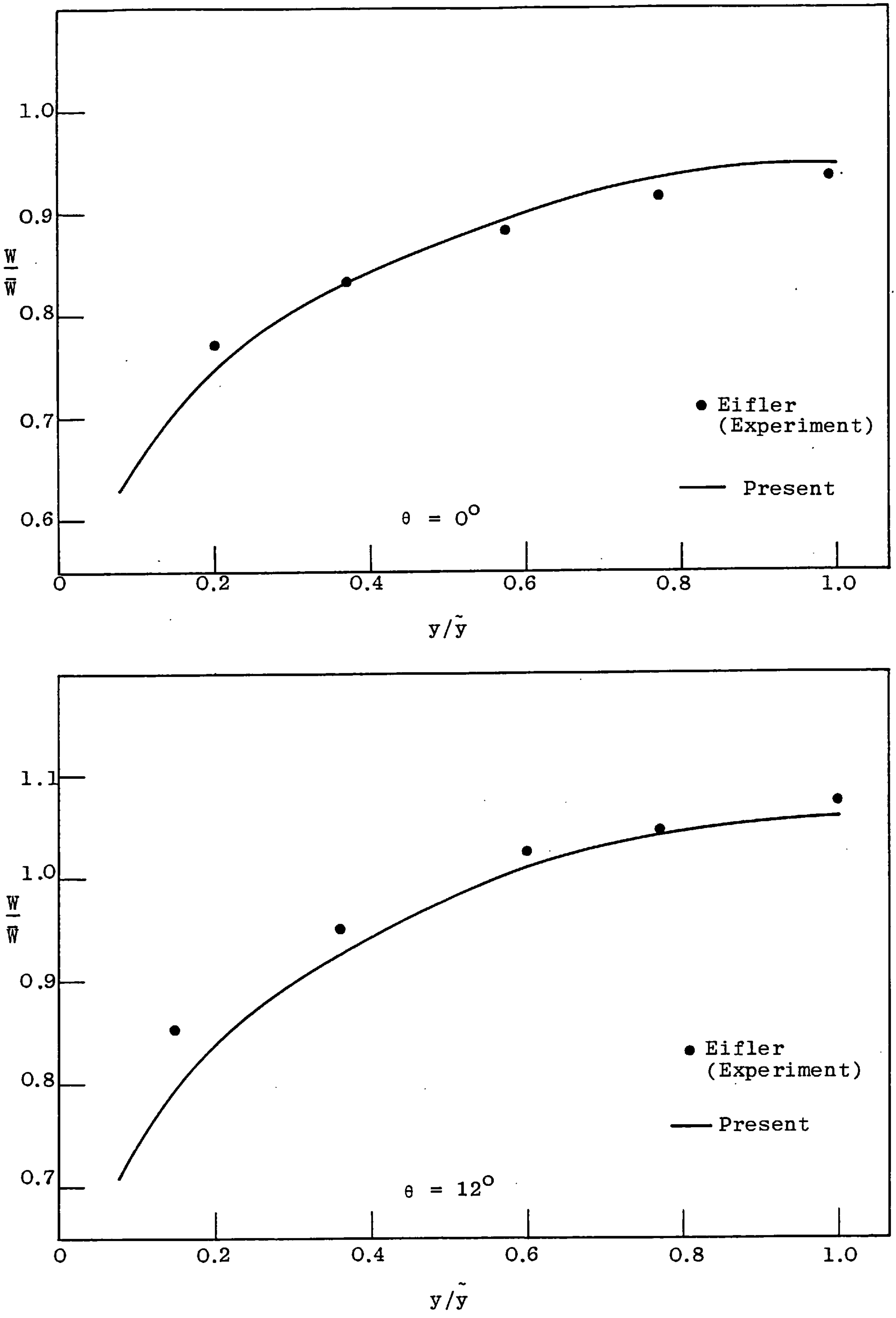

FIGURE 7.3.3(a): AXIAL-VELOCITY DISTRIBUTIONS; P/D = 1.10, Re = 28000.

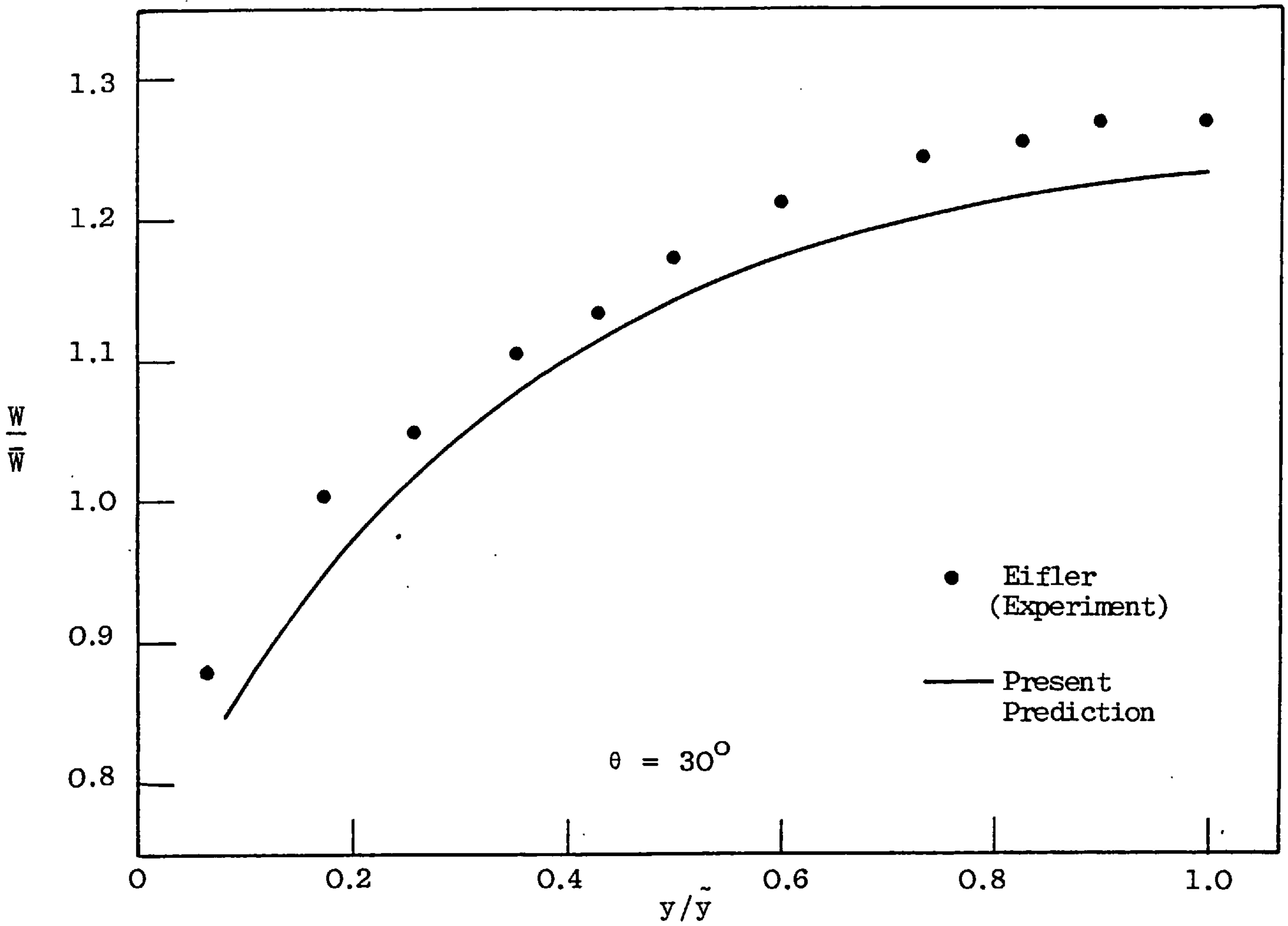

FIGURE 7.3.3(b): AXIAL-VELOCITY DISTRIBUTION, P/D = 1.10.

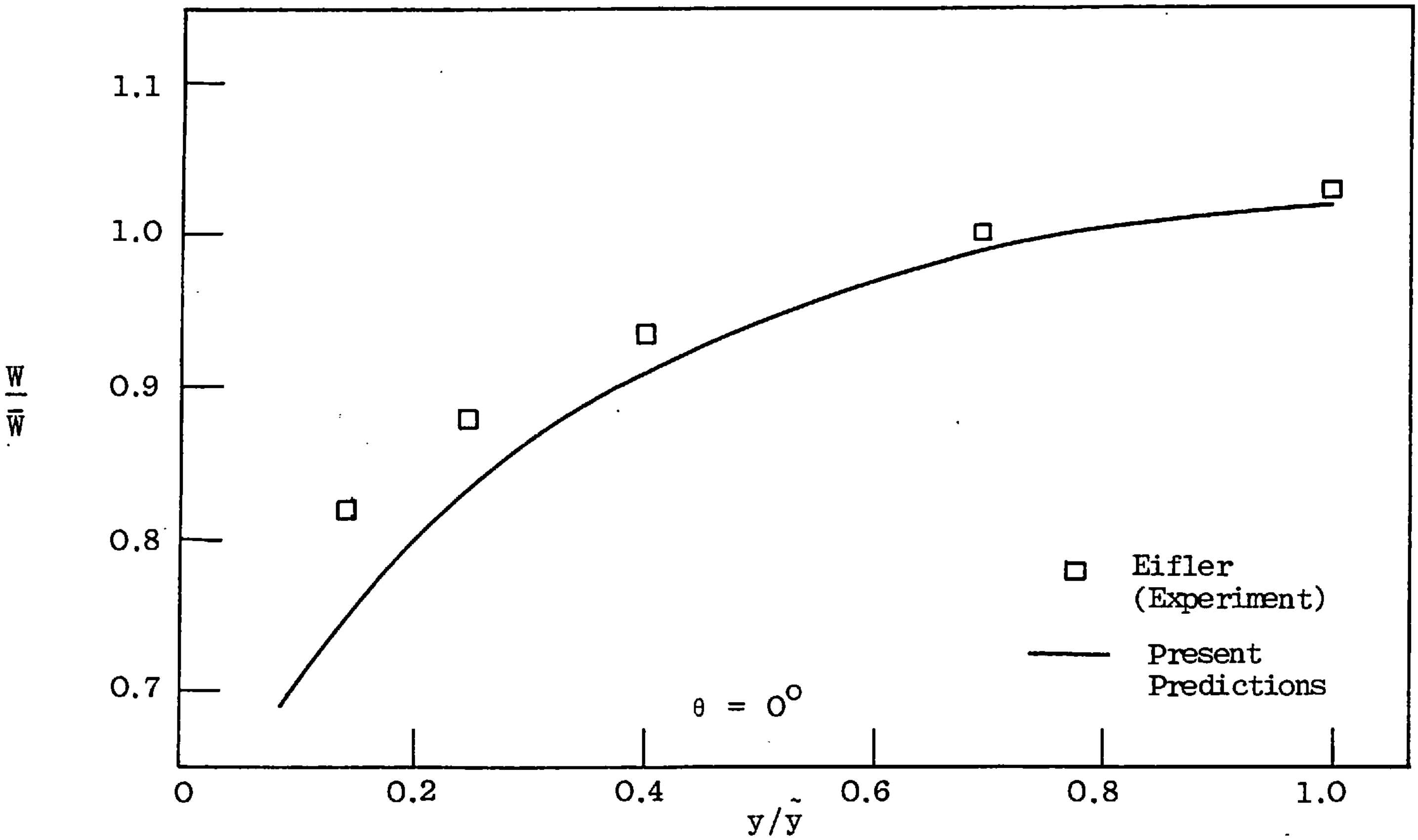

FIGURE 7.3.4(a): AXIAL-VELOCITY DISTRIBUTION, P/D = 1.15.

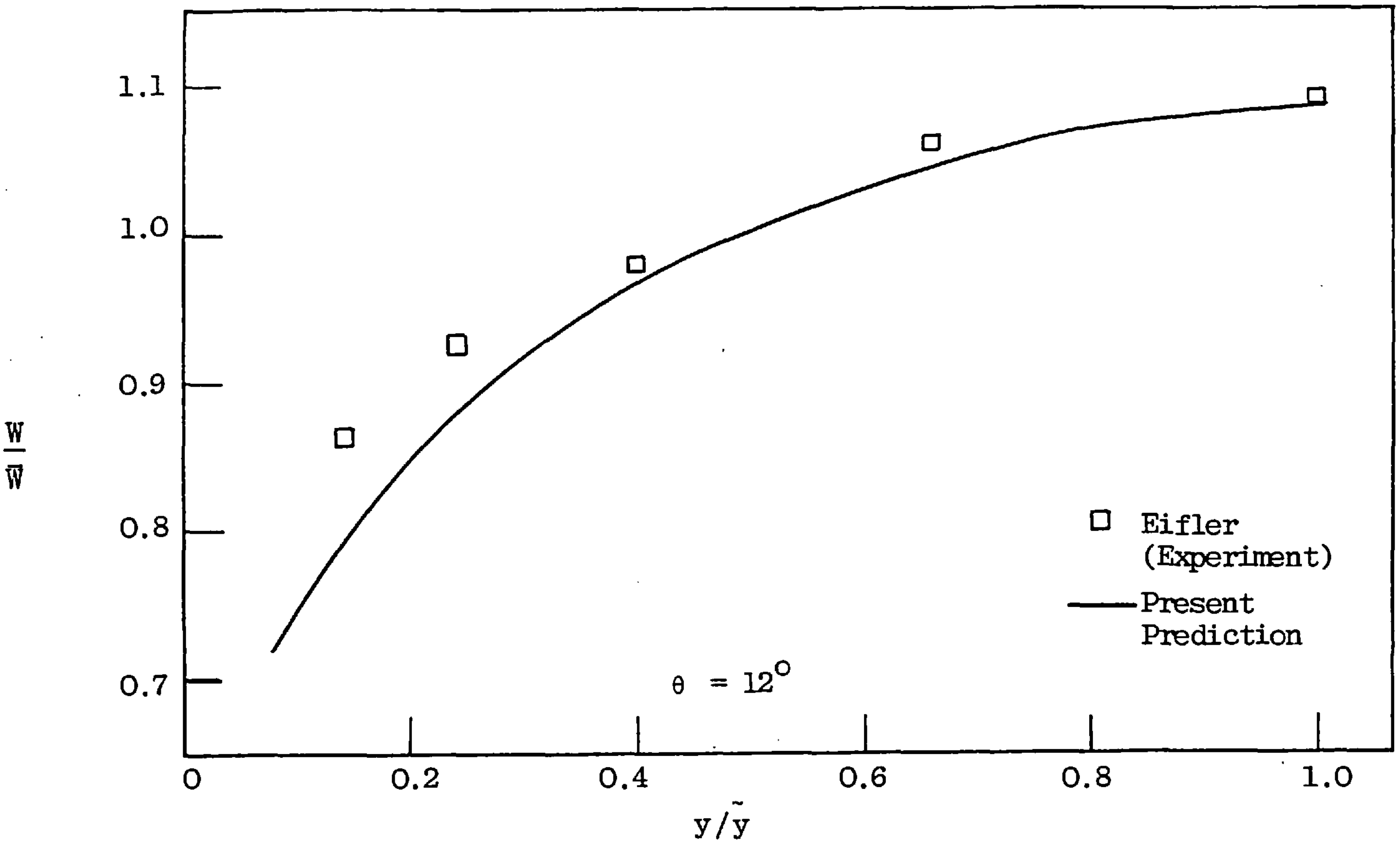

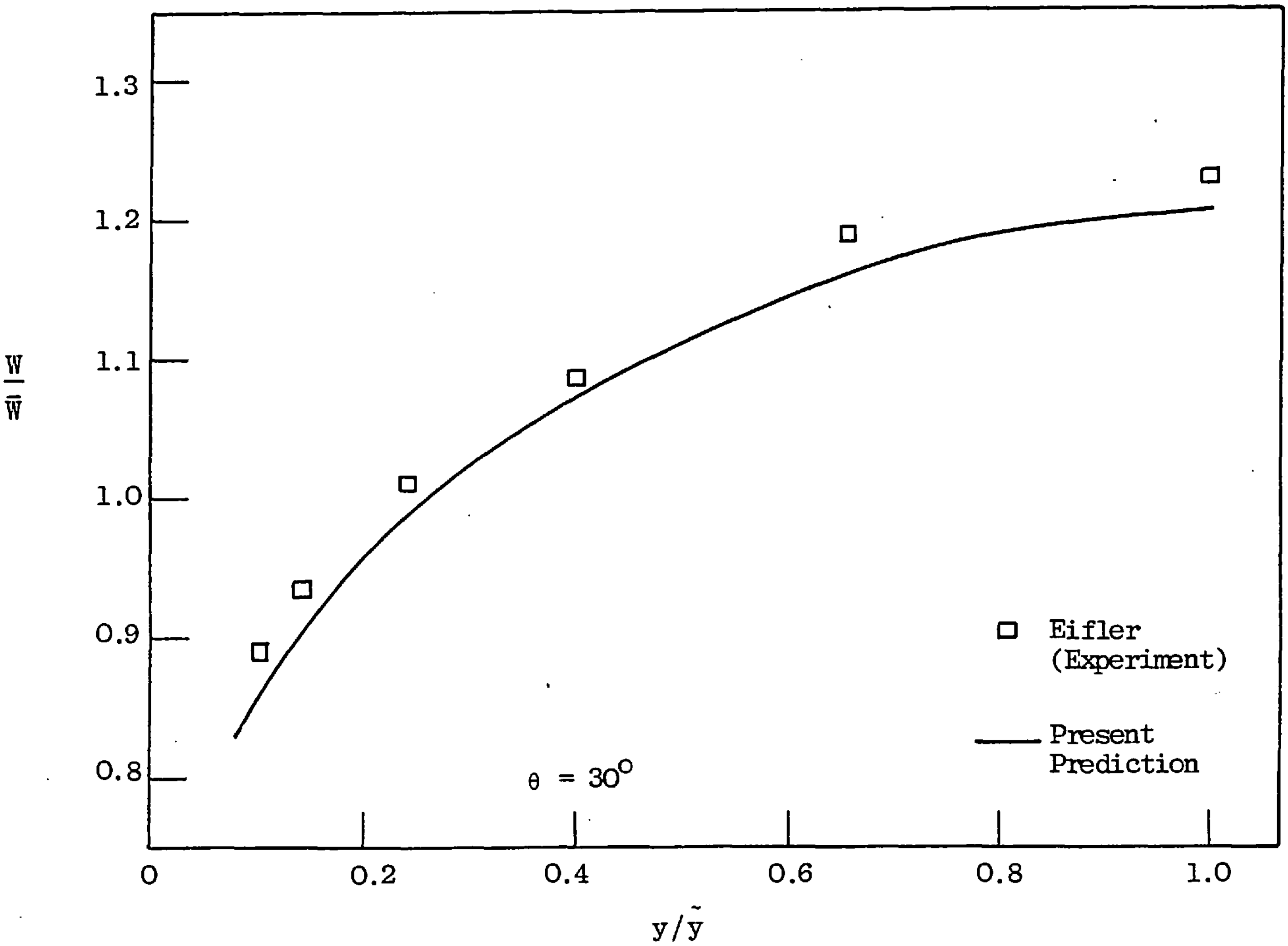

FIGURE 7.3.4(b): AXIAL-VELOCITY DISTRIBUTIONS, P/D = 1.15, Re = 26000.

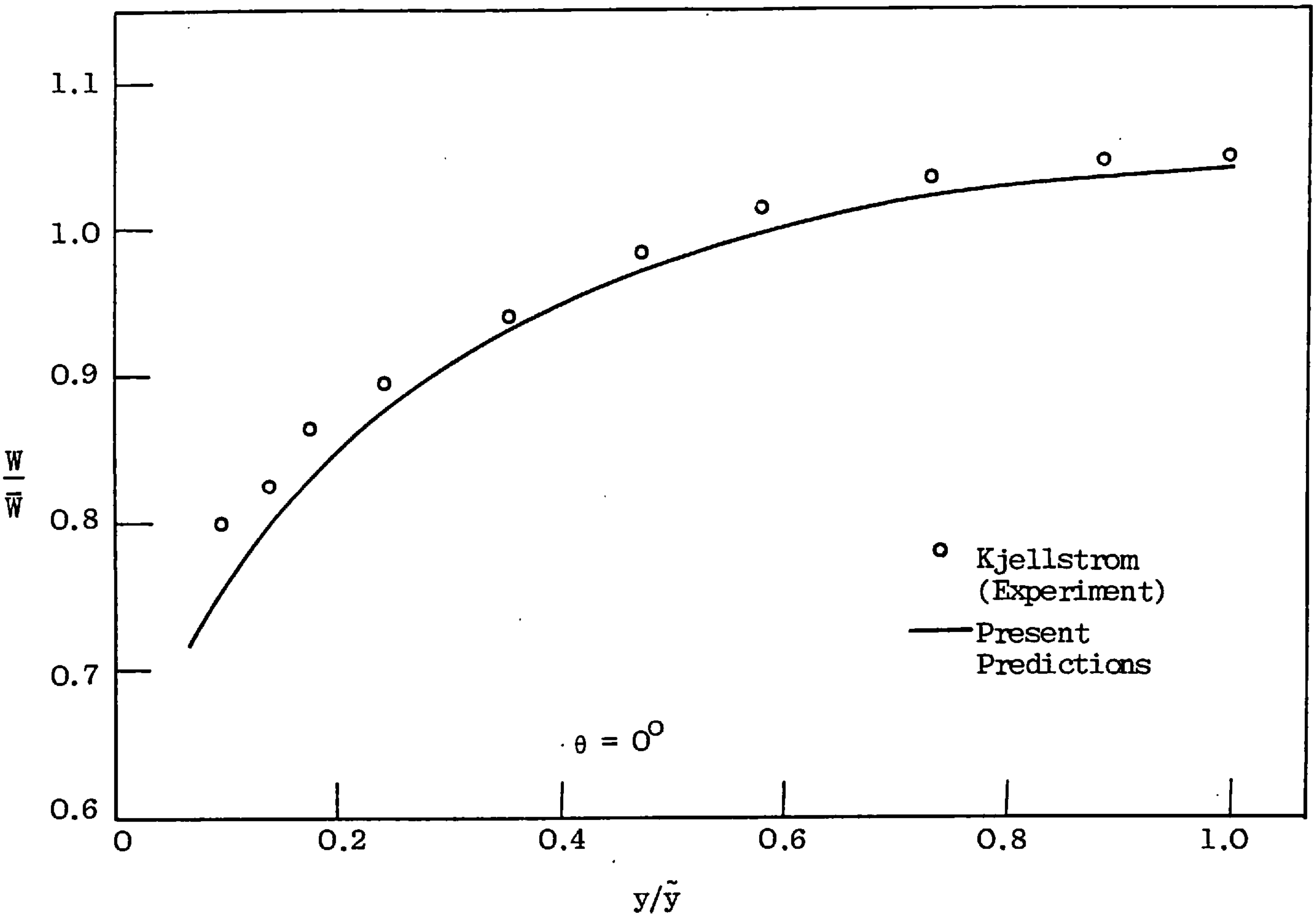

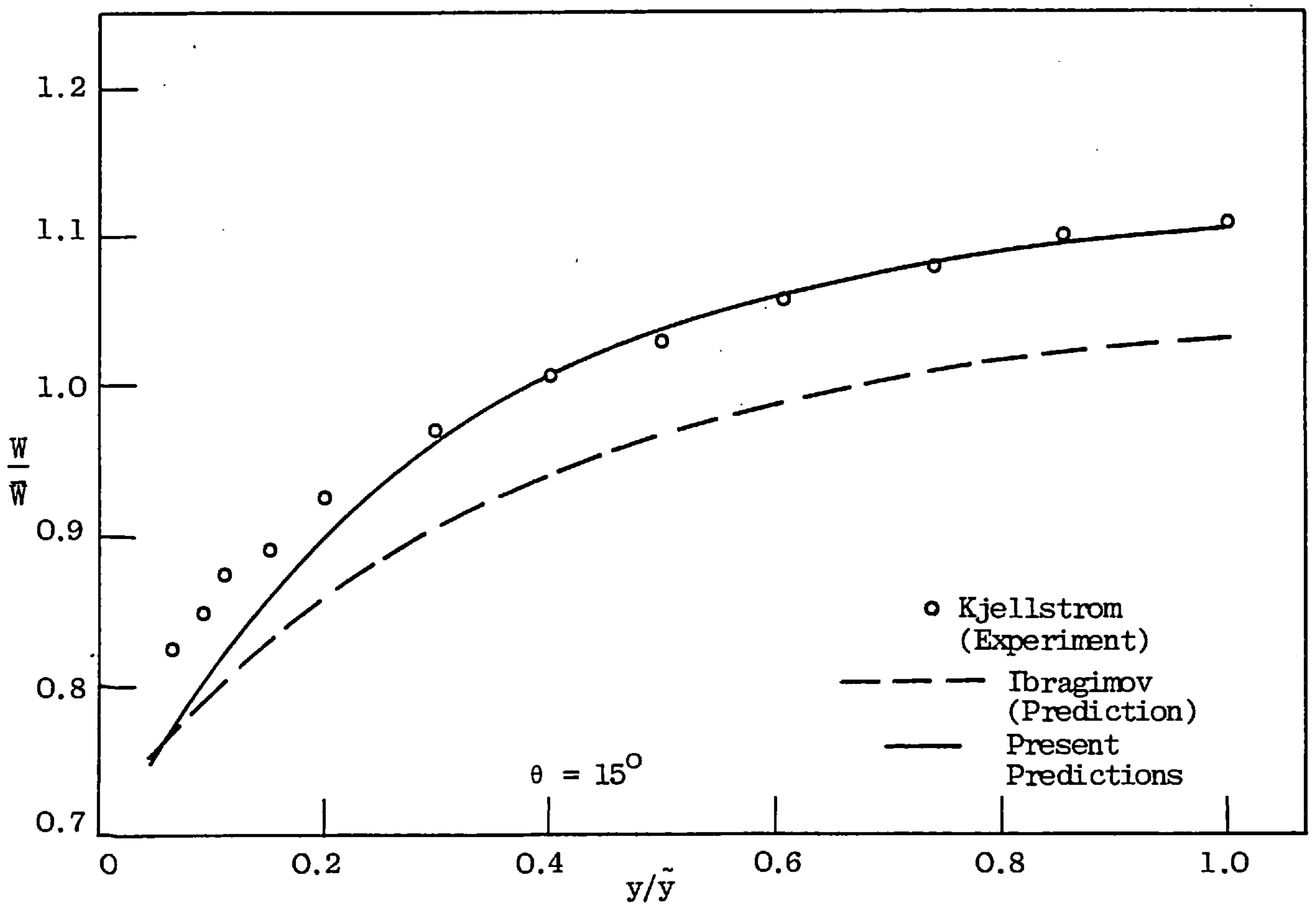

FIGURE 7.3.5: AXIAL-VELOCITY DISTRIBUTIONS, $P/D = 1.217$, $Re = 1.49 \times 10^{5}$

possible error of about 10% near the wall, and about 4% in the region where the profile is nearly flat. The present calculations are thus seen to be in very satisfactory agreement with their measurements.

Predicted axial-velocity distributions are plotted in a similar manner in figure (7.3.5) for comparison with the data of Kjellstrom (1971) for an array aspect ratio of 1.217 and a Reynolds number of 149 000 . Agreement between the two sets of results is good. Also shown is the curve obtained by Ibragimov's (1966) semi-empirical method (section 2.3.1), which, apart from its other defects, did not take into account any secondary flow.

The experimental measurements of Carajilescov and Todreas (1976) have been reproduced in figure (7.3.6), along with the w-profiles obtained with the present numerical procedure. The error bands shown represent uncertainties in the measurements, and were attributed by the authors to the electronics associated with laser Doppler anemometry. It is clear that the present calculations yield values that are in quite good agreement with the data; the worst deviations arise in the gap region ($\theta = 0^{o}$) where the velocities are under-estimated by up to 4%. Carajilescov (1975) has indeed suggested that the velocity distribution in the gap may not have been quite fully-developed at the measuring station; and since the velocities here tend to decrease (see figure 7.3.2) with longitudinal distance, this could well be the reason for, at least, part of the discrepancy. The experimental and

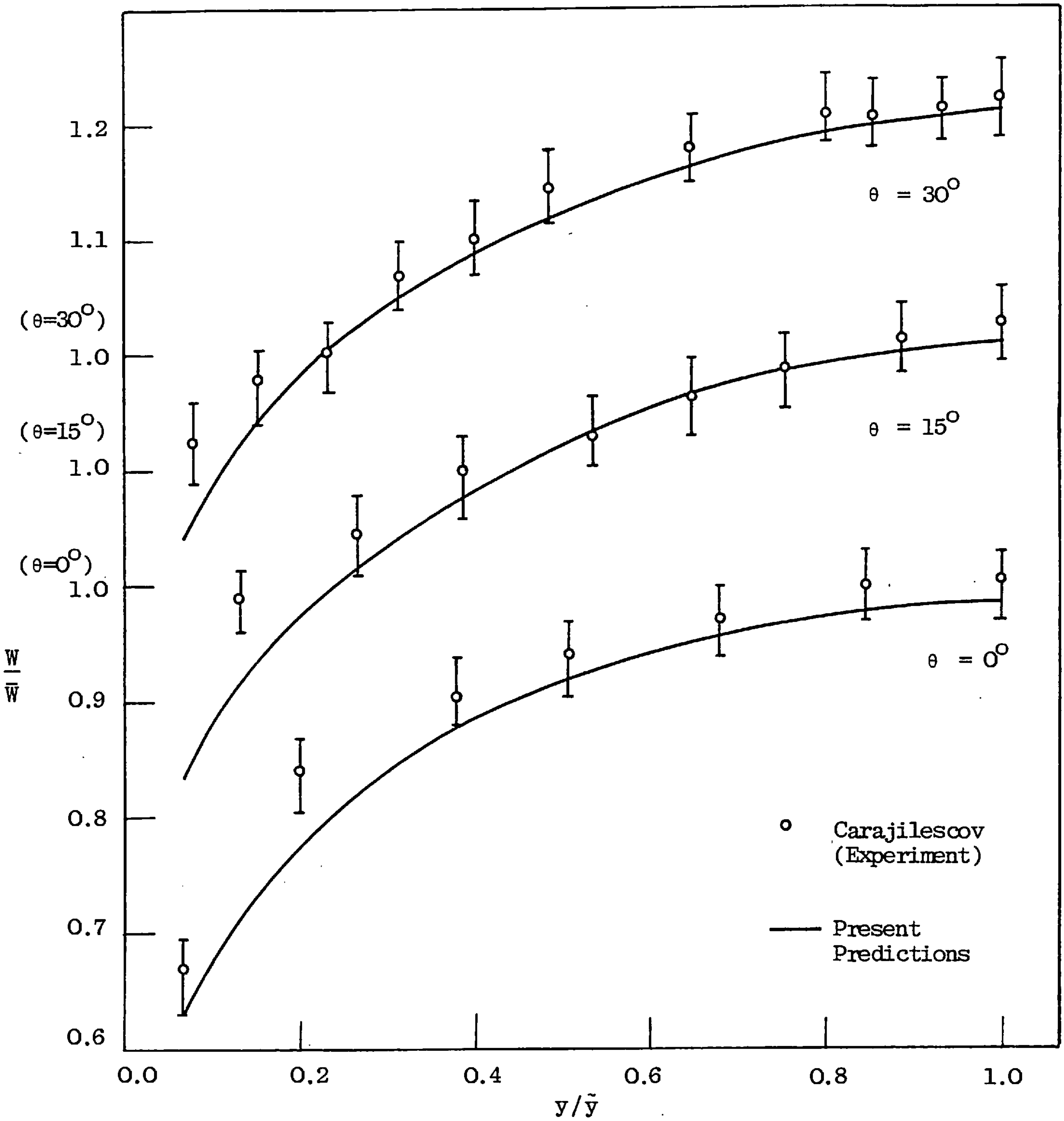

FIGURE 7.3.6: AXIAL-VELOCITY DISTRIBUTIONS, P/D = 1.123, Re = 27000.

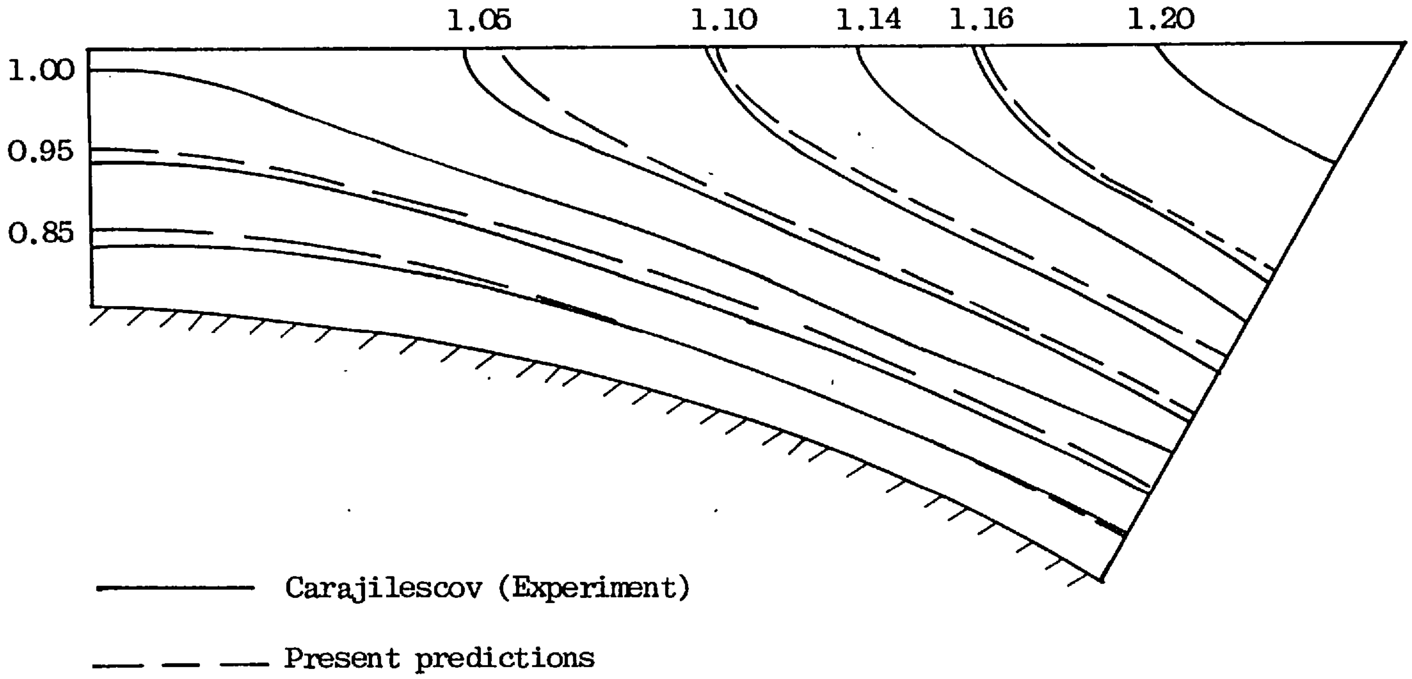

FIGURE 7.3.7: COMPARISON OF EXPERIMENTAL AND PREDICTED ISOVELS ($\frac{W}{\overline{W}}$); P/D = 1.123, Re = 27000.

predicted velocity fields have also been plotted in the form of isovels (constant-velocity lines) and super-imposed on each other in figure (7.3.7). The curvature of the isovels for $\theta \sim 30^{\circ}$ reflects the existence of secondary currents which move away from the wall and towards the subchannel symmetry (maximum-velocity) line.

The present prediction method has also been tested against the experimental data of Trupp and Azard (1975). Figure (7.3.8) displays the peripheral variations of the axial velocity (non-dimensionalized through division by the bulk velocity) in an array with P/D equal to 1.35: the solid curves represent the present calculations for several fixed values of the radial distance, y, measured from the rod surface. The velocity measurements were performed with a Pitot tube and a differential pressure manometer, and the accuracy of the results was estimated by the authors to be typically about two per cent. The computed distributions agree very well with the data, although there are deviations of about 4% near the intersection of the maximum-velocity line ($y=\tilde{y}$) and the radial ($\theta=30^{\circ}$) boundary; a probable cause is the lack of exact symmetry at the $y=\tilde{y}$ boundary in the experimental test section, which would result in the exchange of momentum between adjacent subchannels. Trupp and Azard report that comparisons were made between their velocity data and the prediction techniques of Buleev (1964) and Bender and Switick (1968), and substantial discrepancies, especially in the gap region ($\theta=0^{\circ}$) were noted. The present method, however, has taken into consideration secondary flows which can convey

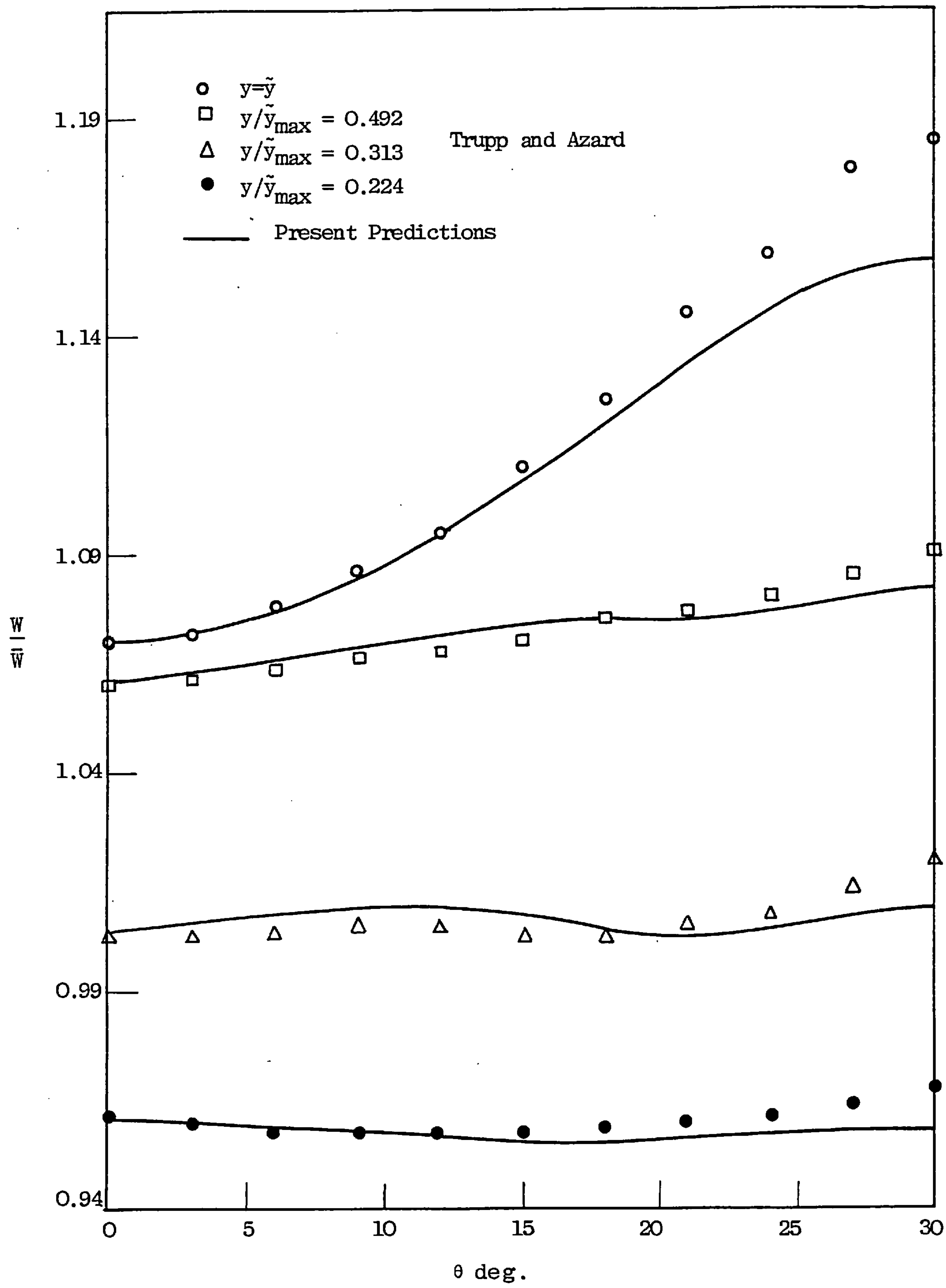

FIGURE 7.3.8: DISTRIBUTION OF AXIAL VELOCITY IN PERIPHERAL DIRECTION, P/D = 1.35, Re = 36000.

momentum into the gap, and thus succeeded in predicting the measured velocities.

7.3.3 Secondary flow

The predicted secondary flow distribution in rod arrays was a complex function of the aspect ratio (P/D) and the Reynolds number. Figures (7.3.9(a)) and (7.3.9(b)) are qualitative representations of the flow patterns in triangular and square arrays respectively, for identical values of the P/D ratio and Reynolds number. The latter conditions were selected to correspond with those in the experimental study of Carajilescov and Todreas (1976). In either case, the basic secondary flow pattern consists of a single cell of counter-clockwise circulation, fluid being convected away from the wall along a path parallel and adjacent to the east boundary of the domain, and returning to the wall via the gap separating neighbouring rods. This pattern is identical to that postulated by Nijsing (1972), (q.v. figure 2.3.1), but is contrary to that predicted by Carajilescov and Todreas (figure 2.3.2); it is likely that the latter's calculations were ill-converged.

The greatest secondary velocities were found to occur in the region close to the rod surface and in the flow adjacent to the maximum-velocity boundary of the subchannel. For the triangular array, the maximum velocities were about 1.1-1.2% of the bulk velocity, while in the square array a maximum velocity of about 1.5% $\bar{w}$ was predicted. The strength of the flow, when scaled on the bulk velocity, was

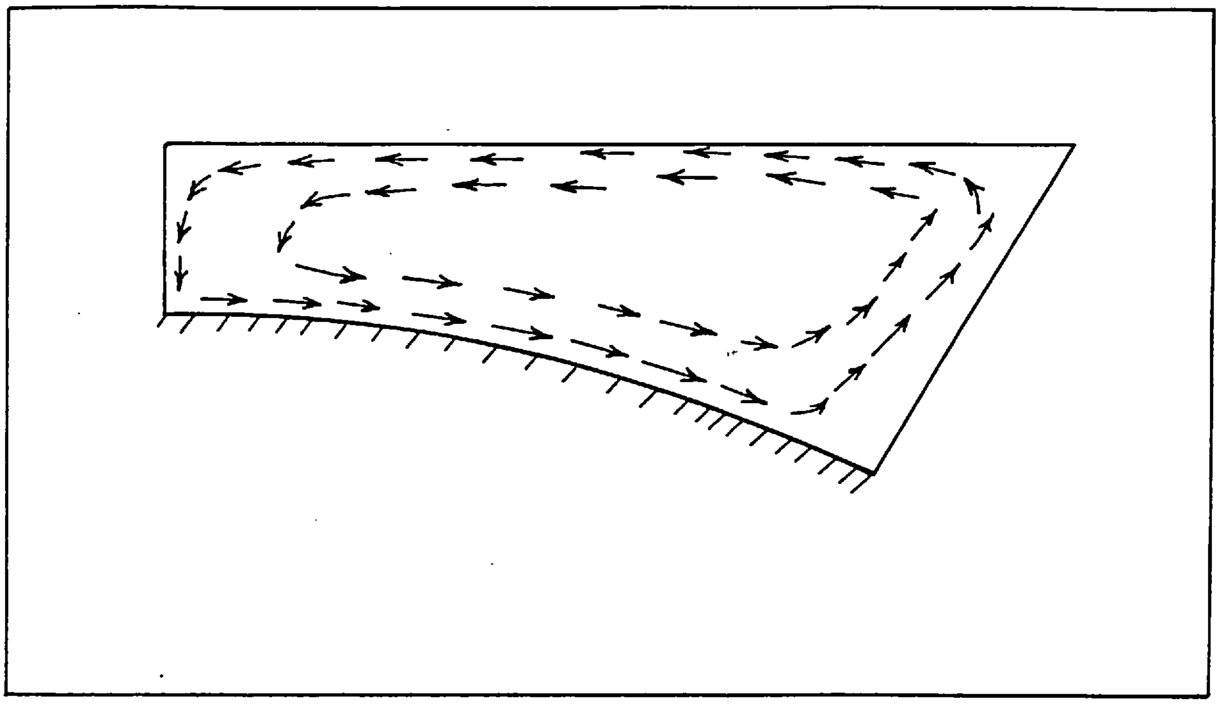

FIGURE 7.3.9(a): SECONDARY FLOW PATTERN IN TRIANGULAR ARRAY; $P/D = 1.123$, $Re = 2.7x10^4$

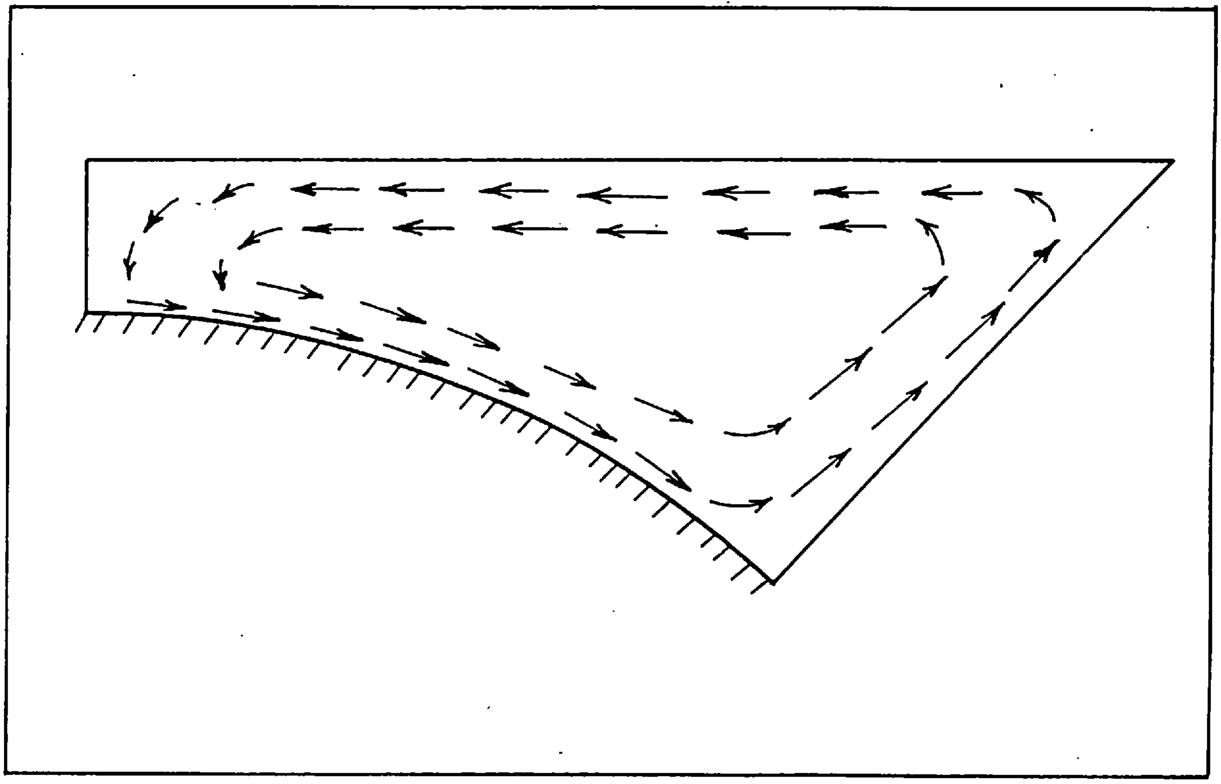

FIGURE 7.3.9(b): SECONDARY FLOW PATTERN IN SQUARE ARRAY; $P/D = 1.123$, $Re = 2.7x10^4$

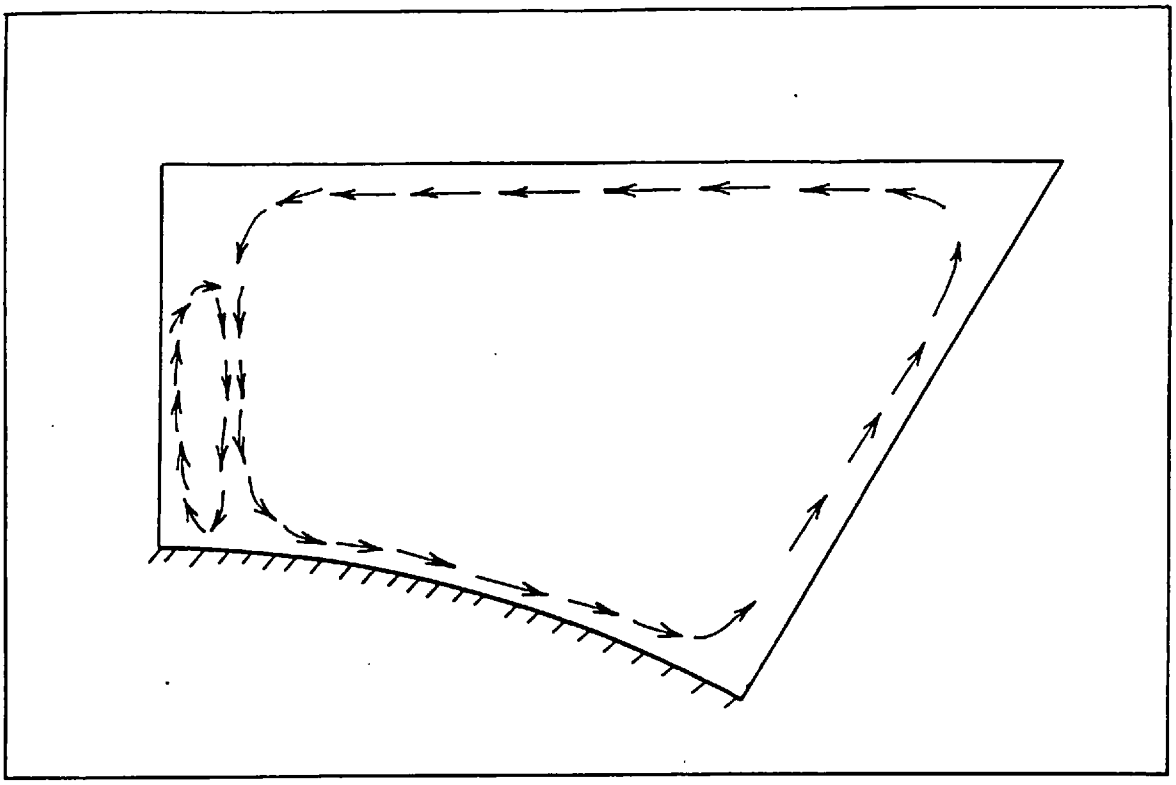

FIGURE 7.3.10(a) SECONDARY FLOW PATTERN, TRIANGULAR ARRAY;
P/D = 1.35, Re = 60000.

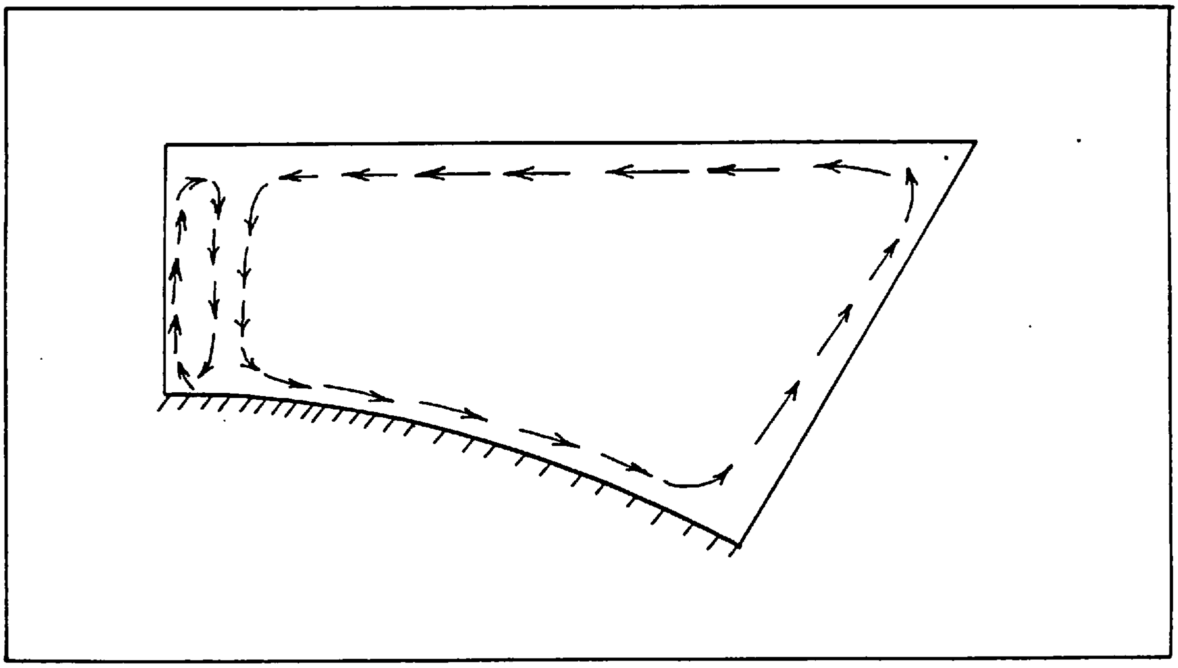

FIGURE 7.3.10(b): SECONDARY FLOW PATTERN, TRIANGULAR ARRAY;
P/D = 1.217, Re = 270000

only weakly dependent on the Reynolds number, but decreased with increasing aspect ratio.

In contrast with the above results, it was observed that for P/D values greater than about 1.20, the calculated secondary flow pattern was a strong function of the Reynolds number. Figures (7.3.10(a)) and (7.3.10(b)) show the qualitative flow distributions for P/D ratios of 1.35 and 1.217 respectively. A small secondary swirl, rotating counter to the main loop, was found to exist very close to the gap separating neighbouring rods. The strength of this swirl was less than the main one, but grew with increasing Reynolds number. For both geometries shown (and under the given flow conditions) the maximum velocities were about 0.6% of the bulk velocity in the main swirl and about 0.3% of $\bar{w}$ in the smaller one. For the smaller aspect-ratio array (figure 7.3.10(b)) this minor swirl disappeared altogether when the Reynolds number was reduced below about $1x10^5$. Similar patterns were computed for the secondary flow field between rods arranged in a square pattern.

The geometry and Reynolds number represented by figure (7.3.10(b)) are identical to the experimental conditions in the study of Kjellstrom (1971), who attempted to measure the distribution of the circumferential velocity u. The present predictions have been plotted, along with his scattered data, in figure (7.3.11) for three different angular locations. Although no definite conclusions can be drawn, the analytical results do follow the general trend of the data.

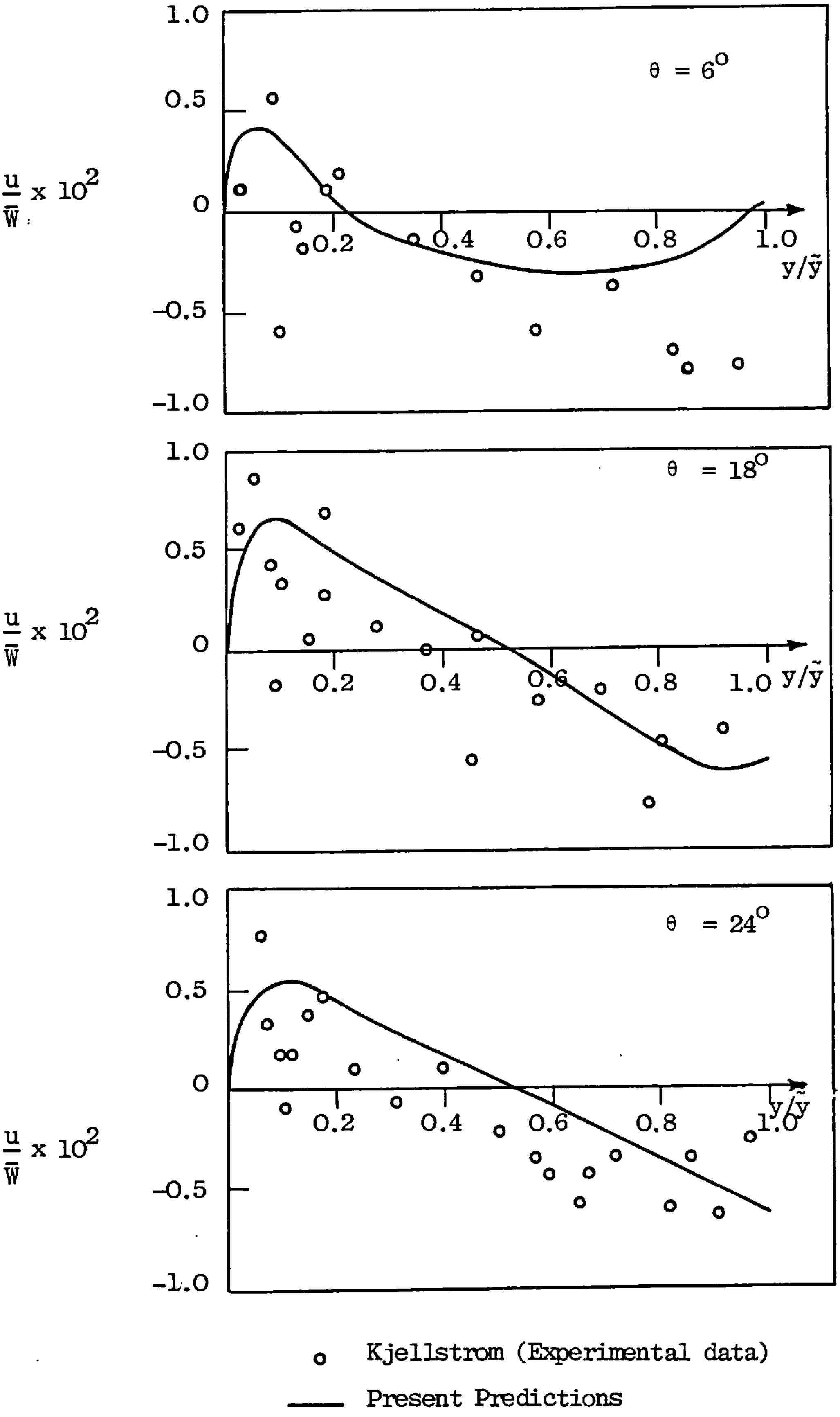

FIGURE 7.3.11: COMPARISON BETWEEN PREDICTED SECONDARY FLOW PROFILES AND EXPERIMENTAL DATA (P/D = 1.217, Re = 2.7×10^5.

7.3.4 Wall-shear-stress distributions

The distribution of the local shear stress around the periphery of the rod surface is of considerable interest. As in laminar flow (section 5.3.3.1) this variation diminishes with increasing aspect ratio (P/D). However, the secondary flows discussed above tend to greatly reduce the non-uniformity of the shear-stress distribution, as is demonstrated in figure (7.3.12). The ordinate in the figure represents the local wall shear stress (normalized with respect to the peripherally-averaged value) corresponding to any angular position θ. The steepest curve in the figure is that obtained by the assumption of an isotropic turbulent-viscosity hypothesis for the turbulent stresses in the cross-stream momentum equations, thereby neglecting to account for secondary motions. The predicted homogenizing of the shear stress is expected from the secondary flow distribution indicated in figure (7.3.9(a)). It is also seen from figure (7.3.12) that for the given pitch-diameter ratio the wall shear variation is only slightly influenced by the Reynolds number.

The predicted wall shear stress distribution for P/D = 1.10 is compared with the experimental curve of Subbotin et al. (1971) in figure (7.3.13). The agreement between the two is very close. Also indicated in the figure is the analytical result deduced via the semi-empirical method of Ibragimov (1966) which is embodied in the VELVET II code of Bender and Magee (see section 2.3.1).

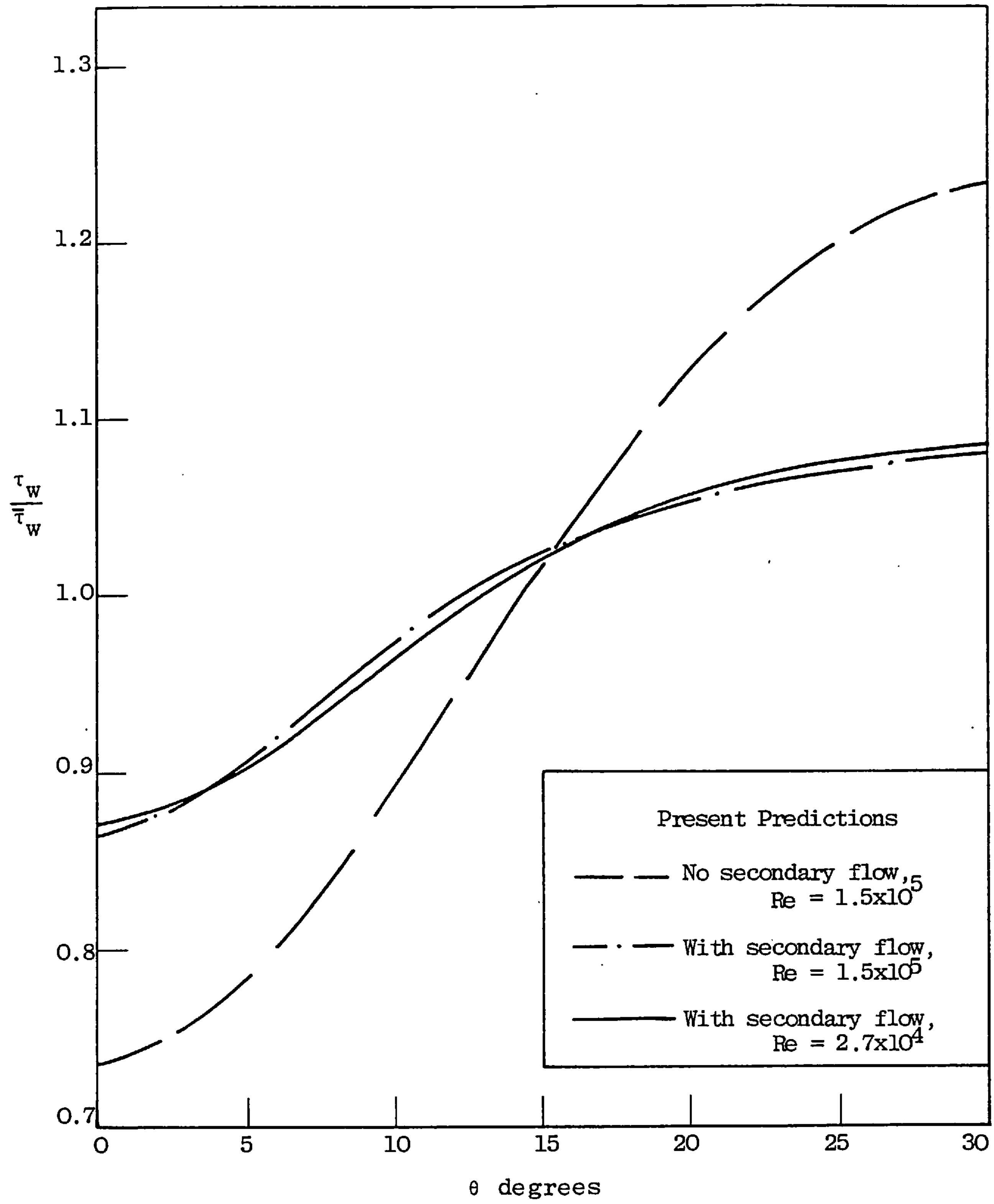

FIGURE 7.3.12: PERIPHERAL DISTRIBUTION OF WALL SHEAR STRESS: P/D = 1.10.

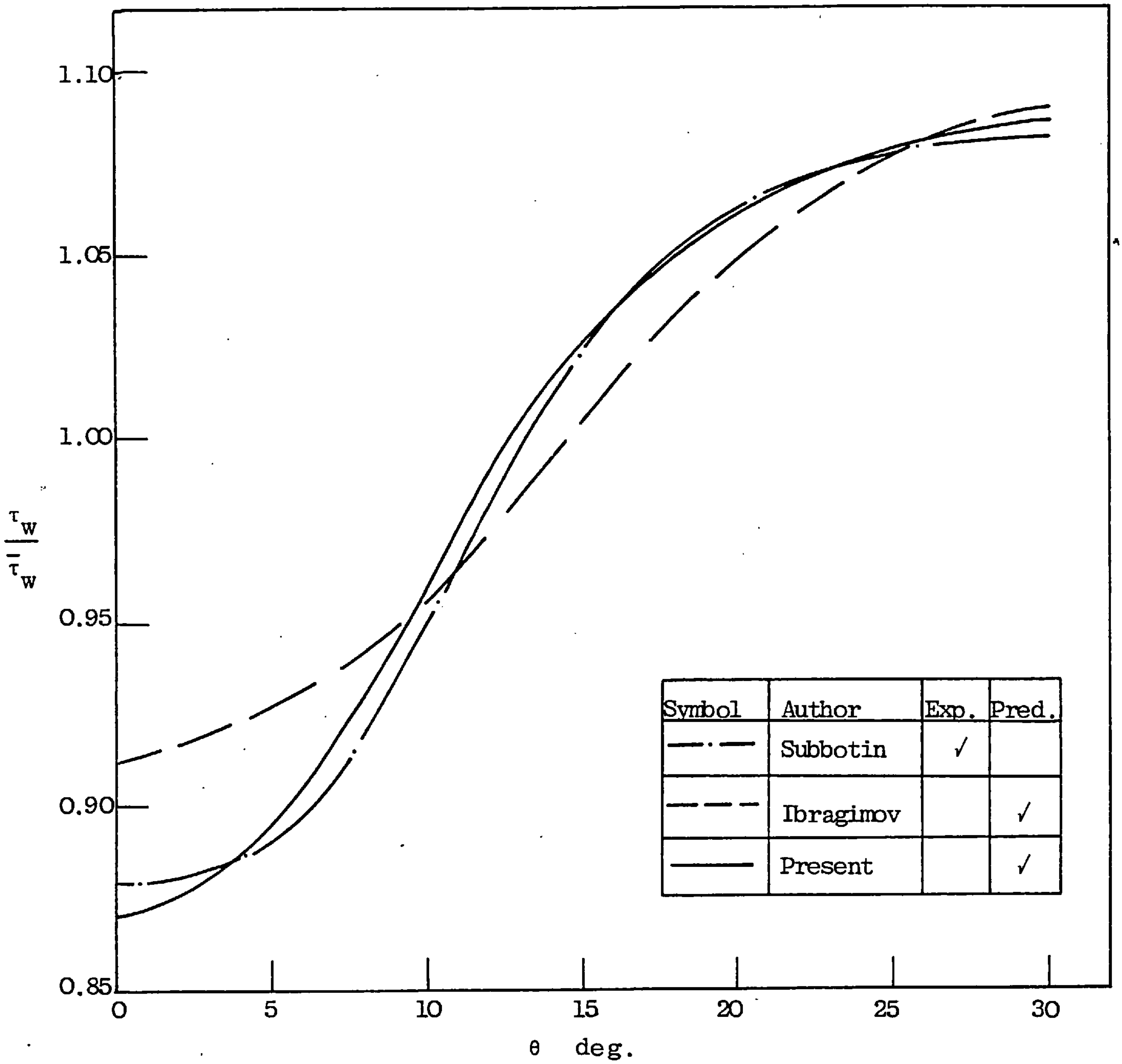

FIGURE 7.3.13: SHEAR-STRESS DISTRIBUTION: COMPARISON WITH EXPERIMENT, P/D = 1.10, Re = 28000.

Variations in the local wall shear stress about the rod perimeter for an aspect ratio of 1.217 have also been computed, and the results are displayed in figure (7.3.14), where $\bar{\tau}_w$ is, as before, the rod-averaged shear stress. Comparisons are made with the results of other investigators. Both the data of Hall and Svenningsson (1971) and Kjellstrom (1971) indicate that the wall shear does not increase monotically as is predicted by computational schemes that neglect secondary flows (e.g. Ibragimov (1966)). The profile peaks instead at $\theta \approx 20^o$. The present calculations are in very favourable agreement with the experimental measurements and, moreover, represent an overall improvement on the predictions of Carajilescov and Todreas (section 2.3.1).

Comparison of the present results with the experimental data of Trapp and Azard (1975) are illustrated in figures (7.3.15) and (7.3.16). In the former figure, the predictions reveal a smooth increase of wall shear stress with angle, and deviate from the experimental points near the radial boundary ($\theta = 30^o$). The latter points are suspect, however, owing to an asymmetry effect in the test section. Otherwise, the agreement between the present results and the experimental data is good. In contrast, the method of Bender and Switick (1968) predicted variations in the shear stress of about 24% around the rod periphery for P/D = 1.20.

Measurements via a Preston tube of the shear stress variations for P/D = 1.35 are shown in figure (7.3.16). Maximum variations of about 4%, with a peak occurring at $\theta \approx 18^o$ were observed. The predicted curve tends to slightly over-

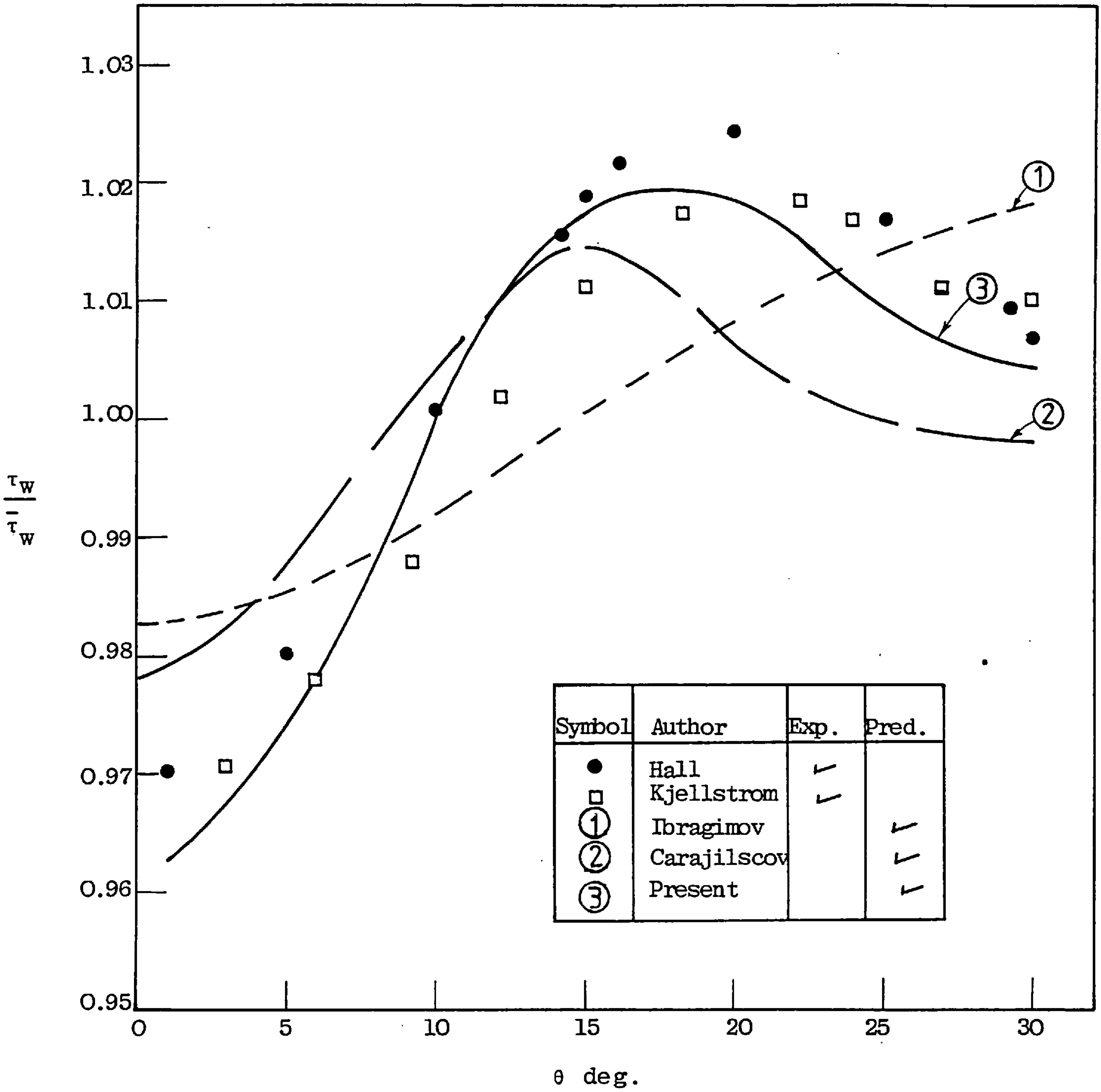

FIGURE 7.3.14: WALL SHEAR-STRESS DISTRIBUTION, P/D = 1.217, Re = 2.7 x 10^5

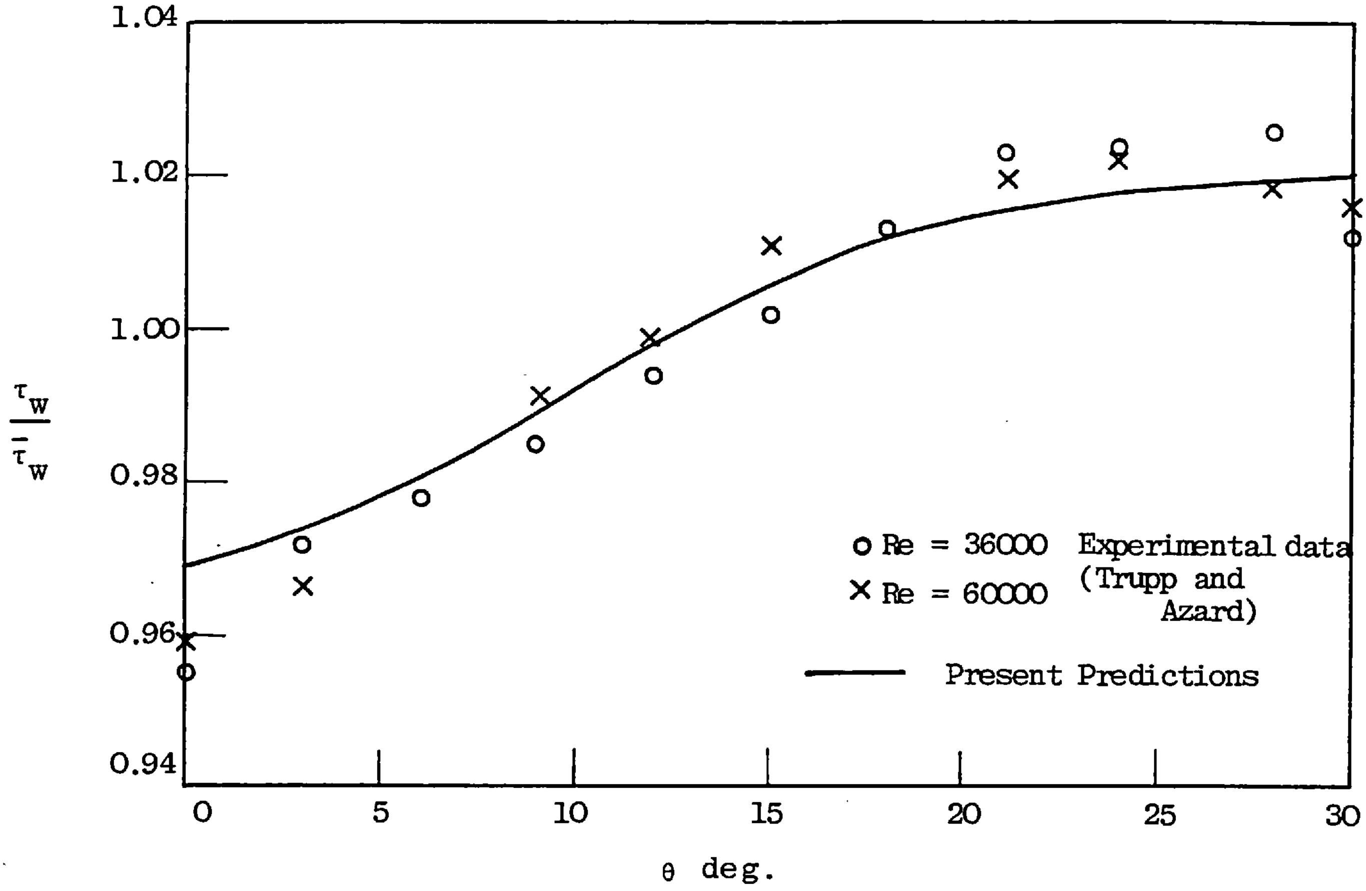

FIGURE 7.3.15: LOCAL WALL SHEAR-STRESS DISTRIBUTIONS, P/D = 1.20.

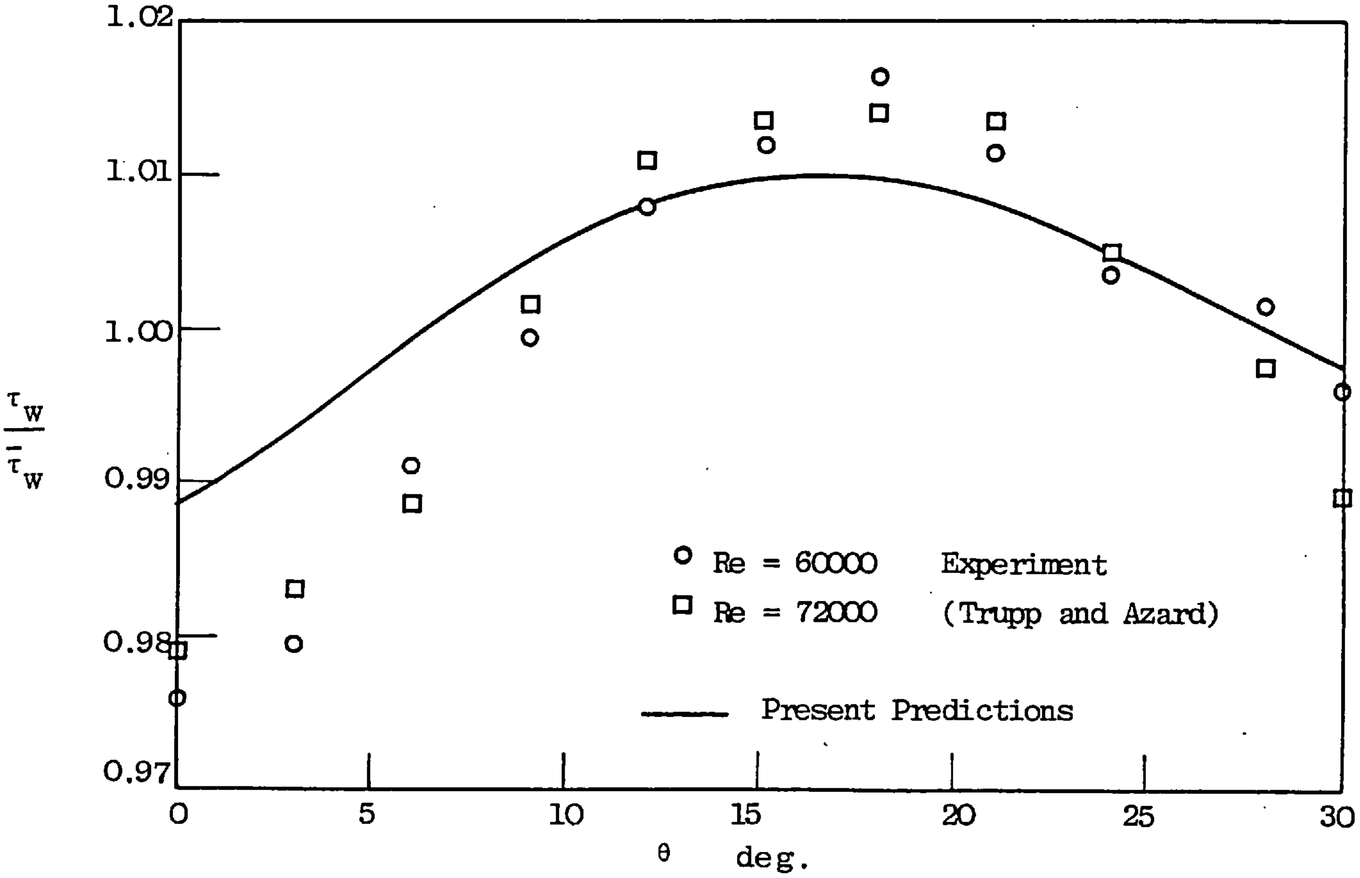

FIGURE 7.3.16: LOCAL WALL SHEAR-STRESS DISTRIBUTIONS, P/D = 1.35.

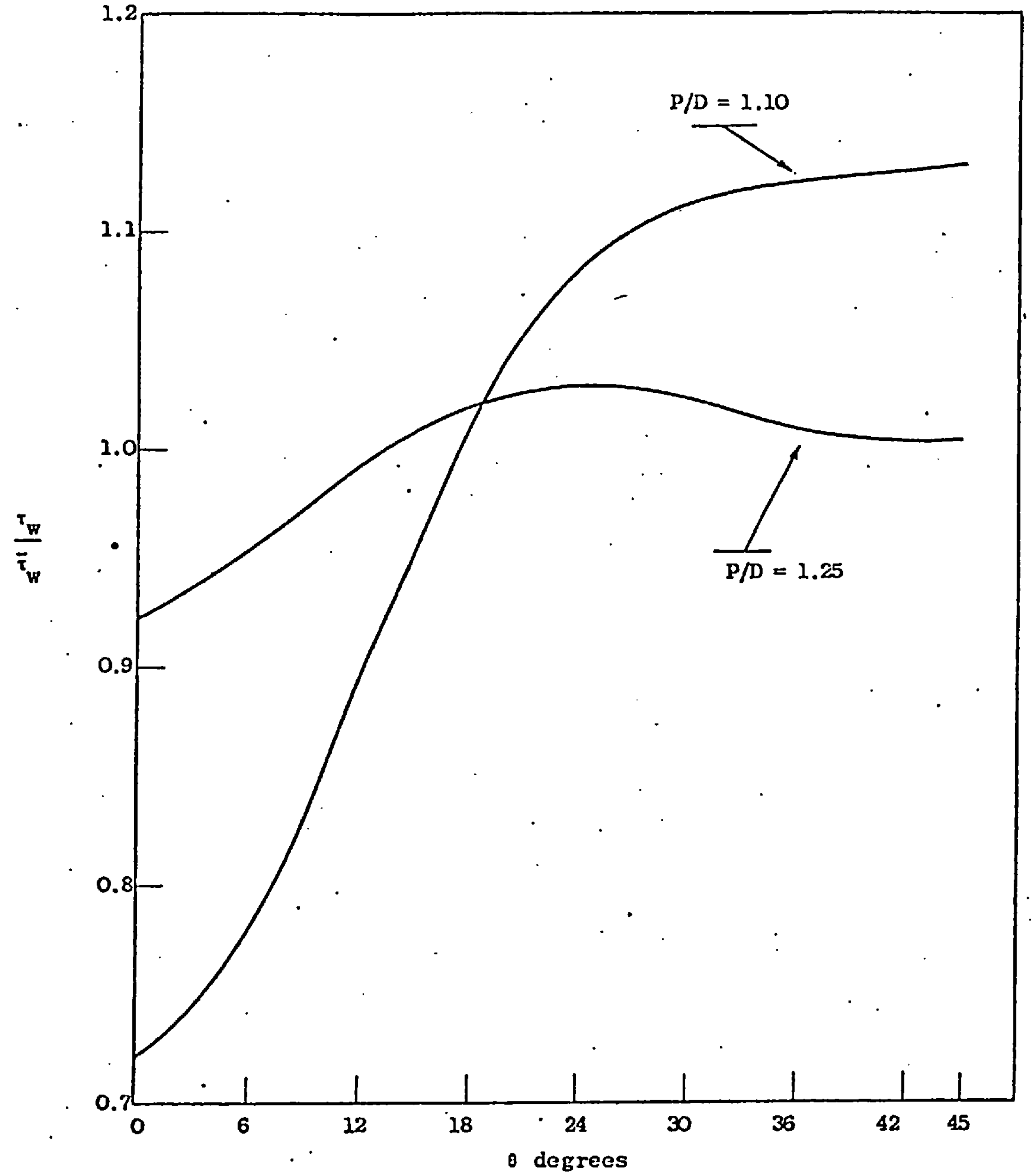

FIGURE 7.3.17: COMPUTED PERIPHERAL DISTRIBUTION OF WALL SHEAR STRESS IN SQUARE ARRAY (Re = 1.2×10^5).

estimate the influence of secondary flow in homogenizing the shear stress, but agreement is within the experimental error. Predictions performed for aspect ratios greater than 1.40 indicated an essentially uniform shear-stress distribution for all values of the Reynolds number. The shear-stress variations in square arrays are similar to those predicted for triangular arrays; two representative shear-stress profiles are depicted in figure (7.3.17).

7.3.5 Friction factors

The computed fully-developed values of the friction factors for pitch-diameter ratios greater than 1.1 were found to be higher than for flow through smooth circular tubes at the identical Reynolds number. The present results for P/D values of 1.20 and 1.35 are compared with the results of experimenters over the same Reynolds-number range in figure (7.3.18). For the smaller aspect ratio, the calculated friction factors lie, on average, 7% above the Blasius predictions for pipe flow, but about 4% below the mean experimental data. Corresponding figures for the larger (P/D = 1.35) array are 8% and 5% respectively.

7.3.6 Turbulent kinetic energy distributions

Calculated turbulent kinetic energy fields have been compared against the limited number of experimental data available. One such comparison is shown in figures (7.3.19(a),(b)): the experimental points are the hot wire measurements of Kjellstrom, performed in a triangular array of aspect ratio

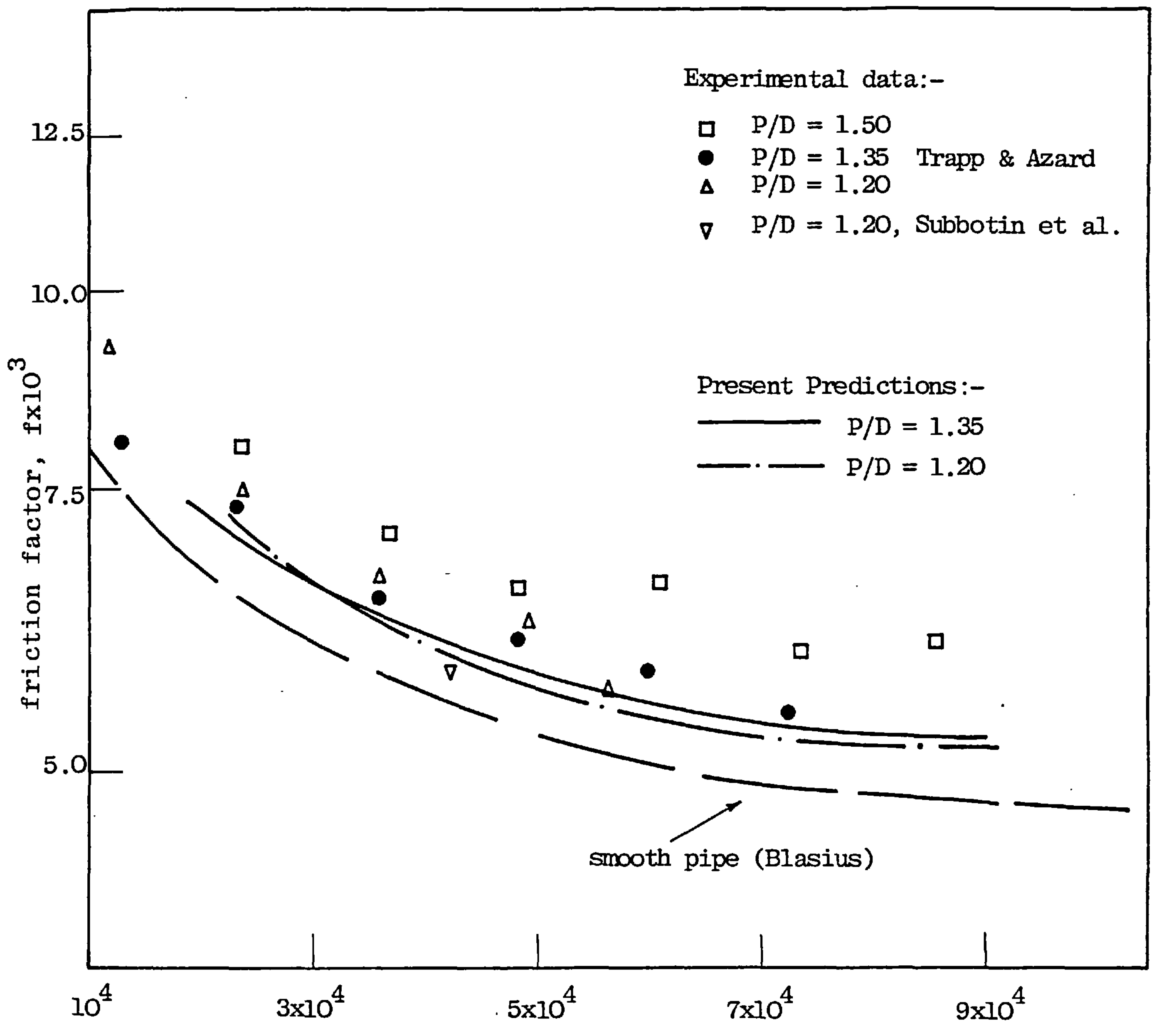

FIGURE 7.3.18: COMPARISON OF EXPERIMENTAL AND PREDICTED FRICTION FACTORS.

1.217. The kinetic energy values have been scaled with respect to the local friction velocity u_τ, and radial distributions for three different azimuthal positions in the flow have been plotted. Agreement with the present predictions is excellent, except in the region approaching the wall, where the measuring errors are likely to be significant owing to the influence of the wall on the probe. It will be observed that the turbulent energy levels in the outer regions of the flow are higher for $\theta = 18^o$ than for the two radial boundaries. This is probably caused by the secondary flows which, as seen from figure (7.3.10(b)), convey turbulent energy from the wall where it is generated into the 'core', induce mixing, and then turn inward towards the wall.

In figure (7.3.20) the radial distribution of turbulent energy has been compared with the hot-wire measurements of Trupp and Azard (1975), for a pitch-diameter ratio of 1.35. Here, the k-values are normalized with respect to the average friction velocity. As before, an angular dependence, especially in the regions far from the wall, is observed. Agreement between the two sets of results is very satisfactory.

The present predictions have been compared with the experimental data of Carajilescov and Todreas (1976) for a relatively close rod spacing (P/D = 1.123). Distributions of the turbulent energy along the radial boundaries of the flow domain, and for the angular location $\theta = 15^o$, are presented in figures (7.3.21(a), (b) and (c)). The error bands around

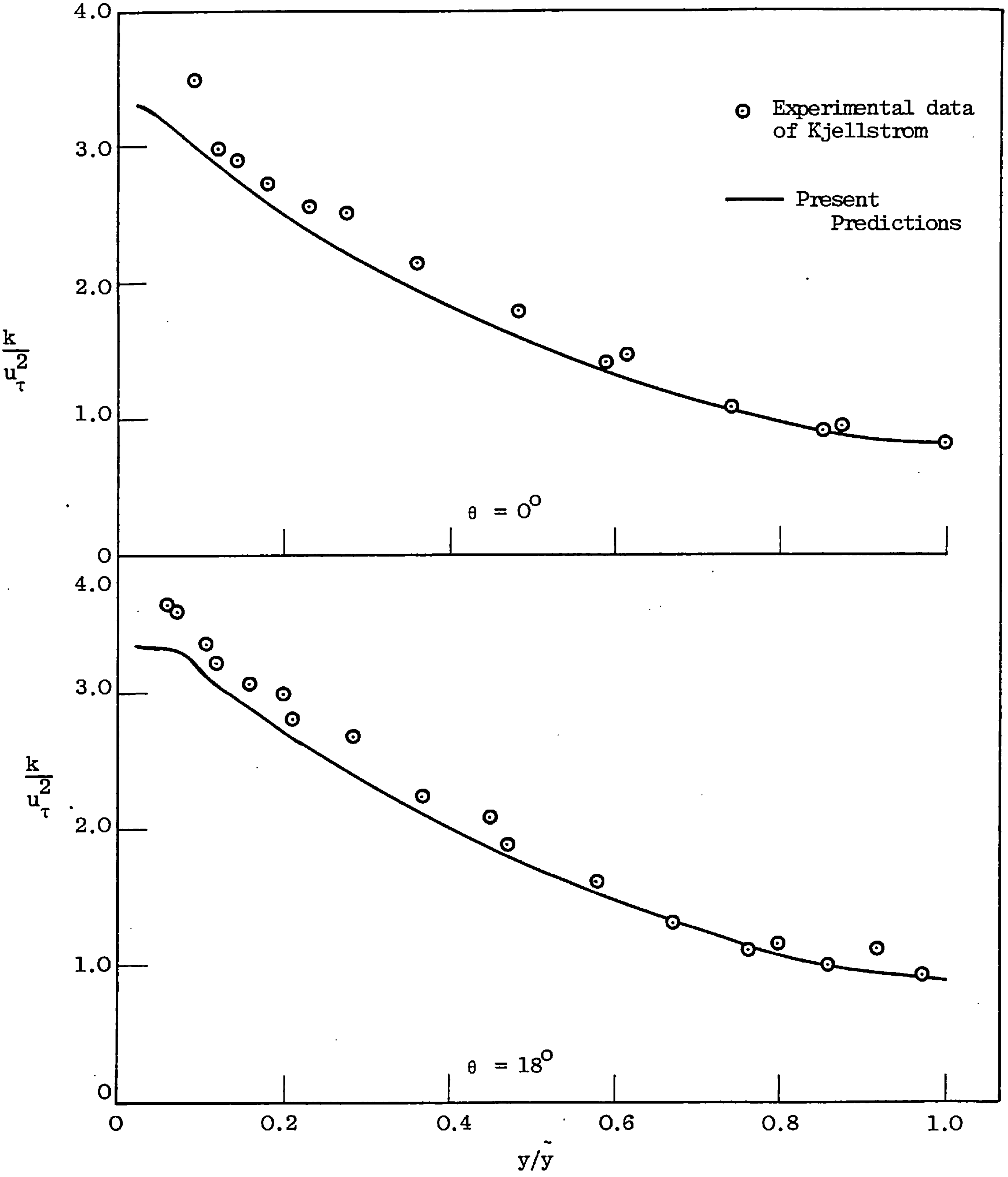

FIGURE 7.3.19(a): TURBULENT KINETIC ENERGY PROFILES, P/D = 1.217, Re = 1.49×10^5

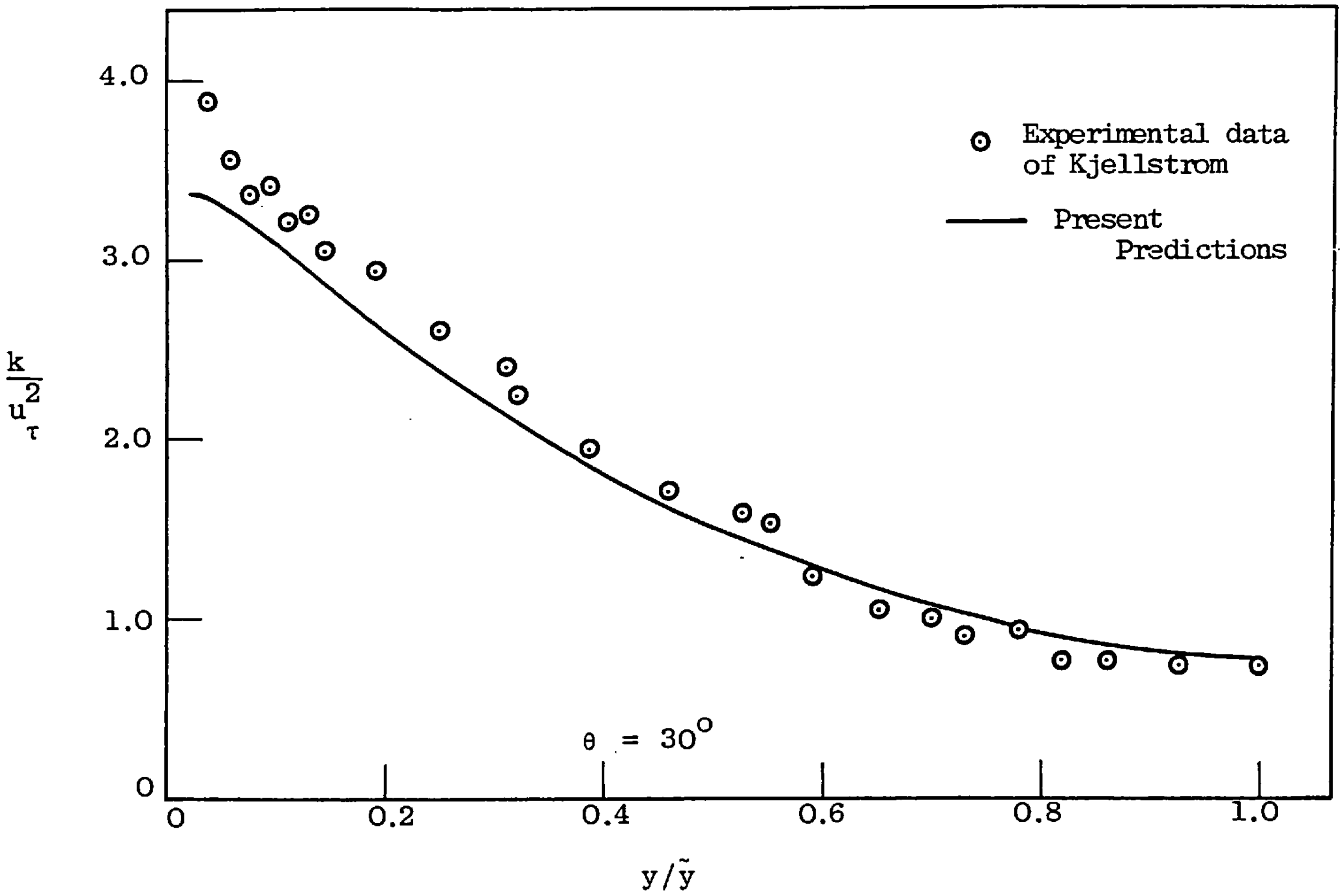

FIGURE 7.3.19(b): TURBULENT KINETIC ENERGY PROFILES, $P/D = 1.217$, $Re = 1.49 \times 10^5$

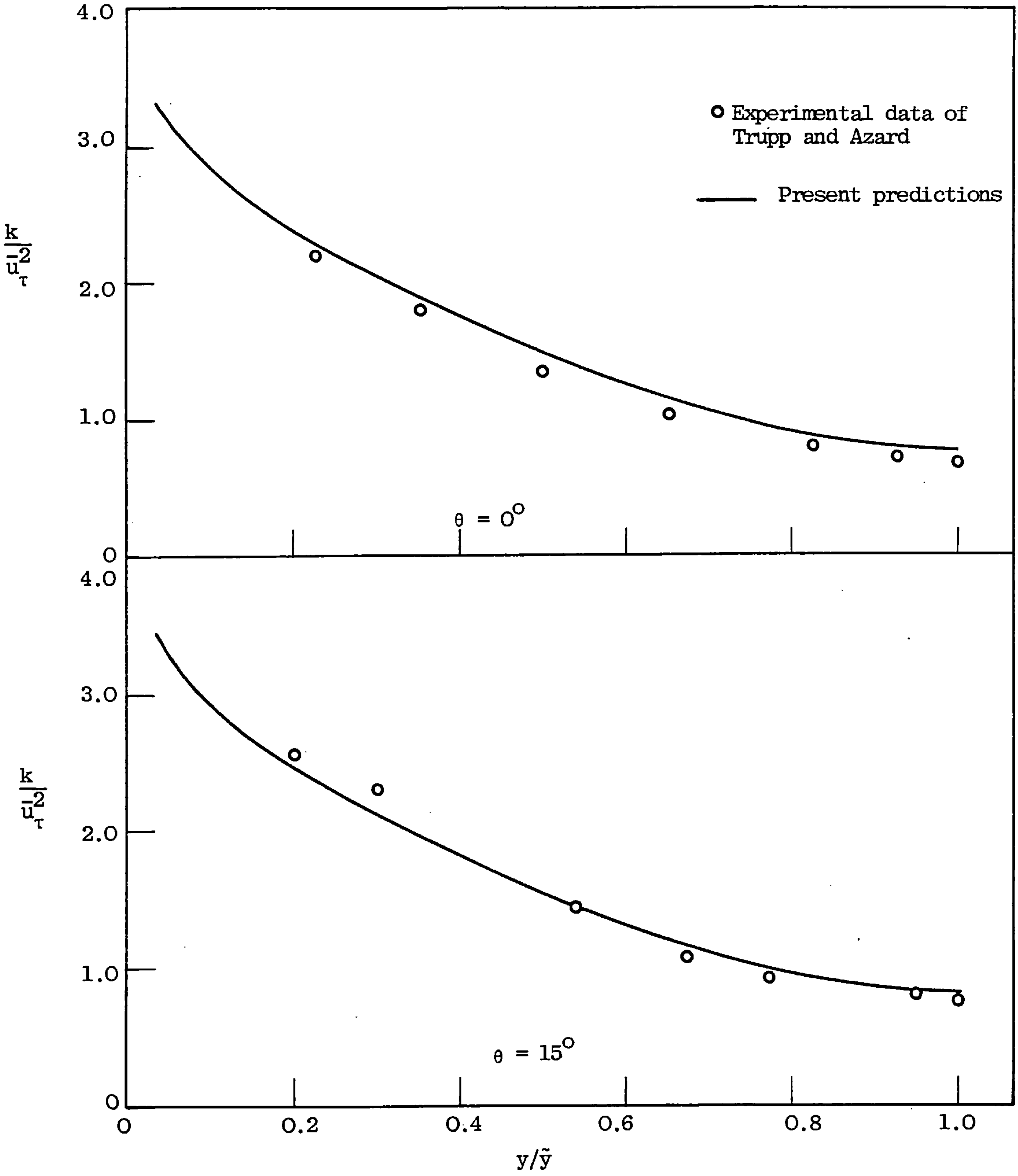

FIGURE 7.3.20(a): TURBULENT KINETIC ENERGY DISTRIBUTIONS, P/D = 1.35, Re = 60000.

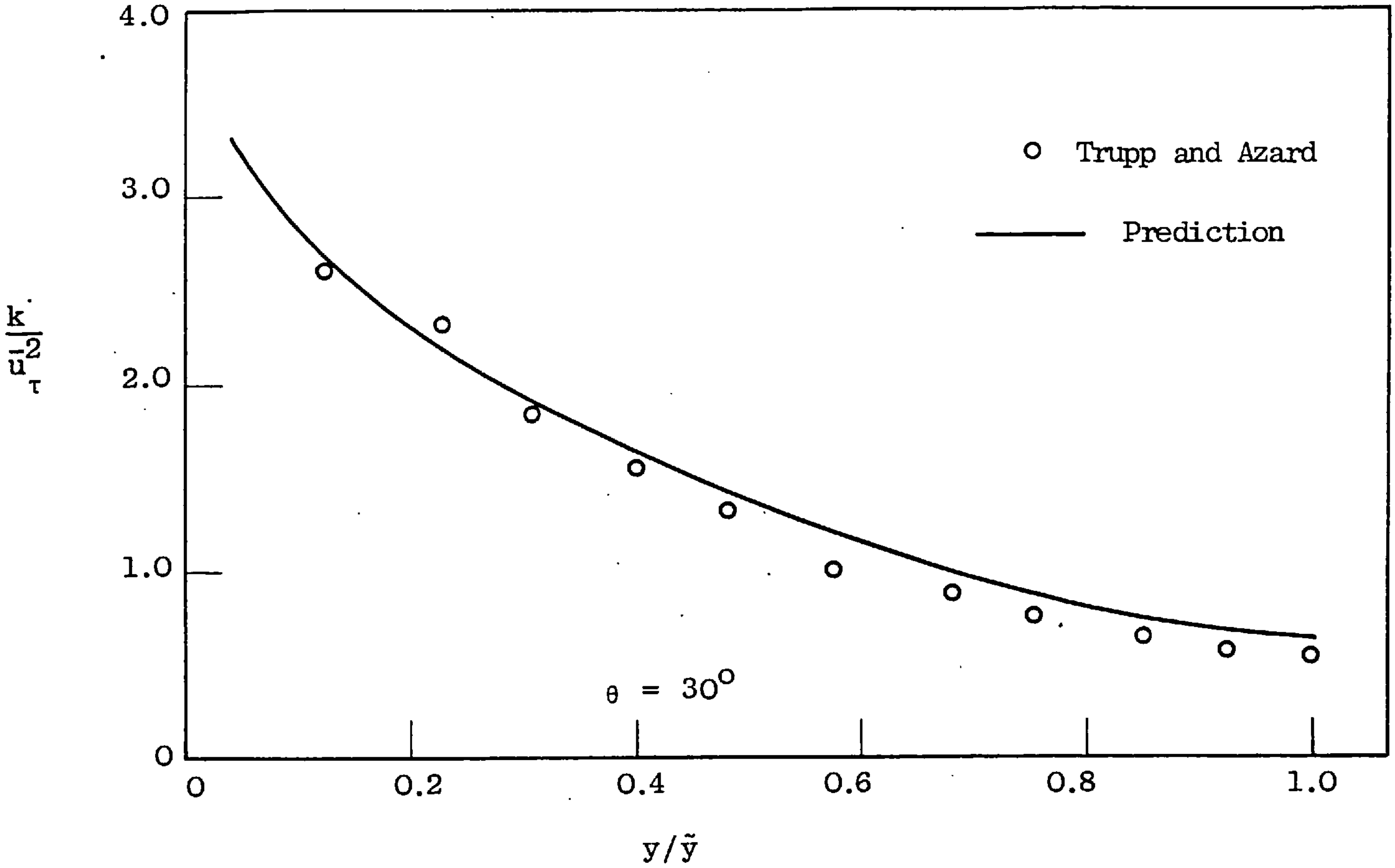

FIGURE 7.3.20(b): TURBULENT KINETIC ENERGY DISTRIBUTION
P/D = 1.35, Re = 60000.

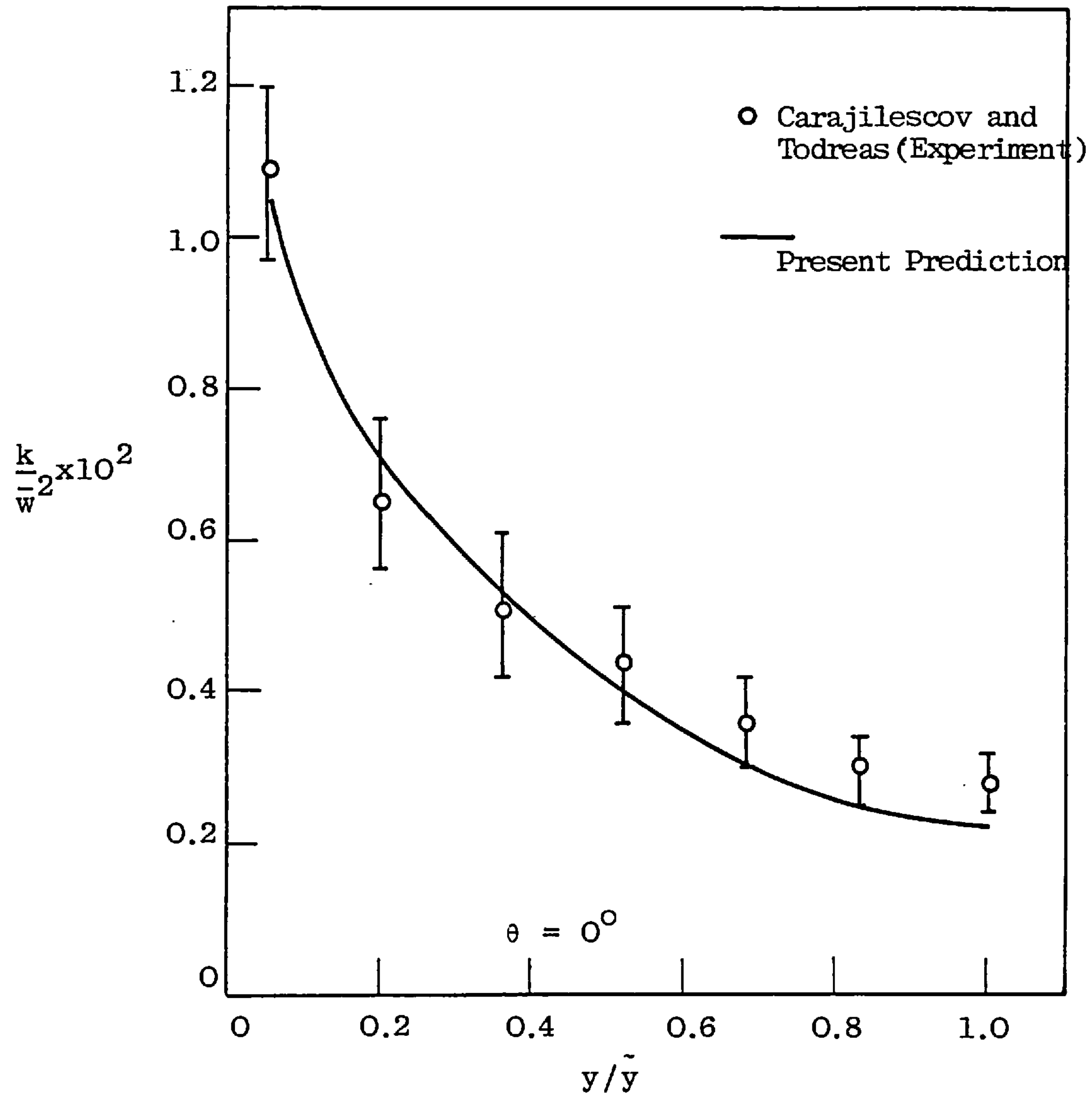

FIGURE 7.3.21(a): COMPARISON BETWEEN MEASURED AND COMPUTED KINETIC ENERGY PROFILES (P/D = 1.123, Re = 27000)

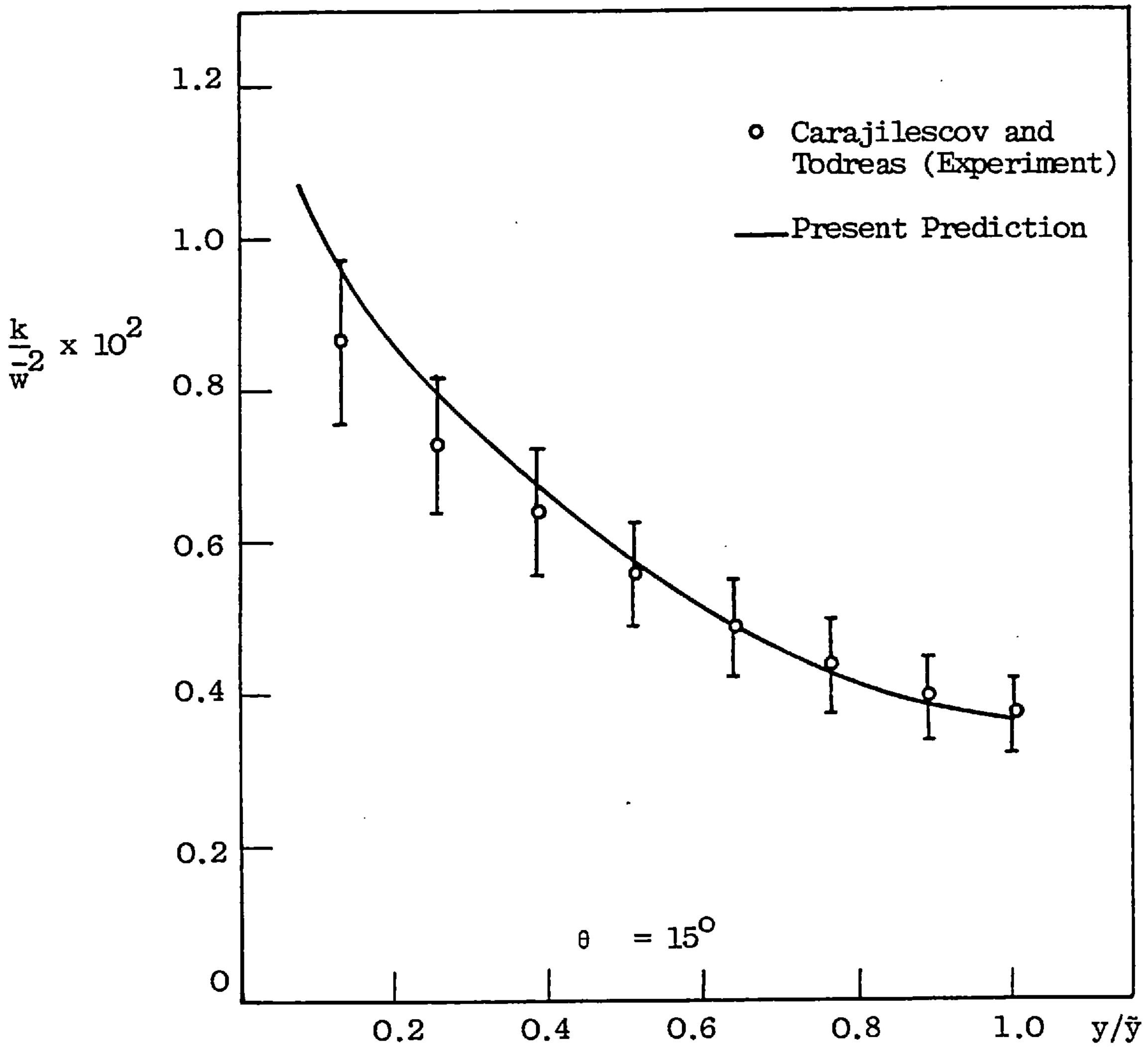

FIGURE 7.3.21(b): COMPARISON BETWEEN MEASURED AND COMPUTED KINETIC ENERGY PROFILES (P/D = 1.123, Re = 27000.

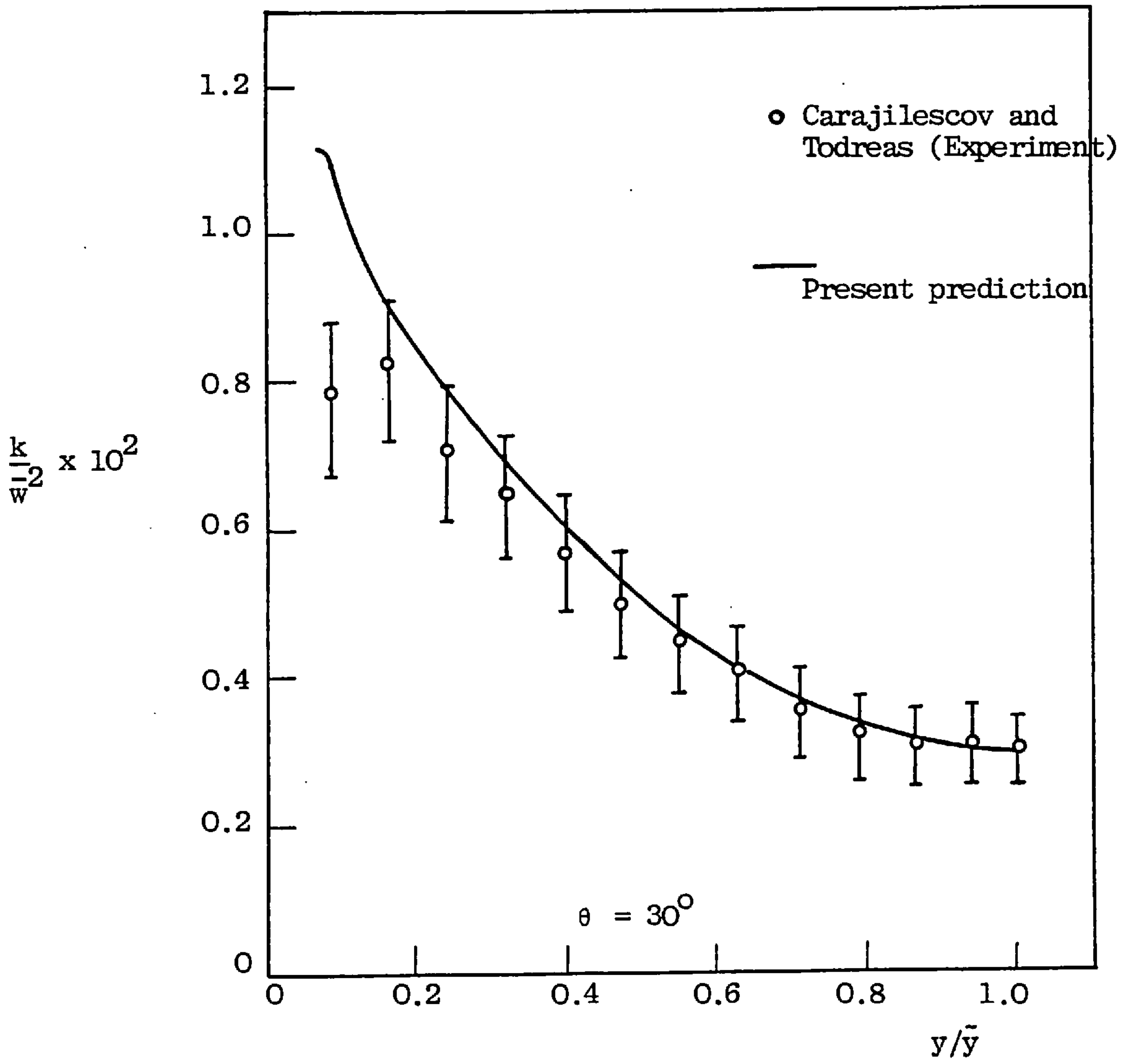

FIGURE 7.3.21(c): COMPARISON BETWEEN MEASURED AND COMPUTED KINETIC ENERGY PROFILES (P/D = 1.123, Re = 27000).

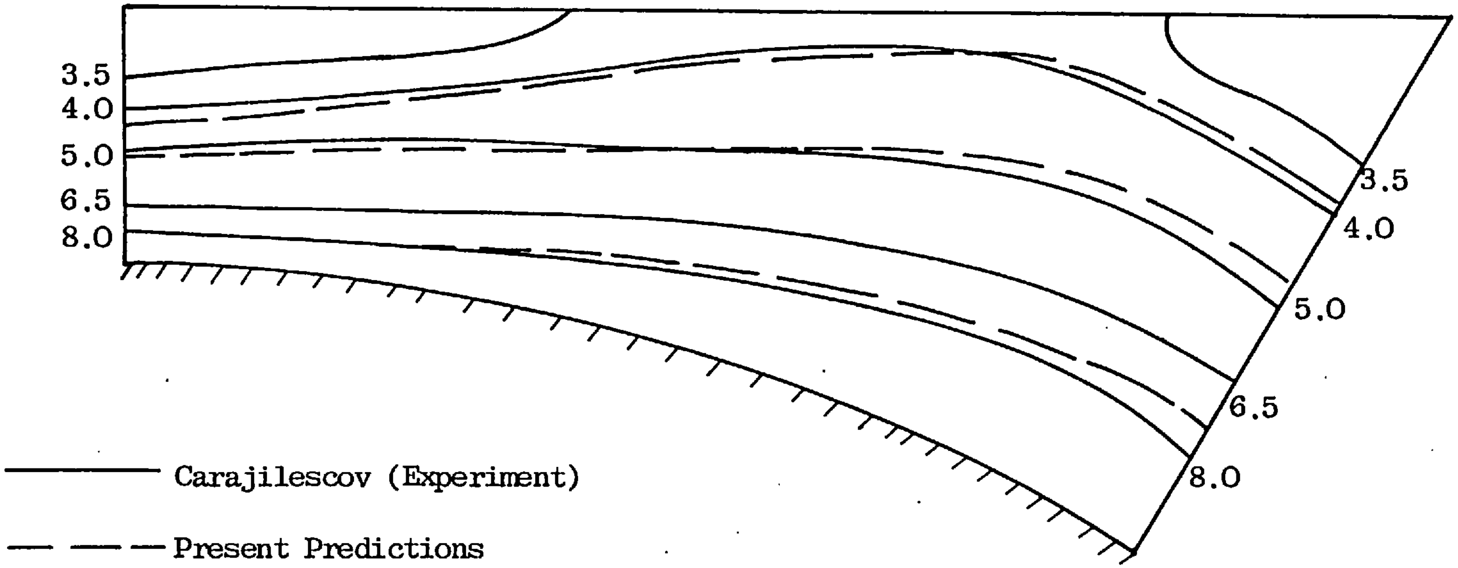

FIGURE 7.3.22: COMPARISON OF COMPUTED AND EXPERIMENTAL CONTOUR PLOTS OF $\frac{k}{\bar{w}^2} \times 10^3$; P/D = 1.123, Re = 27000.

the experimental points represent measurement uncertainties associated with the laser Doppler technique employed. Note that the kinetic energy values have been scaled by the mean axial velocity in the channel. Once again, in view of the enhanced inaccuracies in measurements near the wall, the results predicted with the present method are extremely favourable.

The above results have been cast into the form of constant-kinetic-energy contours; these are displayed in figure (7.3.22). The satisfactory agreement between the predicted levels and the experimental profiles is evident.

7.3.7 Reynolds-stress distributions

The experimental mean turbulent energy values discussed above were deduced from measurements of the individual turbulence intensities $\overline{v'^2}$, $\overline{u'^2}$ and $\overline{w'^2}$. Typical results for one such component, viz. $\overline{v'^2}$, for the test section used for Trupp and Azard, are shown in figure (7.3.23). The ordinate is equivalent to the square root values of the radial normal stress divided by the average wall shear stresses. The abscissa is, as usual, the radial distance from the rod surface normalized by the distance to the maximum-velocity line ($y=\tilde{y}$). The distribution of the radial turbulent intensity for fully-developed pipe flow, as determined by Laufer (1954), has been included for purposes of comparison. The latter deviates from the rod-bundle data by about twenty per cent. The divergence of the present predictions from the mean data is of the order of experimental error.

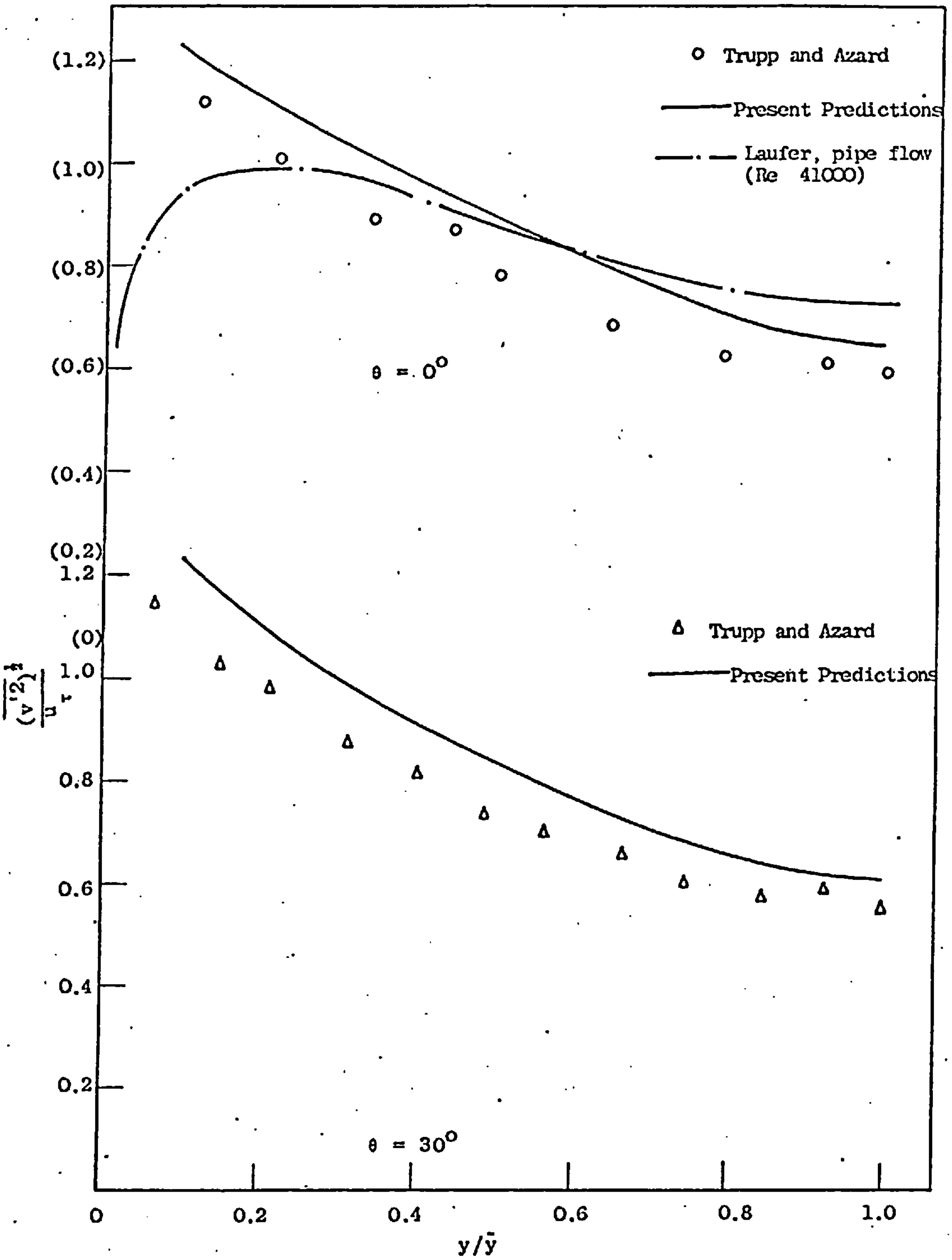

FIGURE 7.3.23: RADIAL TURBULENCE INTENSITIES, P/D = 1.35, Re = 60000.

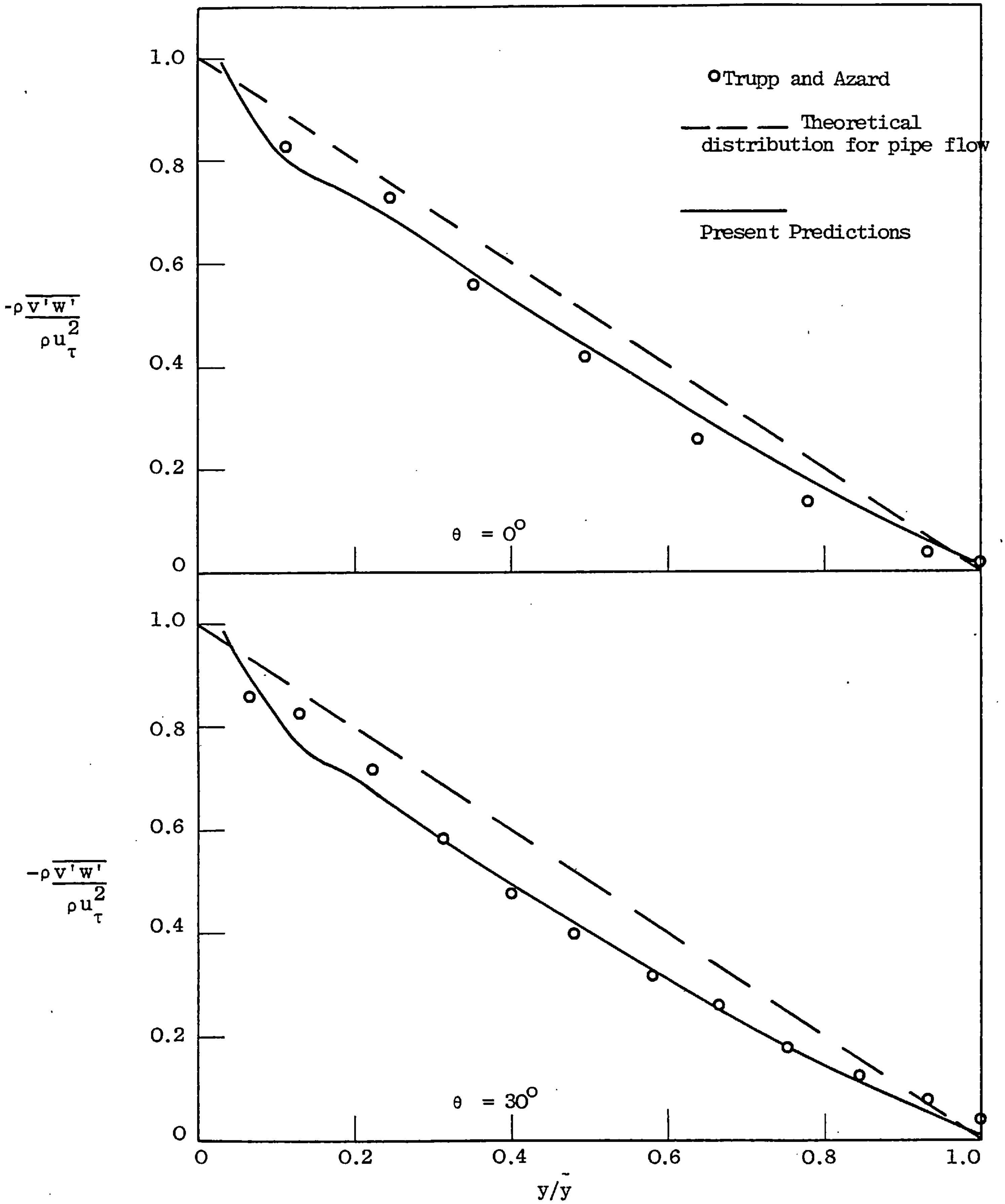

FIGURE 7.3.24: RADIAL DISTRIBUTION OF REYNOLDS STRESS $\rho\overline{v'w'}$; P/D= 1.35, Re = 60000.

The measured radial distributions of the shear stress $\overline{\rho v'w'}$ (generally the primary stress) along the $\theta = 0^o$ and $\theta = 30^o$ boundaries of the flow cell in an array of aspect ratio 1.35 are reproduced in figure (7.3.24); also shown for reference is the theoretical distribution for pipe flow. The mean data exhibit a linear trend over much of the channel, but lie about twenty per cent below the pipe flow profile. In contrast, the results obtained with the present numerical procedure are in good agreement with the measurements of Trupp and Azard.

7.3.8 Local heat-transfer coefficients

Computations have been performed for the case of a uniformly heated triangular array of rods, and the distribution of the local wall temperature - and hence the rate of heat transfer - around the periphery of the rods was determined. The results of one such calculation, corresponding to the experimental situation investigated by Redman et al (1966), are displayed in figure (7.3.25). The ordinate is the fully-developed Stanton number at any arbitrary angular location θ, normalized by the peripherally-averaged value. The Stanton number has been defined in the conventional manner, viz.

$$St = \frac{h}{\rho c_p \bar{w}} = \frac{\dot{Q}''_w}{\rho c_p \bar{w}(T_w - T_m)} \quad . \tag{7.3.1}$$

where h represents the local heat-transfer coefficient and T_w the wall temperature at the azimuthal position θ. $\dot{Q}''_w$ is the (constant) heat flux at the wall.

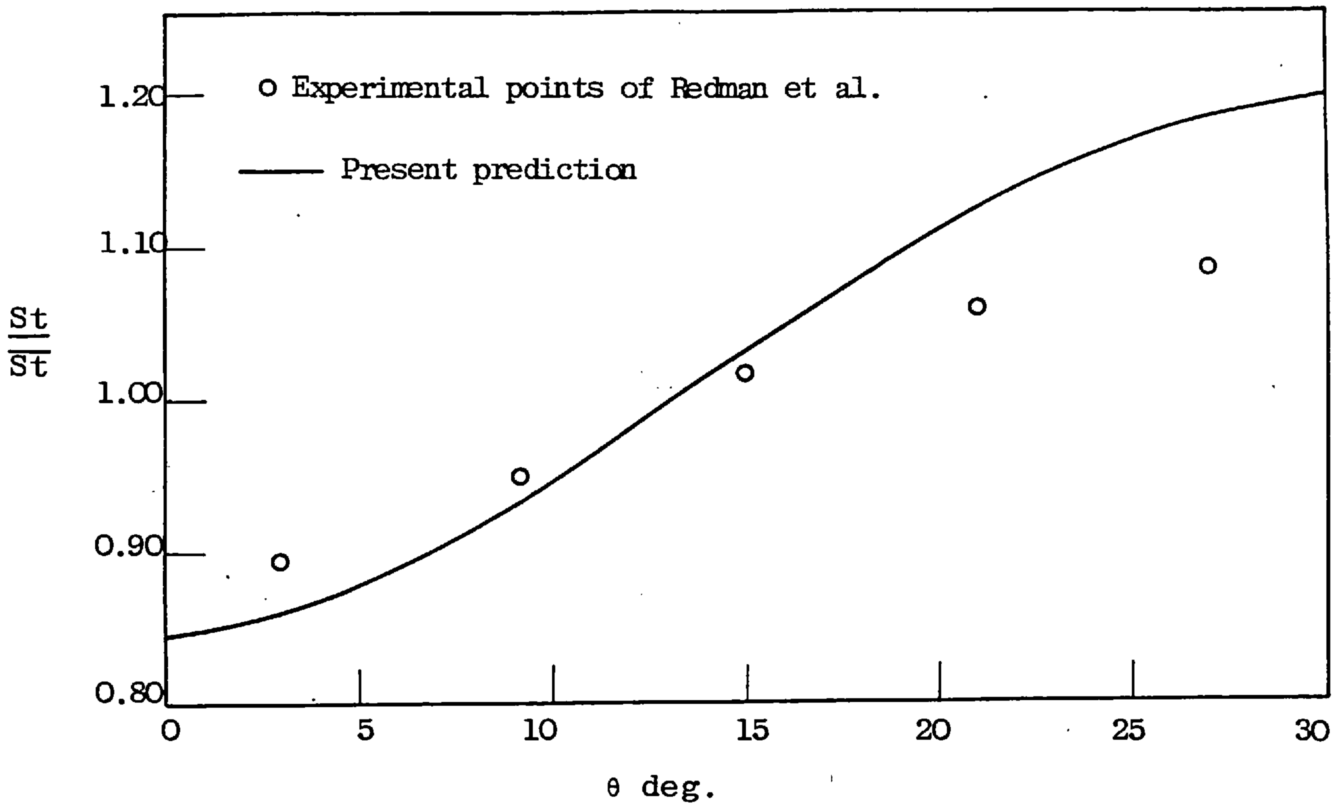

FIGURE 7.3.25: LOCAL STANTON-NUMBER VARIATION AROUND ROD PERIPHERY; P/D = 1.10, Re = 75000

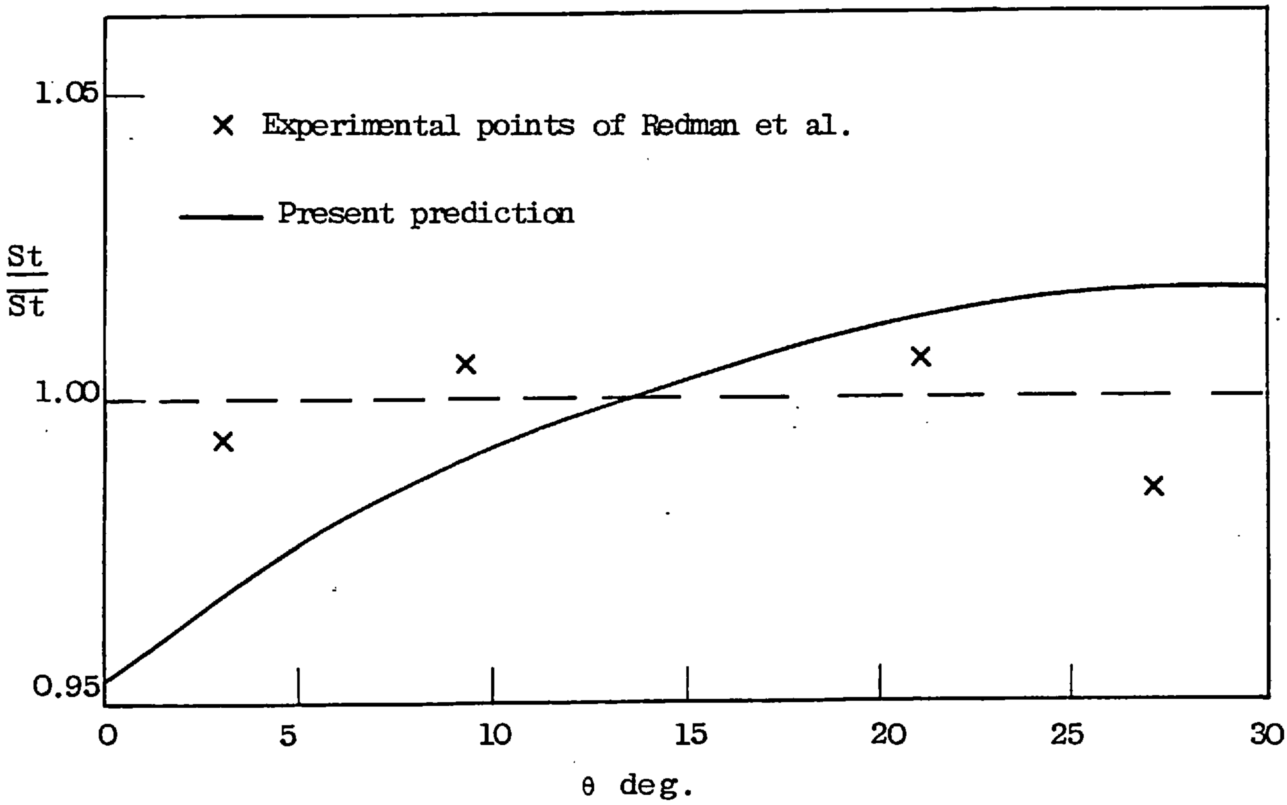

FIGURE 7.3.26: LOCAL STANTON-NUMBER VARIATION AROUND ROD PERIPHERY; P/D = 1.25, Re = 1.5×10^5

The experimental values shown in the figure were deduced by superposition of the measured "heat-influence functions" (see section 2.4.2). As expected on physical grounds, the least effective cooling of the surface occurs at the position corresponding to the minimum separation between adjacent rods ($\theta = 0^{\circ}$) where the velocity of the coolant is a minimum. It is seen that the present method tends to overestimate the circumferential heat-transfer dependence: variations of ±17% in $St/\overline{St}$ about the central position ($\theta = 15^{\circ}$) are predicted, in contrast with the value of ±10% indicated by the experiments. In the case of the larger aspect-ratio array (P/D = 1.25) investigated by Redman et al, the experimental points plotted in figure (7.3.26) represent the scatter about the mean line $St/\overline{St} = 1$, indicating an essentially uniform heat transfer rate around the rod. The present predictions, however, yield a variation of about 6% between the positions $\theta = 0^{\circ}$ and $\theta = 30^{\circ}$.

The discrepancies between the predicted and measured peripheral heat transfer are very probably due to finite-array effects which are present in any actual experimental test section. Enthalpy exchange by turbulent 'mixing' arises between adjacent subchannels that are never entirely homogenous. Also, 'cross-flows' can be induced which serve to augment the influence of the secondary motions in flattening the peripheral Stanton-number distributions in the array. Such mixing between subchannels has not been taken into consideration in the present model, and so the non-uniformity

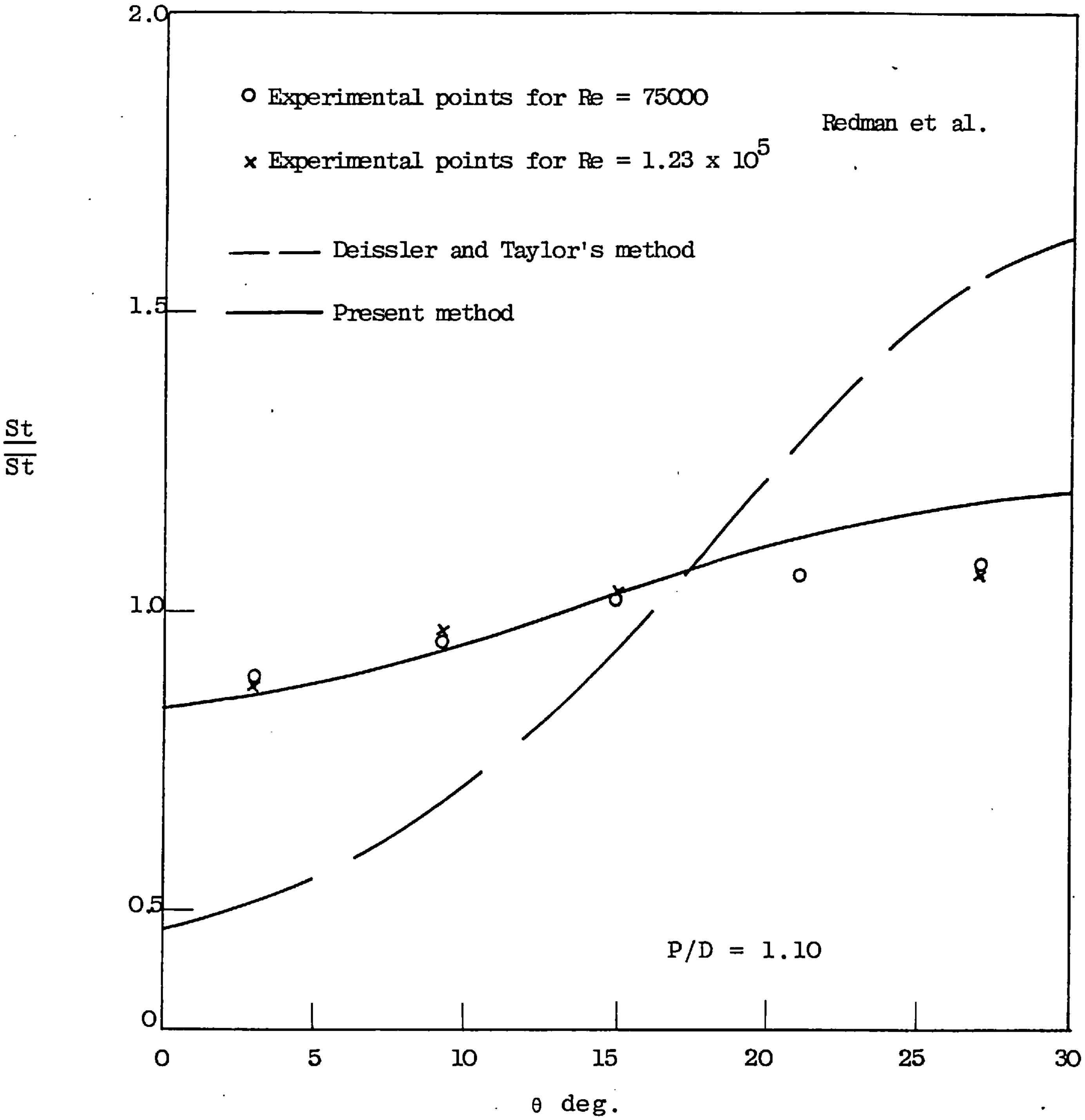

FIGURE 7.3.27: PERIPHERAL STANTON-NUMBER VARIATIONS: COMPARISON OF PREDICTIONS WITH EXPERIMENT

of the peripheral heat-transfer rate has been overestimated. However, the present method yields predictions that are very much superior to other theoretical schemes which attempt to calculate the heat transfer by neglecting secondary flow. For purposes of comparison, the results of figure (3.7.25) have been reproduced in figure (7.3.27), along with the local Stanton-number distribution calculated by the technique of Deissler and Taylor (see section 2.3.1) which is included in the paper of Redman et al. It is clear that the latter method grossly exaggerates the percentage variation in the local heat-transfer coefficient. Note also that a very weak dependence of this variation on the Reynolds number was detected by means of the present procedure: this is consistent with the observations of Redman et al.

7.3.9 Overall Nusselt numbers

The fully-developed mean Nusselt numbers were compared with the data of Redman et al and found to be underpredicted by about fifteen per cent. The experiments yielded an average value (for P/D = 1.10) that lay approximately twenty per cent above that calculated from the Dittus-Boelter correlation for pipe flow, viz.

$$Nu = 0.023\ Re^{0.8}\ Pr^{0.4} \quad . \qquad (7.3.2)$$

where Pr is the laminar Prandtl number of the fluid. The underprediction of the overall heat transfer by the present calculation method is in accord with the earlier discussion (section 7.3.8), where it was pointed out that enthalpy interchange through turbulent mixing and 'cross-flow' between subchannels served to enhance the level of heat transfer in any practical test section involving a small number of rods.

Predictions have also been made for a pitch-diameter ratio of 1.15 over the range of Reynolds number investigated by Sutherland and Kays (1966). The latter concluded from their measurements that equation (7.3.2) above gave pessimistic predictions of the heat-transfer rate in triangular rod arrays with P/D = 1.0. In the following table, the experimental values for the mean Nusselt number are compared with both the Dittus-Boelter correlation and the present computations over a relatively wide range of Reynolds number.

Re	Nu (Exptl)	Nu (Present)	Nu (eqn.7.3.2)
10 000	40	-*	31
15 000	54	-	43
20 000	67	59	55
30 000	91	82	76
50 000	135	121	114
70 000	176	159	150
100 000	230	209	200
150 000	320	286	275
200 000	400	359	347

The values in the third column of the above table were computed with a constant value of 0.85 ascribed to the 'turbulent

---

*footnote: The lower Reynolds numbers shown cannot be accurately investigated with the present turbulence model, and hence no attempt was made to obtain solutions in this range.

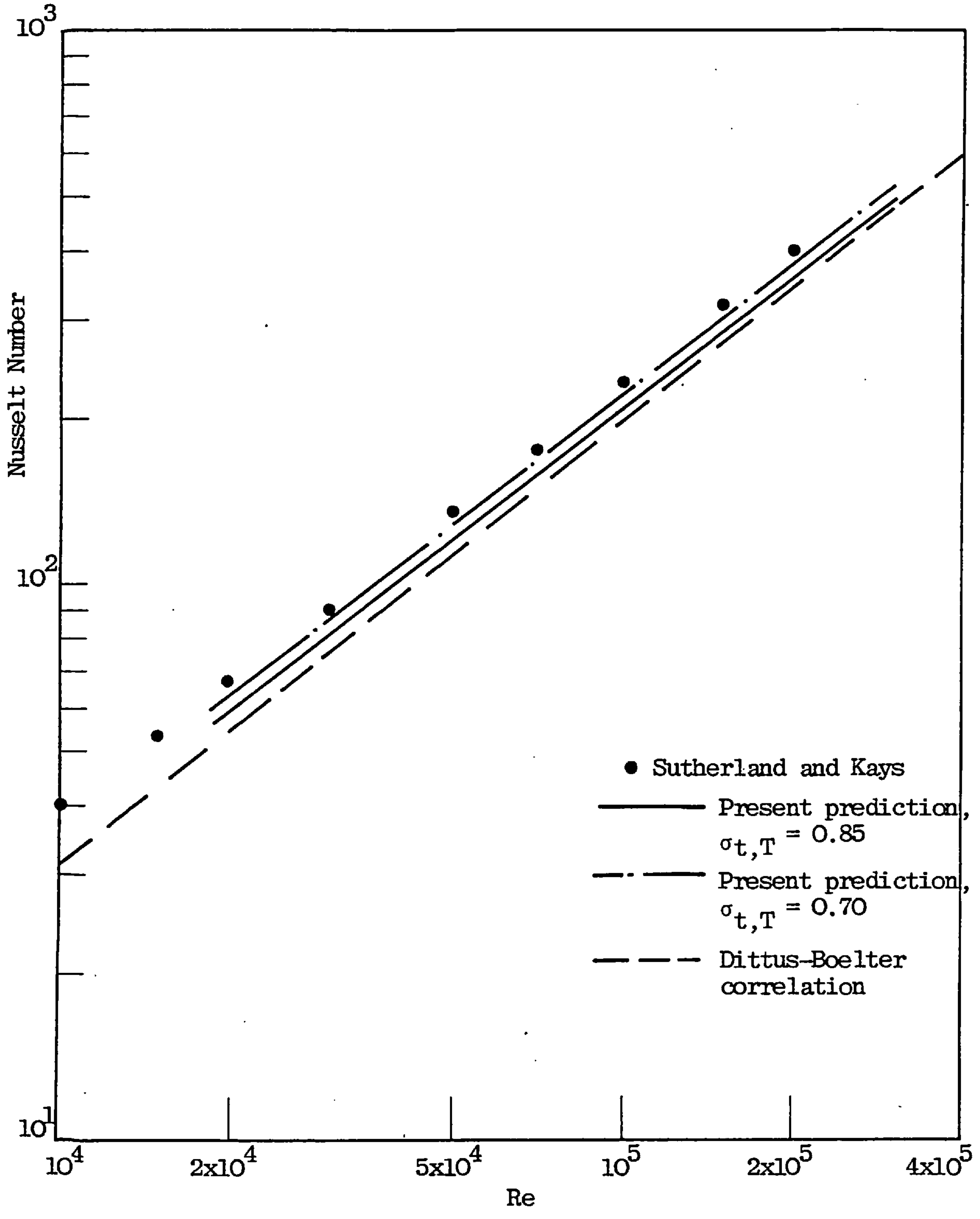

FIGURE 7.3.28: AVERAGE NUSSELT NUMBERS FOR P/D = 1.15. COMPARISON WITH DATA OF SUTHERLAND AND KAYS (1964)

Prandtl number', $\sigma_{t,T}$, for temperature (section 3.5 and Table 3.9.1). It was observed that the calculated Nusselt numbers were very sensitive to the value chosen for $\sigma_{t,T}$, generally increasing with decreasing Prandtl number. This is illustrated by way of figure (7.3.28) where the contents of the above table have been graphically represented. Also indicated in the figure is the prediction obtained when $\sigma_{t,T}$ was reduced to 0.7 in the temperature equation. In the latter case, the computed Nusselt numbers fall within the experimental uncertainty associated with the measurements of Sutherland and Kays. Consequently, no definite statement on the accuracy of the present model for heat transfer can be made until more reliable information converning the distribution of the 'turbulent Prandtl number' for temperature in rod bundles becomes available.

An interesting observation from figure (7.3.28) is that, for the particular aspect ratio investigated, both the experimental Nusselt numbers of Sutherland and Kays and those predicted by the present method show a dependence on the Reynolds number that is consistent with the 0.8-exponent in the Dittus-Boelter relation (equation 7.3.2.).

7.4 CLOSURE

In this chapter, the results of calculations performed with the $k \sim \varepsilon$ model of turbulence and the Launder-Ying formulation for the cross-stream Reynolds stresses have been presented. The emphasis has been placed on the prediction of flow and heat-transfer situations investigated by experimental workers; hence fully-developed flow in triangular arrays has received the greatest attention. Calculated distributions of axial velocity, wall shear stress, pressure drop, turbulence intensities etc. were found to be in very favourable agreement with the available experimental data. A secondary flow pattern consisting of a single loop of anti-clockwise rotation was predicted for smaller pitch-diameter ratios; at P/D values greater than about 1.20, a small counter loop began to form very near the gap, but became significant only at high Reynolds numbers. Generally, the strength and influence of the secondary flow field increased with diminishing aspect ratio. The computed levels of heat transfer were somewhat lower than experimental measurements, and the peripheral variation of the local heat-transfer coefficient was overestimated by a few per cent. Apart from deficiencies in both model and experiment, the most likely explanation is that finite-array effects influence the enthalpy exchange across subchannel boundaries more than they do for momentum. However, the present results represent a very appreciable improvement on other theoretical analyses hitherto performed.

CHAPTER 8

CONCLUDING REMARKS

8.1 PRESENT ACHIEVEMENTS

In conclusion, the main achievements of the research described in this thesis may be summarized as follows:-

a) A non-orthogonal finite-difference formulation that is, in principle, capable of application to three-dimensional flow problems in ducts of arbitrary geometry, has been successfully demonstrated. The major advantage of this approach is that, being based on a boundary-fitted coordinate system, it easily permits the accurate prescription of the conditions at the flow boundaries which generally determine the solution to the governing equations. This technique has been embodied in a three-dimensional computational procedure for parabolic flows, devised by Patankar and Spalding (1972).

b) Numerical solutions have been obtained for laminar flow and heat transfer in infinite rod arrays arranged on both square and equilateral-triangular lattices. This work represents the first application of finite-difference procedures to such problems. Wherever possible, predictions of axial velocities, wall shear-stress distributions, pressure drops, local heat-transfer coefficients, overall Nusselt numbers et cetera have been compared with existing analytical results;

very good agreement was observed. The greater flexibility of the present method over earlier analyses, however, has been illustrated by the ready accommodation of diverse wall heating conditions in a single analysis. Moreover, the developing flow region in these geometries, which has not been investigated to date, has been predicted.

c) A two-equation ($k\sim\varepsilon$) model of turbulence, in conjunction with the algebraic formulation for the Reynolds stresses in the cross-stream plane developed by Launder and Ying (1973), has been employed in the calculation of the fully-developed flow in an equilateral-triangular duct. The secondary flow field and its influence on both the local and bulk parameters of the flow have been successfully predicted. The universality of the model was preserved by making no alterations to the currently accepted values of the empirical constants contained within it. The Launder-Ying model has thus been demonstrated to be an accurate and efficient tool for the investigation of duct flows of interest to the engineer.

d) The present work represents the first reported three-dimensional analysis of the turbulent flow and heat-transfer behaviour in central subchannels of rod arrays. The use of the $k\sim\varepsilon$ model has obviated the need to depend on rod-bundle experimental input or empirical formulae in the computational procedure. This has been employed in conjunction with the algebraic shear-stress formulation of Launder and Ying (1973). As above, no modifications to the constants in the model were necessary, so that its universality was preserved. Results obtained with the present procedure compare very favourably with available experimental data and, even in the few cases of relatively poor agreement, represent a significant improvement on other hitherto published calculations. Moreover, such improvements have been secured at only modest computational expense. Consequently, the present method has proved itself as a powerful and efficient means of obtaining fundamental knowledge for rod-bundle design.

8.2 TOPICS FOR FUTURE CONSIDERATION

The following topics, stemming from the present work, are considered worthy of further investigation:-

a) With regard to the non-orthogonal coordinate system, it is anticipated that when duct cross-sections of very severe "non-orthogonality" are considered, poor convergence owing to the neglect of the extra terms in the pressure-correction equation will arise. Consequently, future work involving highly "distorted" flow domains may require the formulation of the full pressure-correction equation and the adoption of a more efficient means of solution than the ADI technique employed here.

b) The extension of the present method to wall and corner subchannels in a full rod bundle is the next logical step. However, there is experimental evidence that the anisotropy of the turbulence is even more severe here than in the central regions of the bundle. Hence, it will probably be necessary to replace the present model with one that involves the solution of equations (either differential or algebraic) for all components of the Reynolds stress. This step awaits further progress in the art of turbulence modelling.

c) Detailed experimental investigations of the turbulence structure in rod bundles have only recently been initiated. Moreover, as was discussed in chapter 2, many of the reported investigations leave much to be desired. In the narrow regions characteristic of most rod-bundle designs, the use of measuring probes that interfere with the flow is very undesirable. Consequently, the application of recent advances in laser-Doppler anemometry offers the greatest promise in the elucidation of the correct secondary flow distribution and turbulence structure in rod arrays.

d) Attention was drawn in chapter 7 to the fact that the turbulent heat-transfer calculations were sensitive to small changes in the value of $\sigma_{t,T}$. More information of both a theoretical and an experimental nature concerning $\sigma_{t,T}$ and the temperature "wall function" is necessary: this is especially true for liquid-metal flows, where much of the available information is still in a state of confusion.

e) The present method has not been applied to the solution of (turbulent) rod-bundle flows at low Reynolds numbers in very 'tight' (i.e. P/D less than about 1.08) clusters; this was because of the invalidity of the turbulence model under such conditions. However, almost all practical rod bundles are designed for normal operation at relatively high Reynolds numbers. Further extension of the present method to low-Re flows at narrow rod spacings would require the use of the low-Re version of the $k\sim\varepsilon$ model mentioned in section 3.6.

REFERENCES

ALY AMM, TRUPP, A.C. & GERRARD, A.D. (1978): "Measurements and prediction of fully developed turbulent flow in an equilateral triangular duct", J. Fluid Mech. Vol. 85, part 1, pp. 57-83.

AXFORD, R.A. (1967): "Two-dimensional multiregion analysis of temperature fields in reactor tube bundles", Nuc. Eng. & Des. Vol. 16, pp. 25-42.

BENDER, D.J. & MAGEE, D.M. (1969): "Turbulent heat transfer in a rod bundle with liquid metal coolant", GEAP-10052.

BENDER, D.J. & SWITICK, D.M. (1969): "Turbulent viscosity distribution in a rod bundle", ASME 68-WA/HT-36.

BENDER, D.J., SWITICK, D.M. & FIELD, T.H. (1967): "Turbulent velocity distributions in a rod bundle", GEAP-5411.

BRUNDRETT, E. & BAINES, W.D. (1964): "The production and diffusion of vorticity in duct flow", J. Fluid. Mech. Vol. 19, pp. 375-394.

BULEEV, N.I. (1963): "Theoretical model of the mechanism of turbulent exchange in fluid flow", AERE Translation No. 957.

BULEEV, N.I. (1964): "Theoretical model of turbulent transfer in three-dimensional fluid flow", 3rd U.N. Intern. Conf. Peaceful Uses of Atomic Energy, Geneva, paper no. 329.

CARAJILESCOV, P. (1975): "Experimental and analytical study of axial turbulent flows in an interior subchannel of a bare rod bundle", Ph.D. Thesis, Massachusetts Institute of Technology.

CARAJILESCOV, P. & TODREAS, N.E. (1976): "Experimental and analytical study of axial turbulent flows in an interior subchannel of a bare rod bundle", J. Heat Transfer, Trans. ASME, Vol. 98, pp. 262-268.

CARLSON, C.W. & IRVINE, T.F. (1961): "Fully developed pressure drop in triangular shaped ducts", J. Heat Transfer, Trans. ASME, Vol. 83, p. 441.

CREMERS, C.J. & ECKERT, E.R.G. (1962): "Hot-wire measurements of turbulence correlations in a triangular duct", J. Applied Mech. Trans. ASME, Vol. 29, pp. 609-614.

DALY, B.J. & HARLOW, F.H. (1970): "Transport equations of turbulence", Phys. of Fluids, Vol. 13, pp. 2634-2649.

DEISSLER, R.G. & TAYLOR, M.F. (1956): "Analysis of axial turbulent flow and heat transfer through banks of rods or tubes", Reactor Heat Transfer Conf., New York, TID-7529.

DEISSLER, R.G. & TAYLOR, M.F. (1959): "Analysis of turbulent flow and heat transfer in noncircular passages", N.A.S.A. Tech. Rep. R-31.

DINGEE, D.A. & CHASTAIN, J.W. (1956): "Heat transfer from parallel rods in axial flow", Reactor Heat Transfer Conf., New York, TID-7529.

DUNWOODY, N.T. (1962): "Thermal results for forced convection heat-transfer through elliptical ducts", J. Applied Mech., Trans. ASME, Vol. 29.

DWYER, O.E. (1966): "Analytical study of heat transfer to liquid metals flowing in-line through closely packed rod bundles", Nuc. Sci. & Engn. Vol. 25, pp. 343-358.

DWYER, O.E. & BERRY, H.C. (1970): "Laminar-flow heat transfer for in-line flow through unbaffled rod bundles", Nuc. Sci. & Engn. Vol. 42, pp. 81-88.

DWYER, O.E. & TU, P.S. (1960): "Analytical study of heat transfer rates for parallel flow of liquid metals through tube bundles: part I", Chem. Eng. Progn. Symp. Ser., 56, no. 30, p. 183.

EIFLER, W. & NIJSING, R. (1967): "Experimental investigation of velocity distribution and flow resistance in a triangular array of parallel rods", Nuc. Eng. & Des. Vol. 5, pp. 22-42.

FRIEDLAND, A.J. & BONILLA, C.F. (1961): "Analytical study of heat transfer rates for parallel flow of liquid metals through tube bundles: part II", Am. Inst. of Chem. Eng. J., 7, no. 1, p. 107.

GERARD, R. (1974): "Finite element solution for flow in non-circular conduits", Proc. ASCE, Vol. 100, HY3, p. 425.

GESSNER, F.B. & EMERY, A.F. (1976): "A Reynolds stress model for turbulent corner flows - part I: development of the model", J. Fluids Engn. 76-FE-C pp. 1-8.

GOSMAN, A.D., PUN, W.M., RUNCHAL, W.K., SPALDING, D.B. & WOLFSHTEIN, M. (1969): "Heat and Mass Transfer in Recirculating Flows", Academic Press, London.

HALL, C.H. & SVENNINGSSON, P.J. (1971): "Secondary flow velocities in a rod bundle of triangular array", Report AE-RL-1326, AB Atomenergi, Sweden.

HANJALIC, K. & LAUNDER, B.E. (1972): "A Reynolds stress model of turbulence and its application to thin shear flows", J. Fluid Mech. Vol. 52, pp. 609-638.

HARLOW, F.H. & NAKAYAMA, P.I. (1968): "Turbulent transport equations", Phys. of Fluids, Vol. 8, p. 2182.

HINZE, J.O. (1959): "Turbulence", McGraw Hill, New York.

HOFFMAN, H.W., WANTLAND, J.L. & STELZMAN, W.S. (1961): "Heat transfer with axial flow in rod clusters", Int. Developments in Heat Trans., paper no. 65, ASME, pp. 553-560.

IBRAGIMOV, M.K. et al. (1966): "Calculation of the tangential stresses at the wall of a channel and the velocity distribution in a turbulent flow of liquid", Soviet Atomic Energy, Vol. 21, no. 2, pp. 731-739.

IBRAGIMOV, M.K. et a. (1967): "Calculation of hydraulic resistivity coefficients for turbulent fluid flow in channels of noncircular cross section", Soviet Atomic Energy, Vol. 23, no. 4, pp. 1042-1047.

IQBAL, M., KHATRY, A.K. & AGGARWALA, B.D. (1972): "On the second fundamental problem of combined flow and forced convection through vertical non-circular ducts", Appl. Sci. Res. Vol. 26, pp. 183-208.

JAYATILLEKE, C.V.L. (1969): "The influence of Prandtl number and surface roughness on the resistance of the laminar sub-layer to momentum and heat transfer", Prog. in Heat Mass Transfer, Vol. 1, ed. by Grigull U & Hahne E, Pergamon Press, London.

JONES, W.P. & LAUNDER, B.E. (1969): "Prediction of low-Reynolds number phenomena with a two-equation model of turbulence", Int. J. Heat Mass Transfer, Vol. 16, pp. 1119-1130.

KESTIN, J. & RICHARDSON, P.D. (1963): "Warmeubertragung in turbulenten Grenzschichten", Forschung auf dem Gebiete des Ingenieurwesens, B.29, no. 4, pp. 93-104.

KHALIL, E.K.H., SPALDING, D.B. & WHITELAW, J.H. (1975): "The calculation of local flow properties in two-dimensional furnaces", Int. J. Heat Mass Transfer, Vol. 18, p. 775.

KJELLSTROM, B. (1971): "Studies of turbulent flow parallel to a rod bundle of triangular array", Report AE-RV-196, AB Atomenergi, Sweden.

KLINE, S.J., REYNOLDS, W.C., SCHRAUB, F.A. & RUNSTADLER, P.W. (1967): "The structure of turbulent boundary layers", J. Fluid Mech., Vol. 30, pp. 741-773.

KOKOREV, L.S., KORSON, A.S., KOSTYUNIN, B.N., PETROVICHEV, V.I. & STRUENZE, R.L. (1921): "Effect of secondary flows on the velocity distribution and hydraulic drag in turbulent liquid flows in noncircular channels", Heat Transfer-Soviet Research, Vol. 3 (1), p. 66.

KOLMOGOROV, A.N. (1942): "Equations of turbulent motions of an incompressible turbulent fluid", Izv. Akad. Nauk SSSR Ser. Phys, Vol. 6, No. 1/2, pp. 56-58 (Translated into English as Imperial College, London, Mech. Eng. Dept. Report ON/6, 1968).

LAUFER, J. (1954): "The structure of turbulence in fully-developed pipe flow", Nat. Adv. Comm. Aeron. (NACA) Report no. 1174, Washington.

LAUNDER, B.E., MORSE, A.P., RODI, W. & SPALDING, D.B. (1972): "The prediction of free shear flows - a comparison of six turbulence models" NASA Free Shear Flows Conf. Virginia NASA Report no. SP-311.

LAUNDER, B.E., REECE, G. & RODI, W. (1973): "Progress in the development of a Reynolds-stress turbulence closure", Imperial College, London, Mech. Eng. Dept. Report HTS/73/31.

LAUNDER, B.E. & SPALDING, D.B. (1972): "Mathematical models of Turbulence", Academic Press, London.

LAUNDER, B.E. & YING, W.M. (1973): "Prediction of flow and heat transfer in ducts of square cross-section", Proc. I. Mech. Engngs. Vol. 187, pp. 455-461.

MAREK, J., MAUBACH, K. & REHME, K. (1973): "Heat transfer and pressure drop performance of rod bundles arranged in square arrays", Int. J. Heat Mass Transfer, Vol. 16, pp. 2215-2228.

MARESCA, M.W. & DWYER, O.E. (1964): "Heat transfer to mercury flowing in-line through a bundle of circular rods", J. Heat Transfer, Trans. ASME, Vol. 86, p. 180.

MEYDER, R. (1975a): "Solving the conservation equations in fuel rod bundles exposed to parallel flow by means of curvilinear orthogonal coordinates", J. Comp. Phys. Vol. 17, p. 53.

MEYDER, R. (1975b): "Turbulent velocity and temperature distribution in the central subchannel of rod bundles", Nuc. Eng. & Des. Vol. 35, pp. 181-189.

McGUIRK, J. (1975): "Prediction of turbulent buoyant jets in co-flowing streams", Imperial College, London, Mech. Eng. Dept. Report HTS/75/24. Ph.D. Thesis, University of London, 1975.

NAOT, D., SHAVIT, A. & WOLFSHTEIN, M. (1972): "Fully-developed turbulent flow in a square channel", Report TME

154, Mech. Eng. Dept., Technion, Haifa, Israel.

NIJSING, R., GARGANTINI, I. & EIFLER, W. (1966): "Analysis of fluid flow and heat transfer in a triangular array of parallel heat-generating rods", Nuc. Eng. & Des. Vol. 4, pp. 375-398.

NIJSING, R. (1972): "Heat exchange and heat exchangers with liquid metals", AGARD-LS-57-72.

NIKURADSE, J. (1926): "Untersuchungen uber die Geschmindigheits in turbulenten Stromungen", Forrschft. Ver. dt. Ing. 281.

NIKURADSE, J. (1930): "Untersuchungen uber turbulente Stromungen in nicht Kreisformigen Rohen", Ingenieur-Archiv. Vol. 1, pp. 306-322.

PALMER, L.K. & SWANSON, L.L. (1961): "Measurements of heat transfer coefficients, friction factors and velocity profiles for air flowing parallel to closely spaced rods", Intern. Developments in Heat Transfer, paper no. 63, ASME, V3, pp. 535-542.

PATANKAR, S.V. & SPALDING, D.B. (1970): "Heat and Mass Transfer in boundary-layers", Intertext Books, London.

PATANKAR, S.V. & SPALDING, D.B. (1972): "A calculation procedure for heat, mass and momentum transfer in three-dimensional parabolic flows", Int. J. Heat Mass Transfer, Vol. 15, pp. 1787-1806.

PRANDTL, L. (1925): "Bericht uber Untersuchungen zur ausgebildeten Turbulenz", Z angew Math Mech (ZAMM), Vol. 5, no. 2, pp. 136-139.

PRATAP, V.S. & SPALDING, D.B. (1975): "Numerical computations of flows in curved ducts", Aero. Quarterly, Vol. 26, pp. 219-228.

RAMACHANDRA, V. & SPALDING, D.B. (1976): "Flow and heat transfer in square and rectangular-sectional ducts", Imperial College, London, Mech. Eng. Dept. Report HTS/76/21.

RAMM, H. & JOHNANNSEN, L. (1975): "A phenomenological turbulence model and its application to heat transport in infinite rod arrays with axial turbulent flow", J. Heat Transfer, Trans. ASME, Series C, Vol. 97.

REDMAN, J.D. McKEE, G. & RULE, I.C. (1966): "The influence of surface heat flux distribution and surface temperature distribution on turbulent forced convection heat transfer in clusters of tubes in which the flow of coolant is parallel to the axis of the tubes". Proc. of 3rd Intern. Heat Transfer Conf. Vol. 1, pp. 186-198.

RODI, W. (1972): "The prediction of free turbulent boundary-layers by use of a two-equation model of turbulence", Imperial College, London, Mech. Eng. Dept. Report HTS/72/24.

ROHSENOW, W.M. & HARTNETT, J.P. (1973): "Handbook of Heat Transfer", Prentice-Hall, New York.

ROTTA, J. (1951): "Statistiche Theorie nichthomogener Turbulenz", Z. Phys. Vol. 129, pp. 547-572.

ROWE, D.S. (1973): "Measurement of turbulent velocity intensity and scale in rod bundle flow channels", BNNL-1736, UC-80, Battelle, USA.

RUNCHAL, A.K. (1969): "Transfer processes in steady two-dimensional separated flows", Imperial College, London, Mech. Eng. Dept. Report HTS/69/18.

SCHENK, J. & BONG SWY HAN (1967): "Heat transfer from laminar flow in ducts with elliptic cross-section", Appl. Sci. Res. Vol. 17.

SHAH, R.K. & LONDON, A.L. (1971): "Laminar forced convection heat-transfer and flow friction in straight and curved ducts - a summary of analytical solutions", Technical Report 20.75, Dept. of Mech. Eng. Stanford University.

SINGHAL, A.K. & SPALDING, D.B. (1975): "Prediction of two-dimensional boundary layers with the aid of the $k\sim\varepsilon$ model of turbulence", Imperial College, London, Mech. Eng. Dept. Report HTS/75/15.

SPARROW, E.M. & LOEFFLER, A.L. Jnr. (1959): "Longitudinal laminar flow between cylinders arranged in regular array", A.I.Ch.E. Journal, Vol. 5, pp. 325, 329.

SPARROW, E.M., LOEFFLER, A.L. Jnr. & HIBBARD, H.A. (1961):

"Heat transfer to longitudinal laminar flow between cylinders", J. Heat Transfer, Trans. ASME, Vol. 83, pp. 415-422.

SUBBOTIN, V.I. et al. (1964): "Heat removal from the reactor fuel elements cooled by liquid metal", 3rd Intern. Conf. on Peaceful Uses of Atomic Energy, no. 28, p. 328.

SUBBOTIN, V.I. et al. (1971): "Velocity field of turbulent fluid flow in a longitudinal streamline of clusters of rods", AEC-translation no. 7189.

SUTHERLAND, W.A. & KAYS, W.M. (1966): "Heat transfer in parallel rod arrays", J. Heat Transfer, Trans, ASME, Vol. 88, pp. 117-124.

TATCHELL, D.G. (1975): "Convection processes in confined, three-dimensional boundary layers", Ph.D. Thesis, University of London. Also, Imperial College, London, Mech. Eng. Dept. Report HTS/75/20.

TRUPP, A.C. & AZAD, R.S. (1975): "The structure of turbulent flow in triangular array rod bundles", Nuc. Eng. & Des. Vol. 32, pp. 47-84.

VAN DRIEST, R. (1976): "On turbulent flow near a wall", Journal of Aerosp. Sci. Vol. 23, no. 11, pp. 1007-1011.

NOMENCLATURE

Symbol	Meaning
a	Radius of circular pipe (fig. 5.2.1(a)) or semi-major axis of elliptic duct (fig. 5.2.1(b)).
A	Coefficients in the general finite-difference equation (eqns. 4.3.8, 4.3.9).
b	Semi-minor axis of elliptic duct (fig. 5.2.1(b)).
B	'Source-term' in the general finite-difference equation (eqns. 4.3.8, 4.3.9).
C_1, C_2	Empirical constants appearing in transport equation for ε. Values given in Table 3.9.1.
$C_{\phi 1}$, $C_{\phi 2}$	Constants in Launder-Ying algebraic stress model (eqns. 3.7.9-3.7.10). Values given in Table 3.9.1.
C_μ	Empirical constant, defined via eqn. (3.6.1).
C_p	Specific heat at constant pressure.
C_{sec}	Constant in Nijsing's secondary-flow profile, eqn. (2.3.10).
D	Diameter of rod.
D_e	Equivalent hydraulic diameter, defined as 4 x flow area/wetted perimeter.

E	Empirical constant in logarithmic law of the wall, eqn. (4.5.1).
f	Fully-developed friction factor, defined by equation (5.3.22).
G	Geometric function, expressing non-orthogonality of calculation domain: definition - eqn. (3.4.12).
G_k	Rate of generation of the turbulent energy per unit volume, given by eqn. (3.8.3).
h	Local heat-transfer coefficient
$\bar{h}$	Wall-averaged heat-transfer coefficient.
k	Time-averaged turbulent kinetic energy: eqn. (3.4.22).
k_L	Molecular thermal conductivity of fluid.
ℓ	Length-scale of turbulence: $\ell = C_\mu k^{3/2}/\varepsilon$.
m_p	'Mass error' in pressure-correction equation, defined through eqn. (4.4.3).
Nu	Mean Nusselt number, defined by eqn. (5.3.23).
p	Pressure
$\bar{p}$	Mean pressure at any longitudinal station.
P	Pitch of rod array (fig. 1.1.2).
P_T	'Jayatilleke P-function' for temperature: eqn. (4.5.5).

Pr	Molecular Prandtl number of fluid.
$\dot{Q}''_w$	Wall heat flux.
r	Radial coordinate in cylindrical-coordinate system.
r_s	Radius of rod (=D/2) in rod-bundle flow.
Re	Reynolds number, usually defined as $\bar{w}D_e/\nu$.
St	Stanton number, defined by eqn. (7.3.1).
$\overline{St}$	Rod-averaged Stanton number, defined as $\overline{h}/\rho c_p\overline{w}$
T	Temperature (^oC).
T_W	Local wall temperature.
$\bar{T}_W$	Average wall temperature.
T_m	"Cup-mixed" mean temperature.
u_τ	Local 'friction velocity', defined as $(\tau_w/\rho)^{\frac{1}{2}}$.
$\bar{u}_\tau$	Mean friction velocity, defined as $(\bar{\tau}_w/\rho)^{\frac{1}{2}}$.
u,v,w	Time-averaged velocity components in circumferential, radial and axial directions respectively.
$\bar{w}$	Volume-averaged (bulk) velocity in the duct.
W_{IN}	Mean axial velocity at the inlet.
y	Normal distance from a wall.

$\tilde{y}$	In rod bundles, radial distance from rod wall to maximum-velocity surface for arbitrary angular location.
$\tilde{y}_{max}$	Maximum value of $\tilde{y}$ in a given geometry. In triangular arrays this corresponds to $\tilde{y}$ at $\theta = 30^o$.
z	Axial coordinate. Distance downstream of the inlet.

Greek symbols

α_1, α_2	Empirical constants, defined through eqns. (3.7.9) and (3.7.10).
Γ_ϕ	Laminar "exchange coefficient" for general variable ϕ.
$\Gamma_{t,\phi}$	Turbulent "exchange coefficient" for ϕ.
$\Gamma_{eff,\phi}$	Effective "exchange coefficient" for ϕ: eqn. (3.5.7).
Δr, $\Delta\theta$	Geometrical parameter, defined by eqns. (3.4.10) and (3.4.11).
ε	Dissipation rate of turbulent kinetic energy per unit volume
$\varepsilon_{M.r}$, $\varepsilon_{M.\theta}$	Eddy diffusivities for momentum in radial and peripheral directions respectively.
η , ξ	Cross-stream coordinates in non-orthogonal coordinate system.

θ	Angular coordinate. In rod bundles, measured from the line of least separation between rods.
κ	Constant in logarithmic law of the wall, eqn. (4.5.1).
λ	Aspect ratio $(\frac{b}{a})$ of elliptic duct.
μ	Molecular viscosity.
μ_t, μ_{eff}	Turbulent and effective viscosities respectively: eqn. (3.4.23).
ν	Kinematic viscosity $(=\mu/\rho)$.
ϕ	General scalar variable.
ρ	Density (constant) of fluid.
$\sigma_{t,\phi}$	Turbulent Prandtl-Schmidt number for T. Defining eqn. (3.5.6).
τ_w	Local wall shear stress.
$\bar{\tau}_w$	Average wall shear stress.

APPENDIX A

A.1 TRANSFORMATION OF THE CONTINUITY AND MOEMTUM EQUATIONS INTO THE (η ,ξ ,z) COORDINATE SYSTEM

Combination of the equations (3.4.1) to (3.4.4) with the shear-stress expressions (3.4.5) to (3.4.9) yields the following differential equations for continuity and momentum in the (r,θ,z) coordinate system:-

Continuity

$$\frac{1}{r}\frac{\partial}{\partial r}(rv) + \frac{1}{r}\frac{\partial u}{\partial \theta} + \frac{\partial w}{\partial z} = 0 \quad , \qquad (A.1.1)$$

u-velocity

$$\frac{\rho}{r}\frac{\partial u^2}{\partial \theta} + \frac{\rho}{r}\frac{\partial}{\partial r}(rvu) + \rho\frac{\partial (wu)}{\partial z} + \rho\frac{uv}{r} = -\frac{1}{r}\frac{\partial p}{\partial \theta}$$

$$+ \mu\left[\frac{1}{r^2}\frac{\partial^2 u}{\partial \theta^2} + \frac{1}{r}\frac{\partial}{\partial r}\left(r\frac{\partial u}{\partial r}\right) + \frac{2}{r^2}\frac{\partial v}{\partial \theta} - \frac{u}{r^2}\right]$$

$$- \rho\left[\frac{\partial \overline{u'^2}}{r\partial \theta} + \frac{\partial \overline{(u'v')}}{\partial r} + \frac{2\overline{u'v'}}{r}\right] \quad , \qquad (A.1.2)$$

v-velocity

$$\frac{\rho}{r}\frac{\partial}{\partial \theta}(vu) + \frac{\rho}{r}\frac{\partial (rv^2)}{\partial r} + \rho\frac{\partial (wv)}{\partial z} - \rho\frac{u^2}{r} = -\frac{\partial p}{\partial r} + \mu\left[\frac{1}{r^2}\frac{\partial^2 v}{\partial \theta^2}\right.$$

$$\left. + \frac{1}{r}\frac{\partial}{\partial r}\left(r\frac{\partial v}{\partial r}\right) - \frac{2}{r^2}\frac{\partial u}{\partial \theta} - \frac{v}{r^2}\right]$$

$$\rho\left[\frac{\partial \overline{v'^2}}{\partial r} + \frac{1}{r}\frac{\partial \overline{(u'v')}}{\partial \theta} + \frac{(\overline{v'^2} - \overline{u'^2})}{r}\right], \qquad (A.1.3)$$

w-velocity

$$\frac{\rho}{r}\frac{\partial(uw)}{\partial\theta} + \frac{\rho}{r}\frac{\partial(rvw)}{\partial r} + \rho\frac{\partial w^2}{\partial z} = -\frac{d\bar{P}}{dz} + \mu\left[\frac{1}{r^2}\frac{\partial^2 w}{\partial\theta^2} + \frac{1}{r}\frac{\partial}{\partial r}\left(r\frac{\partial w}{\partial r}\right)\right]$$

$$-\rho\left[\frac{1}{r}\frac{\partial}{\partial r}\left(r\overline{v'w'}\right) + \frac{1}{r}\frac{\partial}{\partial\theta}\left(\overline{u'w'}\right)\right]. \qquad \text{(A.1.4)}$$

The transformation of the above equations proceeds by way of the transformation identities:

$$\frac{\partial}{\partial r} \equiv \frac{\partial}{\partial\eta}\cdot\frac{\partial\eta}{\partial r} + \frac{\partial}{\partial\xi}\cdot\frac{\partial\xi}{\partial r} \quad ,$$

$$\text{(A.1.5)}$$

$$\frac{\partial}{\partial\theta} \equiv \frac{\partial}{\partial\eta}\cdot\frac{\partial\eta}{\partial\theta} + \frac{\partial}{\partial\xi}\cdot\frac{\partial\xi}{\partial\theta} \quad .$$

From the definitions (3.2.1) and (3.2.2), we obtain the following relations:

$$\frac{\partial}{\partial r} \equiv \frac{1}{\Delta r}\frac{\partial}{\partial\eta} \quad , \qquad \text{(A.1.6a)}$$

$$\frac{\partial}{\partial\theta} \equiv \frac{1}{\Delta\theta}\frac{\partial}{\partial\xi} - \frac{1}{\Delta r}\left[\frac{\partial r_s}{\partial\theta} + \eta\frac{d(r_n - r_s)}{d\theta}\right]\cdot\frac{\partial}{\partial\eta} \equiv \frac{1}{\Delta\theta}\frac{\partial}{\partial\xi} - \frac{Gr}{\Delta r}\frac{\partial}{\partial\eta} \; .$$

$$\text{(A.1.6b)}$$

where Δr, $\Delta\theta$ and the geometric function G have been defined via equations (3.4.10) to (3.4.12).

On employment of (A.1.6a) and (A.1.6b), and after some tedious but straight forward manipulation of terms, equations (A.1.1) to (A.1.4) now transform to the forms (3.4.13) to (3.4.16) presented in section 3.4 of this thesis.

A.2 TRANSFORMATION OF THE ϕ -EQUATION INTO THE NON-ORTHOGONAL COORDINATE SYSTEM

The conservation equation for the general scalar variable has been given in polar-cylindrical coordinates in section 3.5 (namely, equation 3.5.1).

The use of the transformation relations (A.1.6a) and (A.1.6b) in equation (3.5.1) leads to:

$$\begin{aligned}
&\frac{\rho}{r\Delta r}\frac{\partial}{\partial\eta}(rv\phi) + \frac{\rho}{r\Delta\theta}\frac{\partial}{\partial\xi}(u\phi) + \rho\frac{\partial(w\phi)}{\partial z} - \rho\frac{G}{\Delta r}\frac{\partial(u\phi)}{\partial\eta} \\
&\quad = \frac{1}{r\Delta\theta}\frac{\partial}{\partial\xi}\left[\frac{\Gamma_\phi}{r\Delta\theta}\frac{\partial\phi}{\partial\xi} - \Gamma_\phi\frac{G}{\Delta r}\frac{\partial\phi}{\partial\eta}\right] - \frac{G}{\Delta r}\frac{\partial}{\partial\eta}\left[\frac{\Gamma_\phi}{r\Delta\theta}\frac{\partial\phi}{\partial\xi}\right. \\
&\quad \left. - \Gamma_\phi\frac{G}{\Delta r}\frac{\partial\phi}{\partial\eta}\right] + \frac{1}{r\Delta r}\frac{\partial}{\partial\eta}\left(\frac{r\Gamma_\phi}{\Delta r}\frac{\partial\phi}{\partial\eta}\right) - \rho\left[\frac{1}{r\Delta\theta}\frac{\partial(\overline{u'\phi'})}{\partial\xi}\right. \\
&\quad \left. + \frac{1}{r\Delta r}\frac{\partial}{\partial\eta}(r\overline{v'\phi'}) - \frac{G}{\Delta r}\frac{\partial(\overline{u'\phi'})}{\partial\eta}\right] + S_\phi \quad , \qquad (A.2.1)
\end{aligned}$$

The terms on the right-hand side of equation (A.2.1) may be re-arranged as follows:

$$\begin{aligned}
\text{R.H.S.} \equiv\; &\frac{1}{r\Delta\theta}\frac{\partial}{\partial\xi}\left[\frac{\Gamma_\phi}{r\Delta\theta}\frac{\partial\phi}{\partial\xi} - \Gamma_\phi\frac{G}{\Delta r}\frac{\partial\phi}{\partial\eta}\right] + \frac{1}{r\Delta r}\frac{\partial}{\partial\eta}\left[\frac{r\Gamma_\phi(1+G^2)}{\Delta r}\frac{\partial\phi}{\partial\eta}\right. \\
&\left. - \Gamma_\phi\frac{G}{\Delta\theta}\frac{\partial\phi}{\partial\xi}\right] - \frac{1}{r\Delta r}\frac{\partial}{\partial\eta}\left(\frac{G^2 r\Gamma_\phi}{\Delta r}\frac{\partial\phi}{\partial\eta}\right) + \frac{1}{r\Delta r}\frac{\partial}{\partial\eta}\left(\Gamma_\phi\frac{G}{\Delta\theta}\frac{\partial\phi}{\partial\xi}\right) \\
&- \frac{G}{\Delta r}\frac{\partial}{\partial\eta}\left(\frac{\Gamma_\phi}{r\Delta\theta}\frac{\partial\phi}{\partial\xi}\right) + \frac{G}{\Delta r}\frac{\partial}{\partial\eta}\left(\Gamma_\phi\frac{G}{\Delta r}\frac{\partial\phi}{\partial\eta}\right) \\
&- \rho\left[\frac{1}{r\Delta\theta}\frac{\partial(\overline{u'\phi'})}{\partial\xi} + \frac{1}{r\Delta r}\frac{\partial}{\partial\eta}(r\overline{v'\phi'}) - \frac{G}{\Delta r}\frac{\partial\overline{u'\phi'}}{\partial\eta}\right] + S_\phi \quad ;
\end{aligned}$$

On simplifying, this becomes:

$$\text{R.H.S.} \equiv \frac{1}{r\Delta\theta}\frac{\partial}{\partial\xi}\left[\frac{\Gamma_\phi}{r\Delta\theta}\frac{\partial\phi}{\partial\xi} - \Gamma_\phi\frac{\partial\phi}{\partial\eta}\right] + \frac{1}{r\Delta r}\frac{\partial}{\partial\eta}\left[\frac{r\Gamma_\phi(1+G^2)}{\Delta r}\frac{\partial\phi}{\partial\eta} - \Gamma_\phi\frac{G}{\Delta\theta}\frac{\partial\phi}{\partial\xi}\right]$$

$$+ \left[\frac{\Gamma_\phi}{r\Delta\theta}\frac{\partial\phi}{\partial\xi} - \Gamma_\phi\frac{G}{\Delta r}\frac{\partial\phi}{\partial\eta}\right]\cdot\frac{1}{r\Delta r}\frac{\partial(Gr)}{\partial\eta} - \rho\left[\frac{1}{r\Delta\theta}\frac{\partial(\overline{u'\phi'})}{\partial\xi}\right.$$

$$\left. + \frac{1}{r\Delta r}\frac{\partial(\overline{rv'\phi'})}{\partial\eta} - \frac{G}{\Delta r}\frac{\partial(\overline{u'\phi'})}{\partial\eta}\right] + S_\phi \quad . \qquad (A.2.2)$$

The left-hand side of equation (A.2.1) may be written as:

$$\text{L.H.S.} \equiv \frac{\rho}{r\Delta r}\frac{\partial}{\partial\eta}\{r(v-uG)\phi\} + \frac{\rho}{r\Delta\theta}\frac{\partial(u\phi)}{\partial\xi} + \rho\frac{\partial(w\phi)}{\partial z} - \rho\frac{G}{\Delta r}\frac{\partial(u\phi)}{\partial\eta} . \qquad (A.2.3)$$

The combination of equations (A.2.3)and (A.2.2) yields the desired result, namely equation (3.5.3) of section 3.5.

APPENDIX B

The effective-viscosity form of the momentum equation in the (η,ξ,z) coordinate system

The equations (3.4.17) to (3.4.21) relate the Reynolds stresses to the 'turbulent viscosity', μ_t. Direct substitution of these relations into the momentum equations (3.4.14) to (3.4.16) yields - after some rearrangement of terms - the desired equations in terms of the 'effective viscosity', μ_{eff}, given by:

$$\mu_{eff} \equiv \mu_t + \mu \quad . \tag{B.1}$$

The algebraic manipulation is straightforward but rather tedious. The final equations are given below.

u-velocity

$$\frac{\rho}{r\Delta r}\frac{\partial}{\partial\eta}\{ru(v-uG)\} + \frac{\rho}{r\Delta\theta}\frac{\partial u^2}{\partial\xi} + \rho\frac{\partial(uw)}{\partial z} + \rho\frac{uv}{r} = -\frac{1}{r\Delta\theta}\frac{\partial p}{\partial\xi}$$

$$+\frac{G}{\Delta r}\frac{\partial p}{\partial\eta} + \frac{1}{r\Delta\theta}\frac{\partial}{\partial\xi}\left[\frac{\mu_{eff}}{r\Delta\theta}\frac{\partial u}{\partial\xi} - \mu_{eff}\frac{G}{\Delta r}\frac{\partial u}{\partial\eta}\right]$$

$$+\frac{1}{r\Delta r}\frac{\partial}{\partial\eta}\left[\frac{\mu_{eff}(1+G^2)r}{\Delta r}\frac{\partial u}{\partial\eta} - \mu_{eff}\frac{G}{\Delta\theta}\frac{\partial u}{\partial\xi}\right]$$

$$+\left(\frac{\mu_{eff}}{r\Delta\theta}\frac{\partial u}{\partial\xi} - \mu_{eff}\frac{G}{\Delta r}\frac{\partial u}{\partial\eta} - \rho u^2\right)\frac{1}{r\Delta r}\frac{\partial(Gr)}{\partial\eta} + \frac{1}{r\Delta\theta}\frac{\partial}{\partial\xi}\left(\frac{\mu_{eff}}{r\Delta\theta}\frac{\partial u}{\partial\xi}\right)$$

$$+\frac{1}{r\Delta r}\frac{\partial}{\partial\eta}\left(\frac{\mu_{eff}}{r\Delta\theta}\frac{\partial V}{\partial\xi}\right) + \frac{2}{r^2\Delta\theta}\frac{\partial}{\partial\xi}(\mu_{eff}V) + \frac{\mu_{eff}}{r^2\Delta\theta}\frac{\partial V}{\partial\xi}$$

$$- \frac{u}{r\Delta r}\frac{\partial \mu_{eff}}{\partial \eta} - \mu_{eff}\frac{u}{r^2} - \frac{1}{r\Delta\theta}\frac{\partial}{\partial \xi}\left(\mu_{eff}\frac{G}{\Delta r}\frac{\partial u}{\partial \eta}\right)$$

$$- \frac{G}{\Delta r}\frac{\partial}{\partial \eta}\left(\frac{\mu_{eff}}{r\Delta\theta}\frac{\partial u}{\partial \xi} - \mu_{eff}\frac{G}{\Delta r}\frac{\partial u}{\partial \eta}\right) - \frac{1}{r\Delta r}\frac{\partial}{\partial \eta}\left(\mu_{eff}\frac{G}{\Delta r}\frac{\partial v}{\partial \eta}\right)$$

$$- \frac{G}{r\Delta r}\frac{\partial}{\partial \eta}(\mu_{eff}v) - \mu_{eff}\frac{G}{r\Delta r}\frac{\partial V}{\partial \eta} \qquad ; \tag{B.2}$$

v-velocity

$$\frac{\rho}{r\Delta r}\frac{\partial}{\partial \eta}\{rv(v-uG)\} + \frac{\rho}{r\Delta\theta}\frac{\partial(uv)}{\partial \xi} + \rho\frac{\partial(vw)}{\partial z} - \rho\frac{u^2}{r} = - \frac{1}{\Delta r}\frac{\partial p}{\partial \eta}$$

$$+ \frac{1}{r\Delta\theta}\frac{\partial}{\partial \xi}\left[\frac{\mu_{eff}}{r\Delta\theta}\frac{\partial V}{\partial \xi} - \frac{\mu_{eff}G}{\Delta r}\frac{\partial v}{\partial \eta}\right]$$

$$+ \frac{1}{r\Delta r}\frac{\partial}{\partial \eta}\left[\mu_{eff}\frac{(1+G^2)r}{\Delta r}\frac{\partial v}{\partial \eta} - \mu_{eff}\frac{G}{\Delta\theta}\frac{\partial v}{\partial \xi}\right]$$

$$+ \left(\frac{\mu_{eff}}{r\Delta\theta}\frac{\partial v}{\partial \xi} - \mu_{eff}\frac{G}{\Delta r}\frac{\partial v}{\partial \eta} - \rho uv\right)\frac{1}{r\Delta r}\frac{\partial(Gr)}{\partial \eta} + \frac{1}{r\Delta\theta}\frac{\partial}{\partial \xi}\left(\frac{\mu_{eff}}{\Delta r}\frac{\partial u}{\partial \eta}\right)$$

$$+ \frac{1}{r\Delta r}\frac{\partial}{\partial \eta}\left(\frac{\mu_{eff}\, r}{\Delta r}\frac{\partial v}{\partial \eta}\right) - 2\frac{\mu_{eff}}{r^2\Delta\theta}\frac{\partial u}{\partial \xi} - \frac{1}{r^2\Delta\theta}\frac{\partial}{\partial \xi}(\mu_{eff}u)$$

$$- 2\,\mu_{eff}\frac{v}{r^2} - \frac{G}{\Delta r}\frac{\partial}{\partial \eta}\left(\frac{\mu_{eff}}{\Delta r}\frac{\partial u}{\partial \eta}\right) + \frac{G}{r\Delta r}\frac{\partial}{\partial \eta}(\mu_{eff}u)$$

$$+ 2\,\mu_{eff}\frac{G}{r\Delta r}\frac{\partial u}{\partial \eta} \qquad ; \tag{B.3}$$

w-velocity

$$\frac{\rho}{r\Delta r}\frac{\partial}{\partial \eta}\{rw(v-uG)\} + \frac{\rho}{r\Delta\theta}\frac{\partial(uw)}{\partial\xi} + \rho\frac{\partial w^2}{\partial z} = -\frac{d\bar{p}}{dz}$$

$$+ \frac{1}{r\Delta\theta}\frac{\partial}{\partial\xi}\left[\frac{\mu_{eff}}{r\Delta\theta}\frac{\partial w}{\partial\xi} - \frac{\mu_{eff}G}{\Delta r}\frac{\partial w}{\partial\eta}\right] + \frac{1}{r\Delta r}\frac{\partial}{\partial\eta}\left[\frac{\mu_{eff}(1+G^2)r}{\Delta r}\frac{\partial w}{\partial\eta}\right.$$

$$\left. - \mu_{eff}\frac{G}{\Delta\theta}\frac{\partial w}{\partial\xi}\right] + \left(\frac{\mu_{eff}}{r\Delta\theta}\frac{\partial w}{\partial\xi} - \mu_{eff}\frac{G}{\Delta r}\frac{\partial w}{\partial\eta} - \rho uw\right)\frac{1}{r\Delta r}\frac{\partial(Gr)}{\partial\eta} \quad . \qquad (B.4)$$

APPENDIX C

Integration of the ϕ-conservation equation over the main control volume

The partial-differential equation appropriate to the general variable ϕ is equation (4.3.1) of chapter 4. This is to be integrated over the control vell for ϕ, the cross-section of which is depicted in figure (4.3.1). The differential volume element is given by,

$$dV = r\Delta r \; \Delta\theta \; d\xi \; d\eta \; dz \quad . \tag{C.1}$$

The notation used throughout is that of section (4.3.1). The left-hand side (L.H.S) of equation (4.3.1) yields, on integration over the control volume:

$$\begin{aligned} \text{L.H.S.} = & \int_{z_u}^{z_p}\int_{\xi_w}^{\xi_e} \rho(v-uG)r\phi\Big|_s^n \;\Delta\theta d\xi dz + \int_{z_u}^{z_p}\int_{\eta_s}^{\eta_n} \rho u\phi\Big|_w^e \;\Delta r d\eta dz \\ & - \iiint_V \rho \;\phi\; \frac{\partial\Delta r}{\partial\xi}\; d\xi d\eta dz \\ & + \int_{\xi_w}^{\xi_e}\int_{\eta_s}^{\eta_n} \rho w\phi\Big|_u^p \; r\Delta r \;\Delta\theta d\xi d\eta dz \end{aligned} \tag{C.2}$$

On integration, the right-hand side (R.H.S) reduce to:

$$\text{R.H.S.} = \int_{z_v}^{z_p}\int_{\eta_s}^{\eta_n} \left[\frac{\Gamma}{r\Delta\theta}\frac{\partial\phi}{\partial\xi} - \frac{\Gamma G}{\Delta r}\frac{\partial\phi}{\partial\eta}\right]_w^e \Delta r d\eta dz$$

$$+ \iiint\limits_V \left(\frac{\Gamma}{r\Delta\theta}\frac{\partial\phi}{\partial\xi} - \frac{\Gamma G}{\Delta r}\frac{\partial\phi}{\partial\eta}\right)\frac{\partial\Delta r}{\partial\xi}\, d\xi d\eta\, dz + \int_{z_u}^{z_p}\int_{\xi_w}^{\xi_e}\left[\frac{\Gamma(1+G^2)r}{\Delta r}\frac{\partial\phi}{\partial\eta}\right.$$

$$\left. - \frac{\Gamma G}{\Delta\theta}\frac{\partial\phi}{\partial\xi}\right]_s^n \Delta\theta d\xi dz + \iiint\limits_V \left(\frac{\Gamma}{r\Delta\theta}\frac{\partial\phi}{\partial\xi} - \frac{\Gamma G}{\Delta r}\frac{\partial\phi}{\partial\eta} - \rho u\phi\right)\frac{1}{r\Delta r}\frac{\partial(Gr)}{\partial\eta}$$

$$. \; r\Delta\theta\Delta r d\eta d\xi dz$$

$$+ \iiint\limits_V S_\phi \; r\Delta r \; \Delta\theta \; d\eta \; d\xi \; dz \qquad (C.3)$$

Combination of equations (C.2) and (C.3), and re-arrangement of the integral terms leads to the following equation:

$$I_1 + I_2 + I_3 = I_4 + I_5 \quad . \qquad (C.4)$$

where the integrals I_i etc are:

$$I_1 \equiv \int_{z_u}^{z_p}\int_{\eta_s}^{\eta_n}\left[\rho u\phi - \frac{\Gamma}{r\Delta\theta}\frac{\partial\phi}{\partial\xi} + \frac{\Gamma G}{\Delta r}\frac{\partial\phi}{\partial\eta}\right]_w^e \Delta r\; d\eta dz \quad , \qquad (C.5)$$

$$I_2 \equiv \int_{z_u}^{z_p}\int_{\xi_w}^{\xi_e}\left[\rho(v-uG)r\phi - \frac{\Gamma(1+G^2)r}{\Delta r}\frac{\partial\phi}{\partial\eta} + \frac{\Gamma G}{\Delta\theta}\frac{\partial\phi}{\partial\xi}\right]_s^n \Delta\theta d\xi dz, \qquad (C.6)$$

$$I_3 \equiv \int_{\xi_w}^{\xi_e}\int_{\eta_s}^{\eta_n}\left[\rho w\phi\right]_u^p r\Delta\theta \; \Delta r \; d\eta \; d\xi \quad , \qquad (C.7)$$

$$I_4 \equiv \iiint\limits_V S_\phi \; r\Delta\theta \; \Delta r \; d\eta \; d\xi \; dz \quad , \qquad (C.8)$$

$$I_5 \equiv \iiint_V \left(\frac{\Gamma}{r\Delta\theta} \frac{\partial\phi}{\partial\xi} - \frac{\Gamma G}{\Delta r} \frac{\partial\phi}{\partial\eta} - \rho u\phi \right) \left(\frac{1}{r\Delta r} \frac{\partial Gr}{\partial\eta} - \frac{1}{r\Delta r} \frac{\partial\Delta r}{\partial\xi} \right) dV \qquad \text{(C.9)}$$

From the definitions of Δr and G (equations (3.4.10) and (3.4.12)) respectively, the terms in the second bracket of I_5 reduce to:

$$\frac{1}{r\Delta r} \frac{\partial}{\partial\eta} \left\{ \frac{dr_s}{d\theta} + \eta \frac{d\Delta r}{d\theta} \right\} - \frac{1}{r\Delta r} \frac{d\Delta r}{d\theta} = 0$$

Consequently I_5 is identically zero, and the final integrated form of (4.3.1) is given by equation (4.3.3) of the main text.